UNIVERSITÀ DEGLI STUDI DI CATANIA
DIPARTIMENTO DI FISICA E ASTRONOMIA

DOCTOR OF PHILOSOPHY IN PHYSICS
XXXVI CYCLE

Study and development of a new diagnostic system based on SiC technology for relative dosimetry and proton beam range detection

PhD THESIS

MARIACRISTINA GUARRERA

Tutor

Prof. S. Romano

Supervisors

Dr. G.A.P. Cirrone
Dr. G. Petringa

A.A. 2022/2023

Summary

Introduction

Since 1945, when it was initially proposed that the process of arresting charged particles in matter could be exploited for tumor treatment, Hadrontherapy has undergone significant advancements. It has gained widespread recognition globally, marking a remarkable progression in its adoption and application. However, despite its improved ballistic and radiobiological efficacy, the diffusion of Hadrontherapy remains limited compared to traditional radiotherapy carried out with conventional photons and electrons. This is mainly linked to the need for large and expensive acceleration systems, and to the presence of uncertainties, strictly connected to the methods used for treatment planning, affecting the estimation of the in-vivo range of charged particles. The range in tissue is associated with considerable uncertainties caused by imaging, patient setup, beam delivery and dose calculation. Unlike photon radiotherapy, similar uncertainties in proton therapy can result in significantly compromised target coverage and/or normal-tissue sparing, which limits the full potential of proton therapy. To compensate for range uncertainty, the practice of expanding the margins of the treatment volume remains established today. However, this is a partial solution, as the overall dose absorbed by the patient consequently increases.

In this context, the acquisition of the Percentage Depth-Dose distribution (PDD) plays a fundamental role within the beam quality control programs, as it allows for beam range estimation. The dosimetric protocol in force (IAEA TRS 398) recommends the use of the ionometric method for the measurement of the PDD distribution of proton beams, a method which, although well established, is time-consuming and exhibits a spatial resolution of the order of 0.1 mm. Moreover, it is not suitable for high-intensity and high-dose rate beams, such as those required for Flash Radiotherapy, a new possible radiotherapy methodology characterized by a dose release at ultra-high dose rates (>40 Gy/s). The latter has attracted the attention of the scientific community as the release of doses at such rates seems to reduce radio-induced damage to healthy tissues without decreasing anti-tumor efficacy. However, the investigation into the FLASH effects is still ongoing, as the availability of beams with dynamic regimes adequate to achieve FLASH conditions and the procedures suitable for their dosimetric characterization represent a challenge today.

An acceleration method capable of producing particle beams with features suitable for investigating the effects of Flash Radiotherapy is the one based on the interaction of intense laser pulses with ultrathin targets. The laser-target acceleration scheme has attracted the attention of the scientific community thanks to its concrete possibility of representing a new compact and versatile particle acceleration method. Indeed, the laser-target interaction is accompanied by the production of multiple ions (typically, protons are dominant), electrons and electromagnetic radiation. The possibility of generating a multiparticle radiation field with a single acceleration system is of interest for many fields of fundamental and applied research, beyond medical applications. Nevertheless, laser-driven beams exhibit significantly different characteristics from those produced by radiofrequency accelerators (including pulsed regime, high intensity, high angular divergence, high energy spread), which require the development of new dosimetric devices and protocols.

These aspects, described in more depth in Chapter 1 and Chapter 2, have led the scientific community to search for innovative methods that allow optimization of the measurement of the PDD distribution of clinical beams, and which are also suitable for the dosimetric characterization of laser-driven beams, in the perspective of the clinical use of Flash Radiotherapy.

The research work I conducted as part of this thesis fits into this context, and develops within the framework of a project called PRAGUE (Proton RAnGe measure Using silicon carbidE), described in Chapter 3. It concerned the design, realization, and characterization of a multilayer detector based on Silicon Carbide (SiC) technology able to reconstruct online the PDD distribution of a proton beam delivered with both conventional and laser-target acceleration schemes. The peculiar properties of SiC devices, including the high radiation hardness, the linearity of their response with energy, and the independence of the response from LET (Linear Energy Transfer) and dose rate, make them good candidates for the purpose. In particular, PRAGUE will be composed of 60 new-generation SiC devices (sensitive area of 15 × 15 mm^2 and active thickness of 10.3 μm) placed in a stack configuration that will facilitate the acquisition of the PDD distribution (at a distal fall-off longitudinal spatial resolution of ~30 μm water equivalent thickness) of a proton beam with energy between 30 MeV and 150 MeV.

My work covered the realization and characterization of a prototype of the final PRAGUE detector, aimed mainly at studying the ability of a multilayer system of SiC devices to reconstruct the depth dose distribution of proton beams. Specifically, I was responsible for designing the layout of the detector and characterizing the devices that compose it, four p^+n SiC devices with sensible area of 1x1 cm^2, active layer of 10 μm, passive layer of 120 μm, and a doping concentration $N_D = 0.5 - 1 \cdot 10^{14}$ cm^{-3}. Irradiation tests were carried out with conventional proton beams. The first test was carried out with a monochromatic beam of 30 MeV protons, delivered at the Institute of Nuclear Physics Av Čr (Řež ÚJV Řež Centre, in Czech Republic). During this experimental run, the response of the detectors by varying the LET of the incident radiation was analyzed, and the ability of the entire system to correctly reconstruct the PDD distribution was tested. Furthermore, the equivalent water thickness of the devices was estimated. The response of the prototype was compared to a system of Radiochromic Films arranged in a stack configuration, considered in this context as a reference. In parallel, a cross-calibration was carried out between Radiochromic Films and Alanine devices, in light of the first tests with selected laser-driven proton beams. The second experimental run with protons was carried out at the Proton Therapy Center of Trento (Italy), irradiating the device with a monochromatic beam of 70 MeV clinical protons. During this second run, it was possible to confirm the results obtained with 30 MeV protons, again comparing the response of the prototype with a stack of Radiochromic Films. Contextually, the possibility of covering SiC devices with epoxy resin was also explored. The work conducted for the development and characterization of the prototype and the results of the characterization with protons are reported in Chapter 4. Agreement was obtained between experimental runs, in addition to confirming the feasibility of using a multilayer system of SiC devices to reconstruct the PDD distribution of proton beams.

The second part of my work, described in Chapter 5, concerned the design, development and characterization of the final device. Specifically, this involved the post-processing and electrical characterization of 80 p^+n SiC devices with sensible area of 15x15 mm^2, active layer of 10 μm, passive layer of 110 μm, and a doping concentration $N_D = 0.5 - 1 \cdot 10^{14}$ cm^{-3}, conducted at the Industrial Engineering Department of the University of Rome “Tor Vergata” (Rome, Italy). In addition to the electrical characterization, the response of the devices was tested under X-ray irradiation. Based on these tests, it was possible to choose detectors with suitable characteristics to form the PRAGUE detector. Additionally, the tests allowed for the exploration and extrapolation of their operational features, such as the saturation capacitance, depletion voltage, and thickness of the depletion region. Furthermore, the devices' performance were compared. Moreover, I was responsible for the study and characterization of the acquisition system of the device. It is based on a commercial 64-channel current-to-frequency/charge-to-count converter chip, called TERA08, capable of reading the charge (in terms of counts or frequency) produced independently by each of the detectors that compose PRAGUE. The TERA08 chip is coupled with a National Instrument system equipped with a controller and a peripheral input/output module. In this context, a system of interface boards was designed. It is necessary not only to facilitate the communication between the SiC detectors and the TERA08, but also to make the electronic readout system capable of functioning correctly even in the presence of high-intensity pulsed beams, such as laser-driven ones. Finally, the acquisition program in the LabVIEW environment was developed in its first version in collaboration with the DE.TEC.TOR Srl company (Turin, Italy).

Chapter 1

The challenges of hadrontherapy

1.1 Introduction

Hadrontherapy[1] is a term that has become part of the contemporary medical lexicon, encompassing all types of radiotherapy employing particle beams referred to as "hadrons", traditionally studied primarily in fundamental physics research centers.

The first experimental studies aimed at testing the therapeutic potential of hadrons against tumors began immediately after the invention of the cyclotron by Lawrence and Livingston, in 1932. These studies featured fast neutrons, with kinetic energies ranging from a few MeV to a few tens of MeV, and persisted until the 1980s. They illustrated that it was possible to obtain local control of some tumors using neutron radiation. Nevertheless, neutron therapy was progressively abandoned as the dose[2] distribution was found to offer little improvement over that attainable with X-ray therapy techniques [1]. The growing evidence of severe complications affecting normal tissues put the clinical use of neutrons on a long pause, and by the beginning of the 21st-century, neutron facilities have almost all been decommissioned, and only a few such centers are still functioning [2]. The fate of the charged hadrons would have been different: their history in the field of tumor treatment began in 1945, when Ernest Lawrence asked his student Robert Wilson to clarify the process of arrest of protons in matter. Thanks to his studies, Wilson realized that protons stop in matter following the same depth dose profiles already described by Bragg 50 years earlier [3], and he had the intuition that this could be exploited for the localized treatment of tumors. He understood that the “Bragg peak” could have been “spread” with modulator wheels, focusing the dose release on the tumor, and sparing healthy tissues better than what can be done with X-rays [4]. Interestingly, Wilson also realized that carbon ions could be good candidates for clinical treatments. Since then, different types of particles have been the subject of intensive clinical and radiobiological studies in addition to protons: pions, antiprotons, helium, lithium, boron, carbon, and oxygen ions. Among all these possibilities, only protons and carbon[3] ions are nowadays used in clinical practice, and they represent the focus of an ongoing remarkable scientific and technological development [6]. Since Wilson's intuition in 1946, the number of

---

[1] Other terms often used are “hadron therapy,” “hadrotherapy,” “particle therapy,” “heavy ion therapy” and “light ion therapy” [1].

[2] Radiation dose D is defined as the energy absorbed per unit mass and measured in Gray (Gy); 1 Gy = 1 J/kg.

[3] The treatments with carbon ion beams are often referred to as CIRT, which stands for Carbon Ions Radiation Therapy [5].

hadrontherapy centers in the world, as well as the number of patients treated, has grown exponentially over time. It’s important to mention that, until the end of the 1980s, patients were irradiated with accelerators built for nuclear and subnuclear physics research, and adapted to radiotherapy, with all the resulting drawbacks. Only at the beginning of the 1990s, the era of modern hadrontherapy finally began, with the realization of centers dedicated exclusively to clinical activity. The first to be born was the Loma Linda University Medical Center, in California [7]. The facility, dedicated to proton therapy, was equipped with rotating magnetic systems (the so-called “gantries”) of about 10 meters diameter and a mass of about 100 tons that allowed for the first time to vary the direction of incidence of the proton beam on the patient. In Japan, in June 1994, the first patient was treated with a carbon ion beam of about 4000 MeV at the Heavy Ion Medical Accelerator Centre in Chiba [8]. Currently, proton and carbon ion therapy is practiced in 121 clinical centers worldwide, although the location of these centers shows large variations between geographical areas. Figure 1.1 shows the geographical distribution of these centers around the world.

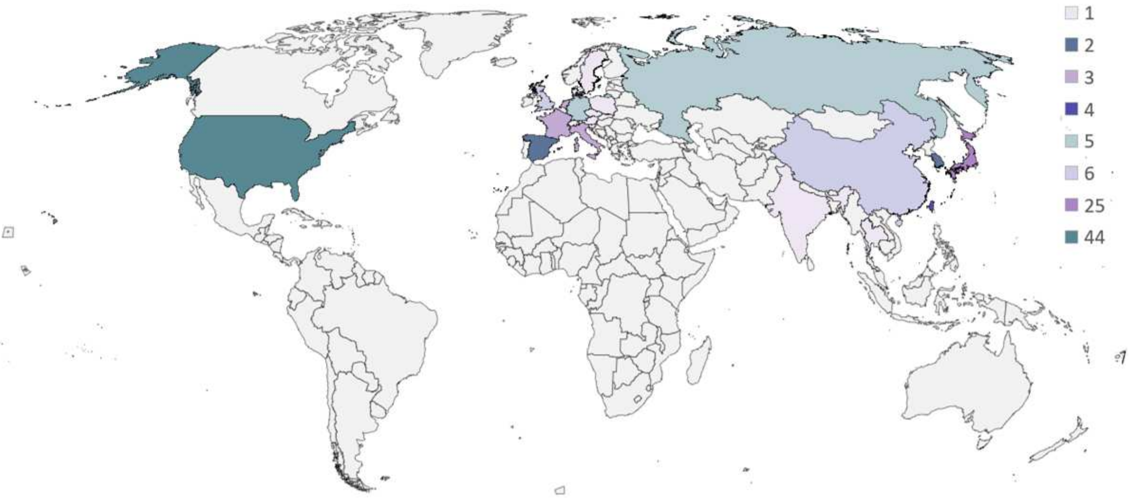

Figure 1.1. Particle therapy facilities in clinical operation; last update August 2023 [9].

Proton therapy centers are mainly located in the United States (44 centers), Europe (20 centers), Japan (19 centers), and the UK (6 centers), while carbon ion centers are located in Japan (7 centers), Europe (4 centers), and China (2 centers) [9]. There are at present 32 proton centers and 5 carbon ion centers under construction, including the first one in the USA. In addition, 35 new facilities (of which 2 will be dedicated to carbon ion therapy) are in the planning phase, with implementation plans expiring by 2026. The overall number of patients treated with protons has reached 300,000 while 50,000 patients have been irradiated with carbon ion radiation therapy worldwide.

Although the success achieved by this therapeutic technique cannot be denied, the worldwide diffusion of hadrontherapy centers remains limited. In fact, the number of patients treated is still very small compared to all the cases that would benefit from proton or carbon ion therapy, and which today are treated with conventional X-ray therapy. A wide implementation of hadrontherapy is difficult because it requires a radio-frequency (RF) ion accelerator (e.g., a rather large cyclotron or synchrotron) and a complex system for transporting and manipulating the ion beam. These technically sophisticated elements have construction, installation, and operational costs[4] that are currently prohibitive for various countries and national healthcare systems. As a result, the high costs of medical services and the need for very large spaces limit their use in hospitals. In this sense, the goal of developing more compact and less expensive technologies represents a challenge for the new frontiers of hadrontherapy.

A possible solution is represented by laser-driven acceleration systems, based on the high repetition rate (up to kHz) interaction of powerful (10^{18}-10^{22} W/cm^2) and short (down to tens of fs) laser pulses with thin (from tens of μm down to tens of nm) target foils [11-15]. Laser-driven systems are attractive due to their potential compactness and low cost compared to RF-accelerators currently operating [10, 16]. Transport lines used for laser light require optical components that are generally small, lightweight, and easy to align compared to the heavy magnets used to transport the ion beam. Moreover, the acceleration schemes based on laser-target interaction can result in the generation of ion beams characterized by very high intensity (up to 10^{10}-10^{14} particles per pulse), broad exponentially decaying energy spectra with a maximum energy of up to ≈100 MeV and very short duration (down to tens of ps) [17]. Such ion beams have the potential to be used in various branches of fundamental physics (i.e., nuclear physics, high energy-density physics, inertial fusion), technology (material engineering), and medical physics (i.e., hadron cancer therapy, production of isotopes for Positron Emission Therapy), and can significantly extend the current scope of ion beam applications [11, 16, 18-26]. In particular, ion beams with such unique characteristics, barely attainable with conventional RF-accelerators, could results in radiobiological dose deposition at an ultrahigh (up to 10^{10}-10^{12} Gy/s) dose rate, making them suitable for investigating the unexplored regimes of what is called FLASH radiotherapy [10, 12, 15, 16, 27-29]. FLASH radiotherapy (FLASH-RT) is a novel radiotherapy methodology defined as an ultra-high dose rate (> 40 Gy/s) radiotherapy that reduces radiation-induced damage to healthy tissues without decreasing anti-tumor efficacy [30-32]. The recent demonstration of these effects for radiation delivered at a very high dose rate has highlighted the FLASH approach as the next step towards an advanced and more effective form of radiotherapy against cancer. The FLASH effect is known to depend on the combination of multiple beam parameters and biological factors. To date, a still large number of questions need to be answered, including the radiobiological explanation of the mechanism that leads to the different response of healthy and diseased tissues to high dose rate radiation, taking into account the entire tumor ecosystem [33-35]. In this context, therefore, the peculiar properties of the laser-driven ion beams can be exploited to continue the scientific investigation on FLASH-RT, favoring the further exploration of the fundamental mechanisms of radiation interaction with biological systems.

---

[4] Costs range from 100 to 200 million euros in the case of a therapeutic center with four treatment rooms [10].

Another element that contributes to the limited diffusion of hadrontherapy is that the latter is a relatively young technique: the consolidated protocols are still limited to solid, non-infiltrating and fixed tumors, and to rare tumors poorly responsive to radiotherapy techniques [36]. Moreover, the precision and accuracy of hadrontherapy are greatly influenced by random and systematic uncertainties associated with the delineation of volumes of interest in 3D imaging, imaging artifacts, tissue heterogeneities, patient immobilization and setup, inter- and intra-fractional patient and organ motion, physiological changes, and treatment delivery [37]. The International Commission on Radiation Units & Measurements (ICRU) Report 24 lists several studies in support of the conclusion that therapeutic systems should be capable of delivering a dose to the tumor volume within 5% of the dose prescribed [38]. It has also been discussed that the uncertainty for an absorbed dose measurement in a phantom[5] should be less than 3–5% [40]. Evidence suggests that a 7–10% change in the dose to the target volume may result in a significant change in tumor-control probability. Such a dose alteration may also result in a sharp change in the incidence and severity of radiation-induced morbidity. Due to the finite range of charged particles, hadrontherapy is more susceptible to tissue-density uncertainties than photon therapy, so achieving the aforementioned dose accuracy in proton therapy is a challenge. In this context, a tool for accurate measurement of the beam range is essential to improve the treatment quality assurance and the therapy effectiveness. In proton therapy, the current attempts of developing a technology capable of a precise verification of particle range are focused both on online/in-vivo techniques and on daily quality assurance methods performed before each treatment session.

All the previous topics represent salient points in the field of current scientific research on hadrontherapy. The subsequent sections will delve into these topics, emphasizing their challenges and prospects.

The physical and radiobiological aspects on which hadrontherapy is based, which have only been mentioned so far, will be explained in the next paragraph (Section 1.2). Specifically, I will focus on proton beams, the latter being the object of the experimental study conducted in this thesis work.

In Section 1.3, the issues relating to the range uncertainty in proton therapy and its clinical impact will be illustrated in more detail, highlighting the importance of making up for them as much as possible.

Below, the innovative aspects, potential, and challenges relating to the clinical success of FLASH beams (Section 1.4) and acceleration systems based on laser-target interaction (Section 1.5) will be explored in depth in the context of new perspectives for greater triumph of hadrontherapy in the world.

---

[5] A medium that has the function of simulating some properties of the human body (or its parts) is commonly denoted in dosimetry as a "phantom" [39].

1.2 The fundamentals of hadrontherapy

Radiotherapy, also referred to as radiation therapy, radiation oncology or therapeutic radiology, is one of the modalities used in the treatment of cancer, the other being surgery[6], chemotherapy[7] and immunotherapy[8]. Cancer is a large family of different diseases affecting practically all the organs of the human body. It appears at the cell level, as a result of a few consecutive genetic mutations. After the neoplastic transformation of a normal cell into a cancer cell, the latter starts to replicate uncontrollably; the quick division produces a tumor volume surrounded by a developed system of blood vessels. At an advanced stage, if cancer cells acquire the ability to spread throughout the body with blood and lymphatic flows, creating secondary tumors named metastases, the cancer disease is called malignant.

Radiotherapy techniques exploit the biological effect of ionizing radiation which, by interacting with the tissue to be treated, releases part of its energy inside the tumor volume, and produces damages to the DNA[9] of cancer cells to the point of inhibiting their ability to divide and reproduce. Biological damage to DNA can be divided into two categories: *direct* and *indirect*. Direct damage occurs when ionizing radiation has the ability to interact directly with DNA, and the ionization processes take place directly on the DNA molecule, altering its structure and functionality. Instead, we speak of indirect biological damage (also called chemical damage) when the ionization phenomenon does not occur directly to the DNA, but to the water molecules present in the cell. This leads to the formation of free radicals[10] which, being very reactive, tend to establish unexpected bonds with the DNA molecule (but not only), deforming its architecture and, again, altering its functionality. Since the cell is mainly composed of water (about 80%) it is easy to understand that the indirect process is the one that is most likely to occur.

In general, the effectiveness of radiotherapy against tumor tissues may be associated with the ability of the radiation to induce DSB[11] (*Double Strand Break*) damage to DNA and the failure of cells to repair it, since DSBs are considered to be a determinant of cell survival and its correct functionality: they can lead to cell death if left unrepaired. The probability of DSB occurring is linked to the intensity[12] of the ionizing radiation, which in turn affects the dose

---

[6] It consists of the surgical removal of the tumor tissue, in part or in its entirety.

[7] It consists of the non-localized administration of drugs with the aim of destroying or preventing, in the most targeted and selective possible way, the cellular reproduction of tumor tissue.

[8] It consists of the administration of drugs capable of awakening and instructing the immune system to recognize and eliminate diseased cells.

[9] The DeoxyriboNucleic Acid (DNA) is the nucleic acid that carries genetic instructions for the development, functioning, growth and reproduction of all known organisms and many viruses. It was isolated for the first time in 1869 [41]. The DNA molecule is a double-stranded organic polymer whose monomers are called nucleotides (the single filament is sometimes called "strand"). The information carried by DNA is contained within genes, made up of a sequence of nucleotides. The sequence of genes in turn constitutes the genetic code [42].

[10] These are electrically neutral atoms or molecules having an unpaired electron in their outermost orbits, a condition that makes them highly reactive.

[11] A Double Strand Break is a radio-induced structural alteration of DNA that consists in the interruption of both the polynucleotide chains of the DNA double helix.

[12] It is defined as $\Phi = dN/da \cdot dt$ and it is the number of particles *dN* that in a time interval *dt* impact on a sphere with maximum section *da* and is measured in [m^{-2}] [43].

rate, and to the spatial microdistribution of the ionization processes along the track of the radiation in the medium, quantified via the Linear Energy Transfer (LET, usually measured in keV/µm) of the radiation [44]. High LET radiation (i.e., alpha, neutrons, ions) produces a dense microdistribution of energy deposition along the particle track, causing more likely direct damage with the production of a clustered DSBs and, therefore, making less effective the mechanisms of cell repair. Low LET radiation, on the other hand, produces an almost uniform spatial microdistribution of ionization events, resulting in damage that is easier for the cell to repair. Figure 1.2 shows the results of the identification and quantification of DSBs induced on DNA by radiation at different LETs through the γ-H2AX foci assay[13] performed at different times after irradiation [46]. Results highlight the different ionization density obtained with different LET radiation and the different repair kinetics for clustered DSBs. The γ-H2AX (or 53BP1, see footnote 13) foci that form in a damaged cell are well known to correlate with the presence of DSBs. Thus, the decrease of foci over time reflects the kinetics of DSB repair (i.e., as the DSBs are repaired, the number of foci decreases).

For densely ionising radiation about 90% of the energy deposited results in clustered damage sites including DSB, while for low LET radiation, about 70% of the energy deposited induces isolated lesions [47]. This is the reason why the same dose absorbed by the same tissue, but released by radiation with different LET, does not produce the same biological effect.

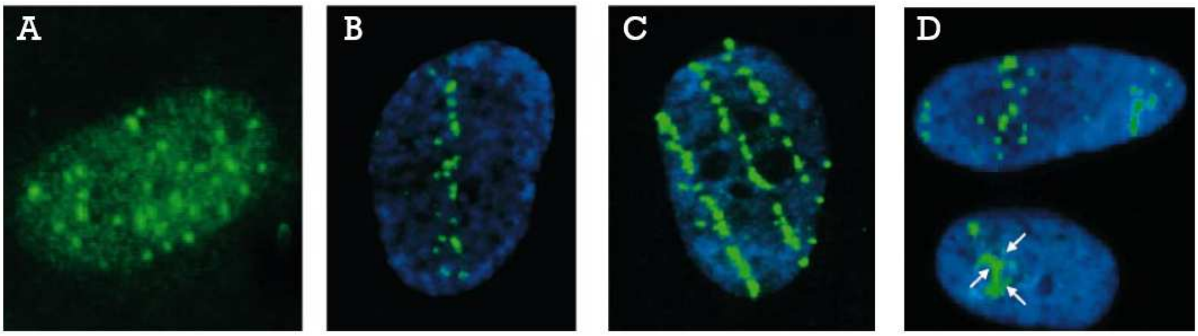

Figure 1.2. γ-H2AX foci assay performed on human fibroblasts irradiated with parallel beams. Results at 10 min postirradiation with (panel A) 2 Gy of γ rays, (panel B) 0.5 Gy of 54 keV/µm silicon ions, or (panel C) 0.5 Gy of 176 keV/µm iron ions. Panel D: result at 5 h after irradiation with 1.7 Gy of iron ions. Arrows indicate areas of possible DNA DSB clustering. Each panel shows the nucleus (blue) and anti-γ-H2AX antibody (green) [46].

---

[13] Nuclear foci induced by DNA damage in response to ionizing radiation represent complexes of signaling and repair proteins that localize to sites of DNA strand breaks in the nucleus of a cell. Technically, cells/tissues are incubated with a specific antibody targeting the signaling/repair protein of interest. The binding of the antibody is then detected with a secondary antibody, which carries a fluorescent tag. Fluorescence microscopy detects the location and intensity of the tag, which can then be quantified. The most commonly assayed proteins for foci formation are γH2AX and 53BP. H2AX is a histone protein, which is rapidly phosphorylated in response to damage to form γH2AX. 53BP1 is also phosphorylated in response to stress and forms nuclear foci at DNA DSB sites [45].

Radiation	**LET [keV/μm]**
Cobalt-60 γ-rays	0.2
250-kV x-rays	2.0
10-MeV protons	4.7
150-MeV protons	0.5
250-MeV protons	0.4
2.5-MeV α-particles	165
4-MeV α-particles	110
5.1-MeV α-particles	88
8.3-MeV α-particles	61

Table 1.1. Typical Linear Energy Transfer values in water [45, 49].

One way to quantify the ability of different radiations to induce biological damage is to evaluate the Relative Biological Effectiveness (RBE[14]), a parameter capable of indicating the effectiveness of a radiation in inducing biological damage compared to a reference radiation. Specifically, RBE is defined as the ratio between the dose released by a 250 keV X-ray beam necessary to produce a certain biological effect and the dose released by the radiation of interest sufficient to produce the same effect, $RBE = \frac{D_{X-Ray}}{D_{Radiation}}$.

The potential adverse effects of radiation therapy are, however, linked to the risk of secondary cancer and/or serious post-radiation complications arising from the unavoidable exposure of healthy tissues. Consequently, the primary objective of radiation therapy is to administer a sufficiently high dose to the tumor while minimizing exposure to surrounding tissues and adjacent organs. In essence, for radiation to be therapeutically effective, it must control the tumor at a dose lower than the one that would cause severe toxicity in healthy tissue. In the clinical context, this consideration is typically assessed by evaluating the Normal Tissue Complication Probability (NTCP) and the Tumor Control Probability (TCP) (Figure 1.3). The TCP is the probability that no clonogenic cell can survive in the treated volume at the end of the treatment, while NTCP describes the likelihood of expected side complications [48].

---

[14] RBE depends on numerous factors, such as the type of ion used, the energy of the beam, the type of tissue to be irradiated as well as its repair capacity, the LET of the radiation, the dose released, and the level of tissue oxygenation. Its value increases as LET increases and dose decreases.

Both TCP and NTCP depend on cell biological effects[15] such as repopulation, repair, redistribution, and re-oxygenation [49]. The region between the NTCP and TCP curves is called the therapeutic window, within which the optimal dose value to be released during treatment is defined. This dose is chosen so as to find a favorable balance between the TCP (ideally equal to 1) and NTCP (ideally equal to 0): for a good radiotherapy treatment it is required to have $TCP \geq 0{,}5$ and $NTCP \leq 0{,}05$.

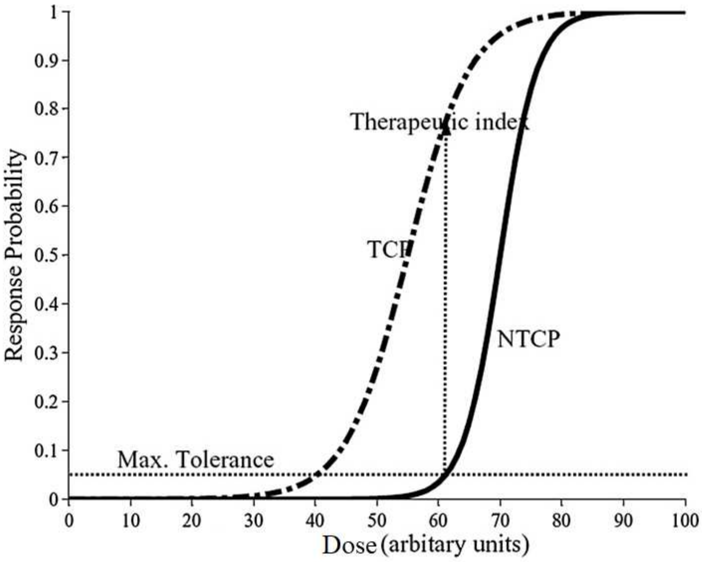

Figure 1.3. Qualitative representation of Normal Tissue Complication Probability (NTCP, solid line) and the Tumor Control Probability (TCP, dashed line) curves. As can be seen, the values assumed by TCP and NTCP undergo an increase as the dose value increases, following a sigmoidal trend. Their slope depends on physical and radiobiological factors, such as the dose rate and the LET of the radiation, the radiosensitivity of the tissue, the design of the treatment plan, and the precision with which it is implemented. The maximum probability for tumor control without normal tissue complications is reached at the Therapeutic index corresponding to maximum required NTCP tolerance [56].

The primary objective of radiotherapy research is to widen therapeutic windows, aiming for an optimized treatment with an increased difference between TCP and NTCP [50-52]. This result can be reached by performing a dose delivery technique that conforms as much as possible to the tumor volume, and exploiting radiation with high RBE [58]. Currently, external beam radiotherapy predominantly employs X-rays (less frequently, electrons as

---

[15] In addition to cell biological effects, TCP and NTCP depend also on the statistical model used. Dose distribution in both the tumor and organs at risk is calculated using specific dose calculation algorithms. Based on the predicted dose distribution, radiobiological models are capable of estimating the TCP and NTCP. These models depend on various statistical and mathematical concepts. The most prevalent TCP models are based on the linear-quadratic (LQ) model, based on clonogenic cell survival curves, including the effects of repair between treatment fractions. It quantifies the effects of both unrepairable damage and repairable damage susceptible to misrepair after tumor irradiation. Other TCP models were proposed [53] in the literature such as the birth-death [54] and Poisson-based [55] models. These models and their variations use information only about the dose distribution and fractionation [56]. The most frequently used analytical NTCP model is the Lyman–Kutcher–Burman (LKB) model, which is a phenomenological approach [57]. Lyman’s model only applies to fractional volumes receiving uniform doses.

well). However, the interaction of photons with matter is characterized by a peak energy release at the beginning of the path, followed by an exponential decay. This characteristic makes X-rays less suitable for treating deep tumors or tumors located near organs at risk, as it becomes challenging to avoid irradiating healthy tissues. To enhance the efficiency of X-ray therapy, various irradiation procedures have been developed over the last few decades. These include Intensity Modulated Radiotherapy (IMRT), Cyberknife, and Tomotherapy [36, 44].

Charged atomic nuclei, such as protons or carbon ions, exhibit a markedly different energy deposition curve compared to X-rays (refer to Figure 1.4). Their dose distribution within tissues features a minimal dose release in the region where the beam enters, followed by a flat area (referred to as the plateau) where the dose released to the medium remains relatively constant, ranging from 10% to 20% of the maximum. Subsequently, as the penetration depth approaches the particle range, the curve experiences rapid growth until reaching the peak region of dose release, known as the Bragg peak. This peak is well-localized and characterized by a sharp decay [59]. There is no dose deposition after this peak for protons and a weak dose deposition for carbons[16] [60]. As will be seen later, the position of the Bragg peak can be set by tuning the incident energy of the particles so that the maximum dose release value occurs at the exact depth at which the tumor is located [59]. In this way, charge particles produce most of the damage to the diseased cells, while sparing both traversed and deeper located healthy tissues. Due to the very small size of the peak (few mm), to paint the volume of a tumor different beam energies are used and superimposed on each other. In that case, the plateau resulting from the combination of different beam energies is called the Spread Out Bragg Peak (SOBP). The dose deposition before the SOBP may be quite large (more than 50% of the maximum) depending on the size of the tumor and the number of beams used to paint it. Another advantage of the particle therapies is that, while traversing biological tissue, heavy charged particles in comparison to electrons or photons, experience less lateral and longitudinal diffusion. They remain well collimated and are characterized by a more precisely defined range, exhibiting reduced range and angular straggling (as described in Section 1.2). These conditions enable the delivery of doses with millimetric precision, contributing to enhanced control over dose delivery. Furthermore, heavy charged particles are more effective in causing tissue damage due to their greater Linear Energy Transfer (LET) and Relative Biological Effectiveness (RBE) in the Bragg peak region. This characteristic makes them particularly well-suited for treating radioresistant tumors [60].

This is particularly true for carbon ions and heavier ions ($Z>6$). In general, indeed, protons exhibit a relatively low ionization density at the entrance that slowly increases near the end of the beam range: at the Bragg peak there is a narrow region of high ionization density. The

---

[16] The nuclear fragmentation process of ^{12}C projectiles leads to deposit some dose beyond the Bragg peak and to spread the dose deposition around the beam direction. The basic knowledge of this process is of crucial importance to compute the dose deposition with an accuracy better than 3%. Additionally, the fragments produced by this fragmentation process can be used for a real-time monitoring of the dose deposition in the patient [44].

local dose deposition and ionization density for ^{12}C ions[17] (due to the z^2 factor in the Bethe-formula, see Section 1.2.1) are higher than those of photons already at the entrance of their path into the material, becoming much higher at low energies near the Bragg peak. As a consequence, for ^{12}C ions it is sufficient to release a dose equal to approximately one third of the dose necessary to obtain the same biological damage caused by X-rays. For protons and alpha particles the necessary dose is respectively 10% and 20% lower than the dose delivered by X-rays.

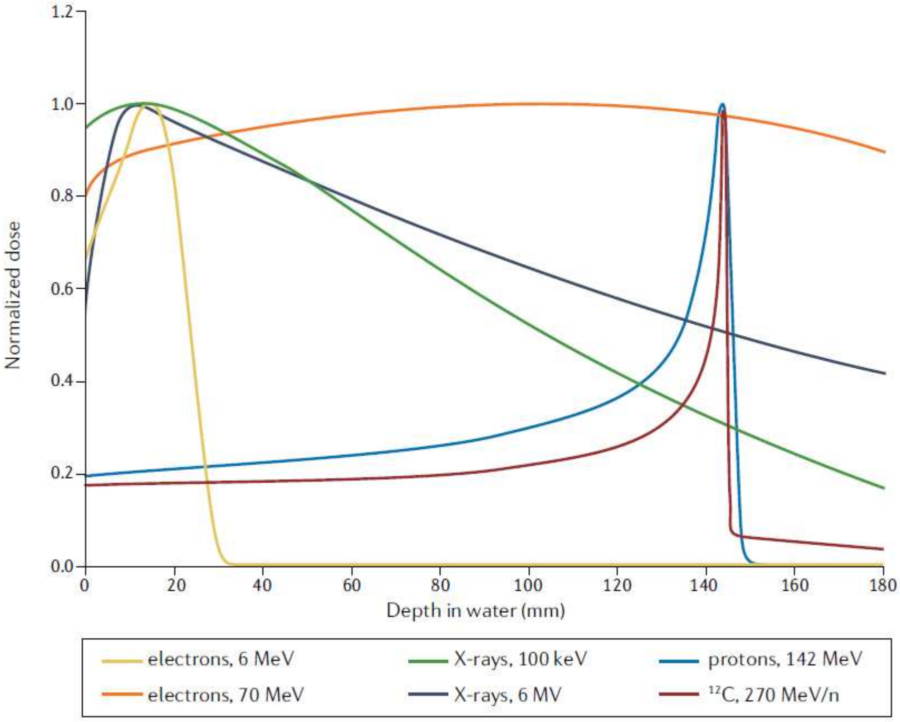

Figure 1.4. Trend of dose release with respect to depth of penetration into water for different radiation fields, water being a convenient proxy for biological tissue. The dose (i.e., the energy deposited per gram of matter) is low when the hadron beam enters the body and is mainly concentrated at the end of the path [32].

In summary, the clinical significance of hadrontherapy stems from its capability to provide precise treatment of tumors with an enhanced RBE, all while minimizing damage to healthy tissue. The physical aspects that make hadrontherapy techniques distinctly favor those of X-ray radiotherapy are based on the radiation-matter interaction methods of heavy charged particles.

A full understanding of the radiation-matter interaction modes of charged particles allows us to solve the two main physics problems that arise in proton radiotherapy: designing beam lines and predicting the dose distribution in the patient [37].

When a beam of charged particles passes through a material, interaction phenomena with the nuclei and electrons of the atoms of the absorbing medium can occur, mainly through three distinct modalities:

---

[17] In particle physics, carbon ions are considered relatively light particles. The convention is different in hadrontherapy, where carbon ions are often referred to as heavy particles to distinguish them from protons.

1. Inelastic interactions with the electrons of the atomic orbitals, called *stopping interactions*: it is the main process that governs the loss of energy of a beam of charged particles when it passes through matter; for this reason this is the interaction mainly taken into account in hadrontherapy planning treatment.

2. Elastic interactions with the nuclei of the atoms of the absorbing medium, called *scattering interactions*: elastic scattering with the target nuclei is a relatively infrequent event that becomes important only for ion energy values lower than 10 keV/u, i.e. in the last micrometers of the projectile's path; this phenomenon is therefore classified as negligible in hadrontherapy.

3. Inelastic interactions with the nuclei of the atoms of the absorbing medium, called *nuclear interactions*: nuclear interactions are the rarest; several semi-empirical geometric interaction models are available to predict their reaction products; they produce alterations in the radiation field which are relevant only for heavy ions such as carbon, while for protons their effect is considered negligible.

Other types of interaction can also take place, such as Cherenkov or bremsstrahlung radiation but, due to their low cross section at the energies of interest in hadrontherapy, they are not considered [44, 60]. In general, the products of these interactions are either excited atoms or ion pairs. Each ion pair is made up of a free electron and the corresponding positive ion of an absorber atom from which an electron has been totally removed. Ion pairs naturally tend to recombine, forming neutral atoms. However, this recombination is intentionally suppressed in certain types of detectors, allowing the ion pairs to serve as the foundation for the detector's response [43].

1.2.1 Stopping Interaction and longitudinal straggling

Heavy charged particles interact with matter primarily through Coulomb forces between their positive charge and the negative charge of the orbital electrons of the absorber atoms, giving rise to inelastic collisions. This process involves a transfer of small fractions of energy from the projectile ion to the target electrons that it encounters along its path: the maximum energy that can be transferred from a charged particle of mass m with kinetic energy E_c to an electron of mass m_e in a single collision is $4E_c{\cdot}m_e/m$, about 1/500 of the particle energy per nucleon [43]. Because this is a small fraction of E_c, the incident particle will lose all of its initial kinetic energy only after many interactions. Furthermore, during its path, it interacts simultaneously with many electrons, at such a high frequency that the process can be considered continuous, according to the so-called *continuous slowing-down approximation* (csda), although it is in fact discrete and stochastic [61]. In addition, because electrons are much lighter and interactions occur simultaneously in all directions, ions transmit their energy without deviating appreciably from their input trajectories. As a consequence, the incident particle is slowed down maintaining its track in the material almost straight (except for the end of their path, in which they will have very low speeds and may suffer deflections).

If the energy transferred to the electrons is high enough to completely remove the electrons from the atom (that is, ionization occurs), they will be able to move away from the atom. Ionization occurs more likely when the projectile passes very close to the atom with which it interacts, giving rise to what are called *close collisions*. Otherwise we speak of *distant collisions*, following which the transfer of energy to the electrons will generally be lower than in the previous case, giving rise more frequently to excitation phenomena (i.e., raising the electron to a higher-lying shell within the absorber atom). The secondary electrons set in motion by the primary radiation are called δ-rays when they possess sufficient energy to generate further ionization. The range of such particles is small compared to that of primary ions: they deposit their energy in the immediate vicinity of the point where they were created, so the ionization is still formed close to the primary track. On a microscopic scale, this implies that ion pairs do not normally appear as randomly spaced single ionizations (like for photons), but there is a tendency to form many "clusters" of multiple ion pairs distributed along the path of the particle.

To describe the energy loss of an ion beam following the stopping interactions, a physical quantity known as *electronic stopping power*[18], $S = -\, dE/dx$, is introduced. S is defined as the infinitesimal loss of energy dE suffered by the incident particle in crossing a thickness dx of the absorbing medium and is usually measured in [MeV/cm]. A first attempt to derive a mathematical expression capable of describing this quantity is due to Bohr who, with a classical approach, conducted his reasoning using the concept of impact parameter [62]. Subsequently, Bethe and Bloch extended the result making it valid also for relativistic particles by resorting to the concept of momentum transfer. The energy loss per unit length is therefore described by the so-called Bethe-Bloch formula:

$$-\frac{dE}{dx} = \frac{2\pi r_e^2 m_e c^2 \rho z^2 N_a}{\beta^2} \cdot \frac{Z}{A} \cdot \left[log\left(\frac{2 m_e \gamma^2 v^2 W_{max}}{<I>^2} \right) - 2\beta^2 - \delta - 2\frac{C}{Z} \right] \tag{1.1}$$

where:

- m_e and r_e are respectively the rest mass and the classical radius of the electron (m_e=0.5110 MeV/c^2, r_e=2.818 fm);
- ϱ is the density of the crossed material;
- c is the speed of light (c = 299 792 458 $m/s \approx 3x10^8\, m/s$);
- z and v are respectively the charge of the projectile in units of e and its velocity (e is the charge of the electron, $e = 1.602x10^{-19}C$);
- N_a is Avogadro's number ($N_a = 6.022x10^{23}$);
- Z and A are respectively the atomic number and the mass number of the material;
- $\beta = v/c$;

---

[18] In a first approximation we can identify the Stopping Power, the LET, and the absorbed energy in the elementary volume of thickness dx. The LET value for protons is around 3 MeV/mm at the Bragg Peak. For ^{12}C ions, the LET value is around 80 MeV/mm [44].

- $\gamma = \frac{1}{\sqrt{1-\beta^2}}$ is the Lorentz Factor;
- δ is the density correction factor, important at high energies;
- C is the shell correction factor, important at low energies;
- W_{max} is the maximum energy transferable in a single collision;
- $< I >$[19] is the average value of the ionization potential of the medium.

The Bethe-Bloch formula is valid when the energy of the incident particle is much higher than $< I >$. The characteristic that makes equation (1.1) interesting in a therapeutic point of view is the dependence of $-dE/dx$ on the $1/\beta^2$ factor (Figure 1.5(a)):

1. for high speed (i.e. energy) values, the factor $1/\beta^2$ takes on almost constant values and the logarithmic term becomes dominant;

2. as the particle passes through the medium, it loses energy and its speed decreases to the value $v = 0.96\ c$ corresponding to the minimum value of $-dE/dx$, called Minimum Ionizing Point (MIP);

3. at speeds lower than $v = 0.96\ c$, the dependence of the stopping power on the factor $1/\beta^2$ dominates, resulting in $-dE/dx$ proportional to $1/\beta^2$: this means that the energy loss increases as the speed of the projectile decreases;

4. at lower velocities (for light ions below about 10 MeV/u), the Bethe formula begins to fail as charge exchange between the particle and the absorber becomes important: the positively charged particle will tend to pick up electrons from the absorber, which effectively reduces its charge. Consequently, Bethe-Bloch formula is no longer valid: to extend its validity also in this energy range, z in equation (1.1) has to be replaced by the effective charge z_{eff}, which can be described by the empirical formulas [60].

The curve that describes the trend of energy loss as a function of the depth of penetration into the absorbing material is called the Bragg curve and is characterized by the presence of a peak, called the Bragg peak (Figure 1.5(b)). The maximum rate of energy loss, corresponding to the Bragg peak, is reached at a projectile velocity of:

$$v_{peak} = z^{2/3} \cdot v_0 \tag{1.2}$$

where $v_0 = e^2 \cdot 2\pi/h$ is the Bohr velocity and corresponds to a value of $\beta = 1/137$ [60]. According to what has been said, three main conclusions can be reached:

---

[19] <I> regulates the energy loss of the projectile (and consequently its range) in the medium. It can be determined experimentally and the ICRU recommended value for biological tissue is 75 eV. A variation of the <I> value equal to 5 eV leads to a variation on the particle range of approximately 1 mm [44].

1. most of the energy of the particles is lost at the end of the path in the material (few mm), when the particles are about to stop;
2. the path of charged particles in a given absorber material is characterized by a well definite distance beyond which no particles will penetrate, a quantity called range;
3. the penetration depths at which the range and the Bragg peak are found depend only on the type of particle and its initial energy for the same crossed medium.

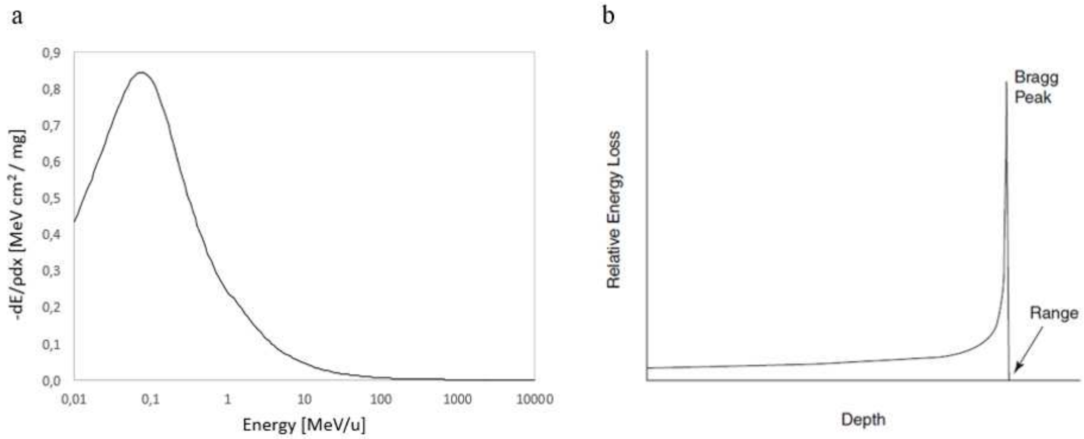

Figure 1.5. a) Evolution of the proton energy loss per unit length in water. Calculated through SRIM [63].
b) Qualitative representations of the Bragg curve.

An essential consideration, however, is that the processes governing the interaction of radiation with matter, dictating how energy is released in a medium, are primarily dominated by stochastic effects. This implies that, given a beam of N identical particles with initial kinetic energy E_c passing through the same material, the type, number, and intensity of the interactions that each of the N particles will have with the atoms of the material does not will be exactly the same of the other $N - 1$ particles in the beam. This, in turn, results in each particle losing energy slightly differently than the others. Therefore, following the passage of an initially monoenergetic beam of charged particles through an absorber, there will always be a broadening of the energy spectrum, an effect called *energy straggling* [43]. Naturally, considering that the maximum distance that they can reach before stopping in a medium depends on the energy possessed by the particles, the presence of energy straggling will have as a direct consequence the *range straggling* or *longitudinal straggling* σ_R, evaluated as Gaussian to first approximation. Range straggling is nothing other than the fluctuation of the stopping distance of the individual particles belonging to an initially monoenergetic beam. If the initial kinetic energy E_c of the particle and the stopping power $- dE/dx$ are known, in the hypothesis that the energy loss occurs continuously (according to the csda), the theoretical expression used to calculate the range R of a heavy charged particle in a material is:

$$R = \int_{E_c}^{0} \left(-\frac{dE}{dx}\right)^{-1} dE \tag{1.3}$$

Actually, the experimentally measured range[20] value differs significantly from that expected according to (1.3) due to the phenomenon of dispersion mentioned before. Generally, to calculate its expected value, empirical formulas developed on a case-by-case basis are used. It is shown that the relative value of longitudinal range straggling σ_R is:

$$\frac{\sigma_R}{R} \propto \frac{1}{\sqrt{m}} \tag{1.4}$$

where m is the mass of the projectile. As a consequence, heavier charged particles experience lower relative range straggling than lighter ones. For example, ^{12}C ions have a relative straggling range approximately 3.5 times smaller than protons [44]. To experimentally evaluate R for a beam of $N_{incident}$ particles, the transmission curve of the beam is constructed by analyzing the fraction of particles transmitted $N_{transmitted} / N_{incident}$ as the thickness of the medium crossed varies (Figure 1.6). Starting from the beam transmission curve, the range is determined in terms of the mean R_{mean} or extrapolated R_{extr} range. The first is defined as the thickness beyond which half of the particles initially present are not able to continue. The second is obtained by extrapolating the linear part of the curve to zero. From the difference between R_{extr} and R_{mean} we obtain the value of the straggling range σ_R, corresponding to the standard deviation of the particle range distribution having an average value equal to R_{mean}.

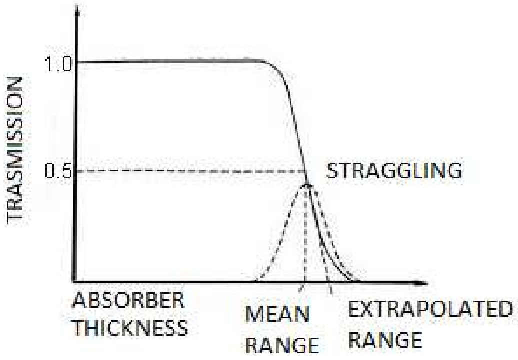

Figure 1.6. Qualitative representation of the transmission curve for charged particle beam; R_{mean}, R_{extr} and σ_R are also reported.

In Figure 1.7 the effect of range straggling on the depth dose distribution in water of a 270 MeV/u ^{12}C beam can be observed. Comparing the dose distribution in depth of the beam (number of particles of the order of 10^8 or more) with that obtained with a single ion, it is clear that the Bragg peak of the beam is broadened. Consequently, the peak-to-entrance ratio is reduced, going from a value of 60 for the ion to a value of 5 for the beam. Of course, the intrinsic width $\Delta E/E$ of the energy distribution with which the beams are produced by accelerators also contributes to range straggling, but it is typically of the order of 10^{-3} (or

---

[20] The range is usually reported in mass thickness, a quantity obtained by multiplying the thickness crossed [*cm*] by the density of the medium [g/cm^3] and expressed in [g/cm^2]: this has the advantage of "normalizing" the absorbing substances, so that as a first approximation the range depends only on type and energy of the particles.

less) and can only be noticed at low energies, when the effects of straggling are smaller (as overall fewer collisions occur before the ion is arrested) and the Bragg peaks can be extremely sharp [44].

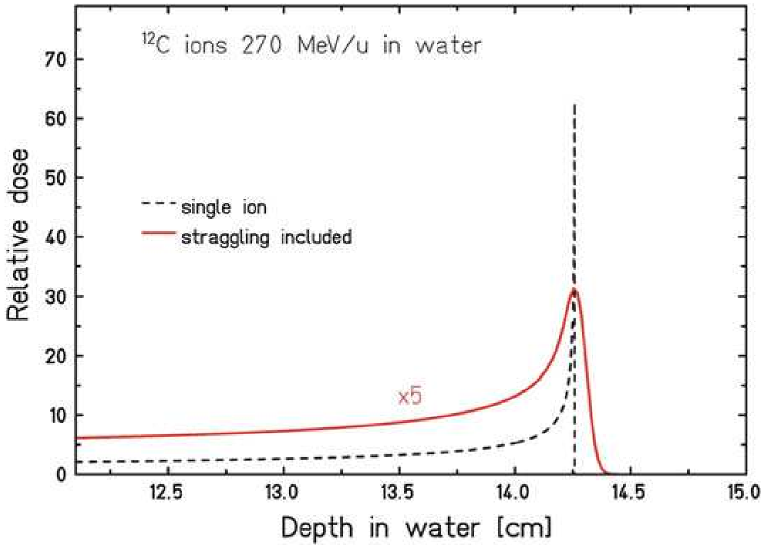

Figure 1.7. Energy deposition of 270MeV/u ^{12}C ions with a range of 14.25 cm in water for a single ion (dashed line) and an ion beam (solid line) [60].

1.2.2 Scattering interaction and lateral straggling

This process, also called Multiple Coulomb Scattering, consists of elastic collisions between the ion and the atomic nuclei, and does not involve the loss of energy by the single ion but its deflection with respect to the direction of incidence of the primary beam. It begins to contribute to the stopping process only for projectile energies lower than 10 keV/u, i.e. at the very end of the particle path (the last few μm) and it is not normally significant in the response of radiation detectors [43]. The cross section of this process was determined by Rutherford in 1911 and it increases as the charge of the projectile increases, while it decreases as the energy increases [64]. Naturally, however thin the target may be, a particle passing through it will interact in succession with multiple nuclei and will therefore undergo several independent deflections: the scattering angle with which it will eventually emerge from the medium will be the result of all the individual deflections. The effect of this type of interaction therefore consists in a *lateral spread* (also called *angular spread* or *angular straggling*) of the beam spot which, consequently, will be less collimated [37].

It is observed that, for small scattering angles θ_0, the spatial distribution of a beam of particles with momentum p and charge z (in units of e) passing through a thickness L of a material medium with mass number A and atomic number Z, studied with respect to the cross section of the beam itself, is almost Gaussian with a standard deviation given by:

$$\sigma_\theta\,[rad] \propto \frac{z}{\beta pc} \cdot \sqrt{L \cdot \frac{Z(Z+1)}{A}} \tag{1.5}$$

This effect is more important for low-momentum particles and for materials with high atomic number Z. Furthermore, the lateral dispersion increases as the length of the segment L traveled through the middle increases. A schematic representation of this effect is shown in Figure 1.8.

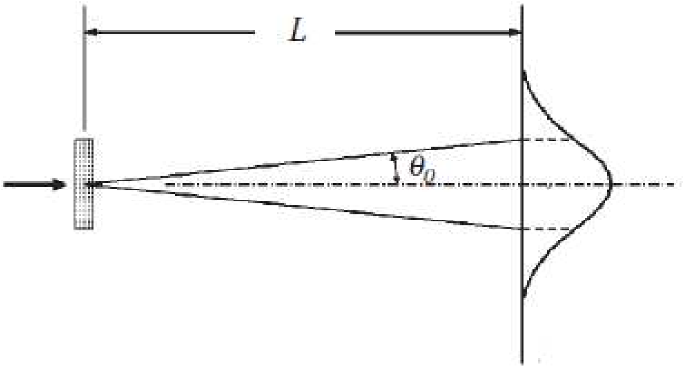

Figure 1.8. Qualitative representation of the angular diffusion experienced by a particle beam after passing through a thickness L of an absorbing material [37].

1.2.3 Nuclear interaction and fragmentation products

At energies of several hundred MeV/u which are required for radiotherapy the most frequent nuclear interactions are peripheral collisions where the beam particles lose one or several nucleons. This phenomenon, in addition to causing an alteration in the nature of the projectile, has as a consequence the emission of secondary particles at energy very similar to the projectile through the processes of fragmentation and evaporation [44, 60]. This holds in particular for heavier ions such as ^{12}C, which may break up (e.g. into three α-particles) in nuclear reactions, producing thereby lighter projectile-fragments at high energies. Proton beams also get attenuated by nuclear reactions, leading among others to the production of secondary neutrons emitted mainly in forward direction. It is known that, for a certain value of initial energy per nucleon, the range of a particle is proportional to the ratio between the mass number A and the charge number z of the projectile A/z^2. Therefore, since the projectile-fragments are smaller in size but with a speed close to the speed of the projectile, they will have a greater range and will deposit their energy at penetration depths greater than that corresponding to the Bragg peak of the primary beam. As a consequence, the energy deposited at the Bragg peak is decreased due to the attenuation of the initial beam and there is the formation of a tail, called *fragmentation tail*, in the depth dose deposition curve. In addition to the projectile, the target nucleus may also undergo fragmentation. However, the target-fragments will have very low energies and will be stopped within a few micrometers of the ion track. In general, therefore, nuclear fragmentation produces a rather complex radiation field which leads to significant alterations in the depth dose distribution. Figure 1.9 and Figure 1.10 show the comparison of the LET evolution in water for ^{12}C (290 MeV/u) and protons (150 MeV) with and without the contribution of nuclear interactions obtained through GEANT4 simulation. As can be seen, the attenuation of the beam due to nuclear interactions is more marked for ^{12}C (where it reaches 50%) than for protons (which stops at 20%). The difference between ^{12}C ions and protons is that the latter only undergo fragmentation of the target, and therefore do not give rise to the fragmentation tail. So, the effect produced by the nuclear interaction on a proton beam is limited to a local increase in energy deposited in the medium along the particle's track, in regions other than the Bragg peak which, consequently, will be less high than theoretically expected in the absence of nuclear interaction.

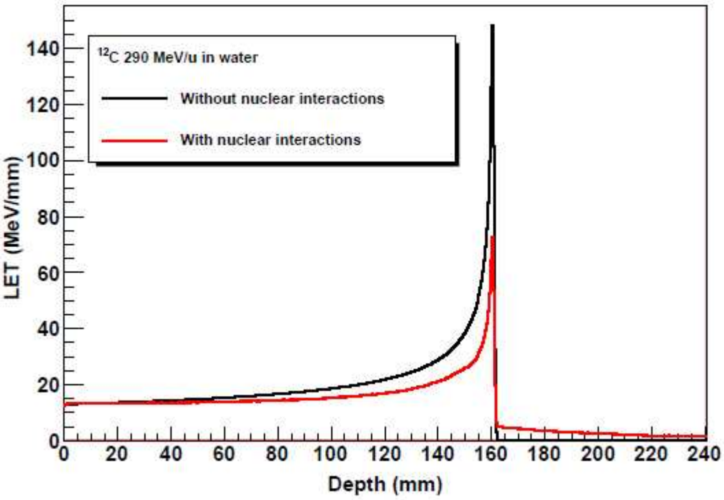

Figure 1.9. Evolution of the mean LET for 290 MeV/u ^{12}C ions with (red line) and without (black line) taking into account nuclear interaction effects. In the presence of nuclear collisions, it is observed that only 50% of the particles of the primary beam reach the Bragg peak, thus leading to a 50% reduction in energy deposition [60].

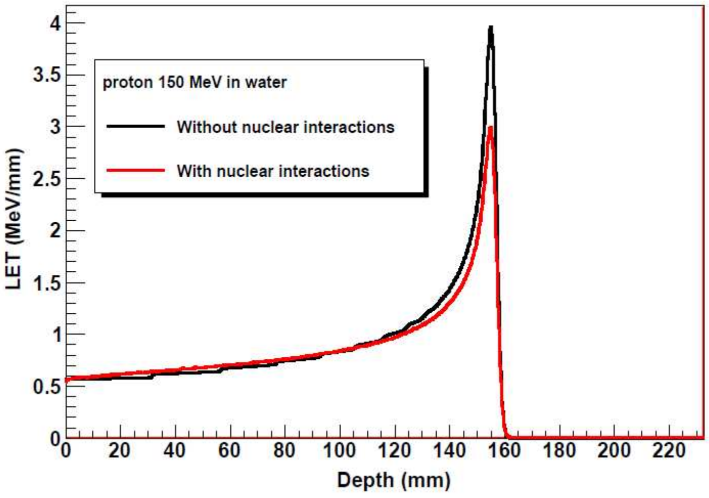

Figura 1.10. Evolution of the mean LET for 150 MeV protons with (red line) and without (black line) taking into account nuclear interaction effects. In the presence of nuclear collisions, the Bragg peak suffers an attenuation of 20%, while at small depths a slight increase in energy release is observed [60].

1.3 Particle range uncertainties

As above mentioned, hadrontherapy plays a pivotal role in the fight against cancer, and the objective of experts is to optimize the treatment's effectiveness in terms of anti-tumour efficacy while minimizing damage to healthy tissue. This objective is pursued through accurate definition of Treatment Planning (TP). The prerequisites for TP are clinical information and a treatment-planning system (TPS).

Clinical information consists of imaging data, usually acquired via computed tomography (CT) examination, dose prescription for the target[21], and dose constraints for surrounding healthy tissues (Organs At Risk, OAR). Imaging data is used to determine the exact location of cancer within the patient and to outline the volumes of interest for the treatment (Planning Treatment Volume, PTV). Magnetic Resonance Imaging (MRI) and Positron Emission Tomography (PET) are often applied in combination with CT to allow for a better definition of the target volume and organs at risk. Moreover, CT provides quantitative information about the anatomical structures of the patient by recording photon attenuation images with a typical pixel resolution of 1 mm and slice thickness of 3 mm [60]. Native CT data (without contrast agents) are essential for calculating the particle range and dose deposited in tissue, and have to be recorded under the same conditions and with the same fixation aids (e.g. head mask) as used later in the treatment. Indeed, through CT scanning it is possible to describe the radiodensity of the tissues. The latter is usually defined through the Hounsfield scale: the Hounsfield unit (HU[22], also termed CT number) is a linear transformation of the original linear attenuation coefficient measurement into one in which the radiodensity of distilled water at standard pressure and temperature (STP) is defined as 0 HU, while the radiodensity of air at STP is defined as −1000 HU. In a voxel with average linear attenuation coefficient μ, the corresponding HU value is therefore given by: $HU = 1000 \cdot \frac{\mu - \mu_{water}}{\mu_{water} - \mu_{air}}$.

Thus, a change of one HU represents a change of 0.1% of the attenuation coefficient of water since the attenuation coefficient of air is nearly zero [36, 66]. To calculate the dose deposition including the exact position of the Bragg peak in heterogeneous tissue, the relationship between HU and stopping power has to be established, in order to perform transformation of patient CT-data to water-equivalent path-length of ions.

The clinical data subsequently serves as input for the Treatment Planning System (TPS), which, considering the specifics of the beam delivery system, enables the determination of the three-dimensional (3D) dose distribution to be administered to the patient. This includes analytical pencil-beam dose calculation algorithms and definition of many beam properties, such as beam direction[23], field shape, and beam weight, in order to provide a 3D dose

---

[21] A prescription for the target consists of a fraction dose and the total number of treatment fractions.

[22] Calibration tests of HU with reference to water and other materials are done to ensure standardized response. The HU is then converted into electron density or relative proton stopping power for photon and proton radiotherapy respectively [36, 65].

[23] Many of the considerations in choosing beam directions also play a role in conformal photon radiotherapy, but they are much more important in proton therapy because of the finite range of protons. An obvious consideration is to avoid organs at risk. In general, beam directions should avoid "skimming" steep density gradients because these may challenge the accuracy of the dose calculation algorithm due to range uncertainties and dose shadowing effects [37].

distribution map for a given accelerator, a given patient, and a specific pathology. Moreover, TPS includes graphic softwares used for reconstruction of a virtual representation of the patient at the moment of treatment delivery. Clinical particle beams are usually provided by cyclotron or synchrotron accelerators and are typically narrow, pencil-like beams centered at the axis of the beam tube. As a consequence, the irradiation of extended target volumes requires the superposition of a number of Bragg curves in order to move the position of the Bragg peak over the whole target volume, giving rise to the already mentioned SOBP. This important task is performed by the beam delivery system, which is designed to distribute the beam over the planned target volume accurately and homogeneously with the desired dose distribution. To date, hadrontherapy treatment can be delivered with passively scattered beams as well as by means of active pencil beam scanning (Figure 1.11).

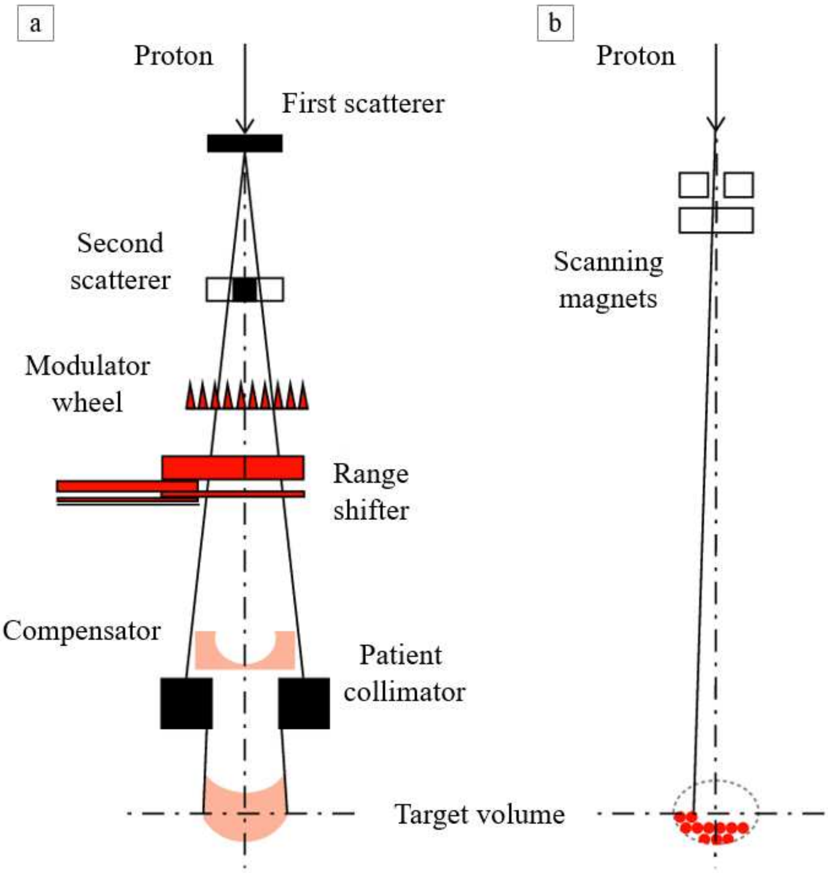

Figure 1.11. Representation of (a) passive and (b) active beam delivery methods [67].

The *passive beam delivery* is obtained by exploiting the natural energy degradation that the beam undergoes by passing through various absorbing materials of variable thickness on its path to the patient. The main components usually present in a passive line are a scattering systems, used to accentuate the lateral dispersion of the beam and to make it homogeneous, a range-shifter, which has the function of modifying the range of the particles, an energy modulator, usually made up of rotating wheels with variable thicknesses, which produce the longitudinal dispersion of the beam, collimators which have the function of conforming the lateral section of the beam to that of the tumor to be irradiated, and, finally, a range compensator which regulates the range of the particles taking into account the complex composition of the tissue crossed and the geometry of the tumor. The main advantage of this method is its simplicity, as the total dose can be delivered without changing the accelerator parameters. Its main drawback is the production of secondary particles (mainly neutrons, protons, and alpha particles) issued from nuclear interaction that may pollute the beam. It also induces longitudinal and lateral spreading. Furthermore, the need to use absorbers made specifically for each patient makes this technique less versatile. This delivery system is widely used in the treatment centers for both proton and ^{12}C beams.

The *active beam delivery* consists in a 3D painting of the tumor by tuning the energy, angle, and point of incidence of the pencil beam directly during its acceleration and extraction. In-depth scanning is obtained by directly modifying the energy of the beam, while the deviation in the two planar directions is obtained through the use of magnets. The target volume is divided into small volumetric elements (voxels) and the pencil beam (typically, with FWHM of 3-10 mm and minimum duration of 1 ms per voxel) is used to deposit the appropriate dose, ideally without any material in the beam path. In this way, a 3D scan of the tumor volume is carried out with potentially much greater precision than passive beam delivery, but it requires excellent beam control and is hence very difficult to achieve.

Before starting the treatment, it is necessary to define the quality Q of the beam being used, a phase indicated as *relative dosimetry*, which in turn is necessary to carry out the dose calibration of the irradiation line, a procedure called *absolute dosimetry*. These operations are usually performed using ionization chambers inside a water phantom and ionization chambers in transmission. These two phases are described in more detail in Chapter 2. In general, during the relative and absolute dosimetry phases, it is necessary to acquire the longitudinal and lateral profiles of the beam, so as to evaluate the particle range and verify that the values assumed by specific characterization parameters fall within the reference ranges established according to the dosimetric protocols in force [40]. The beam characteristics are defined in terms of a set of measurable and calculable parameters, which are used to assess the clinical acceptability of the beams, to benchmark the treatment-planning algorithms used to calculate patient dose distributions, and for routine quality-assurance (QA) purposes [68]. Widely used beam parameters are shown in Figure 1.12. The parameter definitions are as follows:

- *Depth of penetration* (d'_{90}) or *range*[24] is defined as the depth (in g cm^{-2}) along the beam central axis in water to the distal 90% point of the maximum dose value.

---

[24] Ideally, the range would be defined at the position where the dose has decreased to 80% of the maximum dose, i.e. in the distal dose falloff. The reason for this choice is the fact that for a monoenergetic proton beam, the 80% fall-off position coincides with the mean projected range of a proton, i.e. the range at which 50% of the protons have stopped. Furthermore, the 80% fall-off position is thus independent of the beam's energy spread. Nevertheless, in most proton therapy facilities, the prescribed range is defined at the 90% fall-off position in water because of historic reasons [69].

- *Distal-dose fall off* (DDF) is defined as the distance (in g cm^{-2}) in which the dose, measured in water along the beam central axis, decreases from 80% to 20% of the maximum dose value.
- *SOBP length* (m'_{90}) is defined as the distance in water between the distal and proximal 90% points of the maximum dose value.
- *Lateral penumbra* (LP) is defined at a given depth as the distance (in mm) in which the dose, measured along the line perpendicular to the beam central axis, decreases from 80% to 20% of the maximum dose value at that depth.
- *Field size* is defined as the distance (in mm) between the 50% points of the maximum dose value, measured along the line perpendicular to the beam central axis, on the isocenter[25] plane in air.
- *Target* (or *treatment*) *length* is defined as the distance between two DDF lengths (2 DDF) proximal to the distal 50% dose level of the SOBP, and one DDF length (1 DDF) distal to the proximal 90% dose level of the SOBP.
- *Target* (or *treatment*) *width* is defined as the distance between two LP widths (2 LP) from the 50% dose levels of the lateral-beam profile.

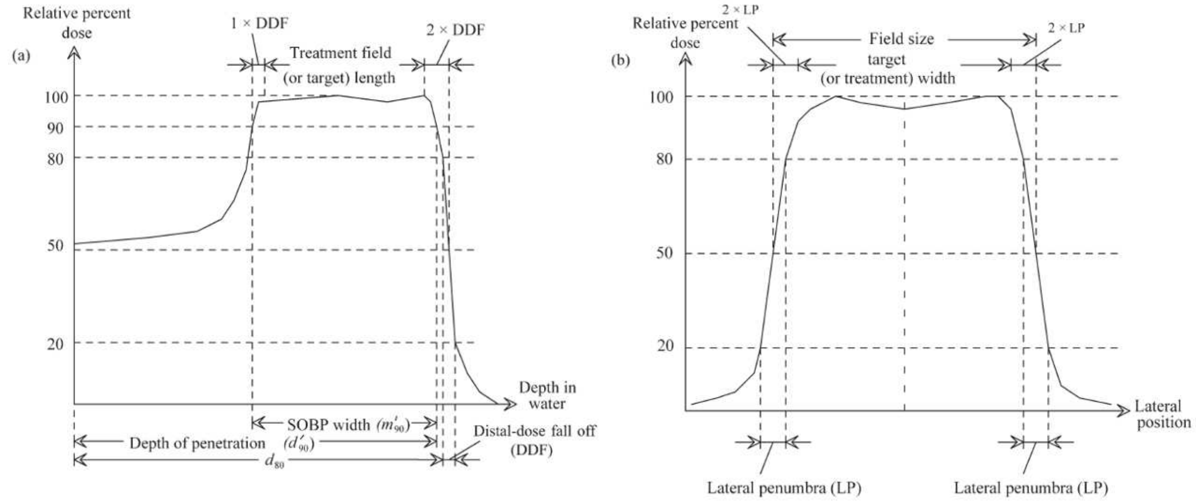

Figure 1.12. (a) Depth–dose curve for an SOBP and (b) a lateral proton-beam profile in the Bragg peak showing some parameters commonly used to characterize the proton dose distribution [68].

From what has been said so far, it is clear that the phases preceding the actual provision of a treatment are multiple and complex. Each of them is affected by an indeterminacy that potentially affects the accuracy and success of the treatment. Similar uncertainties in proton therapy can result in significantly compromised target coverage and/or normal-tissue sparing, which limit the full potential of proton therapy.

The accurate evaluation of the particle range is crucial: once the range has been established, it will be possible to proceed with the dose calibration of the radiation line at the isocenter. It is

---

[25] The point in space relative to the treatment machine about which various components of the delivery system rotate. The gantry rotation defines a horizontal axis which cuts a vertical axis defined by the rotation of the treatment couch. The treatment collimators also rotate about an axis pointing through the isocenter.

clear that the more accurate the range assessment, the smaller the dose uncertainty will be and, consequently, the more accurate the definition of the treatment plan will be. Narrowing our focus to protons, factors contributing to range uncertainties in clinical beams are briefly described below.

- **Inherent physical uncertainties**
  The statistical nature of interactions between radiation and matter for charged particles inherently includes both longitudinal and lateral straggling, as previously noted. Lateral straggling mainly affects the dimension of the LP, the field size, and treatment width, while longitudinal straggling affects the DDF, d'_{90}, m'_{90}, and treatment length (Figure 1.15). Moreover, the loss of energy per unit of path, described by the Bethe-Bloch formula (1.1), shows a dependance from <I>, which regulates the stopping power of the projectile (and consequently its range) in the medium. It can be determined experimentally, but it was found that a variation of the <I> value equal to 5 eV leads to a variation in the particle range of approximately 1 mm. Since hadrontherapy treatments require a particle range precision of 1 mm, this implies that the value of <I> must be known with a margin of error of less than 5 eV [44]. ICRU reports n.37, n.49, and n.73 (1984, 1993, 2005) state a <I> value for water and tissue-equivalent[26] materials respectively of 67, 75, and 80 eV. Results show that this range of <I> values yields a spread of the Bragg peak's depth of up to 3 mm for a 122 MeV proton beam[27] (Figure 1.13). This effect is also energy dependent: it increases as the energy of the beams increases (Figure 1.14) [37, 70].

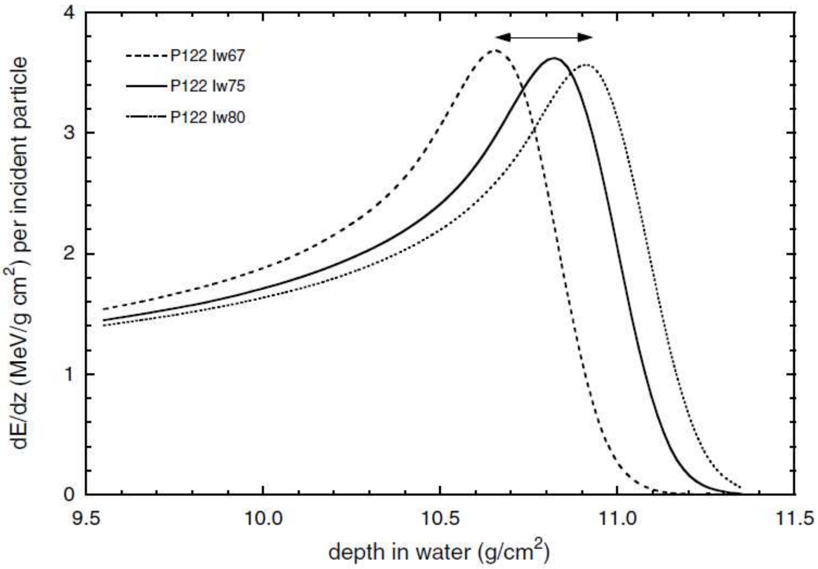

Figure 1.13. Variation of the depth of Bragg peak for the <I> of water 67, 75, and 80 eV for a 122 MeV proton beam: the depth of the Bragg peaks extends over a region of 3 mm [70].

---

[26] Tissue-equivalence describes the property of a material to respond to a given radiation, in a given energy range, in an identical manner as the human body [39].

[27] The value grows up to 7 mm for carbon ions [70].

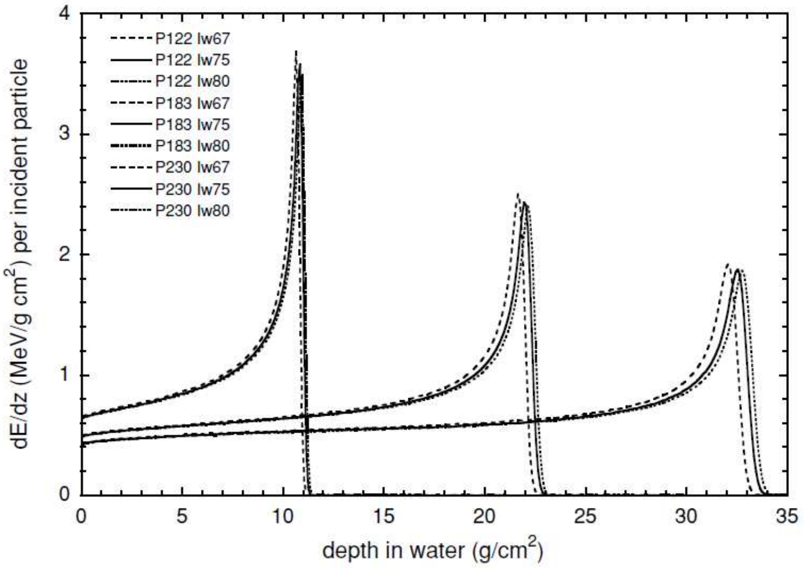

Figure 1.14. Monte Carlo calculated energy-deposition distributions in water irradiated by protons of 122 MeV, 183 MeV, and 230 MeV. For each energy, three distributions are shown corresponding to the <I> of water 67 eV, 75 eV and 80 eV. Differences can be appreciated in these distributions, notably for the highest energies when fragmentation and other energy loss mechanisms compete with electronic interactions. For the 183 MeV protons the spread is about 4.5 mm, while for 230 MeV the spread reaches 7 mm [70].

This implies that empirically determined water I-values from proton (or carbon) depth-dose distributions may vary based on the energy used for experimental determination. This underscores the necessity of allowing the I-value to vary in treatment planning algorithms. This would require an increase in the margins of a clinical target volume and an intrinsic basic physics uncertainty should be added to those margins usually considered in clinical practice. In most cases, attention to the different composition of similar human tissues is also neglected, increasing the uncertainty over the range. This topic will be covered in more detail later.

Another often neglected yet important factor influencing the range of particles in biological tissue is the development of a fragmentation tail resulting from inelastic nuclear interactions. The existence of the fragmentation tail beyond the Bragg peak is an unfavorable circumstance in the context of hadron therapy treatments, as it leads to a release of dose beyond the areas delineated during the treatment planning phase. Protons only produce target fragmentation, so the impact of nuclear interactions in the therapeutic energy range is small except for the shape of the Bragg peak. The nuclear interactions essentially decrease the intensity of the proton beams by producing secondary particles that stop near the projectile track, thus increasing the local absorption of the dose. These particles are important also from the biological point of view because of their higher relative biological effectiveness (RBE) values, but their impact on physical dose distribution is usually considered negligible in clinical context. The probability of nuclear interactions increases with the energy of protons.

- **Inherent uncertainties in the formation of SOBP**

  With both active and passive delivery methods, the range of protons is changed either by inserting absorbers into the beam path or by changing the beam energy upstream. The intrinsic straggling suffered by the particles is therefore accentuated by the presence of absorbers or by the energetic resolution of the beams. Typically, proton-beam energy spread introduces a systematic range of uncertainty of ±0.6–1.0 mm, while the reproducibility of the range is ±1.0 mm for passively scattered proton beams. The nonuniformity of compensator material used in passive delivery methods introduces small uncertainties in their relative stopping power, which in turn affects the range of protons for ±1.0 mm [37]. In addition to longitudinal dispersion, also lateral straggling occurs due to scattering with materials in front of the patient (e.g., vacuum exit window, beam monitor, beam shaping devices, and other elements necessary to perform beam delivery) and scattering in the patient's tissue between entrance point and stopping depth. The contributions of these two scattering sources depend on the type and energy of the incident particle and are illustrated in Figure 1.15. At low energies, the scattering with materials represents the dominant contribution because even a small angular spread translates in a significant broadening of the beam spot due to the traveling distance of typically 0.5 - 1.0 m before entering the patient. This is critical in particular for protons. This is why the material in the beam path in front of the patient should be kept as thin as possible, not contain heavy elements, and be located as close as possible to the patient [60]. At higher energies, the latter contribution becomes almost negligible, while the contribution due to scattering in the patient increases as a consequence of the larger range in tissue. The scattering from the aperture located close to the patient is usually not considered by the analytical algorithm: if not accurately modeled in analytical dose calculations it will mainly affect the proximal part of the Bragg curve, except for very shallow fields [69].

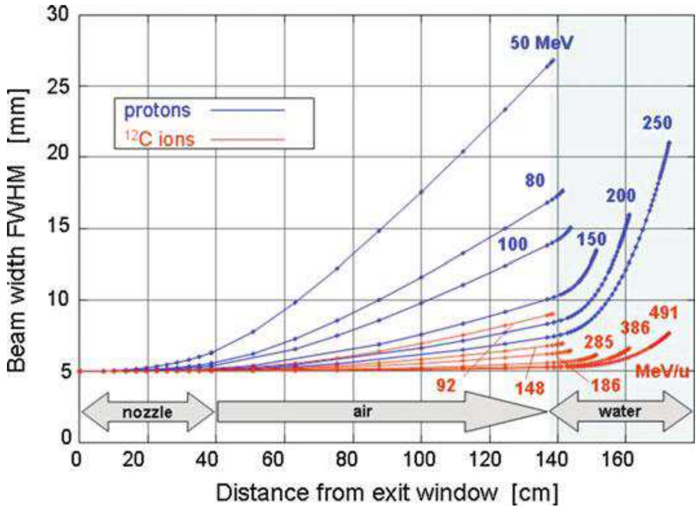

Figure 1.15. Lateral straggling experienced by proton and ^{12}C ion beams in the nozzle, in air and in water (representing patient tissue) for a typical treatment line, measured as the Full Width Half Maximum (FWHM) of the lateral spatial distribution of the beam. In general, a smaller beam spread is observed for ^{12}C ions than for protons [60].

- **CT conversion uncertainties**
  Range uncertainty certainly increases when it comes to predicting range in the patient. Patients are not actually water and present inhomogeneities, so accurate range prediction needs an accurate model of the patient, or more precisely, an accurate model of the relative-linear stopping power (RLSP) of different tissues in the patient. The current state-of-the-art to determine these is by X-ray tomography (CT) imaging [71]. A CT image represents the spatial distribution of X-ray attenuation coefficients. In proton therapy planning systems, the matrix of reconstructed linear attenuation coefficients obtained through the CT image is transformed into a corresponding matrix of Hounsfield unit (HU). HU conversion schemes are then implemented to translate HU into RLSP. There is no simple functional relationship between HU and stopping power [37]. The RLSP values depend on the physical density, elemental composition, and mean excitation energy (I-value) of the material. In previous studies, it has been highlighted that a 4% change in density results in a 4% change in RLSP [72]. The HU-RLSP conversion requires a calibration procedure carried out by scanning tissue phantom materials with known density and elemental composition or through stoichiometric calibration. The accuracy of dose calculation based on CT data is partly determined by the precision of the calibration of HU to RLSP. Several sources of error influence the accuracy of HU-RLSP correlation, like the uncertainty on HU value for homogeneous material (up to 3%), the phantom size, and scanner parameters (such as the photon energy, the scan diameter, and the matrix size) [37, 65]. For sites outside of the lung[28], the range uncertainty due to CT matrix size might be estimated to only about 0.3% for CT resolutions typically used in treatment planning [69]. A final source of error is the approximation of real tissue with phantom material: the chemical composition of commonly used tissue substitutes is different to that of real tissue. Current estimates on the range uncertainty from the whole procedure is of the order of 3%, thus ±3 mm for a Bragg peak at 10 cm water equivalent range in the patient [71]. This is what would be expected for a good quality CT (i.e. CT with high spatial resolution, low noise, and minimal reconstruction artifacts due to high-density materials as metallic implants) and unchanging patients (actually, many patients also change during the course of fractionated therapy, leading to additional changes in in-vivo range). Although new CT acquisitions and reconstruction techniques under investigation can help [73-76], this remains a major source of range uncertainty for some patients. Estimating individual uncertainties for different tissue types enables the use of tissue-specific range uncertainties, which are customized to the specific patient and treatment site.

---

[28] In a relatively homogeneous geometry, the size of the voxels used to divide the geometry for dose calculation plays a minor role. Even for typical head and neck cases significant uncertainties might not be expected based on the CT resolution typically used for treatment planning. Problems could be encountered in highly heterogeneous geometries where the heterogeneities are small, like in lung. Here, materials with low density, i.e. air, and materials with considerably higher density, i.e. soft tissue, might be averaged to obtain the HU for a given voxel.

- **Impact of Tissue-Density Heterogeneities**.
  Even if considerable efforts are put into the conversion of CT Hounsfield units to stopping power or water-equivalent path lengths, the composition of the different body parts plays a major role in governing the interactions of protons and heavier charged particles [70]. Heterogeneities affect the lateral and longitudinal diffusion of protons in the patient. The most extreme scenarios, already highlighted in the 1980s, are found in the region at the base of the skull where protons can be directed along extended bone surfaces or into a complex bone-tissue-air structure, such as the petrous crest or paranasal sinuses. It was found that the distal fall-off from 90 to 20% dose for 160 MeV modulated proton beam passing through regions of the base of skull was increased from its nominal 6 mm to well over 32 mm [77]. Indeed, particularly in this part of the human anatomy, the patient is anything but a homogenous water phantom, and the density heterogeneities through which the beam must pass drastically blur the distal end. Figure 1.16 shows two examples of dose distributions obtained in the presence of high levels of heterogeneity [71].

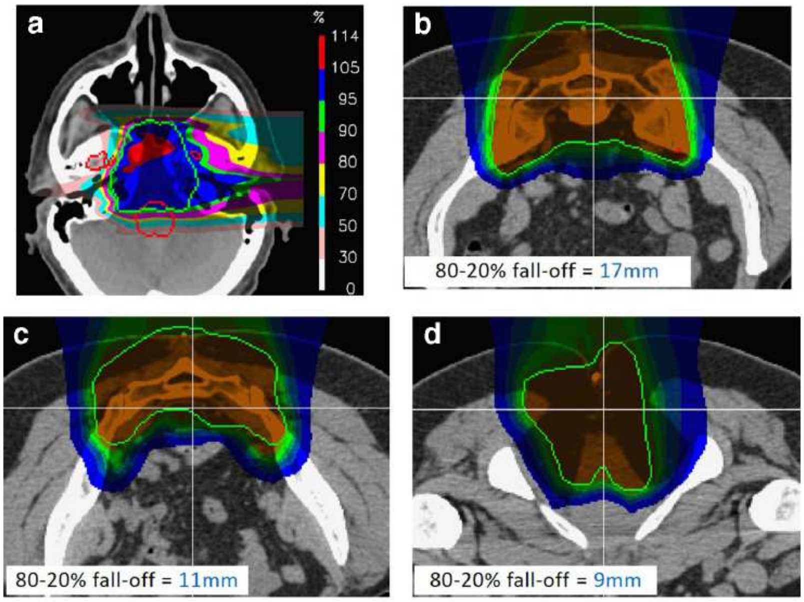

Figure 1.16. Realistic, in-vivo distal fall-offs for proton therapy. (a) Single lateral field to a skull base chordoma. The maximum dose is quite high (114%) and there is an impressive conformation to the target at the 95% dose level (the blue color-wash region). Note the extreme degradation of fall-off at the distal end due to density heterogeneities in the patient. (b–d). Different slices of the same sacral chordoma case [71].

In Figure 1.16(a) a single lateral field to a skull base chordoma can be appreciated. It is optimized to maximize homogeneity and conformality of dose across and to the tumor. However, although the dose drops beyond the distal end of the target, the fall-off is in no way sharp (the lateral fall-off is visibly sharper than the distal). The dose distributions shown in Figure 1.16(b–d) are the results of different levels of a 2-field proton therapy treatment to a sacral chordoma, together with the calculated

80–20% distal fall-offs of the dose distribution along the lines indicated. These vary from 9 mm to 17 mm.

Furthermore, it is essential to take into account the substantial variation in I-values among similar human tissues, although this consideration is typically overlooked in clinical treatment planning involving protons and heavier charged particles. For example, I-values for four different types of the so-called soft tissue[29] range between 70.8 eV and 74.9 eV. Figure 1.17 shows energy deposition distributions of 164 MeV protons in the four soft tissues, and data for two types of muscle, skeletal (82.8 eV) and striated (63.7 eV), have also been included. Even if all the tissues are usually assumed identical in clinical practice, differences of up to 3 mm in the depth of the Bragg peak can be observed [70].

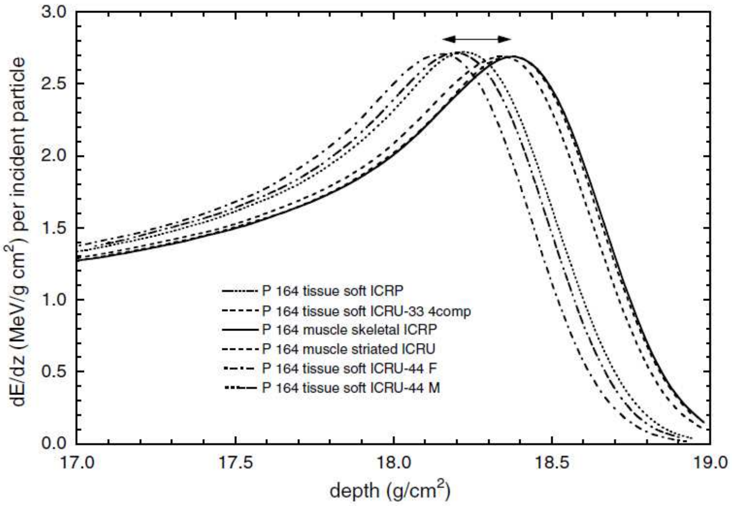

Figure 1.17. Variation of the depth of the Bragg peak for 164 MeV protons in four types of soft tissue (ICRP, ICRU-33 four-component, ICRU-44 adult female and ICRU-44 adult male), and two types of muscle (skeletal and striated), using compositions from ICRU reports 37, 44 and 46 (ICRU 1984b, 1989, 1992).

The results shown in the last figures demonstrate that when different human organs or tissues are to be considered the need for increasing the margins of a clinical target volume, due to the combined effects of tissue composition and the basic physics uncertainty, becomes a matter of importance in proton and heavier charged particle therapy. The dosimetric impacts of these two effects in the presence of heterogeneities in proton beams, relative to what occurs in a homogeneous medium, can potentially be substantial because of the sharp dose falloff characteristics of protons. When designing treatment beams, one must account for the presence of heterogeneities proximal to or within the target volume by not only calculating their influence on target volume coverage but also compensating for range modifications.

---

[29] Under the definition of ICRU-46 (1992), include “all tissues other than osseous tissue, teeth, hair and nails, as well as all the body fluids, muscle-like tissues and fatty tissues (e.g. adipose tissue)”.

Most treatment planning systems use analytical dose calculation algorithms that model range perturbation due to multiple Coulomb scattering in complex structures by using solely the stopping power of materials involved and their water equivalent path length. This approach neglects the position of inhomogeneities relative to the Bragg peak depth and is less sensitive to complex geometries and density variations (e.g. at bone-soft tissue interfaces), simply causing a shift in the distal falloff [69]. Consequently, they are not able to correctly predict the effect of range degradation caused by multiple Coulomb scattering and there is a potential uncertainty in distal edge degradation of at least ±1.0 mm (ignoring the worst case scenario) [37]. It was suggested that Bragg peak degradation can be diminished by increasing the angular divergence of the beam but only at the expense of widening the lateral falloff [77].

- **Range uncertainties due to biological effects**

  In addition to the physical uncertainties, biology can contribute with the so-called biological range extension. This is a consequence of the parallel increase of LET and decrease of dose taking place at the distal fall-off of the SOBP, resulting in an increase of RBE. This effect can result in a significant biological dose in normal tissues beyond the tumor region, thus introducing a shift in the biologically effective range of ~1–2 mm [69]. According to the fixed RBE of 1.1 adopted in proton therapy, this range extension due to a gradually increasing RBE is currently not directly considered in treatment planning. The biological extension does not seem to be dependent on target volume, but it is rather strongly influenced by the width of the distal penumbra, generally becoming more pronounced at higher energies, and by the presence of heterogeneities [78]. Recent radiobiological experiments show that the RBE values at the end of the proton range increase up to 2 [79], supporting the need for proton treatment planning optimization by adopting a variable RBE model [80]. On the other hand, other works suggest the study of approaches that do not depend on tissue parameters or variable RBE models [81]. The production of target fragments as a result of inelastic nuclear interactions of protons can also introduce uncertainty. Target fragments can assume different values of energy and LET. So, it is not a simple issue to determine their contribution to the overall RBE, but since target fragments are usually characterized by low energy and/or high atomic number, they are expected to be associated with an enhanced RBE especially at the entrance channel. It has been reported that about 10% of the biological effect induced in the entrance channel might be associated with target fragments. At the same time, due to the slowing down of primary protons, this contribution is reduced to about 2% when approaching the Bragg peak [78]. In other words, target fragments may contribute to the overall dose deposited in the patient producing a distortion of SOBP if not compensated for in the treatment plan, underlining once again that the setting of RBE=1.1 in treatment planning systems for protons involves an indeterminacy.

- **Positioning, Immobilization, and Localization**
  The ballistic precision of protons can only be exploited if there is a good overlap between the treatment plan and the actual location of the tumor inside the patient. The accuracy of beam placement relative to the patient, that is, relative to the target volume and the organ at risk, is far more important in proton therapy than in photon therapy. Placement accuracies of 1 mm or even less are essential in proton therapy: a positioning inaccuracy can result in no dose or too much dose at the point of interest and/or with the irradiation of nearby critical structures. Achieving the desired placement accuracy requires excellent positioning, immobilization and accurate localization of the patient relative to the treatment equipment. The latter is usually accomplished by the localization of bony landmarks or implanted fiducials. As a result of misalignments of the patient, range will change due to changes in the relative position of density heterogeneities and the patient surface, in relation to the treatment beam [71]. In addition, relative movement of internal structures relative to the target volume that may occur during (i.e. breathing, changes in position, etc) or in the course (i.e. anatomical changes) of treatment may also result in degradation of the high-dose conformation of the distal surface of the target volume. The clinical consequences of these effects can be variable and potentially severe. This kind of range uncertainties are extremely difficult to predict or correct, and for this reason, are also typically ignored in robustness evaluation or optimization. For instance, local range changes of over 1 cm were found simply due to an additional layer of fat resulting from a weight gain of only 1.5 kg in a pediatric patient [82]. For prevention, one should avoid beam directions that require protons to stop directly in front of critical structures and that pass through complex or high-Z heterogeneities and large air cavities that may change due to patient motion or misalignment, or that are tangential to the patient surface.

Uncertain range, resulting from any of the sources discussed above and summarized in Table 1.2, can have consequences on many aspects of treatment, including target coverage, dose conformation, dose homogeneity and critical organ doses. These uncertainties can only be mitigated with better physics data; otherwise, the only solution is to account for them in the margin recipes. For example, at the Massachusetts General Hospital (MGH), treatment planning assumes an uncertainty in the proton beam range of 3.5% of the range plus an additional 1 mm: this results in a deliberate overshoot of 8 mm for a 20 cm range field in soft tissue, which is quite substantial. Other facilities adopt comparable margin formulas: the MD Anderson Proton Therapy Center in Houston, the Loma Linda University Medical Center, and the Roberts Proton Therapy Center at the University of Pennsylvania all apply 3.5% + 3 mm while the University of Florida Proton Therapy Institute uses 2.5% + 1.5 mm [69]

Source of Uncertainty	**Uncertainty before Mitigation**	**Mitigation Strategy**
SOBP delivery	up to 1.0 mm	None
<I>	up to ±7 mm	Rigorous protocols
Range reproducibility	±1.0 mm	Rigorous QA
Compensator and accessories	±1.0 mm	Rigorous QA of compensator material
CT scan and resolution	±3% of range	Site-specific imaging protocols
Positioning, Immobilization, and Localization	Variable, potentially severe	Rigorous patient selection criteria
Complex heterogeneities	> ±1 mm	Rigorous patient selection criteria
Biological factors	± 1–2 mm	Rigorous protocols
Treatment delivery (dosimetric uncertainty)	±1–3.0%	Rigorous QA

Table 1.2. Summary of estimated uncertainties in Treatment Planning and Delivery of non moving targets with Proton Therapy [37, 69]. QA stands for quality assurance.

Advancements in radiation therapy and the reduction of normal tissue complication probability can be attained, in part, by minimizing treatment volumes. The reduction of range margins can be considered only when we enhance our ability to manage range uncertainties. Optimizing beam quality assurance programs is one approach to mitigate some of these uncertainties, potentially improving range reproducibility and reducing dose uncertainties. Chapter 2 of this thesis will delve into this topic, contextualizing the focus of the research.

1.4 Reduction of damage to healthy tissues: the FLASH effect

An unexpected and particularly relevant biological effect for controlling the toxicity of radiotherapy on healthy tissues was observed for the first time in the late 1960s [83, 84], when electron and X-ray beams with much higher dose rates than those traditionally used for clinical applications[30] were used to irradiate mammalian cells. The comparison between the survival curves obtained after irradiation of the cells with both high and conventional dose rate beams showed a reduction in the sensitivity of the cells to radiation for beams with a dose rate greater than 10^8 Gy/min. In other words, at ultra-high dose rates, the damage produced to normal tissues appeared to be decreased. It took the field of radiation oncology 40 years to appreciate and actively reinvestigate this phenomenon. In 2014, *Favaudon et al.* demonstrated not only that the toxicity in mice was reduced at ultra-high dose rate (> 40 Gy/s), but also that tumor control remained the same as for beams with conventional dose rates [85]. They evaluated the toxicity in terms of pulmonary fibrogenesis through histopathological examinations conducted 8, 16, 24 and 36 weeks after irradiation, as illustrated in Figure 1.18. In parallel, the growth inhibition of syngeneic[31] orthotopic[32] tumors and xenografted[33] human tumors (breast, neck and head cancer) was evaluated in mice to compare also the response of diseased tissues to both irradiation modes. The results showed that irradiation in ultra-high dose rate mode protects the healthy tissue from secondary effects, while the anti-tumor efficiency does not appear altered compared to irradiation in conventional mode.

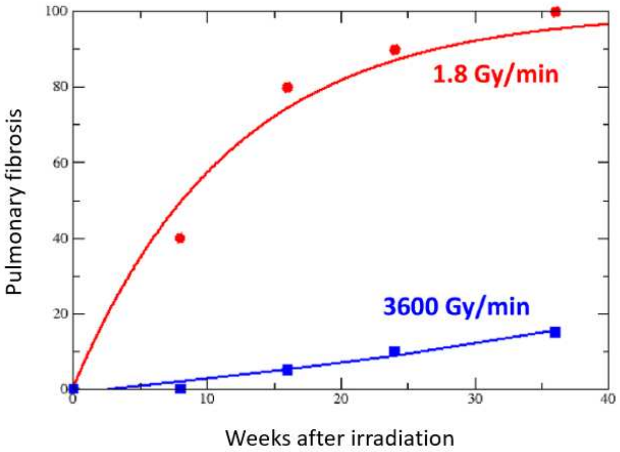

Figure 1.18. Time dependence of pulmonary fibrogenesis in C57BL/6J mice after thoracic irradiation at conventional (red circles; 15-17 Gy released on mice thorax by using ^{137}Cs γ-rays or 4.5 MeV electron, with 1.8 Gy/min dose rate) or ultra-high dose rate (blu squares; 15-17 Gy released on mice thorax by using a single 500 ms pulse of 4.5 MeV electron beams, with 3600 Gy/min dose rate). It is observed that when the percentage of fibrosis detected following irradiation at conventional doses reaches 100%, the corresponding incidence of pulmonary fibrosis following irradiation conducted at ultra-high doses is approximately 15% [30].

---

[30] The standard dose rate during the radiotherapy treatment ranges between 0.5 and 20 Gy/min, depending on the technology used [32].

[31] We speak of a syngeneic transplant when the donor is represented by an identical homozygous twin.

[32] We speak of orthotopic transplant when the tissue is transplanted in the same anatomical position of origin.

[33] We speak of xenotransplantation when the donor of the tissue to be transplanted belongs to a different species.

This unexpected differential effect was named the “FLASH” effect, and began the era of what now is called FLASH Radiotherapy (FLASH-RT, i.e. the irradiation of tissues using > 40 Gy/s dose rate radiation). In 2017, the same authors also found that spatial memory is preserved after whole-brain mouse FLASH irradiation at 10 Gy (delivered in a single electron pulse of 1.8 µs), whereas the same dose at conventional dose rate (0.1 Gy/s electron beam) totally impairs spatial memory, as expected [86]. In 2018, a third study was conducted to evaluate whether FLASH effect could also occur in higher mammals, confirming previous results [87]. This time the different response of healthy tissues to dose delivered in the two modalities was monitored by analyzing the long-term toxic effects in multiple sites of the skin of a piglet (chosen for its resemblance to human skin), where a large amount of dose (from 28 Gy to 34 Gy) was released through an electron beam. The skin response to irradiation was carefully monitored weekly through visual examination: 36 weeks after irradiation macroscopic visualization showed severe fibronecrotic lesions in skin spots irradiated with conventional dose rate beams (0.083 Gy/s) and the normal appearance of the skin spots irradiated with FLASH dose rate beams (300 Gy/s). This initial result then prompted the researchers to conduct a clinical trial on six domestic cats suffering from spontaneous carcinoma of the nasal plane, a tumor generally treated with radiation therapy but characterized by a relatively poor tumor control rate. The treatment was conducted following a release schedule of gradually increasing doses (from 25 Gy to 41 Gy) carried out via a FLASH electron beam. Three cats experienced no acute toxicity, whereas 3 exhibited moderate/mild transient mucositis. With a median follow-up of 13.5 months, the progression-free survival at 16 months was 84%.

The reduction of the normal tissue complication probability associated with FLASH radiotherapy in these experiments is very significant and the potential clinical benefit very large. If tumor control probability is unaffected by dose rate, FLASH radiotherapy would consistently widen the therapeutic window TCP-NTCP (Figure 1.19). As a result, FLASH Radiotherapy has attracted great interest in the radiotherapy community. In the last decade, multiple preclinical studies have been performed to better investigate the phenomenon [30, 31, 88-94]. The results have been subsequently confirmed by the investigators and clinical trials are starting using electrons or protons. The first human FLASH treatment was conducted in 2019 on a 75-year-old patient with skin lymphoma using 5.4 MeV electrons, delivering a single fraction of 15 Gy in 90 ms, demonstrating the feasibility and safety of the treatment, with a favorable outcome both on normal skin and the tumor 5 months later [90]. The same patient was subsequently treated for two additional tumors, receiving the same dose, one with ultra-high dose rate (166 Gy/s) and one with a conventional dose rate (0.08 Gy/s). Comparing the two treatments, there was no difference for acute reactions, late effects at 2 years, and tumor control [35]. These results suggest that the difference between FLASH and conventional radiotherapy can be difficult to detect in this dose range and when skin is the target organ [95]. More recently, the first clinical trial performed by using a FLASH proton beam (> 40 Gy/s) was published [96].

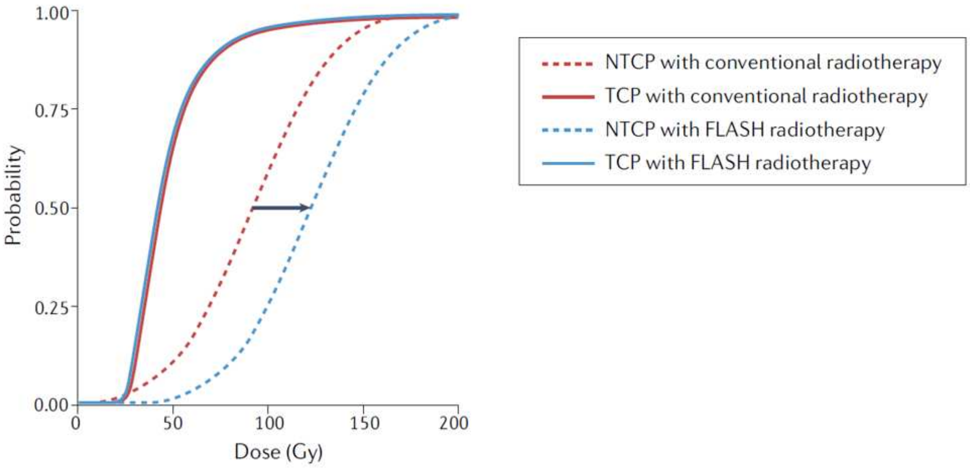

Figure 19. With FLASH radiotherapy, the TCP curve remains essentially the same but the NTCP curve is shifted to the right (higher doses) by a factor (dose modifying factor) between 10% and 50%. This leads to a widening of the therapeutic window [32].

Bone metastases of 10 terminal patients (age range 27-81 years, 50% male) were treated using a single-transmission (i.e., the beam used in the plateau region) proton beam, releasing 8 Gy in a single fraction. In 67% of sites, patients reported pain relief, and in 50% patients reported a complete response (no pain). Other clinical evaluations are currently underway, mainly focused on the feasibility and safety of using FLASH parameters in patients, but also oriented towards an early evaluation of the anti-tumor efficacy and, therefore, the curative potential of FLASH radiotherapy in cancer patients [95]. Reproducing the FLASH effect also for human treatments can have positive results on at least three aspects:

1. reduction of toxicity for tumors in which tumor control has already been achieved with conventional radiotherapy;
2. reduction of the number of fraction[34] without increasing toxicity;
3. extension of the effectiveness of radiotherapy for radioresistant tumors or for tumors that are difficult to cure, such as glioblastomas, inoperable brain metastases or inoperable lung cancers, for which we expect an increased differential effect between tumors and surrounding non-malignant tissues; this result could be obtained exploiting the fact that a dose escalation will no be correlated to an increase in toxicity.

The FLASH effect has, therefore, the potential to dramatically change the landscape of radiotherapy and patient cancer care. Ultra-fast treatments would indeed significantly enhance patient comfort, reduce treatment duration, expand the capacity to treat more patients in clinics, and concurrently decrease the toxicity of the treatment by widening the therapeutic window. The existing preclinical data indicate that, in terms of physical parameters, the

---

[34] Conventional fractionation with external beam therapy involves delivering 1.8–2 Gy per fraction in 30 fractions; hypofractionated regimens involve fewer doses of larger intensity (such as 6–8 Gy per fraction in 3-5 fractions) [95].

FLASH effect is typically observed at average dose rates exceeding 40 Gy/s, as previously mentioned. This is observed with total irradiation times of less than 500 ms and at total doses equal to or greater than 10 Gy administered in a single fraction from a single direction, targeting small volumes (~1 cm^3). For clinical applications, however, these conditions need to be scaled up to large volumes (~1 l), applicable using fractionation (≥3) and multiple beam directions (≥4) to shape the dose conformally on the tumor. However, these FLASH conditions are very challenging to achieve with the currently available technology, with which a single fraction lasts generally >1 min (Figure 1.20, Table 1.3).

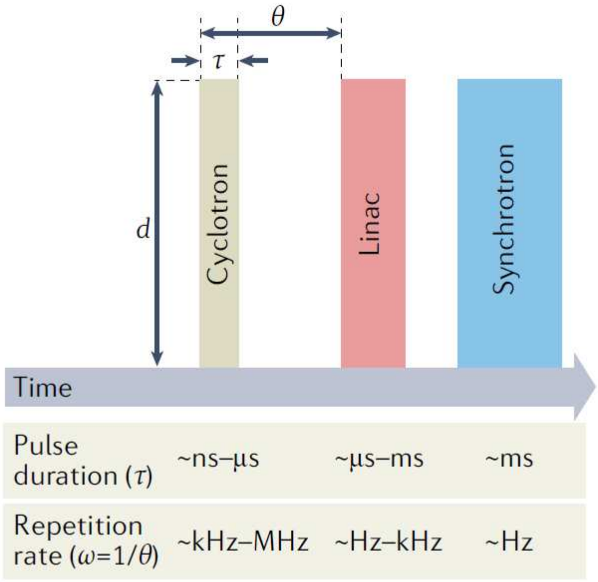

Pulse duration (τ)	~ns–µs	~µs–ms	~ms
Repetition rate (ω=1/θ)	~kHz–MHz	~Hz–kHz	~Hz

Figure 1.20. Typical time parameters of conventional accelerator machines (see also Table 1.3)

	d	D	T	D/T	DT
CONV	~ mGy	2-8 Gy/fraction, 60-90 Gy in target tissue	>1 min	~1 Gy/min	0.1–50%
FLASH	> 1Gy	>8 Gy in a single fraction	<200 ms	> 40 Gy/s	

Table 1.3. Key parameters in conventional (CONV) and FLASH radiotherapy: d is dose per pulse; D=nd is the total dose, where n is the number of pulses in the treatment; T = n(τ+ θ) is the delivery time, where τ is the pulse duration and θ is the pulse period; D/T is the mean dose rate; DT = ωτ(%) is the duty cycle, where ω=1/θ is the repetition rate. These parameters are influenced by the accelerator machine used for the beam delivery. Typical τ and ω values are reported in Figure 1.20 [95].

Ultra-high dose rates have been achieved with electrons (linac) [97], protons (cyclotrons and synchrotrons) [98], soft X-rays (<1 MeV, synchrotron radiation) [99], and hard X-rays (6-8 MeV, superconductive linac) [100]. The main limitation of using protons in FLASH radiotherapy relates to beam delivery. A possible solution to overcome the problem is based on the use of hybrid active–passive systems [101, 102] through which irradiation time is only limited by the scanning, which is extremely fast (<1 s). Recently, an open question is whether the FLASH effect will also be visible with densely ionizing heavy ions such as ^{12}C [103]. Heavy ions are accelerated in synchrotrons, in which FLASH conditions are very difficult to achieve because they generally store a single bunch of particles and the extraction cycle is ~1s. *Tinganelli et al.* in 2022 performed the first in-vivo irradiation of female C3H/He mice with 240 MeV/u ^{12}C ions delivered both at conventional (18 Gy/min) and ultra-high dose rate (18 Gy in 150 ms), demonstrating the presence of the FLASH effect, in terms of normal tissue sparing, together with tumor control and a substantial reduction of metastasis [104]. The basic mechanism of the FLASH effect is still unclear and all models so far proposed - such as oxygen depletion [30, 105-107], free radical recombination [105, 108], intertrack effects [109], and immune cell sparing [110] - are LET-dependent [92]. Therefore, the investigation of the FLASH effect with heavy ions will greatly contribute to understanding the FLASH mechanism itself.

In this context, laser-driven ion beams stand as a potentially ideal solution. Thanks to their peculiar features, like the very high dose rate (≥ 10^9 Gy/s) and the multiparticle field (photons, electrons, protons, carbons, etc), laser-driven beams make possible the study of the FLASH regime, which cannot be easily achieved with conventional acceleration techniques. To achieve this goal, optimizing the stability of the laser-plasma source, refining the collection, transportation, and spectral selection of particles, and establishing beam dosimetry procedures on biological samples will be crucial. Therefore, the routine implementation of this approach in clinical settings will necessitate significant advancements that can only be realized over many years. Up to now, a number of studies have been carried out by using laser-driven particle beams to advance the exploration of their biological effects, primarily with electron [27, 111, 112] and proton [28, 113-123] beams. An in-vivo pilot irradiation study on human tumors in a mouse model was performed by *Kroll et al.* in 2022, delivering 4 Gy using ~60 MeV laser-generated protons at Helmholtz- Zentrum Dresden–Rossendorf (Dresden) [34]. In 2023, *Chaudhary et al.* report the first application of ~10 MeV/n laser-accelerated carbon ions to irradiate radioresistant patient-derived glioblastoma stem-like cells, in a single ultra-short (~400-picosecond) pulse at a dose rate of 2×10^9 Gy/s, demonstrating the feasibility of radiobiology investigations at unprecedented dose rates using laser-accelerated high-LET carbon ions in clinically relevant models [15].

One of the primary challenges associated with FLASH Radiotherapy (FLASH-RT) is the absence of established reference dosimetry. FLASH dosimetry is challenging, and precise procedures for measuring radiation doses at these ultra-high dose rates are essential before implementation in clinical practice. Conventional reference dose measurements using ionization chambers now encounter significant ion recombination effects (>5%) at high dose rates. Many other dosimeters (such as radiochromic films, alanine, semiconductor detectors, faraday cups, scintillators, etc) were revisited and investigated [124, 125].

1.5 Innovative ion acceleration schemes

Proton and ion beam therapy require powerful accelerators in order to reach clinically relevant particle ranges in tissue up to 30 cm. For protons and ^{12}C ions energies respectively up to 250 MeV and 430 MeV/u are required (for heavier ions like ^{16}O the energy rises to more than 500 MeV/u) [60]. To achieve the required energies, most therapy facilities offering exclusively protons are operated with cyclotrons, while facilities with also ^{12}C ions generally rely on synchrotron accelerators [1, 9]. Cyclotrons (3-4 m in diameter) are considered easy to operate, highly reliable, and relatively compact machines: superconducting cyclotrons, in particular, are only 2–3 m in diameter. They offer continuous beam (ideal for beam scanning) and extremely stable and regulable intensities, but no energy variation. Synchrotrons, on the other hand, offer fast energy variation (from pulse to pulse), but are more complex in operation and need an injector and a delicate extraction system. As a consequence, the main drawback is the huge size of such accelerators: they combine injection linacs around 10 m long with synchrotron rings of 20–30 m diameter for ^{12}C ions and 6-8 m diameter for protons. Typical operating parameters of some accelerators in use in hydrotherapy facilities are reported elsewhere [1, 5, 68, 126]. The accelerator is generally connected to 3-5 treatment rooms via a high-energy beam transport line, which contains several magnetic components for beam deflection and focusing, and which may be dozens of meters in length [37]. In general, clinical beams may enter the treatment room at a fixed position or through gantries capable of rotating up to a full 360°, providing tumor irradiation from all needed directions. Gantries are very bulky (with typical diameter of 6-8 m and length of 10-12 m) and can weigh 120 tons or more (up to 600 tons for ^{12}C ions treatments) [10]. These rotational beamlines cover large volumes that need to be shielded by materials capable of stopping fast neutrons emerging from the patients into large solid angles. Typically, walls of concrete having thicknesses of about 2 m or sandwich structures are used to protect the staff. The investment intrinsically tied to this radiation protection measure represents a relevant part of the total costs.

Typically, therefore, hadrontherapy centers require elements of high complexity, size, and cost, conditions that make difficult a wide implementation of hadrontherapy difficult. Investigations are currently being undertaken in several directions aiming at the development of more compact and less expensive technologies. For example, a new generation of compact and cost-effective single-room systems, consisting of a single accelerator and beam delivery system, was recently developed and commissioned [1, 5, 6, 127-130]. This kind of solution is very interesting and challenging from a technical point of view, as it requires the design of a compact gantry and accelerator. Another possibility, fundamentally different from those mentioned above, is based on laser-target acceleration schemes.

1.51 Laser-driven acceleration schemes

Since the 2000s, basic research has led to the development of new techniques of ion acceleration based on the interaction of ultra-intense laser pulses with matter, which is potentially able to accelerate protons up to the energy needed for medical and radiotherapy applications exploiting different acceleration mechanisms [11, 14, 16, 131-137]. Among the various laser-based ion acceleration mechanisms that have been proposed in the last two decades, the Target Normal Sheath Acceleration (TNSA[35]) is one of the most reliable, experimentally investigated, robust, and understood [143]. It is based on the interaction of laser pulses of extremely short duration, ranging from tens (called "short pulses") to hundreds ("long pulses") of femtoseconds, and pulse energy ranging from a few to tens of Joules with thin (~1-100 μm) target [11, 17, 144]. These pulses[36] are focused, using reflective optics consisting of off-axis parabolic mirrors, onto the front side of a solid target, within a focal spot with typical micrometer size. At the focal point, the laser intensity – that is, the power per unit surface – reaches extremely high levels, up to 10^{20} W/cm^2. This interaction immediately leads to the formation of a plasma at the front surface of the target, due to the energy absorption in the target foil (Figure 1.21). The electrons in this plasma are heated up to relativistic energies, penetrate through the target, and emerge from the rear surface. This induces strong electrostatic fields (of the order of MV/μm versus kV/μm of conventional RF accelerator cavity structures), which pull ions and protons out of the target at its rear surface [140, 145].

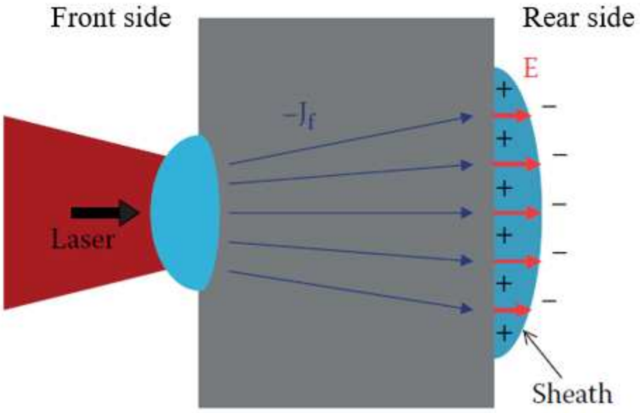

Figure 1.21. The basic scheme of TNSA. The laser pulse incident on the front side of the target generates an intense current density $J_f \sim 10^{11}$ A cm^{-2} of fast electrons which propagate through the target and produce a sheath at the rear side. The induced space-charge electric field E accelerates ions. Protons, which may be present either as a component of the target material or in hydrogen impurities present in a thin surface layer, are favored by the high charge-to-mass ratio and are thus preferentially accelerated at the rear side of the foil [17].

---

[35] The two main mechanisms of laser-driven ion acceleration are TNSA and Radiation Pressure Acceleration (RPA) [138]. Others are Collisionless Shock Acceleration (CSA) and Relativistic Transparency (RT) [17]. Acceleration through TNSA requires relatively lesser intensity of laser (10^{18}–10^{20} W/cm^2) and thicker targets (1-100 μm size), whereas RPA can only be achieved at intensities above 10^{20} W/cm^2 with thinner targets of thickness 10–100 nm. Being more easily accessible experimentally, TNSA is largely much more studied. However, with the advent of increasingly high-performance and powerful lasers, it has recently been possible to investigate the RPA method [139]. A brief review of state-of-the art in laser-driven ion acceleration can be found in [10, 11, 17, 140]. Hybrid schemes involving two or more mechanisms have also been explored.

[36] Laser pulses with these characteristics are generated using the technique known as "Chirped Pulse Amplification," which was demonstrated for the first time in 1985 by G. Mourou and D. Strickland [141], who received the Nobel Prize for Physics in 2018 [142].

This process allows the acceleration of particles on very small distances, up to three orders of magnitude smaller than those required on conventional radiofrequency accelerators. As a consequence, this approach opens the possibility to obtain particle beams, with the typical energy required for radiotherapy applications, using an acceleration scheme of reduced costs. One of the main advantages of laser ion acceleration methods over currently designed schemes is that it can simplify and significantly downsize the system for ion transport to the treatment rooms, as well as the gantry, as illustrated in Figure 1.22. The idea is to situate the target directly at the entrance of the treatment room. Instead of devices containing bulky and heavy magnets required for the deflection of high energy ion beams, it is proposed to use an optical system which bends and rotates the laser beam, arranging its interaction with target in such a process that generates fast ions in the treatment room, not outside it. Moreover, the approach of using a laser to generate beams for proton therapy can be of interest because the laser and light transmission components can be installed in normal rooms, without the need of heavy concrete shielding. In this sense, therefore, the use of a relatively small-size laser ion accelerator in oncological centers can revolutionize hadron therapy, making high-energy proton and heavier ion beams much more accessible, thanks to the creation of relatively inexpensive specialized medical laser proton accelerators having relatively small dimensions (2–3 m) and weighing no more than several tons [16].

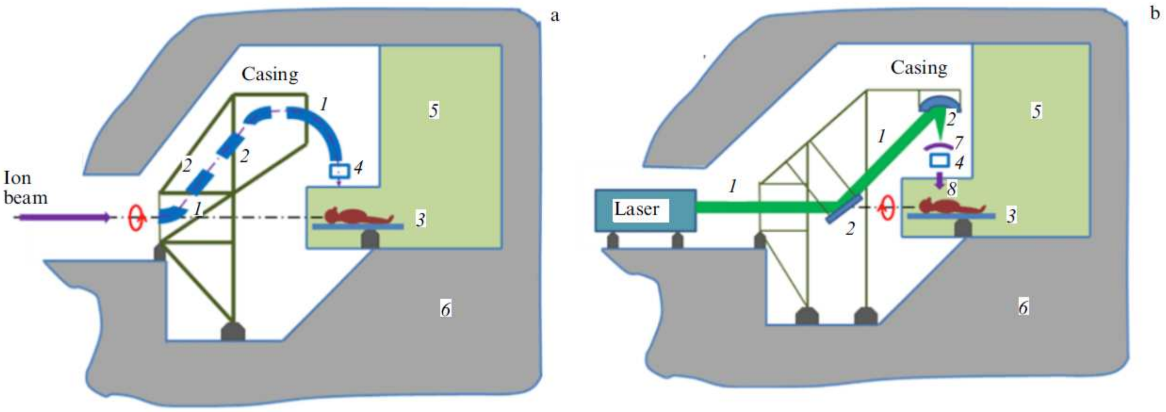

Figure 1.22. Comparison of the classical setup of a gantry and its optical counterpart. (a) The classical setup of a gantry: (1) bending magnets, (2) quadrupole lenses, (3) positioner, (4) system of dose formation and dose monitoring, (5) treatment room, and (6) concrete protection. (b) Individual laser accelerator and the optical setup of the gantry: (1) laser beam, (2) optical system of transportation and focusing of the laser pulse, (3) positioner, (4) dose monitoring system, (5) treatment room, (6) concrete protection, (7) target, and (8) ion beam. In both cases, the casing with the elements mounted on it can be rotated ±180° [10].

It is widely acknowledged that TNSA has been the predominant mechanism for proton acceleration in the majority of reported experiments [11, 132, 146, 147]. In the context of potential applications, one limiting factor associated with laser-driven ion acceleration through the TNSA regime is the maximum attainable energy. Extensive studies have been carried out to enhance the acceleration process either by optimizing the laser pulse or by utilizing targets with particular features [148, 149]. Engineering of the target oriented to perform a spectral manipulation of the emerging ion beams has been realized in terms of chemical composition, thickness, geometrical shape, volume, structure, and even state of matter [150-153]. Advances in laser technology have led to the development of two major laser system philosophies:

1. high-power (multi-petawatt) laser systems, characterized by high pulse energy (tens to hundreds of J), low repetition rate (from few shots per minute down to few shots per day), and long pulses (up to hundreds of ps);
2. low-power (terawatt) laser systems, characterized by low pulse energy (energy from tens of mJ up to few J), high repetition rate (from Hz up to kHz regime), and shorts pulses (down to tens of fs).

Another important laser parameter is the pulse duration which has been decreased over the years from picosecond level to 20–30 fs. Significant results have been achieved in obtaining similar or even higher proton energies using less laser energy. This is a consistent result since the large systems, producing hundreds of Joule pulses, are far from being compact and are generally unsuitable for high repetition rate operation, which is a key requirement for most applications. For this reason, it is of interest to evaluate the progress obtained with "smaller" laser systems which may operate at $10 - 10^3$ Hz rate and typically have a pulse duration of a few tens of fs and an available energy $\lesssim 10$ J [17]. So, the second class of lasers can lead to a practical, compact, and cost-effective alternative to conventional accelerators [151]. Indeed, in the case of laser-driven accelerators, the largest and most expensive element is the laser driver, whose size, cost and complexity grow as the energy of the generated laser pulse increases [140]. From this point of view, the main challenge is to increase the laser-to-ions energy conversion efficiency to a level ensuring a compactness and cost of the accelerator enabling its practical usefulness. Also in this aspect, RPA seems to be the most promising method of ion acceleration, especially at ultra-relativistic laser intensities when the conversion efficiency can reach even tens of per cent.

Figure 1.23 shows a comparison of calibrated spectra from three experiments [Snavely et al., 2000; Gaillard et al., 2011; Wagner et al.,2016] which established new world records for the cut-off energy at the time of the publication of the results in the period between 2000 and 2016. All three experiments were performed with laser systems delivering several tens of joules onto a solid target, with a typical pulse duration of several hundreds of femtoseconds. Figure 1.24 shows experimental results obtained using smaller short-pulse laser systems of different nominal power. The corresponding ranges of pulse duration and intensity on target are 25 - 40 fs and $4 \times 10^{18} - 2 \times 10^{21}\ Wcm^{-2}$, while the targets are planar foils having different thicknesses in the range 0.001 - 4 μm.

In the quest for enhancing TNSA ion energies, scaling laws have been discovered for intensity, target thickness, focal spot size, pulse duration and pulse energy [135, 154, 155)].

In general, ion energy grows with increasing pulse energy and with decreasing pulse duration, focal spot size and target thickness.

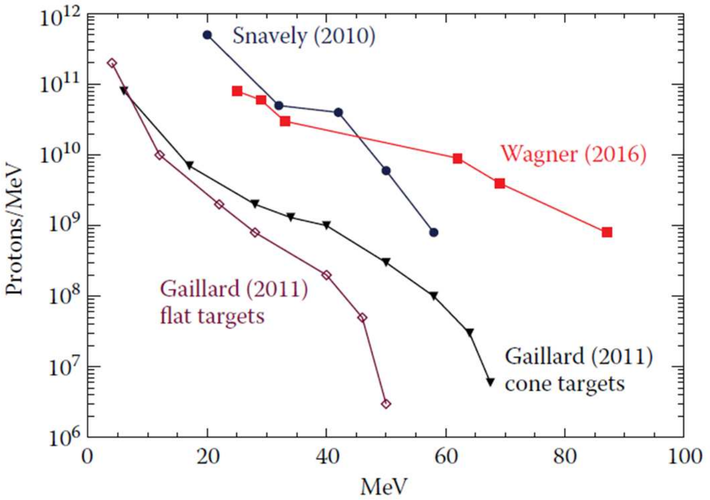

Figure 1.23. Proton energy spectra from the three experiments reporting new world records in the cut-off energy from 2000 to 2016. For the experiment of Gaillard et al. (2011) the record energy was achieved using specially shaped "cone" targets; the spectrum obtained with standard "flat" targets is reported for comparison. See text for parameters and details. The corresponding reported values of the energy "on target" (i.e., contained into the focal spot) and the pulse duration were, respectively: 150 J, 500 fs [156], 39±7 J, 670±130 fs [157], 48–60 J, 500–800 fs [158].

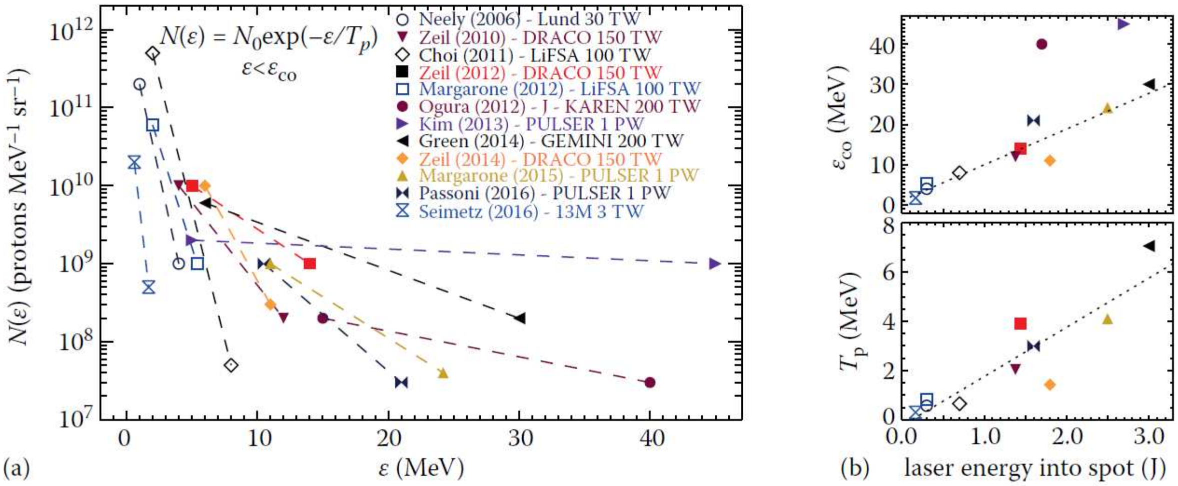

Figure 1.24. Frame a): proton spectral density $N_p(\varepsilon)$ using sub-100 fs, sub-10 J laser pulses, and thin solid targets. The higher energy tail of each experimental spectrum was approximated by a simple exponential function $N_p(\varepsilon)$, where $\varepsilon < \varepsilon_0$, being ε_0 the cut-off energy (dashed lines). Frame b): the parameters ε_0 (top) and T_p (bottom) as a function of the laser pulse energy in the focal spot; the "temperature" T_p is a parameter giving information on the mean proton energy and the spectral roll-off with increasing ε. Empty and filled symbols are for intensities in the $0.4 - 5 \times 10^{19}\ Wcm^{-2}$ and $0.8 - 2 \times 10^{21}\ Wcm^{-2}$ ranges, respectively. More details in [159-170].

Over the years, the study of the laser-target interaction has also led to the exploration of other acceleration regimes capable of exceeding the efficiency of the TNSA in terms of proton energy. *Higginson et al.* [171] in 2018 reported on an experimental demonstration of efficient proton acceleration to energies exceeding 94 MeV via a hybrid scheme of radiation pressure-sheath acceleration in an ultrathin foil irradiated by a linearly polarized laser pulse (Figure 1.25). Two years later, *T. P. Frazer et al.* [172] report on an investigation of the influence of laser focusing on proton acceleration in the ultrathin target regime, finding the highest value of proton energy in the range 94-101 MeV. As extensively illustrated previously, the proton energy window of therapeutic interest ranges between 60 and 250 MeV, depending on the location of the tumor. Recent simulation studies have reported results illustrating proton energy spectra with cut-off energies up to 300 MeV, demonstrating that the required energies for deep-seated tumors, even if still in the future, appear to be within reach, considering ongoing developments in the field [152].

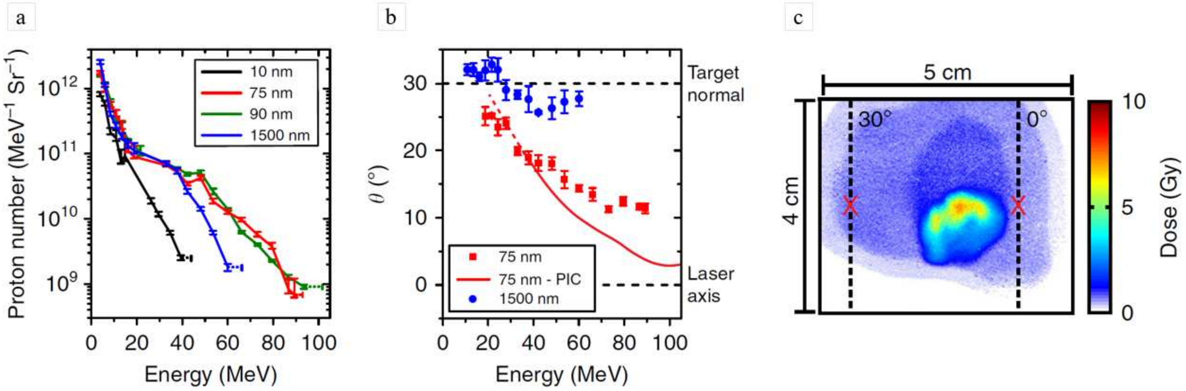

Figure 1.25. Frame a): measured proton energy spectra for given foil thickness, l. Frame b): measured angle of the center of the proton beam, θ, with respect to the laser axis (in the plane of the incident laser beam), as a function of energy, for $l = 75\,nm$ (red) and $l = 1.5\,\mu m$ (blue). An example PIC (Particle-in-cell) simulation result for $l = 75\,nm$ (red curve) is included for comparison. Frame c): Example proton beam 2D dose distribution for proton energies equal to 89 MeV. The red markers at 0° and 30° correspond to the laser axis and target normal axis, respectively. More details in [171].

The characteristics of these beams, however, are peculiar when compared to those produced by conventional acceleration machines. In particular, beams accelerated via laser-matter interaction exhibit:

- a multiparticle field: following the laser-target interaction, electrons, protons, and ions can be produced (in [173]), for example, the progress made in production of electron laser-driven beams is reported). In this context, by removing the proton from the targets, or by choosing H-free targets, the acceleration of heavier ions is favored. The interaction of laser radiation with solid targets is also accompanied by the generation of γ-rays, neutrons, positrons, and other debris from nuclear reactions.
- a broad energy spectrum (the energy spread in the TNSA regime can exceed 100% up to E_{max}): the usual ion energy distribution is an exponential one with a cut-off energy that is dependent on the driving electron temperature (see Figure 1.25(a)); without

special target treatment, and independently of the target material, protons are always accelerated first, as they have the highest charge-to-mass ratio.

- a very high particle number: at present, particle numbers of up to 6×10^{13} protons per pulse with energies above 4 MeV have been detected in experiments [144].
- a large divergence angle (typically 40-60 degrees depending on laser and target parameters) (see Figure 1.25(b)) [149]; moreover, protons with the highest energy are emitted with the smallest opening angle from the source, up to 5° half angle; protons with less energy are subsequently emitted in larger opening angles (Figure 1.26) [144]. Such peculiarity results in a non uniformity dose distribution of the beam (see Figure 1.25(c)). It should be noted that the term "opening angle" is not equivalent to the beam "divergence". The divergence of the protons increases slightly with increasing energy, whereas the emitting area (source size) decreases with proton energy. This results in a total decrease of the opening angle measured experimentally.
- picosecond scale initial burst duration[37] that, combined with the high number of particles per bunch, yields a peak current of several kA (or even higher) [17];

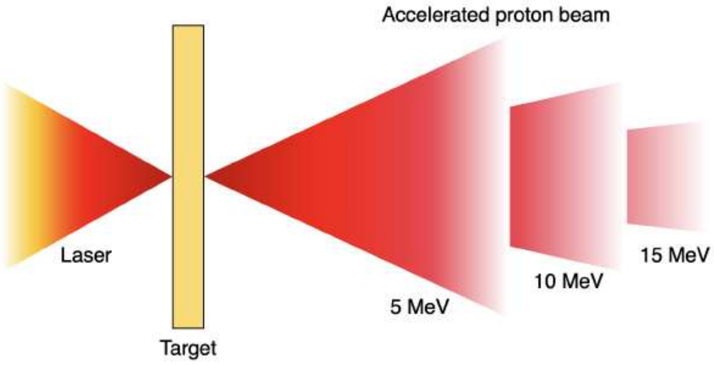

Figure 1.26. Qualitative conical distribution of proton emission from the TNSA regime, showing the highest energy protons to have the lowest degree of angular distribution.

These properties limit the use of laser-driven proton beams for medical applications. First of all, it is necessary to isolate the proton component of the laser driven beams from the other particles. Moreover, an energy resolution of about $\Delta E/E \simeq 10^{-2}$ is required to guarantee a high ratio of the dose in the Bragg peak to the dose at the beam entrance and, accordingly, a sufficiently high dose delivered to the tumor, with an acceptable low dose left in transit of healthy tissues. In addition, the therapeutic beams need to have a very uniform lateral profile, in order to perform an efficient control of the released dose within the limits established by the protocols. As a consequence, it is necessary to prepare a system for selecting, collimating and focusing the beams. However, in this case, the conversion efficiency of laser energy into the energy of fast particles is significantly reduced, and the number of the beam particles

---

[37] Of course the measurement of bunch duration must be associated not only to a well-defined energy band but also to a value of the distance from the source, since velocity dispersion will cause the bunch duration to increase along the propagation path [17].

decreases. A more promising approach is then related to the optimization of the emission parameters of these beams by acting on the laser and target features [16]. Most of these techniques have been developed in the TNSA framework, although they might be adapted to other laser acceleration schemes. Recently, the design of a new target with a metallic wire attached to its rear side, bent in order to form a helical coil coaxial with the proton beam, has proven to simultaneously focus and further accelerate the laser-driven proton beam [174]. Finally, to date laser systems are generally characterized by low repetition rate and shot-to-shot stability and reproducibility. Further progress in this area is associated with the demonstration of more efficient and better controlled ion acceleration mechanisms, with the development of laser technology enabling generation of powerful and stable high-quality pulses of electromagnetic radiation. Although the total number of particles accelerated during the period of one laser pulse is quite large, the beam duration is very short, ranging from picoseconds to nanoseconds. So, the repetition rate required to deliver a planned dose of 4 Gy for each tumor-voxel (in the hypothesis of active scanning systems) of a target volume of 250 cm^3, for example, will be of the order of kHz, which is extremely difficult to obtain with present-day laser accelerators [10]. In any case, the number of particles delivered to one voxel should be controlled with an accuracy of not less than 3%, which in turn assumes the availability of appropriate monitors placed in front of a patient.

The most notable difference between particle irradiation from laser-driven and conventional sources is the dose rate. Dose rates provided by a conventional accelerator are usually of the order of 1 Gy/sec (but can be as high as $\sim 10^3$ Gy/sec for the spot scanning mode). By contrast, with laser-driven radiation, the dose rate can exceed 10^9 Gy/sec and the irradiation time can be much shorter (typically nanoseconds) [135].

Based on what has been said, it is clear that there is still a long way to go before laser acceleration systems are ready to enter the clinical context. The experimental and computational results have shown the great potential of these systems as alternatives to the centers currently widespread in the world. One of the main innovations is represented by the possibility offered by laser-driven systems to produce different species of ions with the same accelerator machine, simply by changing interaction targets. This would allow the treatment of tumors by differentiating the treatment of hypoxic (radio-resistant) areas through the use of heavy ions. The advance represented by this potential scenario is evident if we consider that there are currently only six centers in the world capable of treating patients with both protons and carbon ions [9]. An optimization and better understanding of the laser-target interaction is still necessary, however. Furthermore, the different characteristics of laser beams require the study of their radiobiological effects, which have proven to be different from those of conventional beams, giving rise to the FLASH effect discussed in the previous paragraph, for which there are still many outstanding questions. In addition, the techniques and dosimetric tools used with beams accelerated by radiofrequency machines (i.e., beam transport, delivery system, dosimetric protocols) cannot be applied to laser-driven irradiation. It is necessary to develop new strategies suited to the peculiar characteristics of these beams, which allow them to monitor their quality. This includes single-pulse resolution detection in space and time.

Diagnostic instrumentation must be implemented at the operational repetition-rate and, where possible, should be noninvasive. However, laser-driven proton detection must be more robust than that of conventional ion accelerators due to the high peak current (and, consequently, high dose rate) and the hostile detection environment near the source (the most powerful laser systems can generate a significant electromagnetic pulse, which can interfere with sensitive electronics sufficiently close to the interaction point) [175]. The laser driven ion beam dosimetry techniques proposed so far will be illustrated in the next chapter, highlighting their advantages and critical issues.

Chapter 2

Depth dose distribution and relative dosimetry of proton beams

2.1 Introduction

As above mentioned, one of the primary reasons for opting for external proton therapy over conventional photon-based treatment in cancer patients is the rapid decrease in dose at the distal edge of the proton beam. This characteristic enables more precise and conformal dose distributions. However, in practice, proton range uncertainties (described in Section 1.3) often prevent the sharp dose gradient at the distal beam edge from being fully utilized. This is the reason why, unlike photons, uncertainties in the range of a proton beam carry the potential risk that a portion of the tumor may not receive any dose due to a potential shift in the sharp distal dose fall-off. Simultaneously, these uncertainties pose the risk of underestimating the actual dose reaching the surrounding healthy tissues, particularly compromising the Normal Tissue Complication Probability (NTCP) for organs at risk. To mitigate the impact of range uncertainties, widening the margins of the treatment volume remains a common practice today.

Volume specifications in radiotherapy, illustrated in Figure 2.1, are described in publications 50, 62 and 78 of the International Commission on Radiation Units and Measurements (ICRU) [68, 176, 177]. The Gross Tumor Volume[38] (GTV) is the gross palpable, visible, or clinically demonstrable location and extent of the malignant (or otherwise) growth. The shape, size, and location of a GTV can be determined by clinical examination (e.g., inspection, palpation), and/or various imaging techniques (e.g., X-ray, CT, MRI, PET). The Clinical Target Volume[39] (CTV) is a tissue volume that contains the GTV and/or sub-clinical malignant disease at a certain probability level. The CTV delineation should be based on knowledge of pathways of tumor infiltration in three dimensions. The Planning Treatment Volume (PTV) is a geometrical concept, introduced for treatment planning. It surrounds the CTV with additional margins to compensate for different types of variations and uncertainties, both internal (like physiologic movements or variations in size of the CTV) and external (like set-up uncertainties) to the patient.

---

[38] In the GTV, the tumor cell density is always high (10^6 mm^{-3}). There is no GTV after complete surgical resection.

[39] In some circumstances, the CTV can be coincident with the GTV, for example, in the case of a benign tumor or a well-encapsulated malignant tumor.

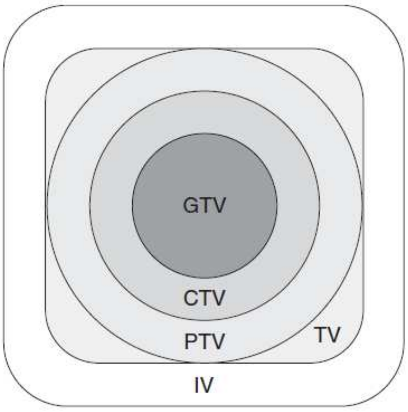

Figure 2.1. Volume definitions in radiotherapy: GTV, gross tumor volume (detectable tumor volume); CTV, clinical target volume (GTV plus the suspected sub-clinical extension of the tumor volumes not directly diagnosed in GTV); PTV, planning target volume (CTV plus safety margin for movements or deformations of CTV, technical uncertainties, etc.); TV, treatment volume (receiving the prescribed dose); IV, irradiated volume (that is exposed to significant doses with regard to normal tissue tolerance) [48]. The GTV and CTV are oncological concepts and are independent of any therapeutic approach. The PTV is a geometric concept, which does not necessarily correspond to tissue or organ borders.

Typically, at least 3.5% of the proton range is added as a range margin around the tumor to ensure full target coverage [69, 76]. However, at the same time, this practice does not represent a solution to the problem, as it determines a greater length of the radiological path to the target, thus increasing the fraction of normal tissues receiving radiation [78]. To maximize the potential benefits of hadrontherapy and minimize safety margins around the CTV, it is essential to predict the range of proton beams in patients as accurately as possible. In this regard, new dosimetric strategies capable of determining the range of a clinical proton beam with greater accuracy and precision than possible today (i.e., using the strategies envisaged by the current dosimetric protocols) are under investigation, relating to both treatment planning and the delivery process.

Concerning range uncertainties, primarily stemming from inaccuracies in photon-derived tissue stopping power, inter-fractional anatomical changes, and patient setup errors, researchers are exploring novel approaches centered on real-time in-vivo range monitoring [5, 6, 44, 60, 178-181], and are also taking into account the feasibility of implementing new beam arrangements at lower levels of range uncertainty [182]. Regarding the beam parameters (such as spot dimension and position, field flatness and symmetry, dose monitoring and verification), optimizing quality assurance[40] (QA) programs can help to reduce sources of error arising from relative and absolute dosimetry processes and delivery systems [183-190]. Within the framework of QA programs involving protons, significant

---

[40] "Quality assurance" in radiotherapy is all procedures that ensure consistency of the medical prescription, and safe fulfillment of that prescription, as regards the dose to the target volume, together with minimal dose to normal tissue, minimal exposure of personnel and adequate patient monitoring aimed at determining the end result of the treatment. "Quality control" is one part of overall quality assurance; it is the regulatory process through which the actual quality performance is measured, compared with existing standards, and includes the actions necessary to maintain or regain conformance with the standards.

attention has been devoted specifically to optimizing relative dosimetry procedures, particularly concerning the acquisition of depth dose distribution profiles of the beams. This is crucial for defining the beam range. Simultaneously, the scientific community is looking for solutions able to perform an accurate dosimetric characterization of FLASH beams, such as those generated by laser-based accelerator machines.

A basic description of the absolute and relative dosimetry procedures currently applied in the clinical practice with protons will be given in Section 2.2.

Section 2.3 is dedicated to describing the characteristics that an ideal dosimeter should have.

Subsequently, an overview of the primary dosimetric solutions under investigation for reconstructing the percentage depth dose (PDD) distribution for both conventional (Section 2.4) and FLASH (Section 2.5) beams will be provided, acknowledging that the coverage may not be exhaustive. For the latter, the focus will be mainly on the solutions proposed for laser-driven beams.

2.2 Dose verification techniques for proton beams

Medical physics is a global enterprise. The International Atomic Energy Agency (IAEA) [191] has supported the harmonization of radiation dosimetry for more than 50 years through calibration, comparison and audit services, the development of international Codes of Practice, scientific and professional guidelines, and the coordination of research and educational opportunities. In particular, the well known TRS-398 is the International Code of Practice for Dosimetry based on Standards of Absorbed Dose to Water for External Beam Radiotherapy [40]. The dosimetric indications that will be reported in this paragraph are extracted from the aforementioned protocol (to which please refer for further information), and refer to proton beams with energies in the range from 50 MeV to 250 MeV[41].

Quality assurance in radiotherapy aims to evaluate clinical requirements and to improve dosimetric and geometric accuracy and precision of dose delivery. Part of the QA procedures is dedicated to defining the quality Q of the beam (*relative dosimetry*, described in section 2.2.1), which in turn is necessary to carry out the dosimetric calibration of the irradiation line (*reference* or *absolute dosimetry*, described in section 2.2.2). In conventional radiation therapy with photon or electron beams these operations are routinely performed using dose-calibrated ionization chambers and a standard water phantom. The same technique is applied to proton or heavy ion beams.

In particular, ionization chambers calibrated in a ^{60}Co beam (of quality Q_0) in terms of absorbed dose to water D_w are recommended for clinical proton dosimetry. This procedure is usually performed in the so-called *reference condition* (summarized in Table 2.1, while in Figure 2.2 the calibration set-up is represented). Chambers of different types[42] and models (cylindrical or plane-parallel) can be used in the radiotherapy context. The selection of one chamber over another is guided by recommendations associated with various clinical conditions, such as the size of the SOBP or whether the objective is relative or reference dosimetry. Calibration reference points vary depending on the chamber type: for cylindrical chambers, it is on the chamber axis at the center of the cavity volume, while for plane-parallel chambers, it is on the inner surface of the entrance window, at the center of the window. In general, to perform calibration in water, for non-waterproof[43] chambers, a PMMA (Polymethyl methacrylate) sleeve preferably not thicker than 1.0 mm should be used. After that, the chamber is positioned in a water phantom, so that its reference point is:

- on the central axis of the beam;
- 1 m away from the source;
- at 5 g/cm² water depth.

---

[41] Relatively low energy protons (below 90 MeV) are employed in the treatment of ocular tumors using field sizes smaller than 4 cm x 4 cm and high dose rates. Higher energy protons (above 150 MeV) are used for the treatment of large or deep seated tumors. For these applications, field sizes and dose rates similar to those used with high energy photons are employed.

[42] IAEA TRS-398 protocol contains tables listing the various types of chambers on the market, together with their main characteristics differentiated based on the model (cylindrical or plane-parallel).

[43] Waterproof ionization chambers may be calibrated without a PMMA water sleeve upon a customer request.

The size of the radiation field at the reference plane is 10 cm × 10 cm. There are no reference values regarding the dose rate of the beam used for calibration, as well as the voltage and polarity used to power the chamber, even if both should always be stated in the calibration certificate.

Influence quantity	**Reference value or reference characteristic**
Phantom material	Water
Phantom size	30 cm x 30 cm x 30 cm
Source-chamber distance	100 cm
Air temperature	20-22 °C
Air pressure	101.3 kPa
PMMA sleeve	1 mm
Depth in phantom of the reference point of the chamber	5 g/cm^2
Field size at the position of the reference point of the chamber	10 cm x 10 cm
Relative humidity	50 %

Table 2.1. Reference conditions recommended for the ^{60}Co calibration of ionization chambers in gamma radiation in standard laboratories.

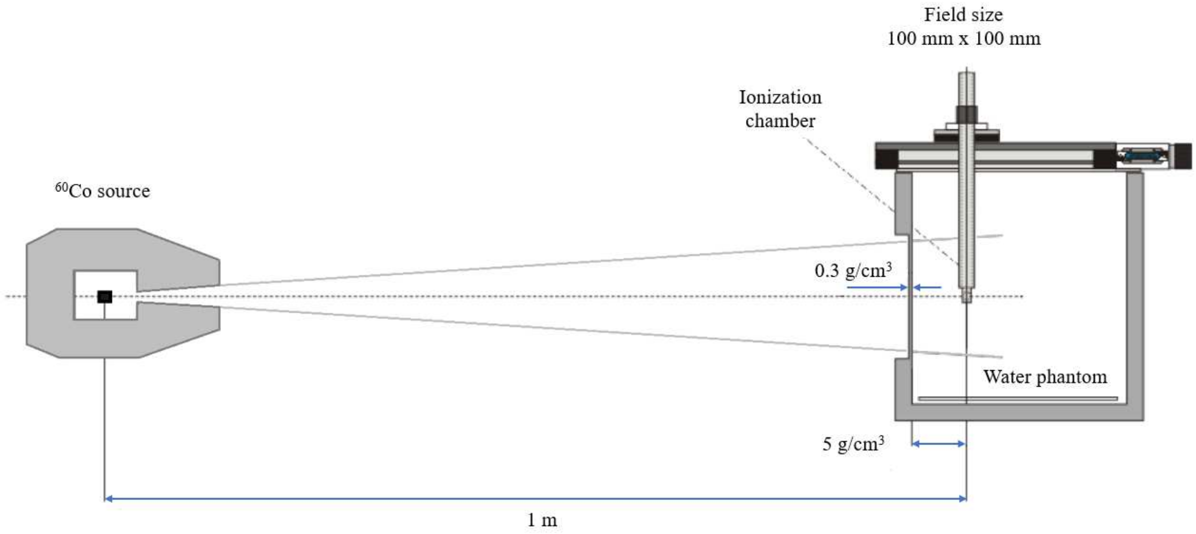

Figure 2.2. Top view of the set-up for ion chamber calibrations in terms of absorbed dose to water using a ^{60}Co source. The dimensions of the water phantom window are also shown. The chamber axis is positioned perpendicular to the central axis of the beam.

In general, N_{D,w,Q_0} represents the calibration factor in terms of absorbed dose to water for a chamber calibrated in reference condition by using ^{60}Co beam. N_{D,w,Q_0} is usually expressed in Gy/C and is obtained from the ratio between the known absorbed dose D_w and the dosimeter reading M. Each commercial ionization chamber for clinical use is supplied with a calibration certificate containing the value of N_{D,w,Q_0}. In most clinical situations, however, the measurement conditions do not match the reference conditions used in the standards laboratory for calibration procedure. This includes not only the quality of the radiation, which in general is $Q \neq Q_0$, but also other influence quantities like pressure, humidity, temperature, etc. These may affect the response of the dosimeter, so it is necessary to correct the measurement of the dose by applying correction factors able to take into account the differentiation between reference and clinical conditions, as we will see later in this chapter. The procedures and methods for both absolute and relative estimation of the delivered dose extend beyond acquiring the Percentage Depth Dose and calibrating the irradiation line. Additional beam parameters must be measured and compared with established standards closely aligned with the necessary clinical requirements, as discussed in Section 1.3 and illustrated in Figure 1.15. However, the focus here will be solely on the latter, as this is the research domain within which this thesis is situated.

2.2.1 Percentage Depth Dose distribution

The radiation quality Q of a beam entering the patient is defined by the energy distribution of the scattered beam (or in scanning applications, of the pencil beam) and the extent of scattering encountered as the beam traverses beamline components and beam-modifying devices [68]. In radiotherapy with protons (or heavier ions), the indicator chosen to define the quality of the beam is the particle residual range R_{res}. The latter is determined by acquiring the longitudinal beam profile, also called PDD[44] distribution, an operation usually carried out using ionization chambers in water[45] phantoms. During irradiation, the chamber is moved with a resolution of the order of 0.1 mm along the direction of propagation of the beam, thus providing a response as the penetration depth varies (i.e., along the Bragg curve). The result of such acquisition is reported in Figure 2.3 for a SOBP, but the procedure is the same also for a pristine Bragg peak. The phantom should extend to at least 5 cm beyond all four sides of the field size employed at the depth of measurement and also extend to at least 5 g/cm^2 beyond the maximum depth of measurement.

---

[44] In proton therapy, measurements of PDD distributions are regularly performed not only to evaluate the particle's range, but also in beam quality control context (i.e., homogeneity and length of SOBP).

[45] Water is the reference material for dosimetry due to its similar composition to human tissue (although this is a source of errors, as fully discussed in the previous chapter). Sometimes it is necessary to evaluate the water equivalent thickness (WET) of a certain degrading material: it can be calculated exactly if the range-energy relationship of the material and that of the water are known [192]. Of course the result will be as accurate as the knowledge about the range-energy relationship. In case this knowledge is not sufficiently accurate, the WET of the medium can be measured by positioning the degrader upstream of a water phantom and measuring the displacement suffered by the Bragg Peak in the depth dose deposition curve (the PDD) [37].

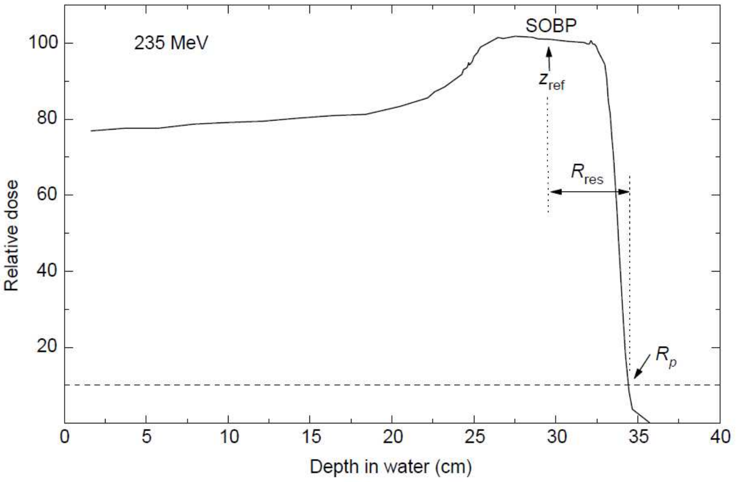

Figure 2.3. PDD distribution for a 235 MeV modulated proton beam. In the figure are reported the reference depth z_{ref} (middle of the SOBP), the residual range at z_{ref} used to specify the quality of the beam, R_{res}, and the practical range R_p. For relative dosimetry, only plane-parallel ionization chambers are recommended. It is easy to understand that R_{res} grows with the extension of the SOBP, while keeping R_p unchanged. This makes it clear why to define the quality Q of a proton beam, determining the range alone would not be sufficient.

For a correct reconstruction of the PDD distribution, the water equivalent thickness (WET) of the phantom window (with a thickness between 0.2 and 0.5 cm) and the chamber sleeve (in case it is not waterproof) must also be taken into account. As already said, the sleeve should be made in PMMA and not thicker than 1.0 mm, while the phantom can be made in PMMA or clear polystyrene. To evaluate the actual depth at which the chamber is positioned in water as respect to the beam, the WET of the two thicknesses must be calculated – by multiplying them by the density of the material (ρ_{PMMA}=1.19 g/cm^3, $\rho_{polystyrene}$=1.06 g/cm^3) – and added to the measured position in phantom.

Once the PDD is acquired, it is possible to proceed with the evaluation of the beam quality Q. The beam quality is expressed in terms of residual range R_{res} (in g/cm^2) as respect to a reference position z_{ref} along the PDD and is defined as follow:

$$R_{res} = R_p - z_{ref} \tag{2.1}$$

where R_p is the practical range, which is defined as the depth at which the absorbed dose beyond the Bragg peak or SOBP falls to 10% of its maximum value. So, according to equation (2.1), it turns out that the quality of a proton beam is not unique but is also determined by the reference depth z_{ref} chosen for measurement. This necessity arises from the existence of two delivery modes for proton therapy, for which it has been deemed appropriate to conduct dosimetric measurements at different depths, as outlined in the subsequent paragraph. The position along the beam's propagation, for which the absolute dosimetry procedure is conducted, aligns with z_{ref}, and it is referred to as the *isocenter*. This point is where the center of the tumor is located during treatment. According to the protocols, z_{ref} corresponds to a depth of 3 g/cm^2 for monoenergetic proton beams and to the center of the SOBP (point called MID) for the modulated ones.

2.2.2 Absolute dosimetry

Once the PDD distribution has been acquired and the beam quality established, the calibration procedure of the irradiation line can be performed. As already mentioned, clinical applications require a relatively uniform dose delivered to the target volume, and for this intent the proton beam has to be spread out both laterally and in-depth. This is achieved by the superposition of Bragg peaks of different intensities and energies obtained using modulation (passive) or scanning (active) techniques. In both methods, non-invasive techniques are required to monitor online the dose delivered to the patient during treatments, ensuring that it complies with what is expected according to the treatment plan. This task is entrusted to the so-called beam monitors, fundamental elements of the dosimetry line, usually constituted by transmission ion chambers[46] located behind the exit window of the beamline in air. Monitor chamber response is usually expressed in terms of relative monitor units (MU). So, to convert the information from MU to absorbed dose in water D_w, it is necessary to calibrate the monitor chambers using an absolute dosimeter. The calibration factor by which the MU response of the monitor chambers is converted into dose is called the Output Factor (OF). It is determined through the cross-irradiation of monitor chambers (placed in air) and the reference chamber placed at z_{ref} (in water). In this way, during patients' treatments, the monitor chambers will continuously indicate the dose released in the isocenter, $D_w(z_{ref})$. However, the calibration procedure slightly differs for beams delivered with passive or active techniques.

For passively scattered proton beams, the PDD distribution already coincides with an SOBP, and a complete treatment field is irradiated “at once”. In this case, the isocenter (or z_{ref}) corresponds to MID point of a reference SOBP (10 x 10 cm^2 field size), and $OF = D_w\left(z_{ref}\right)/MU$ is usually expressed in cGy/MU (Figure 2.4(a)).

For actively scanned beams, the depth dose distribution is produced by superimposing a large number of individual pristine Bragg curves. Thus, beam-scanning systems require the integrated measurement of depth dose curves (and lateral profiles) of monoenergetic pencil beams. Consequently, the MU number must be specified and controlled separately for each of these beams, which implies that monitor chambers must be calibrated for monoenergetic beams. So, in this case, z_{ref} corresponds to a depth of 3 g/cm^2 in the plateau region of pristine peaks. Lastly, as treatment planning systems more easily plan the treatment by considering the number of ions and associated energy for each pencil beam, the monitor calibration coefficient is given in number of ions N_{ions} per MU per spot, rather than $D_w(z_{ref})$/MU (Figure 2.4(b)). The number of particles can be indirectly determined by a dose measurement, so that:

$$OF = \frac{N_{ions}}{MU} = \frac{D_w\left(z_{ref}\right)}{S\left(z_{ref}\right)/\rho} \cdot \frac{\Delta x \cdot \Delta y}{MU} \tag{2.2}$$

---

[46] Monitor chambers are at least two because of safety reasons: the double control through the two devices of the dose delivered to the patient allows to prevent the possibility that during treatments, due to temporary failures or malfunctions, the control of the dose actually delivered may be lost.

where $D_w(z_{ref})$ is the water absorbed dose at z_{ref}, $S(z_{ref})/\rho$ is the mass stopping power at the same depth, and Δx and Δy are the distance of scan points in x-y directions [189].

The procedure can be terminated for clinical applications with a monoenergetic proton beam, such as plateau irradiations, as the isocenter remains at the plateau region of the peak. However, when treating a three-dimensional target volume, once the monitors are calibrated for monoenergetic beams, it becomes crucial to verify that their superposition yields an accurate 3-D dose map. In this case, the previously described procedure for the passive system can be applied, and the isocenter is once again established as the MID.

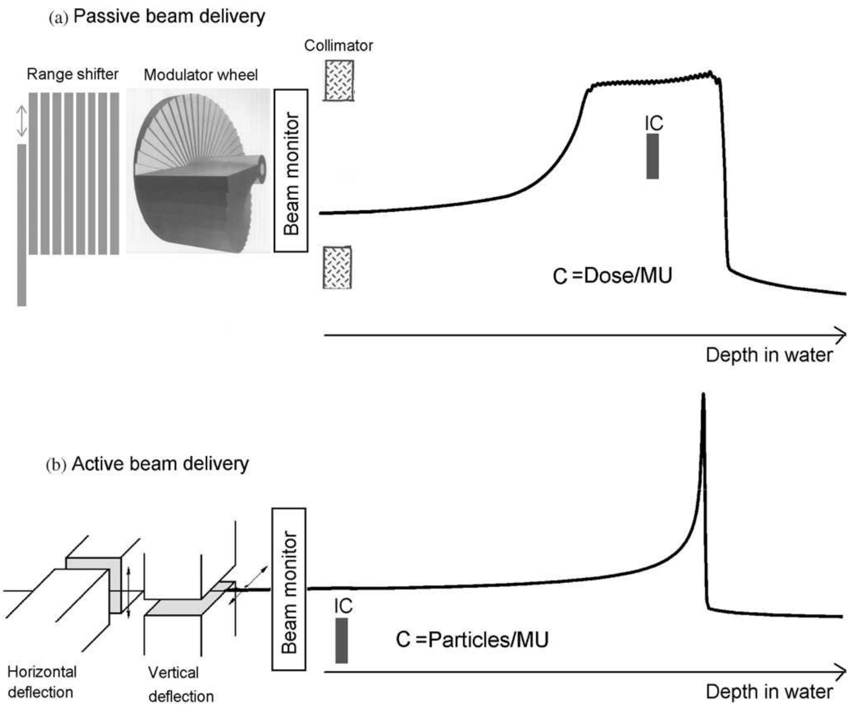

Figure 2.4. Frame a): calibration of the passive delivery beam. The dose is measured with a reference ion chamber (IC) in the middle of the SOBP. The resulting Output Factor is given in terms of dose per MU. Frame b): calibration of the active delivery system. With active scanning, a specified number of particles is delivered for each energy and each scan point. The number of particles is determined by a dose measurement in the entrance region of the Bragg curve. The resulting Output Factor is given in terms of particles per MU [189].

The absolute value of the absorbed dose in water D_w, at the calibration depth z_{ref}, for a proton beam of quality $Q \neq Q_0$, is calculated according to the following expression:

$$D_w = M_Q \cdot N_{D,w,Q_0} \cdot k_{Q,Q_0} \tag{2.3}$$

where:

- M_Q is the response of the chamber, when subjected to radiation of quality Q, with the reference point positioned at z_{ref}, multiplied by corrective factors that compensate for the different environmental conditions compared to those of the reference laboratory, the electrometer calibration, polarity effect, and ion recombination;
- N_{D,w,Q_0} is the dose calibration factor of the chamber in the reference laboratory;

- k_{Q,Q_0} is a chamber specific factor which corrects the chamber response for differences between the reference beam quality Q_0 and the actual quality being used, Q.

The values of the correction factors mentioned above can be found in the TRS-398 protocol for almost all ionization chambers on the market and as the quality of the beam used varies. The protocol also contains an estimation of the uncertainties associated with the physical quantities and procedures involved in the determination of the absorbed dose to water in the user proton beam (Table 2.2). This estimate considers the uncertainties associated with chamber calibration at the standard laboratory (step 1) and those associated with calibration performed in the context of reference dosimetry (step 2), resulting in a total uncertainty of 2% and 2.3% for the determination of the dose absorbed by water in a clinical proton beam with a cylindrical and plane-parallel ionization chamber, respectively.

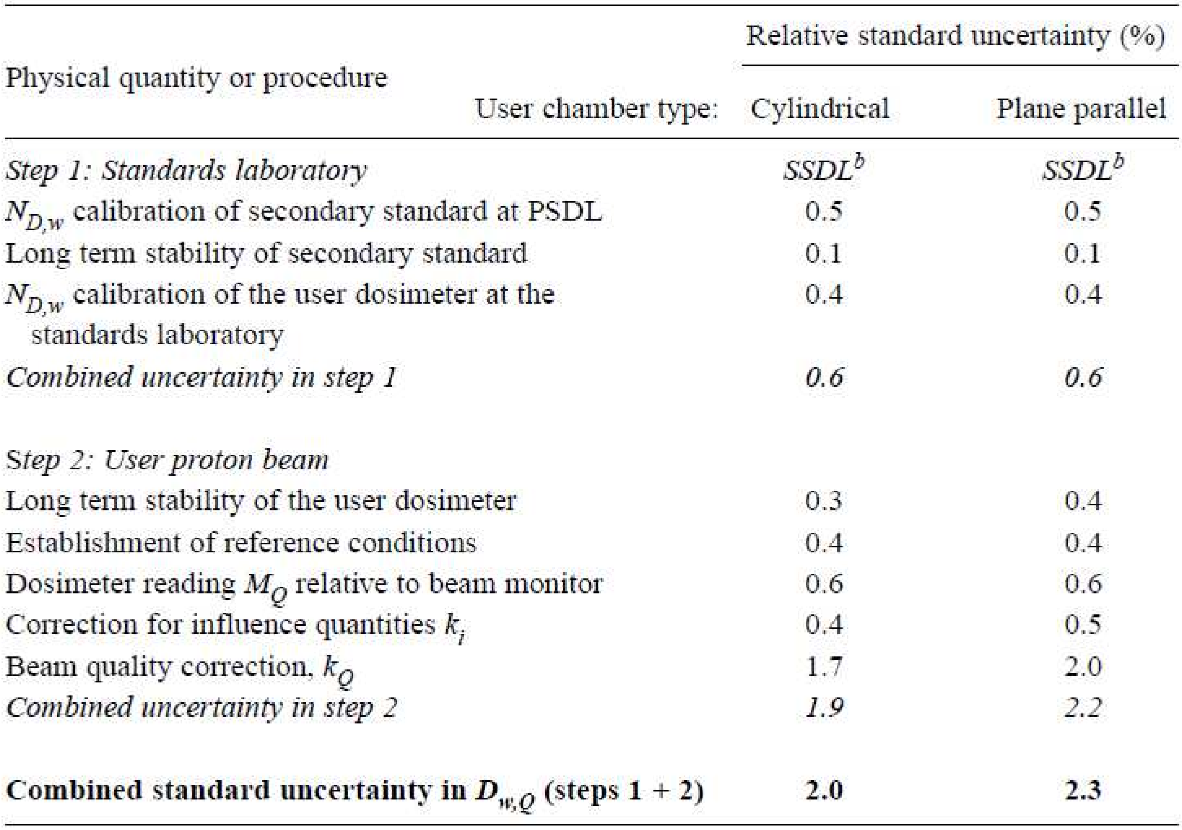

Physical quantity or procedure	Relative standard uncertainty (%)	
User chamber type:	Cylindrical	Plane parallel
Step 1: Standards laboratory	*SSDL*^{b}	*SSDL*^{b}
$N_{D,w}$ calibration of secondary standard at PSDL	0.5	0.5
Long term stability of secondary standard	0.1	0.1
$N_{D,w}$ calibration of the user dosimeter at the standards laboratory	0.4	0.4
Combined uncertainty in step 1	*0.6*	*0.6*
Step 2: User proton beam		
Long term stability of the user dosimeter	0.3	0.4
Establishment of reference conditions	0.4	0.4
Dosimeter reading M_Q relative to beam monitor	0.6	0.6
Correction for influence quantities k_i	0.4	0.5
Beam quality correction, k_Q	1.7	2.0
Combined uncertainty in step 2	*1.9*	*2.2*
Combined standard uncertainty in $D_{w,Q}$ (steps 1 + 2)	**2.0**	**2.3**

Table 2.2. Estimated relative standard uncertainty of $D_{w,Q}$ at the reference depth in water and for a clinical proton beam, based on a chamber calibration in ^{60}Co gamma radiation. The estimates given in the table should be considered typical values; these may vary depending on the uncertainty quoted by standards laboratories for calibration factors and on the experimental uncertainty at the user's institution.

2.3 Radiation dosimeters

The absorbed dose in tissue is the most important physical quantity in radiotherapy. It is measured in Gray (Gy = J/kg) and is defined as the mean energy dE deposited by ionizing radiation in a mass element dm or volume element V with mass density ρ:

$$D = \frac{dE}{dm} = \frac{1}{\rho} \cdot \frac{dE}{dV} \tag{2.4}$$

For a parallel beam with particle fluence Φ the dose deposited in a thin slice (*dx*) of the absorber material can be written as [60]:

$$D[Gy] = 1.6 \cdot 10^{-9} \cdot \frac{dE}{dx}\left[\frac{keV}{\mu m}\right] \cdot \Phi\left[cm^{-2}\right] \cdot \frac{1}{\rho}\left[\frac{cm^{3}}{g}\right] \tag{2.5}$$

Dosimetry deals with techniques for the quantitative determination of absorbed dose in a given medium by ionizing radiation. It represents one of the key procedures aimed at achieving the overall ±3% precision of absorbed dose delivery in treatments. A radiation dosimeter is a device, instrument, or system that measures, either directly or indirectly, the absorbed dose or related quantities of ionizing radiation. This means that the dosimeter must possess at least one physical property that is a function of the measured dosimetric quantity so that it can be used for radiation dosimetry after adequate calibration. To be useful as a dosimeter and to achieve the lower possible uncertainties, especially for measurements in small radiation fields, radiation dosimeters must exhibit several desirable characteristics, such as tissue equivalence of the detector material, high spatial resolution, and high radiation sensitivity. Obviously, like any detector, dosimeters can have different specific properties that can be useful depending on the dosimetric application for which they are used. It is therefore important to characterize the dosimeters to know their performances, to appropriately choose the most suitable device to meet the experimental requirements. In this context, the evaluable properties are listed and briefly described below [36, 43, 61].

- Sensitivity

  The sensitivity of a detector is its capability of producing an appreciable signal for a given type of radiation and energy. No detector can be sensitive to all types of radiation at all energies, but in general, they are sensitive to certain types of radiation in a given energy range. Detector sensitivity to a given type of radiation of a given energy depends on:

  A. the cross section for reactions in the detector;

  B. the detector density and volume: the total quantity of ionization produced increases with the density and/or sensitive volume of the detector;

  C. the intrinsic noise of the detector (and associated electronics): each active detection system is characterized by a fluctuating output signal present in the absence of external radiation. This implies that, in the presence of external radiation, a minimum of ionization events is needed for it to be transformed into a readable signal, i.e. the ionization signal must be larger than the average noise level to be detected and usable;

D. the protective material surrounding the sensitive volume of the detector: this acts like a passive substrate which has the effect of reducing the energy of the incident radiation, setting a lower limit on the energy that can be detected.

In dosimetry it is required that the detectors used demonstrate high sensitivity concerning the radiation field for which they are used, to be able to measure the dose with the precision required according to the protocols.

- Accuracy and precision

  The precision of a detector specifies the reproducibility of the measurements under similar conditions and can be estimated from the data obtained in repeated measurements. High precision is associated with a small standard deviation (random error) of the distribution of the measurement results. The accuracy represents the proximity of the measured values to the "true value" of the measured quantity. High accuracy is associated with a small relative difference between the true value and the measured value. It can be evaluated by subjecting a device to a known stimulus S and allowing the presence of any systematic errors to be highlighted. Both properties are desirable in any application, including dosimetric ones.

- Linearity

  The amount of ionization (or light, for scintillation systems) produced in a detector by the radiation, on which the electric charge contained in the signal depends, is proportional to the energy it loses in the sensitive volume. The relation between the energy lost by the radiation (or quantities related to it) and the total collected charge is referred to as the response function of the detector. The linearity of a detector expresses the direct proportionality between its response and the energy. In general, if present, linearity occurs within a certain range of energies and it does not automatically follow that a detector with linear response for one type of radiation will be linear for another. The linearity range and nonlinearity behaviour are contingent on the type of detector and its physical attributes. Linearity is a desirable property but not a mandatory one. To appropriately utilize a detector within a non-linear working range, it suffices to understand its response function in that range, provided it maintains acceptable resolution values (i.e., the ability to discriminate between different external inputs).

- Dose rate dependence

  At the same radiation energy, the radiation dose rate impacts the frequency of ionization events within the detector. Ideally, the response of a dosimetric system to an absorbed dose D delivered at two different dose rates should remain consistent. However, in reality, the dose rate can influence dosimeter readings, necessitating appropriate corrections. For instance, ionization chambers may experience recombination effects and are unsuitable for pulsed beam dosimetry measurements.

- Energy (or LET) dependence
  Under the same experimental conditions, but with varying beam energy (and consequently, the LET), the detector's response is anticipated to change accordingly. This variation can occur in a directly proportional manner (referred to as linearity with energy, as mentioned earlier) or not. It may happen that as LET increases (or energy decreases for charged particles), beyond a certain value, the detector response saturates, becoming constant. In such cases, we refer to it as energy (or LET) dependence. Operating under saturation conditions involves a loss of information, compromising the ability to discriminate between radiation with different energy or LET. Therefore, it is imperative to understand the operational limits of the detector in question.

- Directional dependence
  Detectors usually exhibit directional dependence (i.e. their response changes with the angle of incidence of the impinging radiation), due to their constructional details, physical size and the energy of the incident radiation. For example, if the direction of incidence changes, the length of the path that the particle can take in the sensitive volume of the detector can change, resulting in a more or less significant variation in the energy loss inside it, depending on the case. Dosimeters used in therapy typically need to be employed in the same geometry as that in which they are calibrated. For instance, it has been noted that the directional dependence of cylindrical ionization chambers is negligible, whereas parallel plate chambers might show significant dependence at large incident angles [66].

- Spatial resolution
  The spatial resolution can be defined in 1D (longitudinal), 2D (lateral) and 3D (volume), based on the dosimetric application for which a detector is used. Three-dimensional spatial resolution is particularly crucial for absolute dosimetry, given that the dose is a point quantity. In such instances, the dosimeter must facilitate the determination of the dose from a very small volume. This is the reason why cylindrical ionization chambers typically have volumes ranging from 0.05 cm^3 to 1 cm^3, depending on the model [40]. 2D-spatial resolution is important in beam spot tracking applications. They allow the homogeneity and lateral profile of the beam to be evaluated. In this framework, Radiochromic Films (or RCF) are detectors typically used as they exhibit a spatial resolution down to 5μm, depending on the model [193]. 1D-spatial resolution is important in applications that involve one-dimensional scanning of the beam both longitudinally and laterally. It therefore has implications on the resolution of beam sampling in the context of the quality assurance program.

Typical longitudinal scanning resolution with ion chambers is 0.1 mm, while lateral spatial resolution with solid state detectors are of the order of 0.5 mm [194].

- Effective atomic number and tissue-equivalence
  A tissue equivalent material is a material with ionization potential I, density ρ, electron density ρ_e, number of electrons per gram n_e, effective atomic number Z_{eff}, atomic mass A, and ratio of effective atomic number to atomic mass Z_{eff}/A equal to that of water (I=75eV, ρ=1g/cm^3, ρ_e=3.343x10^{23} cm^{-3}, n_e=3.343x10^{23} g^{-1}, Z_{eff}=7.42, A=0.1802x10^2 g mol^{-1}, Z_{eff}/A=0.5551) [39, 195]. In general a material is defined as equivalent to another if it has, compared to the other, the same absorption and diffusion properties for a given type of ionizing radiation in a given energy range [196]. Hence the concept of equivalence between two materials lacks absolute value, as it applies to a given type of radiation and a defined interval of its energy. Ideally, for application in clinical radiation dosimetry, a device should possess radiological properties similar to those of water across the energy spectrum of the radiation in use. This ensures that the dosimeter can function effectively as a phantom.

- Convenience of use and reading
  A fact that may be interesting for choosing one detector over another concerns the possibility of reusing the detectors (without significant losses in sensitivity) and whether they allow direct reading or require post-processing processes. Another quality to consider is whether the detector is characterized by good radiation hardness or not, so as to be able to evaluate its potential wear depending on the beam parameters. Depending on the dosimetric application, this evaluation is useful for example to speed up QA programs. For example, alanine are passive and not reusable dosimeters, unlike ionization chambers that are reusable and active.

Based on what has been said, it is clear that an ideal dosimeter should be reusable, water-equivalent and active, and should provide precise and accurate measurements; it should have high reproducibility level, high radiation hardness, high spatial resolution, and a well-described dose–response with high dynamic range [197]. Moreover, the output signal should preferably be proportional to the energy deposited, independent from the dose rate and the LET of the impinging radiation, and should maintain a good sensitivity, reliably following even rapid dose changes.

2.4 Dosimetric systems for conventional ion beams

Since 2000, when the IAEA published the TRS-398 code of practice and recommended procedures for ion chamber reference dosimetry for all types of external beams, this has been widely adopted as the standard in clinical beam dosimetry, including protons and heavy ions. Following the recommendations outlined in the protocols (Section 2.2), it is evident that the more accurately and precisely the range (i.e., the quality) of the beam is defined, the smaller the uncertainty on the measured dose will be. Therefore, the increasingly rigorous measurement of PDD distributions within QA programs is an area of interest for research aimed at optimizing proton therapy clinical treatments. The ionimetric method for measuring PDD is well established and has a spatial resolution of ~0.2 mm, but suffer from recombination effect[47] and is time consuming due to the large number of individual data points required to sample the Bragg curve with adequate longitudinal scanning resolution (0.1 mm). Research in this field is therefore currently focused on improving spatial resolution and acquisition time of PDD.

Numerous studies of Multi-Layer Ionization Chamber (MLIC) [186, 198-204] and Multi-Layer Faraday Collector (MLFC) systems [205-207] have been conducted to address the need for faster measurements of PDD profiles. Using MLIC systems, composed by a stack of plane-parallel ion chambers interleaved with water-equivalent materials, the shape of the depth–dose distribution, and hence the range of the ions, can be checked easily by a single irradiation. Plane–parallel ion chambers may also be designed as segmented chambers using either pixels or strips as sensitive areas [189], allowing the monitoring of the lateral profile of the beam with resolution of a few mm. The combination in a stack of 12 strip-segmented chambers resulted in quasi-3D dosimetric measurements through the so-called "Magic Cube" system [199] was also implemented. Magic Cube proved to have a linear response with beam fluence and reproducibility within 1%, but have a longitudinal resolution of 1 mm. Another MLIC, consisting of 180 parallel-plate ionization chambers, is the commercial "Zebra" detector [198], characterized by setup and measurement times up to 20 times shorter than measurements in the water tank. Zebra demonstrated reproducibility and monitor unit linearity levels better than 1%, but its response was found to be sensitive to radiation field sizes, and presents a longitudinal resolution of 2 mm. A similar model is the commercial "Giraffe" MLIC system [200], composed of 180 air vented plane-parallel ionization chambers. The spacing between chambers is 2 mm, with a nominal ±0.5 mm range accuracy and sensitive area of 10 cm diameter. In MLFC applications, the property of charge collection of Faraday cups - which can give an accurate measurement of the number of collected protons - is exploited to measure the stopping range by using a stack of alternating conductor (usually copper or aluminum, down to 10 μm thick) and insulator plates (Kapton or Mylar, down to 25 μm thick). It was found that by optimizing the layout, such a system can reach a

---

[47] After the interaction with the ionizing radiation, ion pairs are first formed in a column along the track of the ionizing particle, until they are caused to drift or diffuse away from their point of formation. Collisions between positive ions and free electrons (at first along the track, and then in active volume of the detector) may result in recombination in which the electron is captured by the positive ion and returns it to a state of charge neutrality. As a consequence, the charge represented by the original pair is lost and cannot contribute further to the signal in detectors. Recombination increases in importance with LET and irradiation rate [43].

native resolution better than 100 µm water equivalent in the range measurement [207]. However, the disadvantage is that over 600 foils would be required to sample the entire Bragg curve for protons with minimum clinical energy required for treatments (60-70 MeV), implying great efforts for the measurement electronics.

Large 3D-volume liquid scintillator detectors were also used to verify proton range and position for scanned proton beams, showing ability in providing precise position results within 0.7% and an accuracy in proton range within 0.3 mm [208, 209]. However, liquid scintillator materials are not suitable for hospital environments due to toxicity and the need to deoxygenate the scintillator prior to use to optimize the light output [210]. In 2017 the use of the first plastic scintillator larger than the beam field size was investigated for the measurement of the PDD distribution of passive delivered 62 MeV of protons, also analyzing its response to changes in beam energy and dose rate, and implementing correction for the quenching[48] effect [197]. The latter represent the main disadvantage of using scintillator systems. The system showed reproducibility of results of around 0.8%, dose-rate independence within 2%, range uncertainty within 1%. Scintillating screen systems have also been tested (especially for 2D dosimetric applications, for which they are very suitable), allowing real-time measurements and analysis, with a significant time sparing. However, their use for measuring the PDD distribution is still immature (0.5 mm longitudinal spatial resolution and poor peak-plateau ratio) [189, 213].

Radiochromic Films are widely used in the clinical context, mainly for 2D beam monitoring [214, 215]. They are available in different models and are 2D self-developing devices with high longitudinal (down to 150 µm water equivalent thickness) and lateral (down to 5 µm) spatial resolution. If used in a stack configuration, they can acquire the PDD distribution after a single irradiation [216, 217]. Moreover, they are water-equivalent and show a very wide dynamic range (from 10^{-3} Gy up to 10^{4} Gy) and a dose rate independent response (<5% difference for 10 Gy exposures at rates of 3.4 Gy/min and 0.034 Gy/min) [175, 193, 218, 219]. However, the RCF response require up to 48 hours to stabilize and suffers from a saturation[49] effect which appears at high LET values, resulting in an underestimation of the Bragg peak. In addition, the films are quite expensive, are not reusable, and have to be digitized to extrapolate quantitative information after measurements.

---

[48] Plastic scintillators irradiated with high-LET charged particles suffer from a process of suppression of outgoing light called quenching. As protons slow down due to the energy loss (dE/dx), more energy is locally transferred to the medium (higher LET), but a greater proportion of this energy gives rise to interactions which do not emit light. As a consequence, the relative light output is reduced in the single Bragg Peak and at the end of the Spread-Out Bragg Peak (SOBP). This effect is described by Birks Law [211].

[49] RCFs contain a microcrystalline monomeric dispersion deposited on a clear plastic substrate which undergo polymerization upon interaction with ionizing radiation. When the LET of the radiation increases, it may happen that the ionization phenomena occur at too small a distance to trigger the recruitment of the surrounding monomers, resulting in a local saturation of the polymerization process along the particle track, and in an underestimation of the answer [212]. This effect is sometimes also called quenching.

Other techniques based on gel dosimeters [189] ionoacoustic method [220, 221] and optical fibers [188, 222] for range measurements are under investigation. Also the use of scintillating-Gas Electron Multiplier (GEM) chamber system [6] and solid-state radiochromic polymer dosimeter system called PRESAGE^{TM} [223], both water-equivalent and LET dependent, was examined for verification of depth dose distribution in proton beam therapy, resulting in a range uncertainty of about 2 mm. Moreover, PRESAGE^{TM} system is expensive and not reusable, and requires preparation and off-line evaluation. Other proposed solutions investigate the possibility to identify proton range starting from the initial energy of the beam [224].

Some of the devices discussed here have matured into commercial products, but none of them can successfully address the whole spectrum of requirements that a detector must meet in order to characterize a proton beam in a clinical context. By way of example, Table 2.3 lists a compilation of the main detector types used for PDD measurements in ion beam therapy together with their main advantages and disadvantages.

Device	**Advantages**	**Disadvantage**
Radiochromic Films	• water-equivalent • wide dynamic dose range • high longitudinal and lateral spatial resolution • high accuracy and reproducibility • not subject to electromagnetic noise • dose rate independent response	• LET dependent (undergo saturation effect) • directional dependence • passive devices • not reusable
Plastic scintillator	• fast response • linear response with dose and beam fluence • water-equivalent • available in different shapes and sizes • dose rate independent response	• LET dependent (subject to the quenching effect) • low radiation hardness • low longitudinal spatial resolution (0.5 mm)
MLIC	• fast response • water-equivalent • high accuracy and reproducibility • linear response with dose and beam fluence • small LET and energy dependence	• dose rate dependance (undergo recombination effect) • low longitudinal spatial resolution (≥ 1 mm)
MLFC	• fast response • high accuracy and reproducibility • linear response with dose, dose rate and beam fluence • LET and energy independence	• low longitudinal spatial resolution (~mm)

Table 2.3 Comparison between detectors used for PDD distribution measurements.

2.5 Dosimetric systems for FLASH ion beams

As widely said, ionization chambers are the standard detectors for reference dosimetry through which accurate dose measurements in clinical context are made possible through the application of recognized dosimetric protocols. In the context of FLASH-RT, however, the use of non-standard beams and ultrahigh dose-rates disallows the direct application of these protocols. Moreover, the non-negligible effects of ion recombination suffered by gas devices must be carefully accounted for. Even if recombination models and calculation procedures already exist and are used to correct the response of ion chambers in conventional clinical framework, in the context of treatments that would employ ultrahigh dose-rate irradiations, the ability of these models in determining the correction factors for ultrahigh dose-rate irradiations is limited [124]. At the same time, investigations on the production of new ion chambers with improved performance in FLASH conditions are underway [225-227]. When considering laser-driven ion beams, their distinctive features, such as high intensity per pulse, short pulse duration, extremely high dose rates, broad energy spectra, large divergence, and poor homogeneity, not only preclude the use of conventional dosimeters but also pose challenges in establishing a reliable, accurate, and precise dosimetric protocol. Among the primary characteristics essential for a conventional dosimeter, it becomes evident that laser beam dosimeters must first and foremost be independent of the radiation dose rate and possess high radiation hardness. Additionally, they should not exhibit saturation when exposed to such highly impulsive beam currents, and diagnostic features must be operational at the repetition rate of the laser system.

To date, the PDD distribution of laser-driven proton beams is only measured by using passive detectors like CR-39 and RCF devices, or scintillator detectors [11, 175]. As mentioned above, in order to allow PDD curves reconstruction, RCFs are used in a stack configuration, where a number *N* of devices are stacked one behind the other. Using the stack configuration, the incoming radiation hits perpendicularly the *N* films and each RCF acts as a filter for the following one, making possible both a PDD profile reconstruction and an energy-resolved measurement [216, 218, 229]. Depending on the expected dose at a certain depth, different types of RCF with different dynamic ranges can be placed in the stack. Even if RCFs are not sensitive to the ion species, these devices can be efficiently used also in the mixed radiation fields produced by the laser-target interaction, with an approach focused only on protons [175]. Indeed, heavy ions stop within the first few layers of the stack or inside appropriate filter foils positioned at the entrance of the RCF stack, while hot electrons and X-rays travel through the whole stack, causing the formation of a background signal. The latter, however, can be identified beyond the range of the highest energy protons and conveniently subtracted (electrons form a circular halo distinguishable from the homogeneous background signal due to X-rays). Therefore, RCFs offer the possibility of isolating the proton component of the radiation field produced by laser-target acceleration systems. Furthermore, the high 2D spatial resolution allows evaluating the lateral profile of the laser-driven beams with great accuracy, being able to resolve angular distributions of proton energy. Another advantage of using RCF in laser-driven fields is connected to their insensitivity to electromagnetic noise. For this reason, they can be located in the immediate vicinity of the interaction point, acquiring the whole beam at once. Recently, they have been included in the dosimetric framework for a pilot in-vivo irradiation experiment using a laser-driven proton beam [230]. In Figure 2.5 a sequence of RCF films exposed to a laser-driven proton beam is reported.

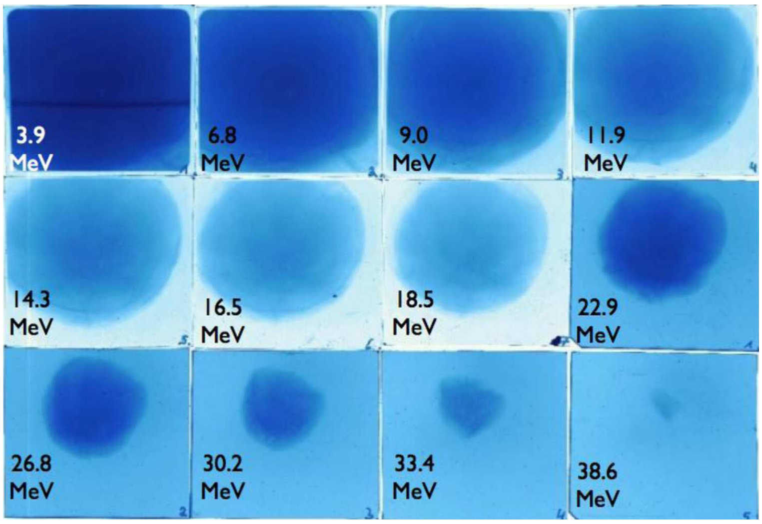

Figure 2.5 RCF stack sequence ordered with respect to the direction of the incident beam. The energy of the protons sufficient to reach and stop in the i-th RCF of the stack (i=1,...,12) is reported [175].

CR-39 are plastic track detectors (typically 0.25–1 mm in thickness, 1.32 g/cm^3 in density) which have the advantage of being insensitive to electromagnetic pulses, X-rays and electrons. When subjected to ionizing radiation, at the point of interaction these devices undergo a local damage (the so-called latent track) related to the loss of energy per unit path length of the impinging particle. These latent tracks can be observed under an optical microscope after an etching procedure in a NaOH solution, which will act more consistently where a damage is present, so that the traces are enlarged and highlighted compared to the undamaged bulk (Figure 2.6). As long as the etching depth is smaller than the particle range, the diameter and depth of the track increase with the increase in etching time. In laser–plasma experiments, CR-39 detectors combined with a fixed-thickness filter can be used to distinguish charged particles, which are generally mixed together. Alpha particles, carbon ions, and protons can be identified by controlling the etching time [231]. So, CR-39 offer the possibility to measure the PDD distribution by resolving the energy distribution of particles (through a direct measurements of the number of particles and an indirect measurement of their energy), but at high particle flux (typically above 10^8 particles per cm^2), or for long etching times, the tracks start to overlap, leading to saturation. They are usually used individually, positioned in front of the biological sample [113, 119], but they can also be used in a stack configuration [116]. The latter method leads to a more precise spectroscopic measurement, as the sensitivity of the single CR-39 plate surfaces depends on the proton energy window and on the etching and detection protocol used.

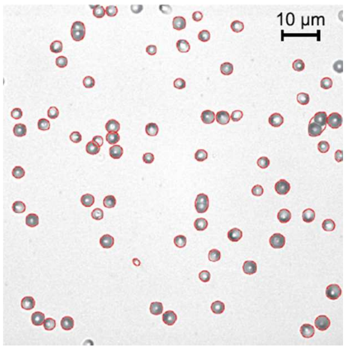

Figure 2.6 Microscopic view on a CR-39 plate (94 × 94µm^2). Tracks are usually identified via an automatic algorithm. Here, they are marked through the red ellipses. In three cases a misregistration occurred by counting two proton tracks close together as only one track [116].

Owing to their excellent tissue-equivalence and the ability to be miniaturized, multiple investigators have recommended the use of organic scintillators for small field dosimetry [125]. In contrast to organic type, inorganic scintillators are usually made with high-Z materials and are therefore not tissue-equivalent. Nonetheless, they have fast rise and decay times, higher radiation hardness and high detection efficiency. To allow 3D measurements, the setup typically consists of a scintillating volume imaged remotely at high spatial resolution (sub millimeter) with a CCD or a CMOS camera. The prompt emission of light, coupled with high frame-rate imaging capabilities of modern imaging sensors, make this technique suitable for dose delivery under FLASH irradiation conditions. The 3D scintillating volume is usually obtained by placing multiple sheets of organic scintillator in the beam path; in this way, each scintillator will respond to a different ion energy range [166]. A proof-of-principle experiment was recently conducted on a compact, scalable, and cost-effective scintillator-based device suitable for the laser–plasma environment [232]. The system is composed of eleven scintillator layers coupled with a CMOS camera. The first tile has a nominal thickness of 3 mm, whereas the others are nominally 1mm thick, forming a 13-mm long stack. To date, it was irradiated with a 35 MeV proton beam delivered by a cyclotron. A reference image of the scintillator stack under irradiation captured with the camera is shown in Figure 2.7. It was found that the position of the Bragg peaks, located at around 10 mm, coincides within ~0.2 mm with that reconstructed using a RCF stack, here used as reference devices.

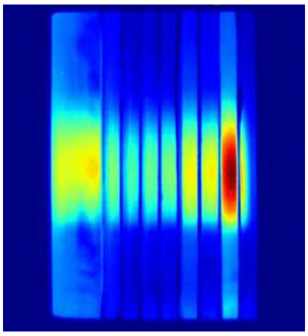

Figure 2.7 Nine out of eleven layers of the complete system. The Bragg peak is located on the eighth scintillator. The proton beam is incident from the left [232].

One FLASH study by *Favaudon et al.* [233] used a 2D scintillating array coupled to a CCD camera for monitoring beam profiles. The scintillating screen was a 0.5 mm thick gadolinium based plastic material with an active area of 300 × 300 mm^2 and a spatial resolution of 0.5 mm. Good repeatability and linearity in a range of dose rates from 2x10^2 to 4x10^7 Gy/s and from 1 mGy to over 30 Gy per microsecond pulse have been obtained with an overall precision better than ± 2% for electron beams. However, the detector response has also been found to be strongly dependent on radiation LET. A similar study is the one reported by *F. S. Englbrecht et al.* in 2018 regarding a scintillator-based system, composed of nine stacked layers of 150 mm polysiloxane, coupled to a CMOS camera, for the spectral characterization of laser-driven proton beam with energy up to 20 MeV [234]. The longitudinal spatial resolution in this case is ~310 mm, due to the presence of some dead teflon layers in the system. Other shortcomings were a low scintillation yield, non-homogeneous response of the layers, uncertainties in the thickness of the scintillation and Teflon layers, bright halo-areas in between scintillation layers, and non-ideal coupling to the CMOS. An upgrade of this type of system is represented by solutions such as the one proposed by *Metzkes et al.* in 2012 [235], a scintillator-based detector coupled with a CCD camera via light guiding able to lead the light signal towards a spacer, in order to obtain a good spatial separation of the different scintillator layers in the imaging plane (Figure 2.8(left)). The system is composed by 10 thin plastic scintillators (each being 50 mm in width, 40 mm in height, and 350 μm in thickness) placed one behind the other, gives access to the angularly resolved proton distribution along one spatial dimension (spatial resolution of ~1.3 mm), and resolves 10 different proton energy ranges (spectral resolution better than 1.5 MeV). The same group in 2016 devised a new way to optimize the characterization of laser-driven proton beams via scintillator-based systems [236]. They thought of using a pixelated matrix with variable absorber thicknesses to be positioned in front of the scintillation system, so that the proton beam is spatially resolved in two dimensions and simultaneously energetically resolved (Figure 2.8(right)). However, the spatial detector resolution reaches down to ~4 mm.

Other interesting innovative studies propose a non-invasive diagnostic to measure the charge of the accelerated ionic group using the Integrating Current Transformer (ICT) [237], and a new method called Ion-Bunch Energy Acoustic Tracing (I-BEAT), based on the recovery of the complete kinetic energy distribution from the acoustic signature that is recorded when a short ion beam deposits its energy in water [238]. Diamond, silicon, or silicon carbide solid-state detectors [124, 125, 189, 228] have also been investigated, gaining ample space and importance in this field. Their properties and potential in the context of conventional and flash dosimetry will be introduced in the next chapter.

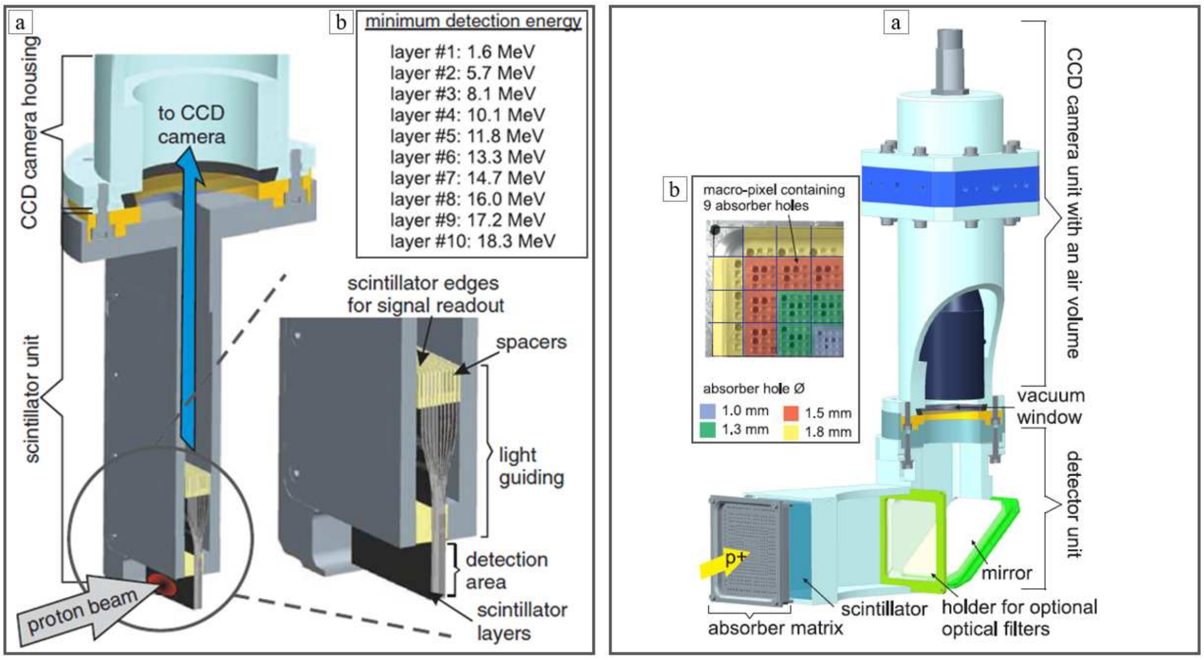

minimum detection energy
layer #1: 1.6 MeV
layer #2: 5.7 MeV
layer #3: 8.1 MeV
layer #4: 10.1 MeV
layer #5: 11.8 MeV
layer #6: 13.3 MeV
layer #7: 14.7 MeV
layer #8: 16.0 MeV
layer #9: 17.2 MeV
layer #10: 18.3 MeV

Figure 2.8 Left panel: (a) Protons irradiating the detection area pass through the stack of 10 thin scintillator layers and deposit an amount of energy characteristic of their initial energy in each individual layer. The produced scintillation light is then guided towards the upper spacers and imaged onto a CCD camera. The online detector resolves 10 different energy layers and offers angular resolution of the proton distribution along the horizontal dimension of the detection area. (b) The table summarizes the minimum initial energy a proton needs in order to reach a specific scintillator layer [235]. Right panel: (a) Technical drawing. (b) Photograph of the upper-left quadrant of the absorber matrix. The different macro-pixels are separated by purple lines and the different zones of absorber hole diameters are color-coded. The matrix is designed in order to be invariant to rotations, and so that the detector can resolve proton beam profiles for up to 9 proton threshold energies [236].

Chapter 3

PRAGUE: Proton Range Measure using Silicon Carbide

3.1 Introduction

The research has been highly active in recent decades in seeking new strategies to accurately and precisely determine the range of charged particle beams, primarily protons, at both conventional and FLASH intensities. Technological advancements in semiconductor materials production have played a crucial role in this pursuit. As a result, there has been a growing interest in exploring the use of solid-state devices in dosimetry, with Silicon Carbide (SiC) technology emerging as a particularly promising avenue. The research project outlined in this thesis is situated within this framework. Specifically, this thesis was conducted within the scope of a project named PRAGUE (Proton RAnGe measure Using silicon carbidE), which received funding from national and international sources. The INFN provided support through a grant for young researchers, while the European Community-contributed funding through the Horizon-2020 program, specifically within the Marie Skłodowska Curie Individual Fellowship program.

PRAGUE project aims to design, realize, and characterize a real-time detector based on SiC technology able to reconstruct the PDD distribution of a 30-150 MeV proton beam with both conventional and FLASH intensity, ranging from 10^4 to 10^{12} particles per second. The detector consists of a stack configuration comprising 60 SiC devices, each with an active thickness of 10 μm and an active area of 15x15 mm². This configuration enables the reconstruction of the distal fall-off of the Bragg peak with an exceptionally high longitudinal spatial resolution of approximately 30 μm of water equivalent thickness.

This Chapter will delve into the features, potential, and challenges associated with silicon carbide material (Section 3.2). A comparative analysis of its physical characteristics with those of widely used silicon (Si) and diamond devices will be presented, along with a detailed description of the PRAGUE project (Section 3.3).

3.2 Silicon carbide devices

The advancement of semiconductor materials and devices has given rise to the burgeoning field of solid-state electronics. Notably, the invention of integrated circuits (ICs) using planar technology has propelled rapid advancements in microelectronics. Si-based components have become integral elements in nearly all electrical and electronic systems. Meanwhile, compound semiconductors have secured unique roles in applications where Si devices face performance limitations due to inherent material properties. A pivotal focus in contemporary technology revolves around enhancing energy efficiency, involving the reduction of energy consumption and dissipation [239]. In this context, SiC has gained recognition as an emerging material. Due to its superior physical properties in comparison to Si, SiC holds great promise for the development of advanced power devices. As a semiconductor, SiC possesses a wide bandgap, high critical electric field strength, and high saturation drift velocity, among other favorable characteristics. Additionally, both n-type and p-type doping can be achieved over a broad concentration range with relative ease. The semiconductor's physical bonds are exceptionally strong, providing it with high mechanical, chemical, and thermal stability.

The main advantage offered by SiC in power applications is its low drift region resistance, which is a key factor for high-voltage power devices. Thanks to its characteristics, more and more companies have invested in SiC technology, which today is considered the frontier of microelectronics, carrying out the important task of developing and optimizing the production processes of this material [240, 241]. However, interest in its semiconducting properties has been dampened by the relative difficulties in producing pure, high-quality crystalline SiC. From the moment of its discovery, we had to wait over 150 years before making the production process mature enough to allow the systematic availability of SiC, with well-defined and reproducible properties. The great inventiveness of the industry towards systematizing the production of this material has also allowed the scientific community to investigate its properties in the field of particle detection and its possible applications, resulting in an emerging and growing interest in the SiC technology applied, among others, to dosimetric systems. In general, the suitability of semiconductor materials for dosimetric applications has been recognized for a considerable time, owing to prior studies involving silicon and diamond devices. Nevertheless, the characteristics of silicon carbide (SiC) render it a more appealing choice compared to silicon and, in certain aspects, even surpassing diamond.

3.2.1 Silicon carbide material for dosimetry

SiC is a semiconductor composed of 50% silicon (Si) and 50% carbon (C). Both Si and C atoms are tetravalent elements and have four valence electrons in their outermost shells. Si-C bond is covalent, giving rise to tetrahedrally oriented molecules of SiC, with a very short bond length and, hence, a very high bond strength (Figure 3.1(a)). From a crystallographic point of view, SiC is the best known example of polytypism[50]. The number of identified SiC

---

[50] Polytypism is the phenomenon where a material can adopt different crystal structures which vary in one dimension (that is, in stacking sequence) without changes in chemical composition [239].

polytypes is higher than 200. Only a few of them, denoted 3C-SiC (pure cubic polytype, sometimes referred to as β-SiC), 4H-SiC and 6H-SiC (hexagonal, with some cubic symmetry, also called α-SiC) are stable enough and thus of technological interest (Figure 3.1(b)) [239, 242, 243]

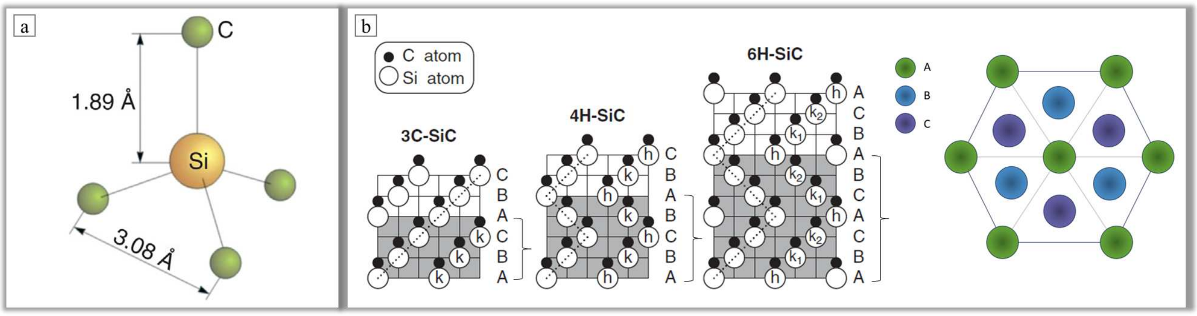

Figure 3.1 SiC crystallography. a) The smallest tetrahedral building element of any SiC lattice. Each Si atom has exactly four C atom neighbors, and vice versa. b) Structural differences of the main SiC polytypes. In a compact hexagonal system there are three possible occupiable sites (in stacking sequence), usually called A, B, and C. The atoms of two sequences (or layers) cannot occupy the same positions (so, for example, the next layer on top of an "A" layer must occupy either "B" or "C" sites). SiC polytypes are named in Ramsdell's notation, where a number represents the number of Si-C layers in the unit cell, and a letter represents the crystal system (C stands for cubic, H stands for hexagonal). So, in 3C-SiC polytype 3 layers of SiC (the site sequence is ABC) are needed to form the basic structure, while for 4H-SiC and 6H-SiC respectively 4 (with sequence ABCB) and 6 (ABCACB) layers are needed.

Each polytype has its physical properties, such as the energy bandgap[51], which ranges from 2.36 eV in 3C-SiC to 3.27 eV in 4H-SiC at room temperature, or the critical electric field, which is much higher for the hexagonal polytypes than cubic one at a given doping density. 4H-SiC exhibits a hole and electron mobility that are respectively slightly higher and almost double than that of 6H-SiC at a given dopant density. Moreover, the mobility anisotropy is relatively small in 4H-SiC (contrary to 6H-SiC). [239]. Due to these characteristics, 4H-SiC is usually considered the most attractive polytype. Among solid-state base detectors, thanks to their intrinsic characteristics, SiC detectors have shown promising performances and represent a good compromise between the maturity of Si detector development and the robustness of diamonds.

Si diodes have been the primary devices used as in-vivo dosimeters, thanks to their sensitivity to radiation at no-bias voltage, good stability, compactness, fast and direct readout, high efficiency, and high resolution [244, 245]. However, silicon is not a tissue-equivalent material due to its high atomic number (Z=14) compared to that of tissue ($Z_{eff} \simeq 7.64$), which leads to a dosimetric response strongly dependent on radiation energy [246, 247]. Silicon detectors also have other disadvantages, such as dose rate dependence, angular dependence and radiation damage susceptibility [248, 249]. This seriously restricts their prolonged use in high radiation

---

[51] The band gap decreases with increasing temperature (because of thermal expansion) and doping concentration (very high impurity doping, above 10^{19} cm^{-3}, causes the bandgap to shrink because of the formation of pronounced tail states near the band edges) [239].

field environments at room temperature [124, 125, 247]. On the other side, tests on diamond [250-259] and SiC [246, 260-269] detectors strongly encourage the use of these devices in radiation dosimetry, also in severe radiation conditions. Unluckily, diamond-based devices have the disadvantage of being very expensive as a consequence of the difficulty of selecting stones with the appropriate dosimetric properties [260]. An alternative with a potentially lower production cost is represented by chemical vapor-deposited (CVD) diamond films [270]. However, their use in radiation dosimetry presents a limitation in both the charge collection efficiency and the uniformity of the electrical quality across the area. These limitations affect the sensitivity and the spatial resolution of the device, giving rise for example to the priming effect[52] [253, 260, 262, 271, 272]. Moreover, they are available in small linear dimensions (of the order of a few millimeters), a geometrical limitation due to the size of the initial seeds used in the growth technique (see Section 3.2.2) [273]. For these reasons the interests of the research community in this field turned towards the SiC detectors, even if it is not nearly as tissue-equivalent ($Z_{eff} \simeq 10$) as diamond [246]. The principal characteristics of SiC, Si, and diamond devices are listed and compared in Table 3.1.

Property	**4H–SiC**	**Si**	**Diamond**
Energy band gap [eV]	3.27	1.12	5.45
Intrinsic carrier concentration [cm^{-3}]	$5x10^{-9}$	$1x10^{10}$	$\sim 10^{-27}$
Critical (breakdown) electric field strength [MV/cm]	2.2	0.25	1-10/5.6
Saturated electron drift velocity [10^7 cm/s]	2.0	1	2.7
Electron mobility [cm^2/Vs]	1000	1400	1900
Hole mobility [cm^2/Vs]	115	600	2000
Thermal conductivity (W/cmK)	3.7	1.49	6-20
Relative dielectric constant	9.76	11.9	5.7
Refractive index at a wavelength of 600 nm	2.64	3.44	2.41
Atomic number [Z_{eff}]	14–6	14	6
Density [g/cm^{-3}]	3.21	2.33	3.52
e–h pair creation energy [eV]	7.78	3.6	13
Threshold displacement energy [eV]	22–35	13–20	40–50
Minimum ionizing energy loss [MeV/cm]	4.4	2.7	4.7

Table 3.1 Main properties at room temperature (300 K) of 4H-SiC compared to Si and diamond [242, 243, 267].

---

[52] It consists of an enhancement of the detector response after irradiation, following which there is a partial capture of the charge carriers, which remain trapped in the detector's defects. This generates the saturation of deep traps which in turn causes a consequent decrease in recombination in subsequent irradiations.

The most beneficial inherent material properties of 4H-SiC over Si are its exceptionally high breakdown electric field, wide bandgap energy, high carrier saturation drift velocity, high displacement atom energy, and high thermal conductivity. The wide bandgap energy allows SiC to maintain semiconductor behaviour, which in turn implies low leakage currents, even at high reverse bias and at much higher temperatures than silicon [267, 268]. SiC does not show any significant increase in intrinsic carrier concentration in a wide range of temperatures, being relatively insensitive to current–voltage fluctuations even at temperatures as high as 800°C, while silicon loses its semiconductor properties around 300°C. The thermal conductivity of 4H-SiC (which is not sensitive to the SiC polytype, but depends on the doping density and the crystal direction) is very high, so its physical properties barely change with increased temperature. This leads to reduced requirements of cooling systems, which lowers the overall system volume and cost, and opens the possibility of using these devices for in-vivo dosimetry of patients that need to be kept at a comfortable temperature with warm air blowing systems [243, 246, 274, 275]. In addition, due to the high energy gap, SiC does not detect visible radiation (thus, does not require light-tight encapsulation for most applications), but it detects very well UV and X-rays with a good level of signal-to-noise ratio at room temperature [246, 262, 276-278]. A small enough electron-hole pair generation energy is important to ensure a high sensitivity and signal-to-noise ratio. In this case, SiC performs better than diamond, while it is exceeded by Si [260, 279]. Another important aspect is the Si-C displacement energy which makes SiC devices more resistant to radiation damage than Si ones (whose lower displacement threshold implies the formation of a higher number of radiation-induced defects at lower energies), and capable of operating for longer periods with unchanged detection properties [265, 280]. The high critical electric field strength (which decreases with increasing the doping concentration) allows operation at high internal electric fields while maintaining low reverse current, minimizing carrier transit time and trapping probability. The high carrier saturation velocity, high electrons and holes mobilities (whose values decrease with increasing temperature and/or dopant density) imply fast response and a more efficient charge collection [267, 268]. Moreover, numerous studies have proved that the response of SiC devices is independent from the dose rate and linear to dose or the energy released in the active region of the detector [246, 262, 281, 292], even in FLASH regimes [266]. SiC devices have also demonstrated particle detection with excellent energy resolution and charge collection efficiency [265, 283, 284, 261, 285, 286], and absence of priming effect [246]. Recently, SiC detectors were tested under clinical proton beams, proving to maintain good performances even at null bias [273, 287], and carbon beams [288-290]. These results indicate that SiC-based devices are suitable for applications in the clinical field in both conventional and high intensity regimes. The high radiation hardness, the fast response, and the independence on dose rate make SiC a good candidate also for FLASH Radiotherapy applications [266] and for the detection of the next generation laser-driven particle beams [261, 291, 292]. The use of large-bandgap semiconductor detectors, such as SiC, allows for a reduction in the low-energy electromagnetic spectrum of laser-generated beams, improving proton/ion sensitivity. Nanosecond time resolution was measured with 4H-SiC diodes during the detection of laser-accelerated plasma radiation [293, 294].

3.2.2 Growth and processing of silicon carbide

SiC is rare in nature (it exists in the form of the very rare mineral moissanite), and synthesis of a compound material containing silicon–carbon bonds was first reported in 1824, in an attempt to synthesize diamond [295]. Since then, other SiC synthesis processes have been tested over the years, such as the *Acheson process* of 1892 [296], or the *Lely method* of 1955 [297]. The latter was able to grow relatively pure cm^2-size hexagonal and flat single crystals (known as "*Lely platelets*"), giving rise to the first evidence of SiC semiconductor-like properties. Starting from these crystals, it was possible to determine in detail the crystallographic, optical, and electronic properties of SiC, and the scientific and technological interest for SiC semiconductor became really significant. However, because of the small size of Lely platelets and unsteady material supply, research and development of SiC semiconductors slowed down in the late 1970s, and the technology remained immature. A real breakthrough occurred in 1978 when the growth of SiC using the sublimation[53] method, also called physical vapor transport (PVT) or deposition (PVD), was demonstrated [298]. Subsequently, several groups followed and further developed the growth process to obtain SiC wafers with a larger diameter and reduced defect density, leading to the first commercialization of SiC wafers (25 mm in diameter) in 1991 by *Cree Research Inc.* (today named *Wolfspeed, Inc.*) [299]. It took more than 10 years for the first commercialization because PVT technique is very difficult to implement and control [242]. Moreover, this process grows SiC crystalline boules (also named ingots or bulks) with typical thickness of 20-50 mm and they need to be cut and polished in order to be usable for semiconductor technology. This posed an additional problem due to the exceptional hardness and chemical inertness of SiC material, which made cutting and polishing procedures challenges. Today SiC boules are usually sliced in wafers (with thickness of ~hundreds of μm) using a multi-wire diamond saw. Another option is to adopt the most recent laser splitting techniques, which however are not free from technical issues either. Slicing using electric discharge is also being investigated to improve the process speed and to reduce induced damage [239]. Following the slicing process, subsequent procedures such as edge grinding, shaping (via lapping or surface grinding), polishing (typically achieved through chemical processes), and cleaning are essential. These steps are undertaken to eliminate as many surface defects as possible. The quality of the wafer surface post-polishing is crucial for ensuring high-quality epitaxial growth and minimizing the occurrence of significant defects. Figure 3.2 collects

---

[53] The sublimation method is useful for growing crystals from vapor. At present, this is a popular method for growing SiC and AlN (aluminium nitride) crystals. All SiC bulk wafers are grown in a heated furnace where a SiC source (solid SiC powder or sintered polycrystalline SiC, or silicon and carbon containing precursors transported in a carrier gas) sublimes and condenses on a single-crystal SiC seed. The distance between the top of the SiC source and the seed crystal is typically 20–60 mm. The seed temperature is about 100 °C lower than the source temperature (2100–2400 °C), so that sublimed SiC species condense and crystallize on the seed. Growth is usually performed at low pressure to enhance the mass transport from the source to the seed. Over the years new growth strategies have been investigated [239, 268]. For SiC production, it is required to have a seed with high quality and with diameter at least of the same dimensions as the ingot to be produced.

some images of SiC in different production stages. Over the years, continuous efforts have been made to be able to create SiC wafers with increasingly larger speed, quality and diameter (Figure 3.3) [239, 268].

Figure 3.2 Silicon carbide in various forms. a) SiC platelets obtained in the Acheson process [239]. b) A SiC single crystal ingot synthesized via the sublimation method [300]. c) SiC wafer (200 mm) ready for subsequent processing [301].

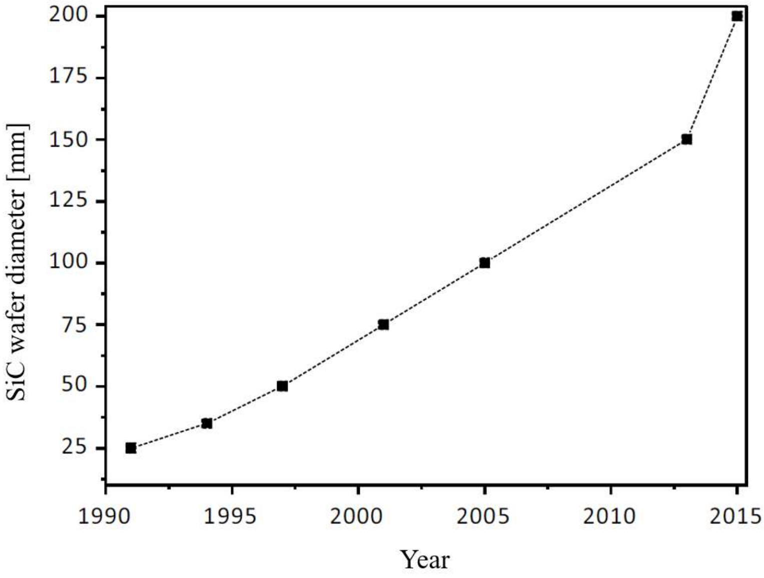

Figure 3.3 Evolution of commercial SiC wafer diameter with time [243].

Even the most advanced SiC wafers exhibit elevated levels of defects and doping concentrations. Consequently, they can only serve as the substrate to facilitate the epitaxial layer growth, which constitutes the active region of the detector. The epitaxial[54] growth, indeed, is essential to produce layers with designed doping density and thickness, and is

---

[54] Epitaxy refers to a type of crystal growth or material deposition in which new crystalline layers are formed with one or more well-defined orientations with respect to the crystalline substrate. The deposited crystalline film is called an epitaxial film or epitaxial layer. The most common choice in SiC detectors is to grow an epitaxial layer of the same politype of the substrate (homoepitaxial).

usually based on Chemical Vapor Deposition (CVD[55]) technique, which has shown remarkable progress over the years [302-305]. The epitaxy of SiC is an active field of research, with numerous improvements (in growth rate, crystal quality, doping control, thickness uniformity, and so on) being made, which is critical for advanced device development [242, 306]. After epitaxial growth of SiC several processing steps are performed to fabricate electronic devices. In general, at this point semiconductor fabrication is grouped into two processes: the front-end process and the back-end process. In the front-end process, wafers are engineered, and in the back-end process, they are separated into individual elements (die or chip, wafer dicing phase), assembled, tested and, eventually, packaged. Figure 3.4 contains a graphic representation of the various steps to be taken to obtain chips starting from the ingot.

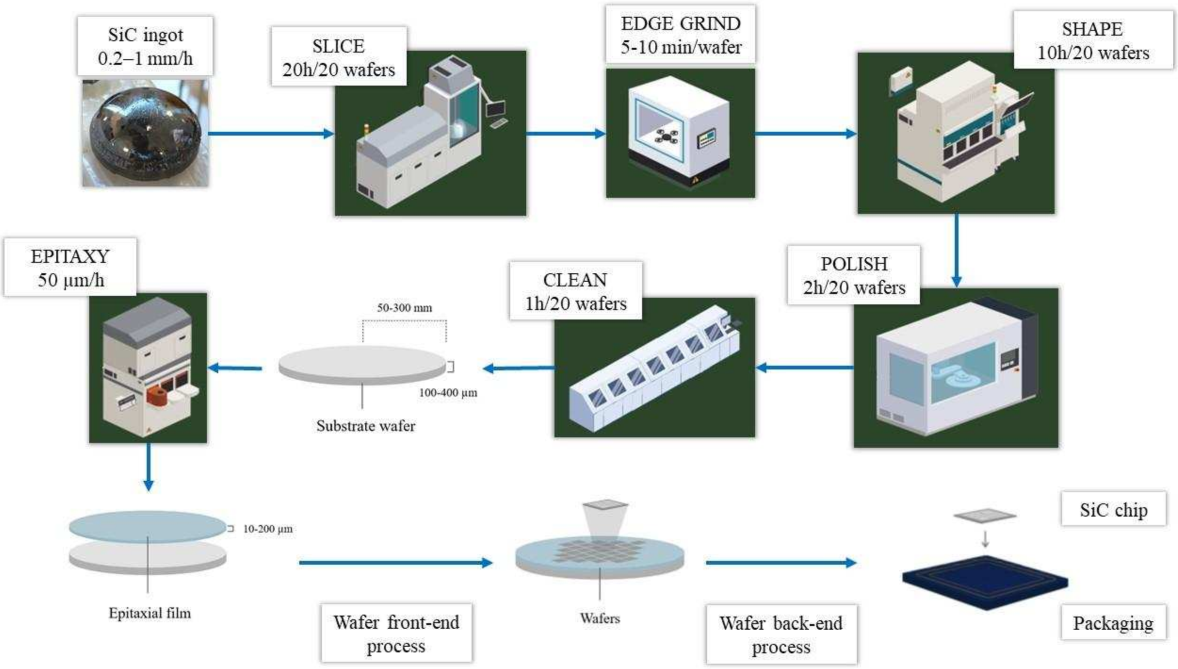

Figure 3.4 Phases of creation of a SiC chip. Starting from a 30 mm thick ingot generated at a speed of 1 mm/h, it takes almost 3 days to obtain a wafer with a 50 um epitaxial layer [268, 307, 308].

---

[55] CVD is a synthesis technique that allows a deposit to be obtained on a solid support starting from a gaseous molecular precursor that decomposes on the surface of the substrate.

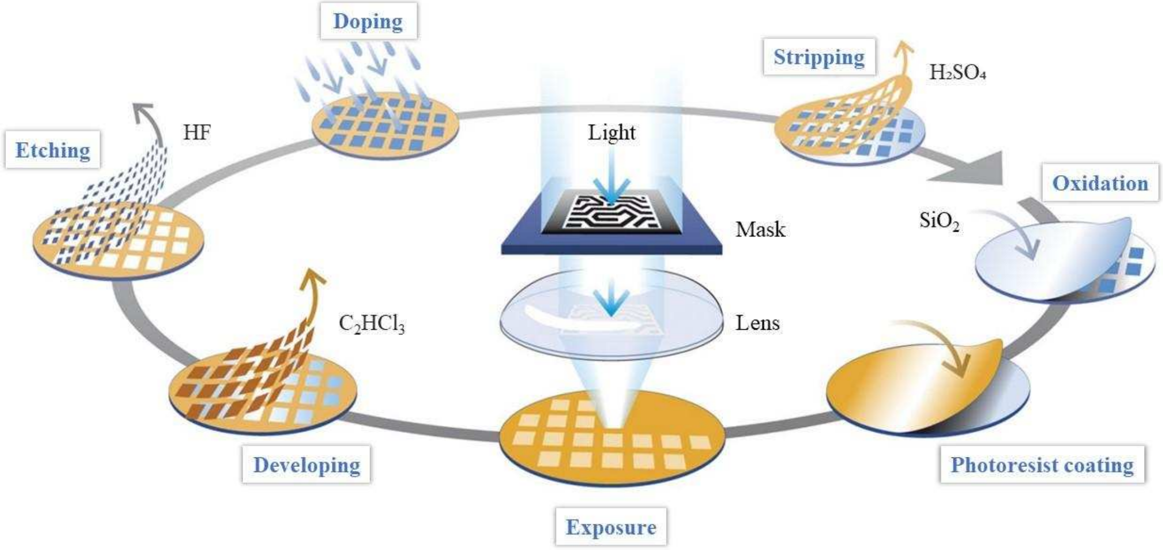

Figure 3.5 Example of a photolithographic cycle typical of planar technology as part of the wafer front-end process. In order it includes: 1) oxidation: it serves to isolate the epitaxial layer; SiC forms silicon dioxide (SiO_2) as a native oxide, and it is an important advantage for device fabrication. 2) Photoresist coating: after the oxidation phase, a photosensitive resin (photoresist) is sprayed on the oxide. 3) Exposure: the resin, after being dried, is exposed to ultraviolet rays through a mask in which the opaque parts correspond to the windows to be opened in the oxide. The photoresist hit by the rays polymerizes, modifying its chemical structure, while the one covered by the opaque parts remains unchanged. 4) Developing: the unpolymerized photoresist is selectively removed with the use of a solvent such as trichloroethylene (C_2HCl_3), opening a window onto the oxide. 5) Etching: the exposed oxide parts are removed using a chemical attack using hydrofluoric acid (HF). 6) Doping: doping can be carried out using different techniques (for example, ion implantation or diffusion) and will only affect the open windows on the epitaxial film, generating p- or n-doped "islands" on the wafer surface. 7) Stripping: the operational phases end with the removal of the polymerized photoresist. This removal can be carried out by mechanical abrasion or by the use of an inorganic solvent such as hot sulfuric acid (H_2SO_4).

Wafer engineering (i.e., front-end processing) today is usually carried out in what is called planar process, patented in 1959 by the American company *Fairchild* [309, 310] which led to the miniaturization of semiconductor devices and, subsequently, to the creation of ICs [311, 312]. Through this technique, all processing operations take place on a single surface of the device. It allows doping and/or metallization of selected areas of the wafer to be performed using the photolithographic technique. The latter exploits the creation of masks deposited on the surface of the wafer which act as protection towards those areas of the surface not to be treated. In Figure 3.5 a schematic diagram of a masking cycle that allows selective doping into the underlying wafer is reported. This cycle can generally be repeated several times. For the metallization operation, all the phases of the photolithographic process are carried out again until, this time, a mask with windows corresponding to the surfaces to be metallized is obtained on the surface of the wafer. This step aims to establish ohmic contacts with the p or n region separately, so as to avoid short circuits. Figure 3.6 shows a wafer after the front-end process. Once the metallization model is created, it is possible to proceed to the subsequent back-end steps (i.e., wafer inspection and dicing, chip attachment and bonding, packaging).

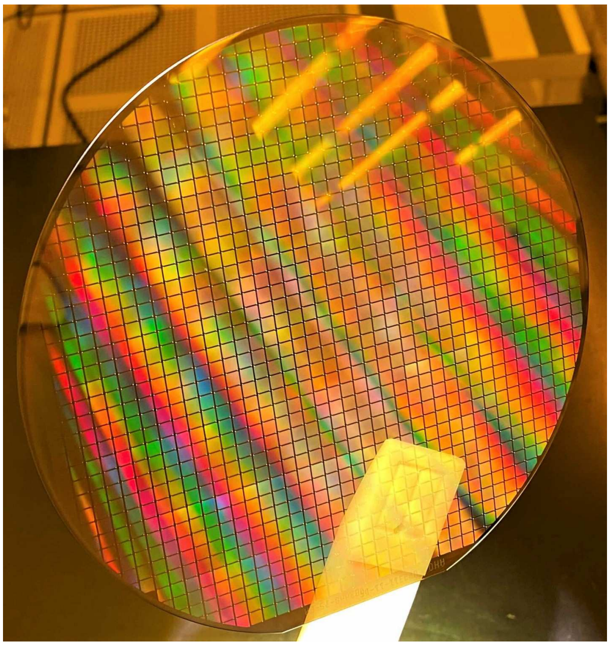

Figure 3.6 SiC wafer after front-end processing. Each single die is also visible. The apparent color of SiC crystals changes following doping. Impurities in SiC not only influence the electronic properties of the material but also the optical ones. SiC pure wafers are generally transparent to visible light.

From what has been said so far it is clear that SiC devices suitable for a demanding semiconductor industry are not easy to produce. The manufacturing processes still need to be optimized both in terms of device quality and costs. Usually, the quality of upstream devices is defined in terms of the purity of the material and evaluated based on the presence of defects within it [239]. Thicknesses and dimensions (detection area) are the actual technological limits on SiC material processing. However, research in this context is progressing rapidly given the ever-increasing interest in this promising material [268, 306, 313, 314].

3.3 The PRAGUE project

3.3.1 Description of the device and operating principle

The PRAGUE project consists in the realization and characterization of a system composed of 60 SiC devices, 10 μm in active thickness and 15×15 mm^2 in active surface, arranged in a stack configuration and dedicated to the acquisition of the PDD distribution of proton beams with both conventional and very high intensity. The operating principle on which the device is based follows the already-known schemes typical of stack configuration systems. As a proton with an initial energy E traverses the N=60 layers of PRAGUE, it undergoes energy loss, denoted as dE, on each layer. This loss is contingent upon the depth at which each SiC detector is positioned relative to the particle's entry channel, following the characteristic trend of the Bragg curve. Consequently, the generation of electron-hole pairs, and thereby the charge produced within each detector, is influenced by the remaining energy of the proton upon impact. Following a meticulous calibration process, it becomes possible to correlate the current (or charge) response of each device to the absorbed dose, facilitating the reconstruction of the depth deposition curve of the original beam. Additionally, through the implementation of a technique known as spectral unfolding (or spectral deconvolution), it becomes feasible to characterize the spectral composition of the beam. In summary, the depth-dose-distribution, incident particle spectra, and particle range can be reconstructed based on the measured integral charge.

The SiC detectors adopted for the realization of PRAGUE were designed within the SICILIA (Silicon Carbide detectors for Intense Luminosity Investigations and Applications) project, whose aim was the development of innovative processes for the production of relatively large area SiC with extremely high performance in terms of energy resolution and radiation hardness [306]. These are p$^+$n junction devices with expected thicknesses and dopants concentrations as illustrated in Figure 3.7. For devices with such characteristics, depletion voltages of around 9 V are expected.

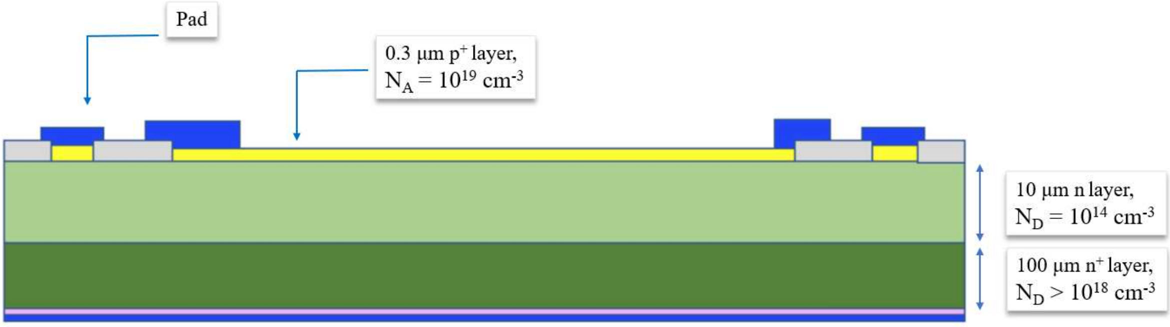

Figure 3.7 A sketch of the detector that will be used for the reconstruction of the entrance part of the Bragg peak curve. N_A and N_D represent respectively the acceptor and donor concentration of dopants. Not in scale.

In order to achieve the highest longitudinal spatial resolution possible, we plan to remove the passive layer of 30 of the 60 SiCs through an electrochemical etching procedure[56] [315]. As already said, SiC is characterized by a remarkable chemical resistance to all acids and bases at room temperature: this can be attributed to the very strong Si–C bond, which must be broken before etching can occur [242]. A recent technique based on an electrochemical etching (ECE) in a hydrofluoric (HF) solution has proved to be effective [317]. ECE is an oxidation/oxide removal process obtained by dipping SiC samples in HF solution and electrically supplying holes for the oxidation through the back metal contact [318]. This procedure selectively eliminates the thick, heavily doped ($N_D > 10^{18}$ cm^{-3}) substrate while preserving the low-doped n-type layers. To prevent damage to the 10 µm active region, a SiC epitaxial layer without any dopant is introduced to halt the corrosive process. This method enables the production of membranes that are as uniform and thin as the growth epitaxial layer.

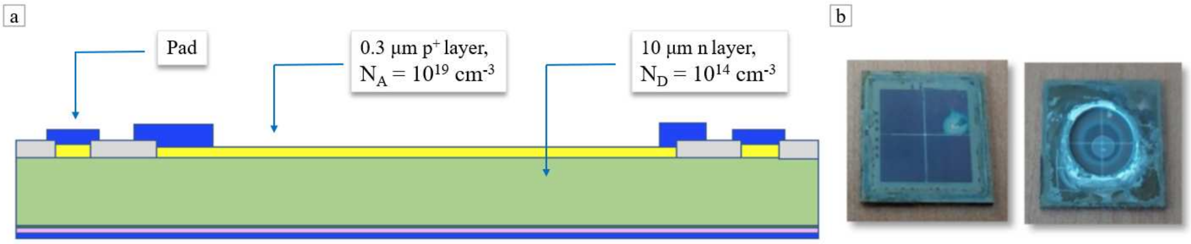

Figure 3.8 a) A sketch of the detector that will be used for the reconstruction of the distal and proximal part of the Bragg peak curve. N_A and N_D are as before. Not in scale. b) Examples of detectors after the etching process.

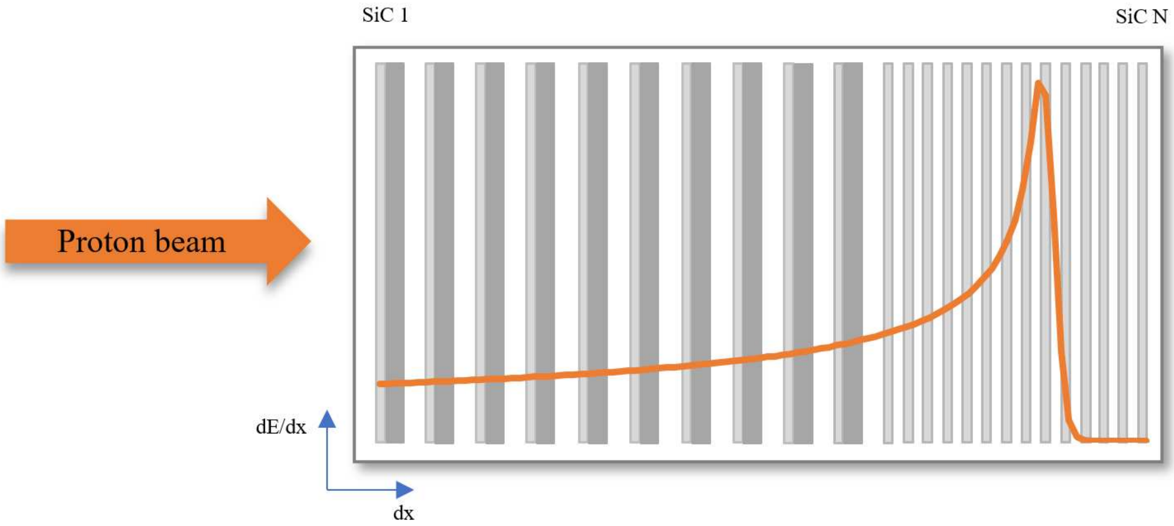

Figure 3.9 Qualitative diagram illustrating the operating principle of the PRAGUE detector. The light gray slices represent the active layer of each SiC device, while the dark gray slices represent the passive layer. The distal and proximal region of the Bragg peak is sampled with a higher spatial resolution than the plateau. Not in scale.

---

[56] This procedure will be performed in collaboration with the IMM-CNR (Institute for Microelectronics and Microsystem - Consiglio Nazionale Delle Ricerche) [316].

Detectors without the passive layer (depicted in Figure 3.8) will be employed for reconstructing the distal and proximal segments of the Bragg peak, characterized by a steep dose gradient, necessitating a higher longitudinal spatial resolution for accurate sampling. Conversely, detectors equipped with a passive layer will be utilized for capturing the plateau region of the Bragg curve. Figure 3.9 provides a qualitative depiction of the final detector, illustrating its configuration and operational principle.

By utilizing all 60 SiC detectors, comprising 30 with a passive layer and 30 without, it becomes feasible to reconstruct the PDD curve of protons up to 30 MeV. Notably, the last 30 SiC devices are capable of detecting protons with residual energy up to 7 MeV, with a longitudinal spatial resolution of 30 μm water equivalent thickness, denoted as t_w. The determination of t_w was carried out using the thin-target approach known as the Stopping Power Ratio (SPR) approximation [192]:

$$t_w = t_m \cdot \frac{\rho_m}{\rho_w} \cdot \frac{S_m(E_i)}{S_w(E_i)} \tag{3.1}$$

where t_m is the physical thickness of the material m with density ρ_m, ρ_w is the water density, and $S(E_i)$ represent the stopping power values of protons with initial energy E_i in the material (subscript m) and in water (subscript w)[57]. To adapt the system for incident proton beam energies exceeding 30 MeV, calibrated thicknesses of equivalent water material can be inserted at the entrance or between the first 30 SiC devices to attenuate the beam. Another approach involves the use of passive detectors, such as Radiochromic Films, between the initial 30 layers of the system. This dual purpose is to attenuate the beam while simultaneously sampling the curve. This modification allows for the detection of energies up to 150 MeV. To stabilize the radiation field and mitigate edge effects, a collimator will be designed. The entire system will be enclosed within a protective and containment case, serving the additional purpose of shielding the devices and electronic chain from the electromagnetic noise characteristic of laser-based acceleration systems.

Several detector parameters, such as the inter-plane distance between the detector layers, the position and thickness of the absorbers, the diameter of the collimator, will be investigated as the incident beam energy varies to optimize the resolution and accuracy provided by the prototype, especially in the distal fall-of the dose curves. In this context, feasibility studies dedicated to the design and realization of a holder suitable for the in-vitro irradiation of biological samples will be conducted. We plan to insert the biological samples between the first SiC layers, that will sample the PDD distribution in the plateau section. The preliminary studies will serve to define the configuration that facilitates the accurate determination of the dose absorbed by the biological sample, even in the presence of laser-driven pulsed beams. In Figure 3.10 a possible configuration for cell irradiation is reported.

---

[57] Based on their arrangement on the PRAGUE detector, the energy of interest for these devices is up to 7 MeV, but for completeness I have evaluated the water equivalent thickness of 10 μm of SiC material for the energies of interest in the clinic with protons, therefore up to 250 MeV, always finding a value up to 30 μm. $S(E_i)$ values were evaluated via SRIM.

The assembly of linear stage motors capable of allowing the modification of the positions of the various SiCs along the direction of propagation of the beam - and therefore the general configuration of the device in its entirety - will also be evaluated in order to make the device suitable for the acquisition of proton beams with energies up to 150 MeV, while maintaining high spatial resolution.

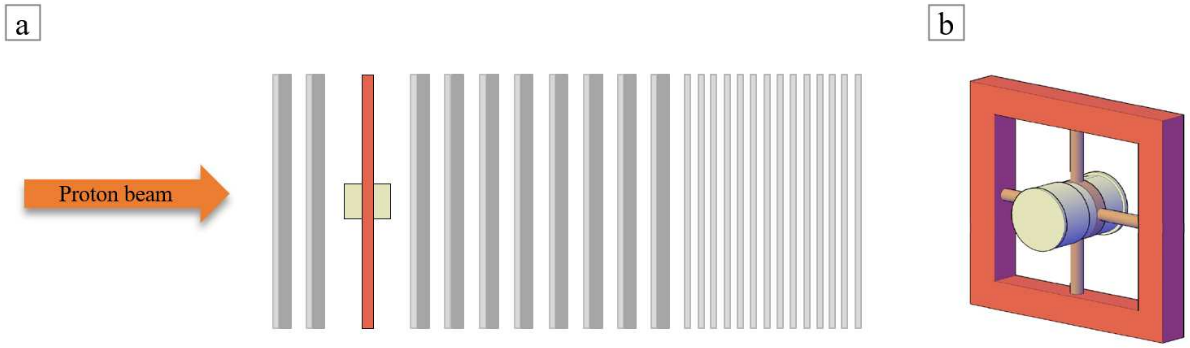

Figure 3.10 a) Preliminary layout of PRAGUE configuration for biological sample irradiation. In red is reported a sketch of the biological sample holder. Not in scale. b) Preliminary layout of the custom biological flask coupled with its holder.

3.3.2 Electronic chain and acquisition software

The innovation of PRAGUE resides not only in the adopted detectors but also in the front-end electronics, which must be designed to function seamlessly with both conventional (continuous) and laser-driven (pulsed) beams. The electronic chain should independently read the 60 signals generated by the detectors, providing high temporal resolution and a broad dynamic range to prevent information loss. The 60 SiC devices will be integrated into a customized electronic board, with each channel connected to an RC system developed and optimized to mitigate efficiency losses in charge collection with pulsed beams. Processed signals will be directed to a digitizer employing an operational amplifier system where the analog input signals from the 60 channels will be continuously sampled in a circular manner. The optimization of the electronic read-out system will occur after characterizing the SiC devices that will form the final detector and estimating the dark and under-beam currents they produce. For a more comprehensive overview of the initial version of the electronic chain, please refer to Chapter 5. Beyond the development of the electronic chain, an acquisition software capable of remotely managing the acquisition parameters of the electronic chain and enabling real-time reconstruction of the PDD distribution will be designed and subsequently implemented

3.3.3 Project impact

Based on the aforementioned details, it becomes evident that the PRAGUE detector has the potential to revolutionize the current status of relative dosimetry for both conventional and high-intensity proton beams in the reconstruction of PDD distribution. The detector meets nearly all the requirements essential for an ideal relative dosimeter (refer to Table 3.2).

The primary drawbacks include non-water equivalence, the limited size of the detectors' active area (closely tied to the current technological limits of silicon carbide production), and the existence of a maximum detectable cut-off energy without degrading the beam, thereby maintaining the same energetic and spatial resolution. However, the latter issue could potentially be addressed by implementing an expanded version of the detector.

Conversely, the advantages of the device are numerous and significant. PRAGUE stands out as the first real-time solid-state detector capable of measuring depth-dose distribution curves of proton beams with high spatial resolution and radiation-hardness while maintaining a response independent of the dose rate and the LET of the radiation. Thanks to its ability to acquire the entire beam at once and to provide an online reconstruction of the PDD distribution with a longitudinal spatial resolution of approximately 30 µm water equivalent thickness, the performance of the PRAGUE detector can exceed that of the devices dedicated to relative dosimetry most commonly used in clinics, in terms of time consumption and accuracy of range estimation. Furthermore, PRAGUE can enable radiobiological investigations to be carried out with a reliable and precise measurement of the dose released on biological samples. This could be a significant advancement for the ongoing investigation into FLASH effect.

Advantages	Disadvantages
• fast response • fast electronics • linear with dose and beam fluence • independent from LET and energy • independent from dose rate • high radiation hardness • high longitudinal spatial resolution • online reading • known dose on biological sample	• non water-equivalence • limited active area • limited detectable energy range (*)

Table 3.2 Advantages and disadvantages of PRAGUE detector. (*) without considering the possible insertion of thicknesses that would degrade the beam.

Chapter 4

PRAGUE Prototype

4.1 Introduction

A prototype of the PRAGUE detector was realized to conduct a preliminary feasibility study of the SiC-assembled system in a stack configuration. The PRAGUE prototype consists of four SiC devices mounted on a guide track and capable of sliding along it. The electronic system utilizes current-voltage (IV) converters coupled to a 4-channel voltage input module. Each Silicon Carbide device underwent electrical testing through the reconstruction of the I-V (Current-Voltage) and C-V (Capacitance-Voltage) curves. Furthermore, the entire assembled system underwent testing with 35 MeV and 70 MeV proton beams. A description of the prototype system and the detectors that compose it will be provided below, as well as the electronic chain adopted (Section 4.2). Characterization tests (Section 4.3) and investigation of PDD reconstruction capability will follow (Section 4.4). The investigation on the possibility of finishing the back-end process of SiC devices with epoxy resin packaging was undertaken as part of the feasibility studies aimed at the development and optimization of the final PRAGUE device (Section 4.5). In particular, the study aimed to adapt the final device for the acquisition of PDD distribution of proton beams with energy up to 150 MeV. The resining process investigation also served to explore the feasibility of developing a dosimetric device based on SiC technology able to acquire the PDD distribution of clinical beams in water.

4.2 Prototype design

4.2.1 Geometry and description of the devices

The 4 SiC devices used to compose the PRAGUE prototype were manufactured in the framework of a collaboration between INFN and IMM-CNR. These are 4H-SiC p^+n planar junctions built by using new technological processes developed in collaboration with ST-Microelectronics company (STM), in Catania [319]. Each device has an active area of 10 x 10 mm^2, a 0.3 µm thick p-layer with a doping concentration $N_A=1 \cdot 10^{19} cm^{-3}$ and a 10 µm thick n-layer with a doping concentration $N_D = 0.5 - 1 \cdot 10^{14}$ cm^{-3}. The substrate is 120 µm thick, with a doping concentration of $N_D > 10^{18}$ cm^{-3}. The layout of the device structure is reported in Figure 4.1(a).

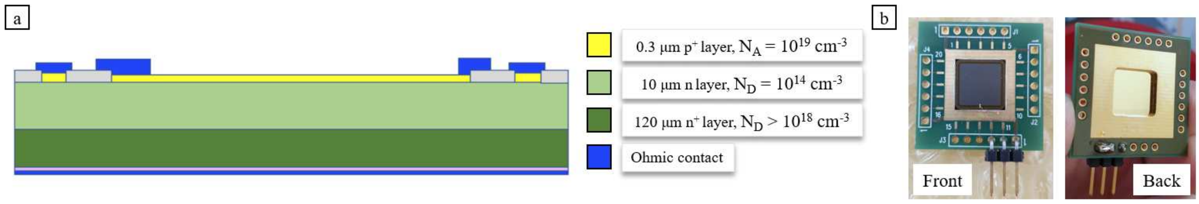

Figure 4.1 a) Schematization of the structure of the devices constituting the PRAGUE prototype. b) Picture of the front and back side of the SiC1 mounted on the drilled PCB.

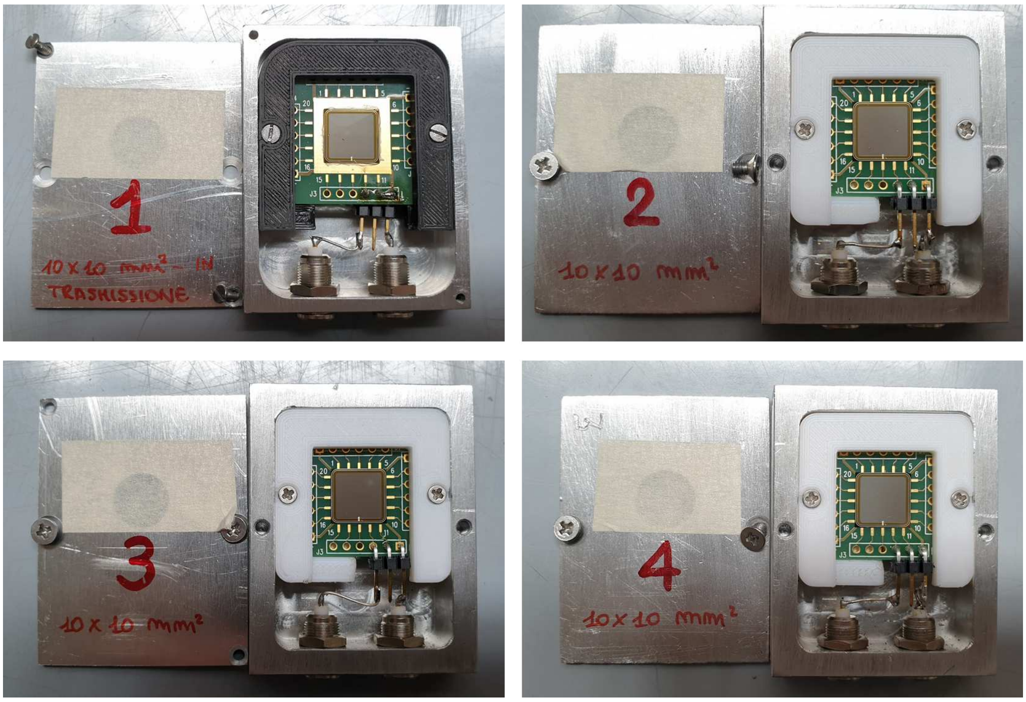

Figure 4.2 PRAGUE prototype detectors placed inside customized aluminum cases. The anode and cathode of the devices were both connected to the copper core of two LEMO connectors, while the ground coincided with the external casing of the supports. Plastic frames ensure insulation of SiC PCBs.

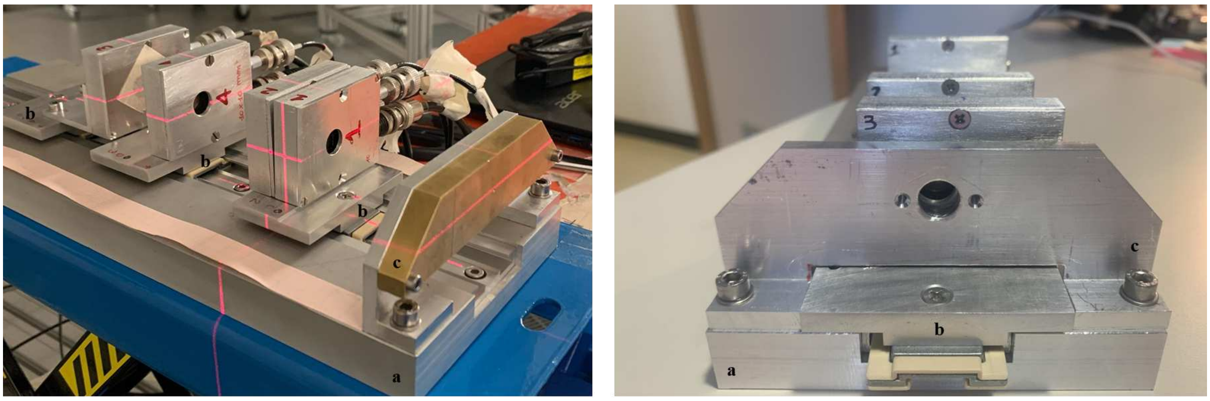

Figure 4.3 PRAGUE prototype system. The markers a - b - c on the images indicate respectively the guide track, sliding carriage and collimation system. Left panel: later view of the device during alignment procedure. Right panel: front view of the device containing three of the four detectors.

To arrange the SiCs in a stack configuration, an aluminum support system was designed with a guide track layout capable of accommodating the four devices stacked one behind the other. To allow the relative motion among the devices, the latter were mounted on independent sliding carriages. In this way, it is possible to move each device along the direction of propagation of an incident beam, after an appropriate alignment procedure. The system, shown in Figure 4.3, has been designed to allow SiCs to be stacked compactly (without air spaces between the aluminum boxes) and in any order. It is equipped with a housing system for collimators with different thicknesses and with a special support designed to contain a stack of RCFs in variable numbers. The latter is designed to replace one of the lids of the aluminum cases containing the SiCs, so as to allow simultaneous irradiation of both detection systems. Figure 4.4 shows a graphical representation of the project and an image of the realized RCF support.

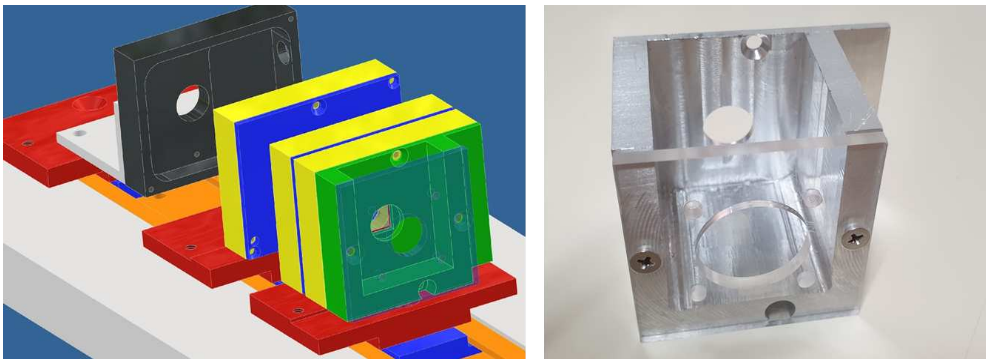

Figure 4.4 RCF holder for PRAGUE prototype. On the left, a graphical representation of the support mounted on a SiC case. On the right, an image of the device. It has an aluminum structure and a plexiglass lid, equipped with a 1.5 cm diameter hole.

4.2.2 Electronic chain and data acquisition (DAQ) system

The data acquisition (DAQ) system used for the readout of the PRAGUE prototype is based on the use of:

A. a commercial power supply, *Up to 5 kV – DT547x (CAEN)* model [320]; it features a single high-voltage channel supplied in both polarities via a SHV connector. The unit is remotely powered and controlled by a USB 2.0 port, through a dedicated LabVIEW-based control software that allows for easy setting and monitoring of high voltage parameters. To power all four SiC devices simultaneously, it was coupled to a four-channel voltage divider.

B. four customized transimpedance amplifiers (TIAs), which act as a current to voltage converters; a simplified diagram of their operating principle is shown in Figure 4.5. The transimpedance gain is based on the feedback resistance R_f. A SiC device added to a TIA can be modeled as a current source and a capacitance C_{SiC}. This capacitance (added to that of the connection cable, ≃100 pF/m) across the input terminals of the operational amplifier (op-amp) introduces instability. To mitigate this effect and improve stability, a feedback capacitor C_f is usually added in parallel to R_f, but it also introduces a low-pass filter in the feedback path. However, in case of working with continuous signals whose frequency band is below the cut-off frequency of the filter, the contribution of C_f can be neglected in the determination of the output voltage. The conversion relationship between the input current and the output voltage will therefore be given by:

$$V_{out} = - I_{in} \cdot R_f \tag{4.1}$$

where the negative sign arises from the configuration of the amplifier being in an inverting mode. In the specific case of the TIAs developed for the PRAGUE prototype, each of them is equipped with three different feedback resistors, manually selectable through a switch. Their values are 0.1GΩ (low gain, L), 1GΩ (medium gain, M), and 10GΩ (high gain, H), through which 1nA of input current is converted into 0.1V, 1V, and 10V respectively (Figure 4.5(b)). Each TIA requires a voltage of ±15V (V-, V+) to operate and is equipped with a customized power supply capable of providing it.

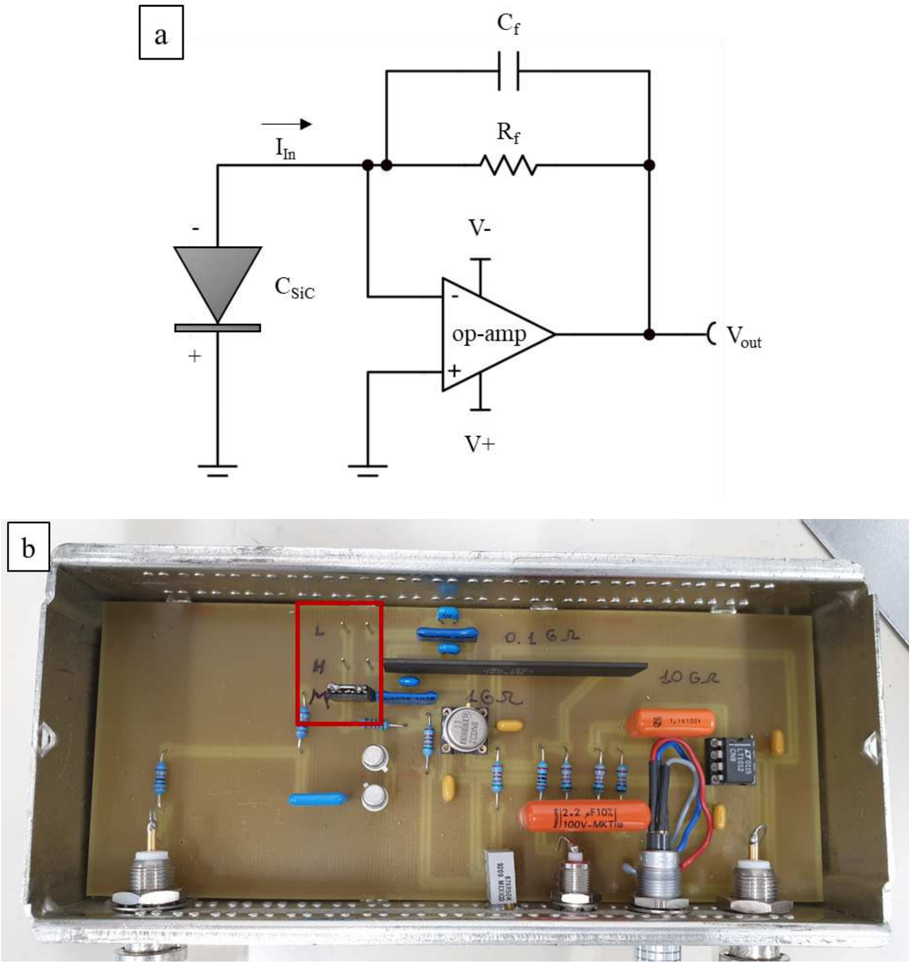

Figure 4.5 a) Simplified scheme of a transimpedance amplifier with a reverse-biased diode. b) Picture of one of the ITA used for the readout of the PRAGUE prototype detectors. In the red box the 0.1GΩ (low, L), 1GΩ (medium, M), and 10GΩ (high, H) gains switch.

C. a commercial high speed digital scope for voltage reading, *National Instrument 4-Channel C Series Voltage Input Module 9223* (NI-9223) [321]; it is equipped with four analog input channels (from 0 to 3) that accept double polarity input voltages in the ±10.5-10.7 V range via BNC connectors. Each channel is processed independently and simultaneously with the others with a maximum sampling rate of 1 MHz.

The DAQ system (schematized in Figure 4.6) is complemented by a custom LabVIEW software and a laptop. The software, called "*9223 reading*", allows the user to set acquisition parameters (such as sampling frequency and acquisition time), concurrently observe processed signals through the NI-9223 module (including elapsed time and instantaneous voltage values for each channel), and store the data.

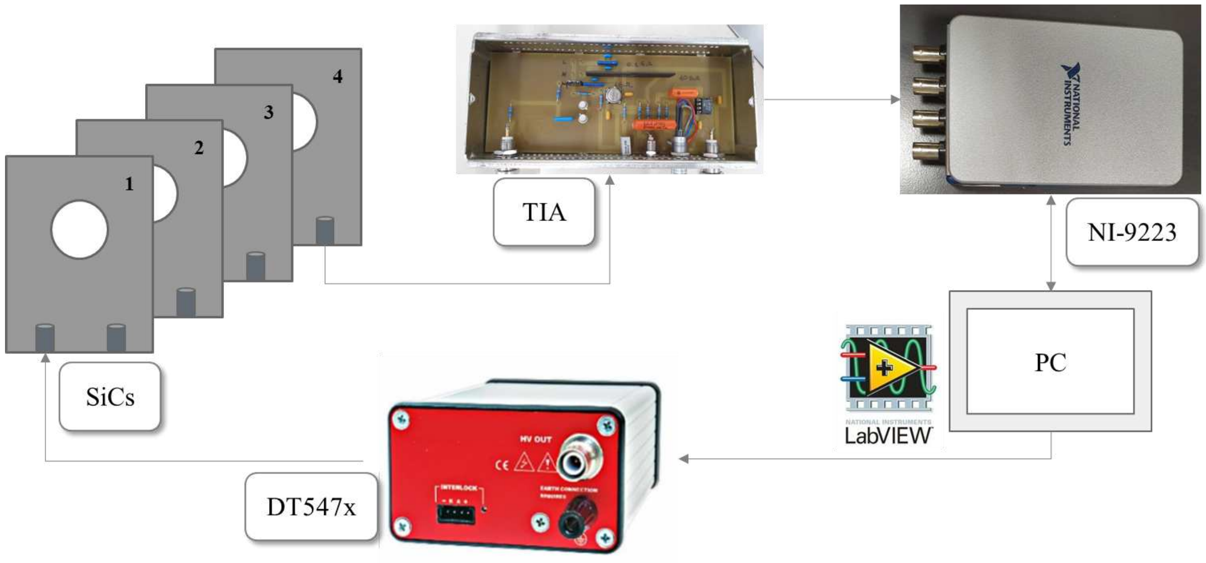

Figure 4.6 Schematization of the DAQ system used for the PRAGUE prototype.

4.3 Prototype characterization

4.3.1 Electrical characterization

One of the advantages associated with the use of semiconductor detectors (specifically, p-n junction) is to exploit the depletion region as an active volume with low free charge density (i.e, low leakage current). Here, when a particle deposits energy, an equal number of conduction electrons and holes are formed along the particle's path within a few picoseconds [43]. The latter will subsequently drift towards the collection electrodes (generating a drift current) under the action of the electric field within the depletion region, and their movement constitutes a basic electrical signal. In this context it is important to apply reverse bias to reduce electronic noise, maximize the signal-to-noise ratio and generally improve charge carrier collection. Ideally, the reverse bias should be high enough to achieve a thickness of the depletion region equal to that of the junction (full depletion region operating regime), resulting in the lowest possible capacitance for the detector (called saturation capacitance). However, to create an electric field large enough to ensure efficient collection of charge carriers, it is generally necessary to impose a larger reverse bias voltage across the active volume. Once the electric field is sufficiently high, charge collection becomes complete and the signal height no longer changes with further increases in the detector bias voltage. This region of operation is called the saturation region (or over depletion regime). Under these conditions, even in the absence of ionizing radiation, the leakage current can increase and the random fluctuations that generally occur will tend to obscure the small current signals that flow following an ionizing event, representing a significant source of noise in many situations. Furthermore, if the bias grows too much it can reach the value at which a sudden breakdown of the diode occurs (called breakdown voltage) accompanied by a sharp increase in the reverse current and, often, irreversible destructive effects. It is therefore clear that it is important to monitor these electrical characteristics to understand the behaviour of each device and set the proper operational conditions. They are typically monitored through I-V (current *vs.* voltage) and C-V (capacitance *vs.* voltage) characterization. The I-V and C-V characteristics of a junction are extremely important, as they allow to obtain several pieces of information on the device [322-324]. Through the I-V curve, it is possible to model the transport phenomena occurring in the device and the potential energy barriers influencing the motion of charge carriers. This allows for the evaluation of the quality of the electrical contacts made and for drawing conclusions about the concentration and nature of defects present in the detector itself. In the context of this thesis work, however, the I-V characterization was useful to identify anomalies in the conductive behaviour of the detector, define the leakage current of the investigated detectors, and establish the breakdown voltage in the voltage range of interest. From the C-V curve, it was possible to obtain information on the device’s saturation capacitance, the thickness of the depletion region (also called transition region, junction region, or space charge region), the depletion voltage, the built-in voltage, and the dopant density and profile. To understand how to extrapolate these quantities from the C-V characterization, the following is a brief theoretical excerpt outlining the laws governing the involved quantities.

It is known that, if no voltage is applied across a pn junction, the junction remains in thermal equilibrium. The thermal equilibrium condition is established through a balance between the diffusion forces acting on the majority charge carriers (electrons in the n region and holes in the p region) and the electric field formed at the edges of the depletion region (from the n to the p region) thanks to the presence of the fixed charges not balanced by the mobile charges. This electric field corresponds to the presence of a potential barrier that prevents the passage of electrons from the conduction band of the n region to the conduction band of the p region. This potential barrier is referred to as the built-in potential barrier and is denoted by V_{bi}. The V_{bi} barrier maintains equilibrium between majority carrier electrons in the n region and minority carrier electrons in the p region, and also between majority carrier holes in the p region and minority carrier holes in the n region. This potential difference across the junction cannot be measured with a voltmeter because new potential barriers will be formed between the probes and the semiconductor that will cancel V_{bi}. Considering a step junction, i.e. a junction in which the dopant concentration is uniform in each region and an abrupt change in doping occurs at the junction, it is shown that the built-in voltage can be calculated as:

$$V_{bi} = \frac{kT}{e} \cdot ln\left(N_A N_D / n_i^2\right) \tag{4.2}$$

where:

- $k = 1.38 \times 10^{-23}$ JK^{-1} is the Boltzmann constant;
- T is the temperature in [K];
- n_i is the intrinsic carrier concentration of the material at T temperature, in [cm^{-3}];
- N_A and N_D are respectively the acceptor and donor concentration of the p and n regions, in [cm^{-3}].

By applying an external voltage V_R concordant to V_{bi} (i.e., reverse polarization condition), the passage of a drift current between the p and n regions borne by the minority charge carriers is promoted, involving an enlargement of the depletion region, the width of which is found as:

$$W\left(V_R\right) = \left\{\frac{2\varepsilon_s\left(V_R + V_{bi}\right)}{e} \cdot \left[\frac{N_A + N_D}{N_A N_D}\right]\right\}^{1/2} \tag{4.3}$$

where:

- $e = 1.6 \times 10^{-19}$ C is the elementary electric charge;
- $\varepsilon_s = \varepsilon_0 \varepsilon_r$ is the permittivity the material, with the permittivity of vacuum $\varepsilon_0 = 8.85 \times 10^{-12}\ F/m$, and the relative dielectric constant ε_r of the material.

Equation (4.3) clearly shows that the total depletion region width increases as we apply a reverse-biased voltage. Moreover, since we have a separation of positive and negative charges in the depletion region, a capacitance C is associated with the pn junction:

$$C\left(V_R\right) = A \cdot \left\{e\varepsilon_s N_A N_D / 2\left(V_R + V_{bi}\right)\left(N_A + N_D\right)\right\}^{1/2} \tag{4.4}$$

where A is the sensitive area of the junction. Comparing equations (4.3) and (4.4), we obtain:

$$C(V_R) = \frac{A\varepsilon_s}{W(V_R)} \tag{4.5}$$

which is the same as the capacitance of a parallel plate capacitor. If we consider a junction with $N_A \gg N_D$, denoted by p^+n (also called one-side junction), (4.3) and (4.4) equations respectively reduce to:

$$W(V_R) = \left\{ \frac{2\varepsilon_s (V_R + V_{bi})}{eN_D} \right\}^{1/2} \tag{4.6}$$

$$C(V_R) = A \cdot \left\{ \frac{e\varepsilon_s N_D}{2(V_R + V_{bi})} \right\}^{1/2} \tag{4.7}$$

From (4.6) it is clear that the width of the space charge region is a reciprocal function of the doping concentration, and that the depletion region will extend further into the lower-doped region. If the applied voltage is further increased, the depletion region may be made to extend all the way to the back surface of the wafer, resulting in the fully depleted junction. The voltage required to achieve this condition is called the depletion voltage, V_D. Its theoretical value is found by setting the nominal thickness W_N of the depletion region in equation (4.6):

$$V_D = N_D \frac{eW_N^2}{2\varepsilon_s} \tag{4.8}$$

Clearly, when the full depletion condition is reached (i.e. $V_R > V_D$), the laws (4.6) and (4.7) no longer apply, since even if the reverse bias voltage increases, W cannot increase and consequently C remains constant. This aspect is usually investigated by analyzing the trend of $1/C^2$ as V_R varies:

$$\frac{1}{C^2} = \begin{cases} \frac{2(V_R + V_{bi})}{eA^2\varepsilon_s N_D} & if\ V_R \leq V_D \\ k & if\ V_R \geq V_D \end{cases} \tag{4.9}$$

where *k* is a constant. By exploiting the condition (4.9) it is possible to determine the depletion voltage V_D, the built-in voltage V_{bi}, and the dopant concentration N_D by applying the interception method. This method consists in finding the two linear functions that best approximate the trend of $1/C^2$ in the region that precedes the depletion voltage (with equation y=mx+q), and in the region that follows the depletion voltage (with equation y=k). V_D will be given by the intersection between the two functions. Furthermore, as easily verifiable, from the knowledge of the parameters m and q it is possible to extrapolate N_D and V_{bi} as follow:

$$N_D = \frac{2}{eA^2\varepsilon_s m} \tag{4.10}$$

$$V_{bi} = \frac{q}{m} \tag{4.11}$$

Figure 4.7 shows the correspondence between the theoretical trend of 1/C^2 and the corresponding extrapolatable quantities. Finally, by combining (4.5) and (4.9) when $V_R \leq V_D$ it is possible to study the dopant profile as W and V_R vary:

$$N_D(W, V_R) = \frac{2\varepsilon_S(V_R+V_{bi})}{eW(V_R)} \tag{4.12}$$

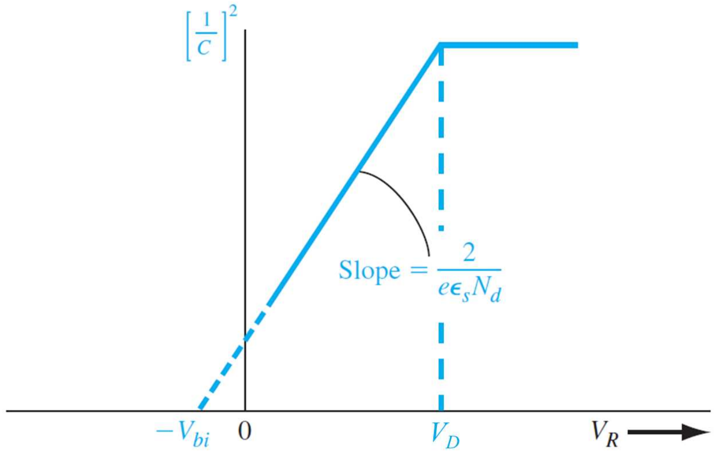

Figure 4.7 1/C^2 versus V_R of an uniformly doped p^+n step junction.

4.3.2 I-V characterization

The I-V characterization involves measuring the current generated by the detector, in the absence of incident radiation, while varying the applied voltage across the junction. Experimental tests were carried out at the INFN-LNS (Catania, Italy). In the I-V measurements, the current generated by the detector was measured using a KEITHLEY 6517B (K6517B, Tektronix company) multimeter, which also served as the bias source for the detector [325]. K6517B offers accuracy and sensitivity specifications unmatched by any other meter of this type and is able to supply up to ±1kV voltage. With reading rates of up to 425 readings/second, the K6517B is significantly faster than competitive electrometers, so it offers a quick, easy way to measure low-level currents. In particular, it can perform current measurements from 1fA to 20mA. Through the K6517B, it is also possible to conduct charge measurements ranging from 10fC to 2μC. This instrument was also utilized as a charge meter during the experimental tests conducted in this thesis. It is equipped with GPIB and RS-232 interfaces. Through the RS-232 serial interface, in particular, it was possible to remotely control the instrument through customized programs that I developed in the LabVIEW environment. The latter, described in more detail in the Appendix (Section A.1 and A.2), include routines to reconstruct the I-V, I-t (current *vs.* time) and Q-t (charge *vs.* time) curves. The I-V software, in particular, allows the user to set several parameters such as the sampling rate, input current and voltage source full scale, voltage ramp and acquisition time, and waiting time before starting the acquisition. For each voltage value, it acquires the current for a time interval established by the acquisition time value. It then returns the average value of it. In Figure 4.8 the DAQ system used to perform the I-V acquisition is reported.

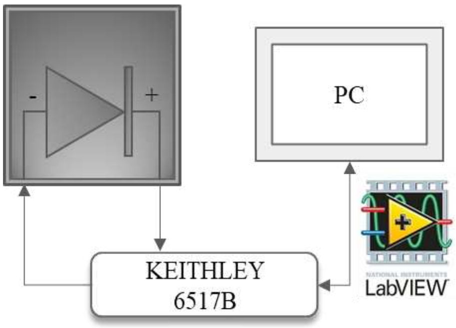

Figure 4.8 Scheme of the DAQ system used for the reverse I-V characterization of the SiCs of the PRAGUE prototype.

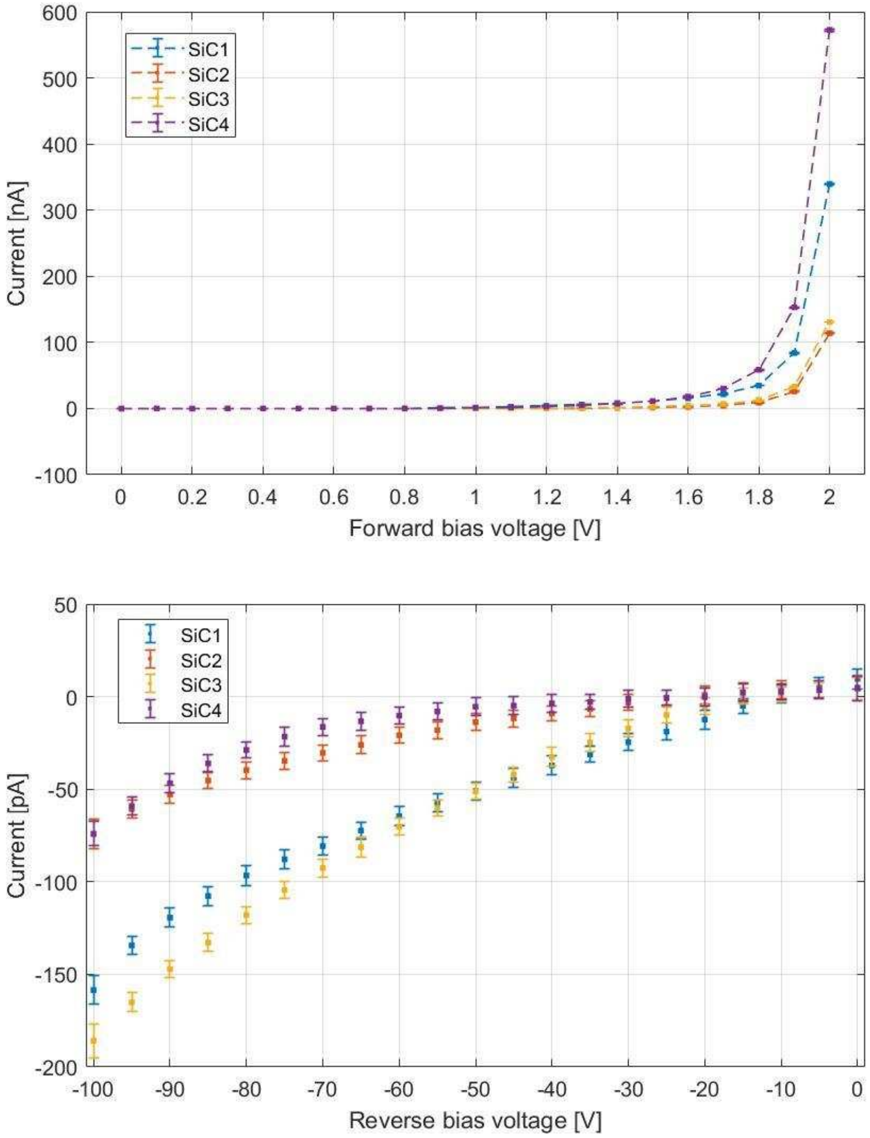

Figure 4.9 I-V profile of the SiCs of PRAGUE prototype. Top panel: direct polarization. Error bars are of the order of 5-50 pA and are calculated propagating the standard deviation on the mean value (~10-90 pA) and the accuracy of the instrument (~0.005-1.2 nA). Bottom panel: inverse polarization. Error bars are of the order of 4-10 pA and are calculated propagating the standard deviation on the mean value (~0.4-0.7 pA) and the accuracy of the instrument (~0.1-2 pA).

I-V measurements were performed at room temperature and in air, applying voltage to the p-type SiC layer while grounding the metallic contact. The I-V profiles were studied in the reverse bias voltage range 0 - 100 V (5 V step, 200 pA and 100 V full-scale) and in the forward bias voltage range 0 - 2 V (0.1 V step, 20-200 nA and 100 V full-scale). In both polarizations, an acquisition time of 60 seconds per voltage value, a sampling rate of 2Hz, and a waiting time of 60 seconds were configured. Figure 4.9 presents the resulting SiC I-V curves in both polarizations. The reverse trend shows a departure from the leakage current, but the breakdown voltage is not reached. The leakage current at 0-50V voltages does not exceed 50 pA. The error bars were evaluated taking into account the standard deviation associated with the mean value and the accuracy of the instrument.

4.3.3 C-V characterization

To perform the C-V acquisition, the capacitance was measured at room temperature and in air by means of an HP precision LCR meter (model 4284A) [326] coupled with a customized interface module allowing the polarization of the device via the K6517B electrometer. The experimental setup used to perform the C-V acquisition is reported in Figure 4.10.

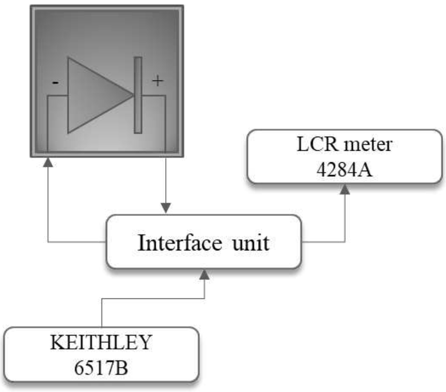

Figure 4.10 Experimental setup used to acquire the C-V profile of the PRAGUE prototype.

The C-V profiles were studied in the reverse bias voltage range of 0–100 V, with a variable step ranging from 0.1 to 5 V (set manually). The adopted capacimeter was set to operate at a full scale of 2 nF with a sample rate of 1 kHz. In Figure 4.11 the resulting C-V curves are reported. Error bars were evaluated taking into account the accuracy of the instrument. In Table 4.1 the physical quantities extrapolated from the C-V characterization for each detector are reported. The errors were evaluated by applying the error propagation theory. In particular, from the experimental values obtained for C, it was possible to determine:

1. The saturation or junction capacitance C_s, experimentally determined as the minimum capacitance value obtained by increasing the reverse bias voltage. The experimental values are compared to the theoretical value $C_s^{th} = \frac{A \cdot \varepsilon_s}{W_N} = 860\,pF$, calculated through equation (4.5) with $A = 10 \cdot 10\,mm^2$, $W = W_N = 10\,\mu m$, and the relative dielectric constant of

SiC, $\varepsilon_r = 9.7$. The results point out a deviation between the experimental values and the theoretical value between 4.2% and 7.3%.

2. The thickness W of the depletion region in full depletion conditions. W was estimated by exploiting the inverse formula of (4.5) relationship, by using the experimental values obtained for C_s. From the comparison between the experimental values of W with the nominal one $W_N = 10\ \mu m$, a difference between 4% and 6.8% is found.

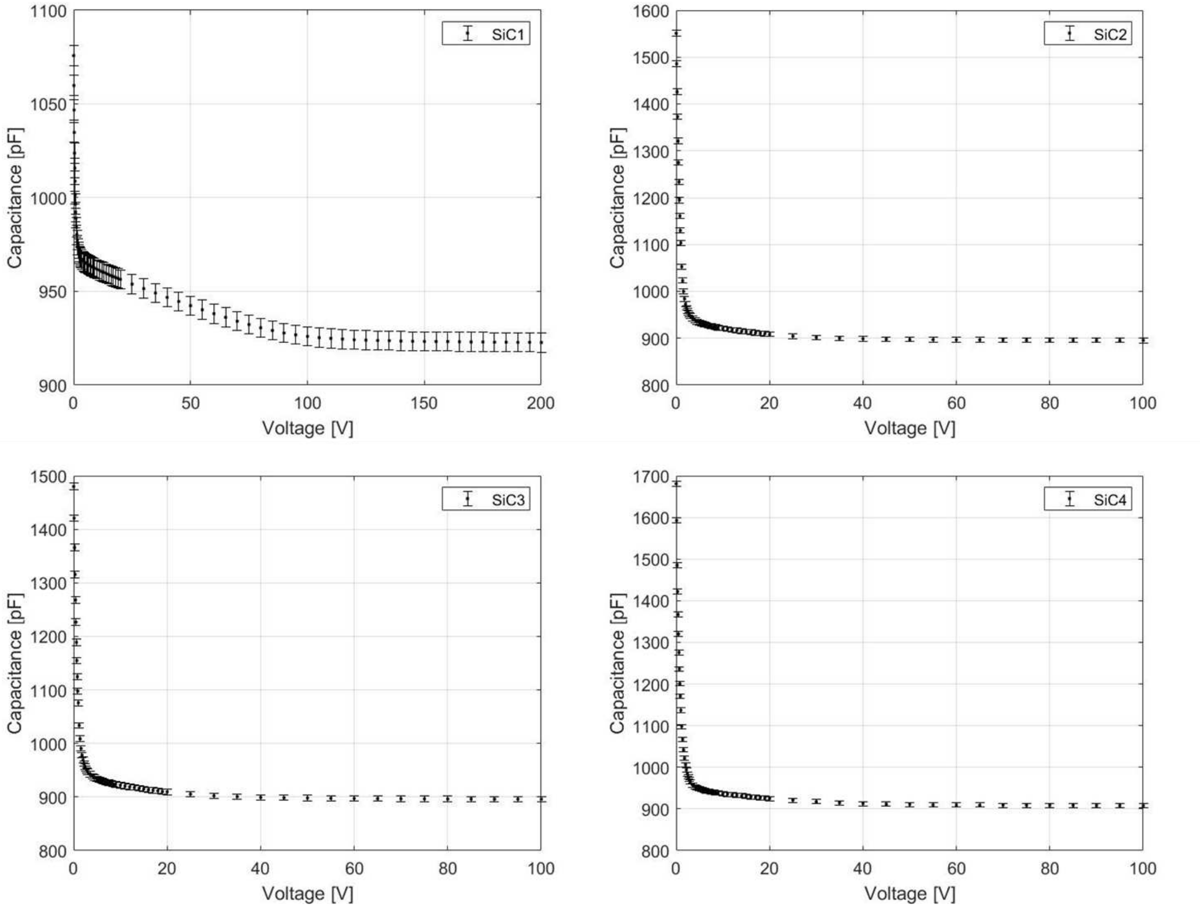

Figure 4.11 C-V profile of the SiCs of PRAGUE prototype. The offset capacitance equal to ~5 pF was subtracted from the measured capacitance values. The C-V characteristic of SiC1 was investigated up to 200 V due to anomalous behavior observed in the trend up to 100 V. Upon visual inspection it was possible to note the presence of a crack on the sensitive surface of the device, a probable cause of the behavior observed.

3. The depletion voltage V_D, the built-in potential V_{bi}, and the donor concentration N_D, determined by applying the intersection method on the $1/C^2$ curves as a function of the applied voltage V. The trend of the $1/C^2$ curves *vs.* applied voltage for each SiC device are reported in Figure 4.12. They show the typical straight line trend at voltages between 0 and 3 V, while for higher biases, the curve shows a gradual change in slope, until reaching constant values at around 20 V. The curve obtained for SiC1 is an exception to this behaviour, probably due to an anomalous crack on the detector surface. The experimental

values of V_D, V_{bi}, and N_D were compared with the theoretical ones; expected $V^{th}_D = 4.7$ - 9.3 V and $V^{th}_{bi} = 2.9$ V were evaluated respectively using equations (4.8) and (4.2), with W_N=10 µm, n_i=5x10^{-9}cm^{-3} for T=300K, and N_D = 0.5 - 1 · 10^{14} cm^{-3}. Calculating the theoretical V_{bi} at the extremes of the range of possible values for N_D, voltage values varying by 0.02 V were found. Indeed, in general, the built-in potential barrier changes only slightly when doping concentrations change by orders of magnitude due to the logarithmic dependence. Since the accuracy of the method used to extrapolate V_{bi} is not high enough to appreciate this variation, it was ignored.

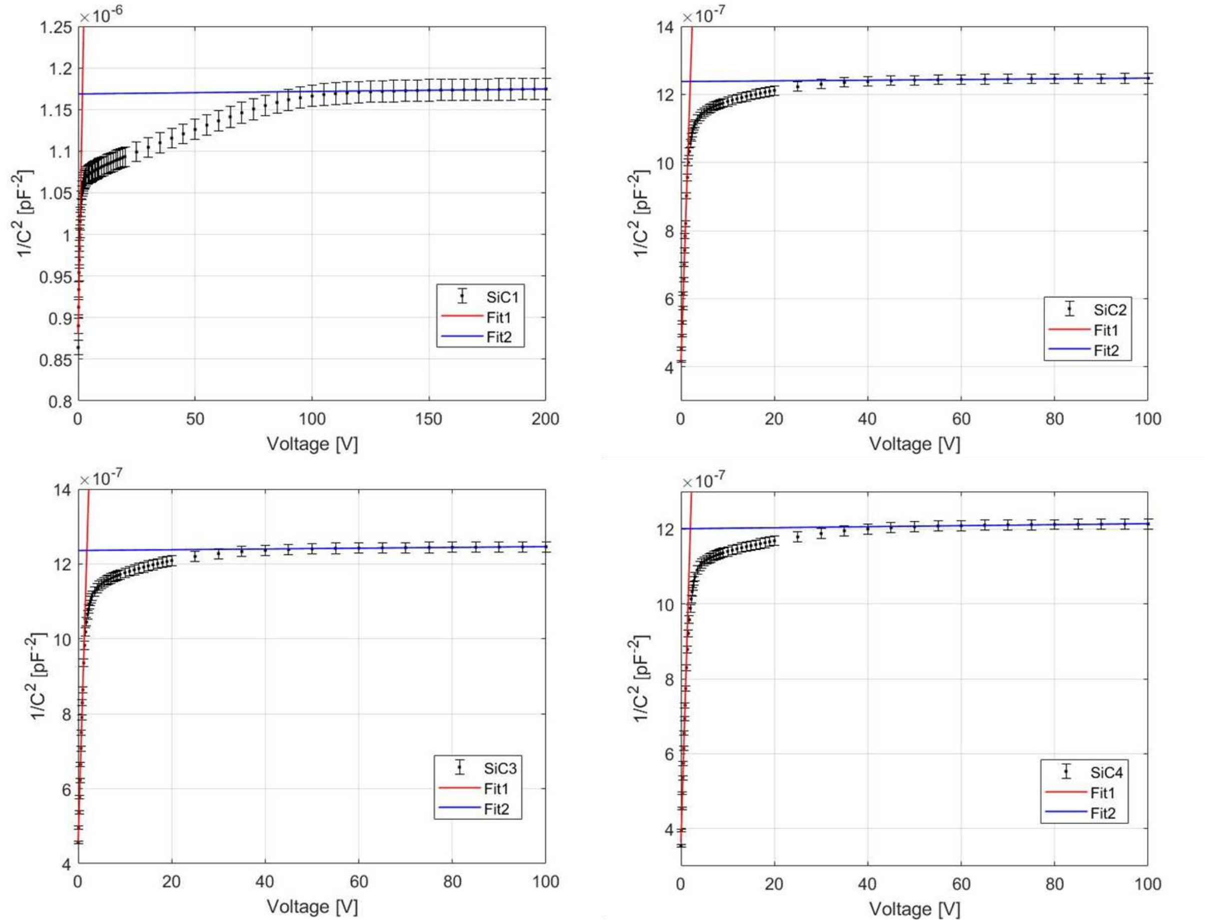

Figure 4.12 Trend of $1/C^2$ *vs*. reverse applied voltage. The linear fits in the low voltage range (Fit1, y=mx+q) and in the saturation region (Fit2, y=k; actually, in the real cases Fit2 is never defined by a constant value, but the functions always have a finite slope different from zero) are also shown. The error bars in the figure are obtained taking into account the accuracy of the instrument (~5 pF).

Comparing the experimental and theoretical data, significant percentage differences emerge. This is primarily attributed to the method employed, which relies on assumptions that may not precisely align with real-world conditions. A practical device might not fully deplete the entire physical thickness of the wafer, leading to a smaller W and larger C_s than predicted. Alternatively, an experimental W smaller than the nominal W_N may indicate that the devices are thinner than expected. Furthermore, comparing the curves obtained in Figure 4.12 with the theoretical trend shown in Figure 4.7, it is evident that the intercept method involves an underestimation of the depletion voltage, since it assumes the presence of a constant dopant concentration and the absence of a gradual transition to the saturation region. N_D, in addition to potentially not being constant, could also be different from the nominal value due to problems related to the production method. To investigate these possibilities, the behaviour of N_D as a function of W and V was studied by exploiting the relation (4.12). Here, the values of $W(V_R)$ were replaced with what was obtained from relation (4.5) by isolating $W(V_R)$ and substituting the experimental C(V) values represented in Figure 4.11 in place of $C(V_R)$, and the values of V_{bi} were replaced with the experimental ones. The trend of the thickness variation of the depletion region as V varies thus obtained is shown in Figure 4.13, while Figure 4.14 reports the experimental trend of $N_D(W,V)$. In both cases, data is shown up to 10V.

From the obtained results, it can be observed that the dopant concentration maintains constant values (within experimental error) across the active thickness of the device, for W reaching nearly up to 9 μm. This width of W is reached for voltage around 3-3.5 V (excluding the anomalous case of SiC1), and, as shown in Figure 4.14, corresponds to the voltage value starting from a relative variation of W less than or equal to 0.1 μm/V is recorded. This behaviour is consistent with the observation that the values at which N_D stabilizes in this thickness interval are lower than the theoretical range anticipated. Typically, N_D values fluctuate within the $3 - 4 \cdot 10^{13}$ cm^{-3} range. Substituting the experimental $N_D = 3 - 4 \cdot 10^{13}$ cm^{-3} and $W_{mean} = 9.5$ μm into equation (4.8), the expected V_D value becomes:

$$V_D^{th'} = 2.5 - 3.7\,V \tag{4.13}$$

	SiC1		SiC2		SiC3		SiC4	
	Exp	Diff %	Exp	Diff %	Exp	Diff %	Exp	Diff %
V_D [V]	1.8±0.3	61%*	2.0±0.3	57%*	1.9±0.3	59%*	2.1±0.3	55%*
V_{bi} [V]	6.3±0.3	115%	1.0±0.3	65%	1.1±0.3	61%	0.9±0.3	68%
C_s [pF]	920±5	7.3%	895±5	4.2%	896±5	4.3%	908±5	5.7%
W [μm]	9.3±0.1	6.8%	9.6±0.1	4%	9.6±0.1	4%	9.5±0.1	5.4%
N_D [10^{13} cm^{-3}]	10.2±0.3	2.4%*	3.5±0.1	29.1%*	3.6±0.1	28.7%*	3.6±0.1	27.7*

Table 4.1 Experimental values (*Exp*) found for the SiC devices of the PRAGUE prototype extrapolated from C-V profiles. The percentage difference (*Diff%*) with respect to the expected value for each of the extrapolated quantities is also reported. Uncertainties were evaluated by applying error propagation theory. The errors calculated on V_D were in the range 0.1-0.3 V. However, it was observed that, by varying the extremes of the range over which perform the best-fit procedure, a variability up to 0.3 V on the V_D value can be found. (*) calculated with respect to the closest extreme of the corresponding theoretical range.

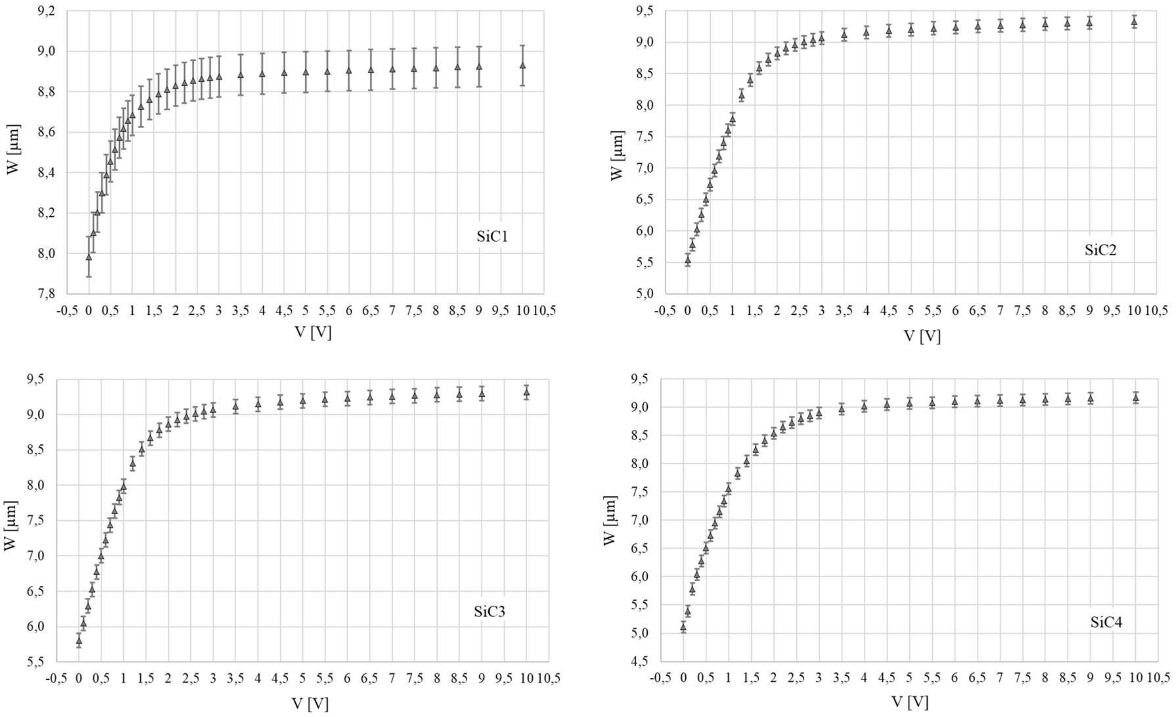

Figure 4.13 Trend of W(V) for the SiC devices of PRAGUE prototype. It is worth underlining that the value of the thickness W at 0V voltage corresponds to the depletion obtained thanks to the built-in voltage alone.

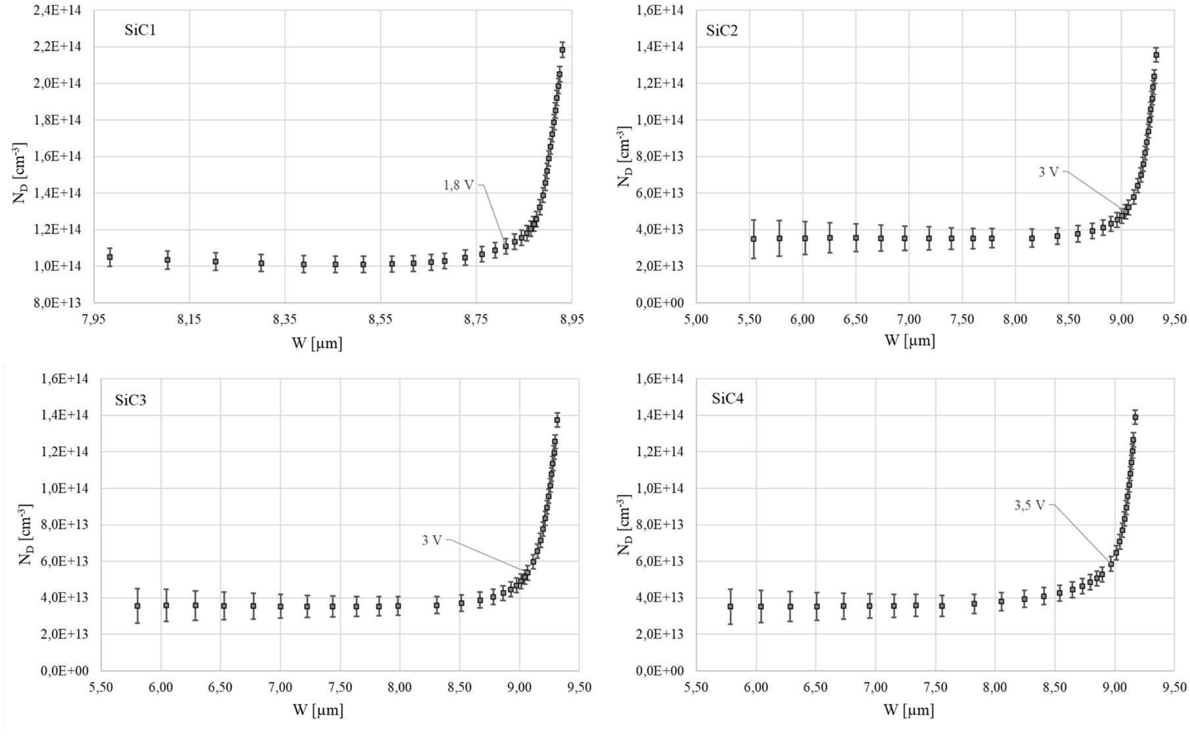

Figure 4.14 Trend of $N_D(W,V)$ for the SiC devices of PRAGUE prototype. In the images is pointed out the experimental data corresponding to the voltage value starting from a $\Delta W/\Delta V$ corresponding to less or equal than 0.1 µm/V is found, where $\Delta W=W(V_{final})-W(V_{initial})$ and $\Delta V=V_{final}-V_{initial}$, calculated between two adjacent data points.

4.4 Reconstruction of the PDD distribution of proton beams

To assess the device's capability to accurately acquire the Percentage Depth Dose distribution of a proton beam, the prototype underwent irradiation with monoenergetic conventional (generated by radiofrequency machines) proton beams. Specifically, two experimental campaigns were conducted: one at the Institute of Nuclear Physics of the Czech Academy of Sciences (Ústav Jaderné Fyziky Av Čr) [327], located in Husinec-Řež, Czech Republic, and the other at the Proton Center Therapy [328], situated in Trento, Italy. These campaigns were crucial not only for establishing the Water Equivalent Thickness of SiC detectors (including the PCBs on which the detectors are mounted) but also for evaluating the performance of SiC detectors in response to radiation at different LET values.

4.4.1 35 MeV at the Institute of Nuclear Physics Av Čr, Řež

The first experimental campaign was carried out at the Institute of Nuclear Physics of the Czech Academy of Sciences with a proton beam of 35 MeV in energy. Here the beam is transported in vacuum to the experimental room, where it exits into the air through a 55 μm aluminium window. The adopted experimental setup is reported in Figure 4.15. After traversing a 45 cm path in air, the beam encounters a circular 8 mm plastic collimator (1 cm thick), situated just before a Secondary Electron Monitor (SEM) composed of a 7 μm tantalum foil, specifically designed for real-time beam current measurements. After travelling an additional 77 mm, the beam undergoes additional collimation with a circular 8 mm aluminum collimator, featuring a thickness of 6 mm. Finally, the collimated beam reaches the PRAGUE detector prototype. The adopted electronic readout for SEM and PRAGUE's prototype has a feedback resistance R_f equal to 10 GΩ (High) and 0.1 GΩ (Low) respectively (the details are reported in Section 4.2.2).

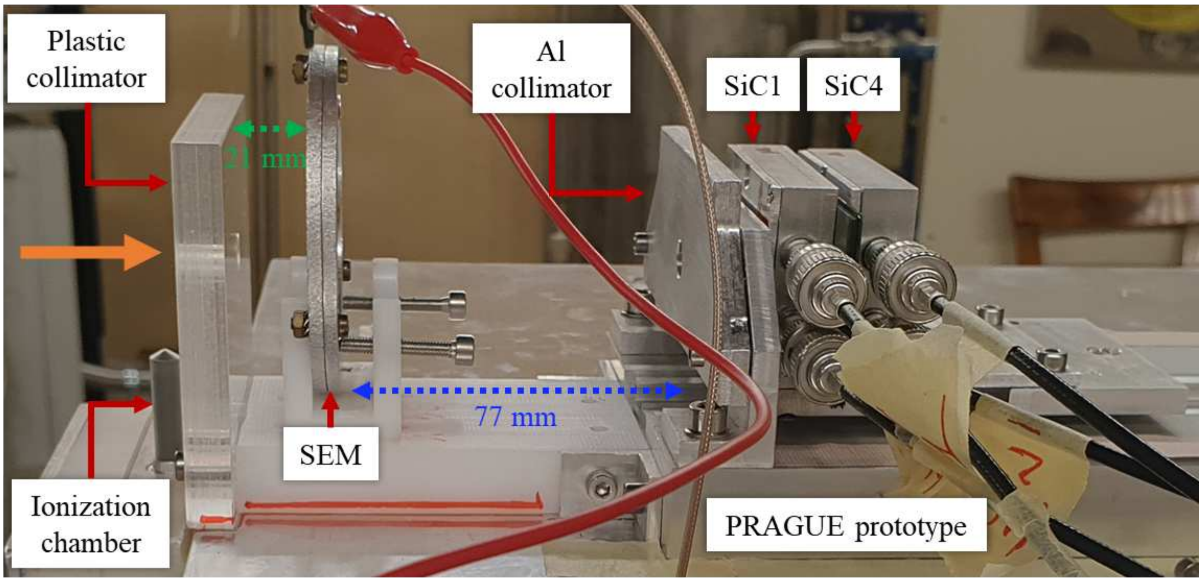

Figure 4.15. Experimental setup used during the experimental campaign conducted at the Institute of Nuclear Physics Av Čr, in Řež. Given the low energy value, only two SiC devices out of the total four were used. In particular, SiC1 (mounted on a perforated PCB) and SiC4 were used. The orange arrow indicates the side from which the proton beam comes.

The irradiation line was equipped with a removable, calibrated ionization chamber dedicated to measuring the beam current. It was placed immediately before the plastic collimator. The calibration law of the device, which allows determining the fluence rate (or intensity) of the beam is:

$$\Phi = k \cdot I_{ch} \tag{4.14}$$

where k=1600 pA^{-1} cm^{-2} s^{-1}, and I_{ch} is the current value read by the chamber. During the measurements, a beam current of I_{ch} = 800 pA was set that corresponds to a beam flux of approximately 10^6 protons/s at the reference irradiation point.

During this experimental run, various characterizations were carried out, listed below:

1. SEM dose calibration: this procedure was necessary to carry out the dosimetric characterization of the irradiation line. For this purpose, EBT3 Radiochromic Films were used as reference dosimeters. The description of the adopted experimental methods is reported in Section 4.4.1.1.

2. irradiation of Alanine pellets; the objective of the measurement was to investigate the comparison between the dose response of alanine dosimeters and that of EBT3, in view of the first experimental test on the PRAGUE detector with laser-driven beams, which is planned at the ELI Beamline laser facility [329]. Here, the first selected laser-driven proton beams will have an energy of 30-35 MeV and the ion diagnostics will also include passive devices such as CR-39, RCFs and alanine devices. In particular, RCFs and alanine pellets, thanks to their independent response from dose rate, will initially be used as reference dosimeters. The description of the adopted experimental methods is reported in Section 4.4.1.2.

3. WET estimation of SiC detectors: this procedure was necessary in order to carry out a correct reconstruction of the dose distribution in water depth through the SiC stack. WET values were measured by observing the Bragg peak shift associated with the introduction of the SiC detectors as absorbers before an EBT3 stack. The description of the adopted experimental methods is reported in Section 4.4.1.3.

4. reproducibility measurements of the SiC response: the investigation served to compare the response provided by the SiC detectors when located in the same experimental conditions. The description of the adopted experimental methods is reported in Section 4.4.1.4.

5. acquisition of the PDD distribution: the measurement aimed to evaluate the ability of the SiC detector stack system to correctly reconstruct the PDD distribution of the 35 MeV proton beam. The performance of the SiC devices was compared with that of EBT3 films. The description of the adopted experimental methods is reported in Section 4.4.1.5.

4.4.1.1 Calibration procedure

Before proceeding with the irradiation of the PRAGUE prototype, the dosimetric characterization of the irradiation line was performed. The latter was realized by carrying out the dose calibration of the SEM which, placed in transmission, allowed the online monitoring of the dose released at a defined depth. To calibrate the SEM, Radiochromic Films were chosen as reference dosimeters. Specifically, the experimental procedure adopted included:

A. dose calibration of the EBT3 films through a 30 MeV monochromatic proton beam delivered at the INFN-LNS (Catania, Italy);
B. dose calibration of the SEM through simultaneous irradiation with the calibrated EBT3 films placed at the entrance (immediately after the aluminium collimator of the PRAGUE prototype) of the 35 MeV proton beam delivered at the Institute of Nuclear Physics (Husinec-Řež, Czech Republic).

4.4.1.1.A EBT3 calibration procedure

As already mentioned, RCFs are 2D self-developing devices which, upon interaction with ionizing radiation, change colour, offering the possibility to obtain a 2D map of absorbed dose [175, 330]. The degree of colouring, indeed, depends on the absorbed dose and is identified in terms of Optical Density (OD). This quantity is a measure of the reduction of the light transmittance through the film and is conventionally defined as:

$$OD = Log\,\frac{I_0}{I} \tag{4.15}$$

where I_0 is the initial intensity of an external light source, and I is the residual light intensity after passing through the film. The films have to be digitized to extrapolate quantitative information. Usually, this is done by scanning the films in the RGB colour model and analysing the data by using an image processing software. In this case, I_0 and I are measured in terms of pixel intensity values, evaluated in a specific colour channel chosen to increase the sensitivity of the measurement. In general, I_0 and I correspond to the average intensity value of the pixels belonging respectively to the film background (i.e. a non-irradiated section of the film) and to the beam track (i.e. the irradiated section of the film), as shown in Figure 4.16. The region of each film selected to evaluate I or I_0 is usually defined as Region Of Interest (ROI).

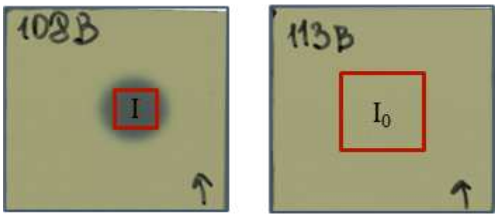

Figure 4.16 Digitized radiochromic films, model EBT3, before (113B) and after (108B) irradiation, shown as an example. The ROIs corresponding to I and I_0 are highlighted.

In this experimental run, the EBT3 model was used. Their main specifications are summarized in Table 4.2. The EBT3 films were firstly calibrated in terms of absorbed dose in water. Their calibration was carried out at the CATANA proton therapy center, in Catania (see Section 4.5.4 for further details on the irradiation line), by means of a 30 MeV proton beam. Here, various films cut into 3x3 cm^2 squares were positioned one at a time at the isocenter (in the same point where absolute dosimetry was previously carried out) and irradiated with gradually increasing known doses, in the range 50-2000 cGy. After irradiation, the scanning procedure was conducted by using a white light EPSON Expression Photo scanner, 206 Model 10000 XL. Although 90% of the polymerization process occurs within milliseconds after irradiation, this process continues its evolution during the next 24 h [175]. Therefore, to avoid loss of accuracy, the EBT3 films were scanned 30 h after the irradiation, with a resolution of 600 dpi and a dynamic range of 48-bit RGB color model (16-bit per color channel). After digitalisation, the measurement of I and I$_0$ was carried out through the image processing program called *ImageJ* [331] by selecting the red channel, as recommended by manufacturer [193]. The dose calibration curve, shown in Figure 4.17, was then obtained by plotting the released dose as a function of the resulting OD, as expressed in (4.15), and by performing a best-fit procedure with a third-order polynomial function.

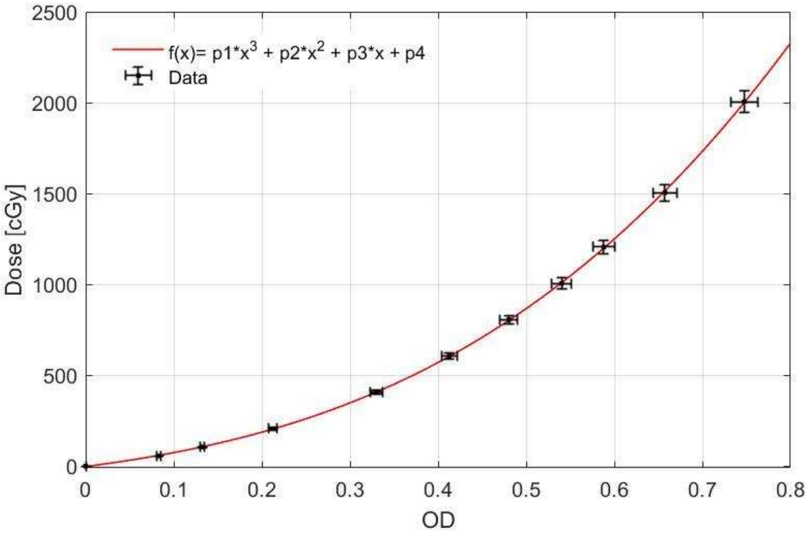

Figure 4.17 EBT3 dose calibration curve obtained with a 30 MeV proton beam (r^2 very close to 1). Error on the dose is equal to 3%, while the error on the OD was evaluated by propagating the uncertainties on I and I$_0$ according to (4.15). Uncertainties on I and I$_0$ are calculated taking into account the standard deviation of the pixel values contained in the ROI over which the I$_0$ and I values are estimated.

Active layer thickness	Passive layer thickness	Number of passive layer	Dynamic dose range	Spatial resolution	WET
28 μm	125 μm	2	0.1-20 Gy	< 25 μm	355 μm

Table 4.2 Specifications of EBT3 films.

4.4.1.1.B SEM calibration procedure

The SEM is basically a beam current monitor: its operating principle is based on the secondary emission of electrons produced following the passage of the beam (Secondary Electron Emission, SEE). The total charge collected can be related to the intensity of the incident beam. However, it can also be used as a dose measuring device, once calibrated against a reference dosimeter. This is achieved by finding a functional relationship between the charge produced by the SEM and the absorbed dose at a specific point in the radiation field (usually the isocenter). In our configuration, a relationship between the charge read by the SEM and the dose absorbed by the EBT3 films was established by irradiating the two devices simultaneously, and by varying the irradiation time of the proton beam (5-10-30-50-100 s). The resulting calibration curve is reported in Figure 4.18. The SEM charge signal was obtained by converting the voltage signal in current, via the equation (4.1) (with a R_f=10GΩ), and integrating the net current signal (subtracting the contribution of the background current) over the irradiation time. The procedure used for the OD reading of the EBT3 was compliant with what was previously described for calibration. In particular, the scanning parameters were kept the same as those set for the digitization of the irradiated EBT3 during the calibration phase. The dose absorbed by the EBT3 irradiated with the 35 MeV beam was estimated using the 30 MeV calibration curve (depicted in Figure 4.17), aware of making a negligible error as the LET in water of the protons at these two energies is very similar (LET_{30MeV}=1.9 keV/µm, LET_{35MeV}=1.7 keV/µm). The EBT3 reading procedure here illustrated is identical also for all the tests illustrated below, so for brevity it will not be repeated.

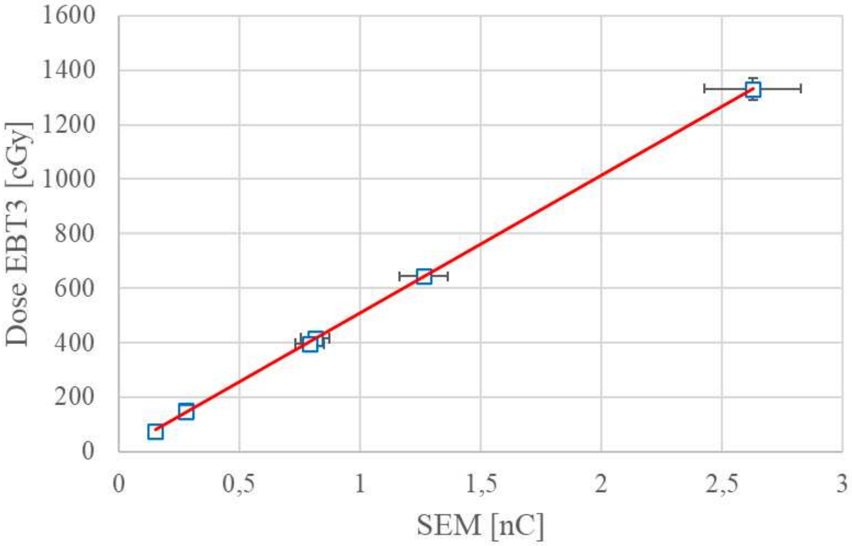

Figure 4.18 SEM dose calibration curve obtained with a 30 MeV proton beam (r^2 very close to 1). The error bars on the dose (~2-40 cGy) were obtained by taking into account the uncertainty on the OD and on the parameters of the calibration curve. The error bars on the charge (~0.01-0.2 nC) were evaluated taking into account the accuracy of the NI-9223 and TIA modules.

4.4.1.2 Alanine dosimeters

Alanine is an amino acid, which forms a stable free radical upon irradiation, and for this reason alanine-based devices are classified as a chemical dosimeter [124, 125]. The concentration of the free radical is proportional to the absorbed dose, which can be probed using an electron paramagnetic resonance (EPR) spectrometer. During this experimental campaign, 15 L-α alanine pellets were irradiated, with characteristics listed in Table 4.3.

Features	L-α-Alanine composition (96%)	Binder composition (4%)	Diameter [mm]	Thickness [mm]	Mass [mg]	Density [g/cm^3]
Value	H: 6.87% C: 39.44% N: 16.73% O: 34.96%	H: 0.34% C: 2.4% O: 0.72% Other: 0.54%	4.8	3	68.0	1.25

Table 4.3 Main features of the adopted alanine dosimeters. The composition of the pellets is 96.0% L-α-Alanine and 4% Binder.

The irradiations were carried out by positioning alanine pellets and EBT3 films immediately after the aluminium collimator of the prototype, and irradiating the devices by varying the irradiation time of the proton beam (10-30-50-70-80-100 s). Figure 4.19 shows the customized support designed to allow the positioning and irradiation of the pellets.

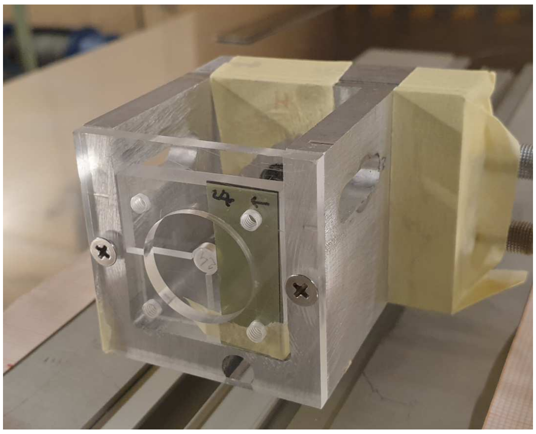

Figure 4.19 Customized holder for alanine pellets used during their irradiation with 35 MeV proton beam. In the center of the holder, an alanine dosimeter can be seen.

Since the dose measurement conducted via alanine dosimeters involves a volumetric investigation of the pellets, while the analysis of the EBT3 depends on the choice of 2D ROI arbitrarily chosen, in the hypothesis that the beam is homogeneous, the investigation of the lateral profile of the beam to verify homogeneity is important in order to make the comparison between the two types of detectors meaningful. To do this, the ability of EBT3 films to provide a 2D distribution of absorbed dose was exploited. Figure 4.20 shows the beam profile expressed in terms of intensity levels.

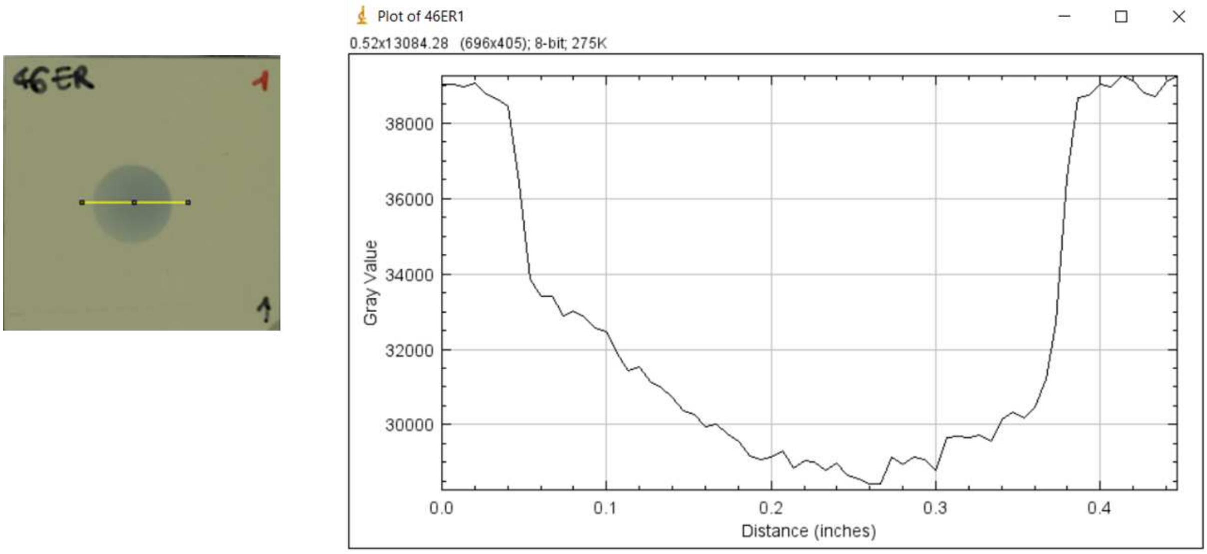

Figure 4.20 Lateral profile of the 35 MeV proton beam in pixel intensity levels shown as an example. The corresponding selected trace on the digitized image of the EBT3 after irradiation is also shown. The measurement refers to an irradiation of 10s. This investigation was conducted using ImageJ software.

As can be seen, the intensity levels along the traced profile deviate from the expected “step” trend up to ~20%. The irradiation of the EBT3 was carried out immediately after the aluminium collimator, therefore the beam trace left on them has a diameter of 8 mm. Since the pellets have a diameter of 5 mm, and considering that their irradiation was carried out in the same position as the EBT3, to make the comparison between the dose measurement with alanine and EBT3 devices as less affected as possible from a systematic error, a circular ROI of 5 mm in diameter, located in the center of the trace, was selected for the EBT3 reading. This study was conducted in collaboration with the University of Palermo, where alanine data were processed. In Figure 4.21, the comparison between the dose values read with alanine pellets and with EBT3 films as the irradiation time varies is shown. In general, good experimental agreement is observed between the data within the experimental error. However, the investigation will continue exploring higher dose (and dose rates) regimens. In general, it is known that at doses below 2 Gy alanine can show considerable relative uncertainty.

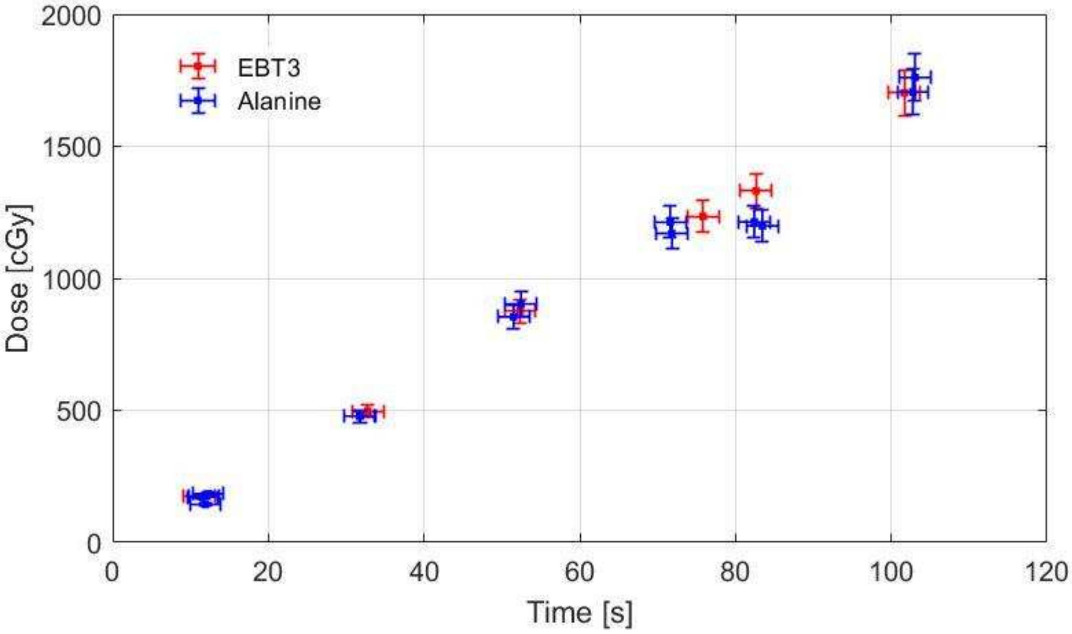

Figure 4.21 Comparison of the dose read by alanine pellets and EBT3. The alanine data were obtained by considering the average values of four readings, each corresponding to a different EPR orientation.

4.4.1.3 WET estimation

Estimating the WET of the SiC detectors is essential to correctly reconstruct the PDD distribution of a proton beam. It is known that the WET of a medium can be measured by placing it upstream of a water phantom and measuring the shift suffered by the Bragg peak in the depth dose deposition curve [37]. The procedure applied in our experimental context was based on this principle, and exploits the possibility offered by RCFs to reconstruct the depth dose distribution in water, when used in what is called a *stack configuration*, where a number *N* of devices are stacked one behind the other. Using this configuration, the incoming radiation hits perpendicularly the *N* films and each RCF acts as a filter for the following one. By plotting the dose read on each RCF as a function of the equivalent depth in water at which each of them is located along the stack, it is possible to reconstruct the dose distribution in depth. To estimate the WET of the detectors, the PDD distribution of the beam was acquired in three experimental configurations (called A, B, C), reported in Figure 4.22.

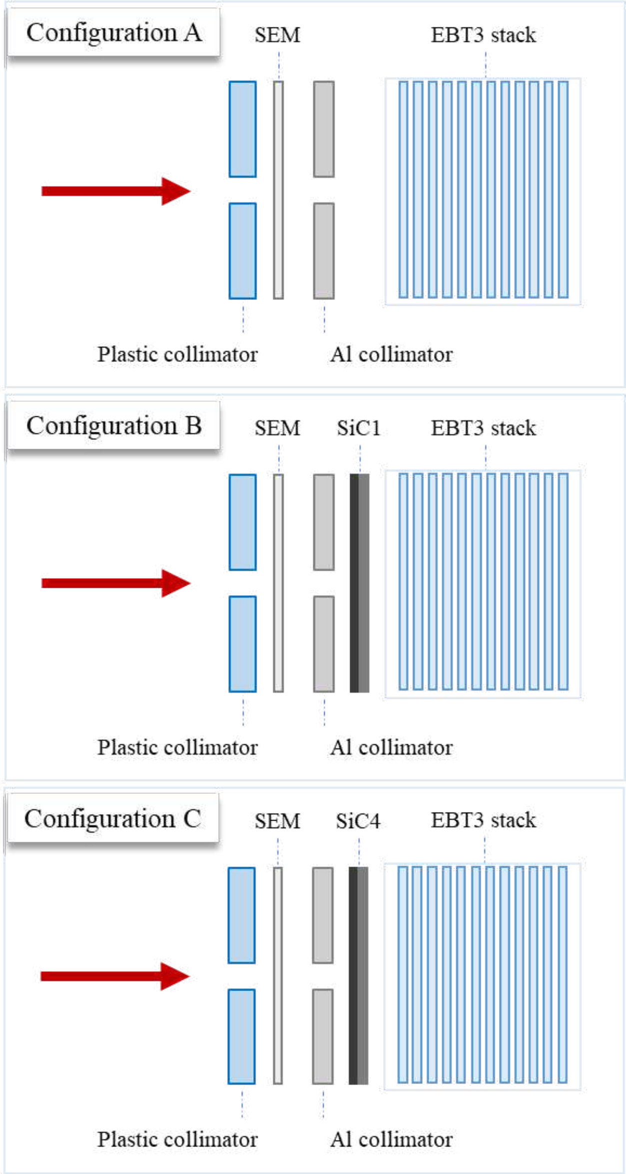

Figure 4.22 Experimental configurations adopted for the WET estimation of the SiC1 and SiC4 detectors.

Specifically, the experimental procedure adopted consisted of the following phases:

1. acquire the PDD distribution of the beam using a stack of EBT3 (Figure 4.22, *Configuration A*), and evaluate the position of the Bragg peak, called P_A; in this case, the irradiation lasted 15 s.
2. acquire the PDD distribution of the beam using a stack of EBT3 positioned after the SiC1 (Figure 4.22, *Configuration B*), and evaluate the position occupied by the Bragg peak, called P_B; in this case, the irradiation lasted 10 s.
3. acquire the PDD distribution of the beam using a stack of EBT3 positioned after the SiC4 (Figure 4.22, *Configuration C*), and evaluate the position occupied by the Bragg peak, called P_C; in this case, the irradiation lasted 10 s.

The PDD distributions thus obtained are shown in Figure 4.23. By comparing the positions of the Bragg peak in Configuration A (P_A=10.65±0.17 mm), with that of Configurations B (P_B=10.29±0.17 mm) and C (P_C=7.10±0.17 mm), it was possible to determine the WET of SiC1 and SiC4, for a 35 MeV proton beam, respectively equal to WET_1=0.355±0.17 mm (approximately 1 EBT3 equivalent) and WET_4=3.5±0.17 mm (approximately 10 EBT3 equivalent). Consequently, considering that the SiC devices are equal to each other, it is possible to extrapolate the WET value of the PCBs used (approximately 9 EBT3 equivalent). Table 4.4 summarizes the results related to this acquisition.

Configuration	Irradiation time	SEM dose [cGy]	EBT3 dose [cGy]	Bragg peak depth [mm]
A	15 s	250±40	280±60	10.65±0.17
B	10 s	140±20	150±30	10.29±0.17
C	10 s	100±20	90±20	7.10±0.17

Table 4.4 Summary of the results related to the acquisitions of the PDD distributions with the EBT3 stack aimed at estimating the WET of the detectors. The dose released at the entrance, quantified via the SEM device, and the dose read on the first EBT3 of each stack is also reported. The error on the dose read by the SEM was evaluated by propagating the uncertainty on the net charge signal and on the parameters of the calibration curve. The error on the peak position was estimated by taking into account the longitudinal spatial resolution of the adopted experimental method.

However, since the Water Equivalent Thickness (WET) of a material depends on the energy of the incident beam, the experimentally obtained value for SiC1 was compared with WET values estimated through both SRIM and LISE code in the energy range of 0.5-250 MeV. Specifically, SRIM was used to calculate the WET of SiC using the thin-target approach, also called the Stopping Power Ratio approximation (see Chapter 3 and equation (3.1)). LISE was used to estimate the WET of the active layer of SiC detectors through a comparative approach. It was used to calculate the energy loss suffered by a 35 MeV proton beam in a SiC thickness equal to 120 μm, and to determine the thickness of water capable of causing the same energy loss. The latter, by definition, represents the water equivalent thickness of a 120 μm thick SiC layer. Both methods yielded consistent evaluations of WET compared to the experimental results (percentage deviation ranging from 0.3% to 9%). The results are depicted in Figure 4.24. The close agreement between simulation data and the experimental point at 35 MeV enables extrapolation of its validity range up to 250 MeV. The same procedure was applied to the 1.75 mm PCB, yielding similar results.

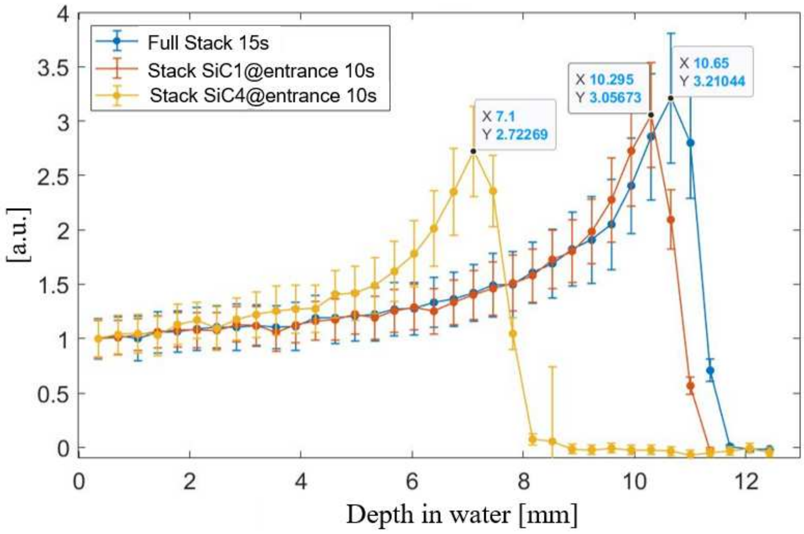

Figure 4.23 PDD distribution of a 35 MeV, normalized at entrance, obtained by irradiating three stacks of EBT3 films: one full EBT3 (blue line), one with the SiC1 positioned at entrance (orange line), another with the SiC4 positioned at entrance (yellow line). The positions occupied by the Bragg peak in the three cases are highlighted. From their comparison, it is possible to trace the WET values for SiC1 and SiC4. The error bars on the dose values read via the EBT3 were calculated taking into account the uncertainty on the OD values and the uncertainty on the calibration curve parameters. Their relative value reaches 40%: this is due to the presence of an inhomogeneity in the beam which affects the evaluation of the standard deviation of I and I_0.

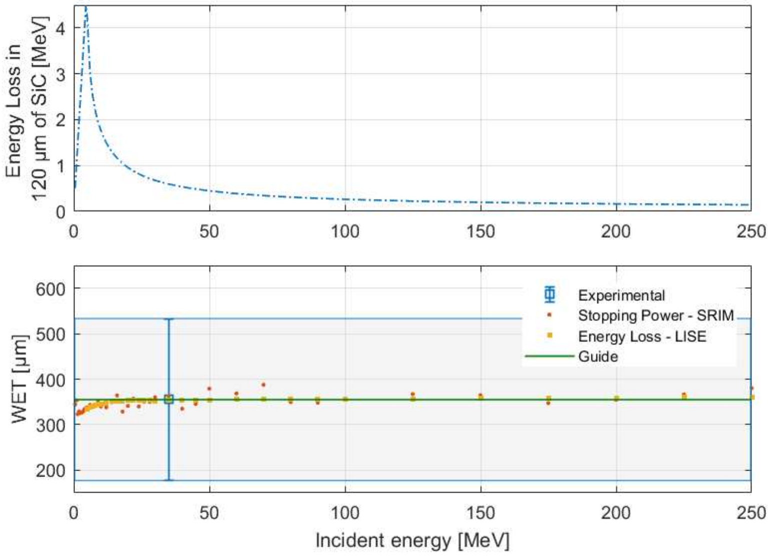

Figure 4.24 Top panel: trend of energy loss suffered by protons with energy between 0.5 and 250 MeV in a 120 μm thick SiC layer (SRIM). Bottom panel: comparison between experimental (35 MeV) and simulated (0.5-250 MeV) WET values obtained for SiC1; the green line is a guide for the eyes; the gray area indicates the interval 0.355±0.17 mm.

4.4.1.4 Reproducibility measurements

To properly reconstruct the PDD distribution using the PRAGUE prototype, it was also necessary to previously carry out tests aimed at characterizing the response provided by the SiC1 and SiC4 devices. Specifically, reproducibility measurements of the signal produced by the detectors were conducted in the same irradiation experimental conditions. Specifically, the following steps were performed:

1. the SiC1 (reverse bias voltage 50V) was placed at the entrance (immediately after the aluminum collimator) and was subjected to 10 irradiations of 10 seconds;
2. afterwards, SiC1 was replaced by SiC4 (reverse bias voltage 50V), and it was subjected to 10 irradiations of 10 seconds as well.

The SiC output voltage signals were converted in current (applying the equation (4.1)) and integrated in time. The same procedure was repeated for the SEM, which was in turn subjected to irradiation together with the SiC devices. After that, by applying the dose calibration curve (Figure 4.18) on SEM charge signals, it was possible to estimate the released dose at the entrance: it was obtained that in each of the 10 irradiations with the SiC1 at the entrance, an average dose of 135±10 cGy was delivered, while in the irradiations carried out with SiC4 at the entrance the delivered average dose was 145±15 cGy.

These results, in agreement within the experimental errors, confirm that the irradiation conditions were the same and that the SiC responses thus found can be compared without committing a non-negligible systematic error. At this point, the charge produced by the SiC devices in each of the 10 irradiations was normalized by the corresponding charge read through the SEM, to take into account the variation in the irradiation time and in the beam intensity (the beam switching operation was managed manually, resulting in effective irradiation times variability up to 25%).

The mean value M and standard deviation σ were then calculated for SiC1 (called respectively M_1, σ_1) and SiC4 (M_4, σ_4) and the adimensional k value was estimated such that:

$$k = M_4/M_1 = 1.4 \pm 0.1 \tag{4.15}$$

from which it can be seen that SiC4 on average has a response 1.4 times higher than SiC1. From this characterization it was also possible to establish the sensitivity S of the detectors, expressed in [nC/cGy]:

$$S(SiC1) = 1.6 \pm 0.1 \tag{4.16}$$

$$S(SiC4) = 2.2 \pm 0.3 \tag{4.17}$$

4.4.1.5 PDD distribution

The acquisition of PDD distributions using the PRAGUE prototype detector was carried out in two measurement configurations, schematized in Figure 4.25.

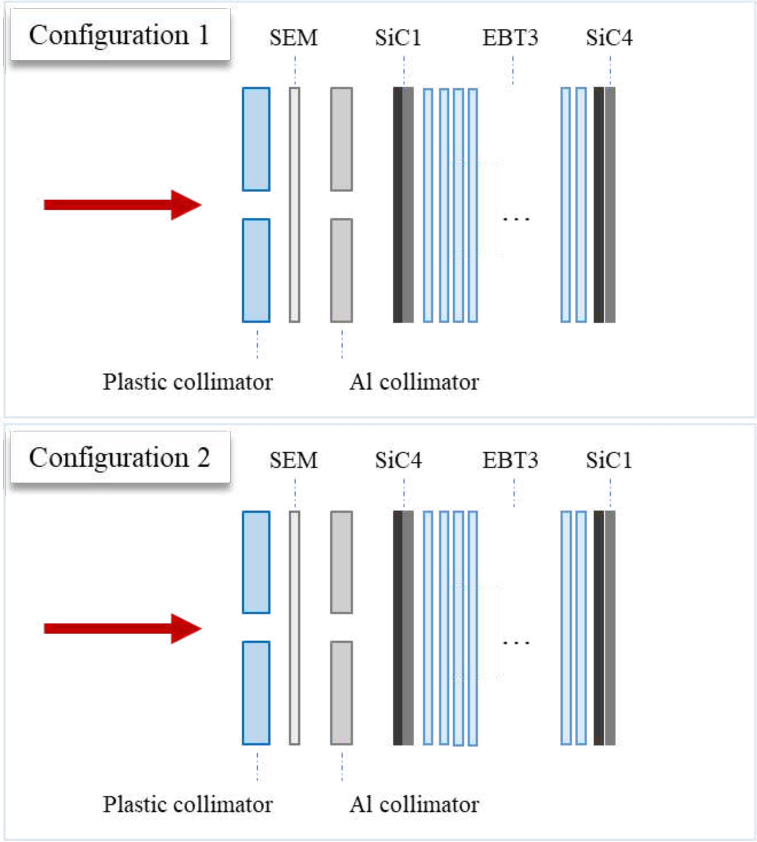

Figure 4.25 Measurement configurations adopted for the acquisition of the PDD distribution of 35 MeV proton beam with the PRAGUE prototype composed of two SiC devices. In both configurations, a set of N EBT3 films was placed between the two SiC detectors. The number of EBT3 was varied from N=0 to N=35 (in steps of 1 EBT3) to reconstruct the dose distribution in depth.

Considering the *Configuration 1*, the experimental method adopted consists of:

- positioning and maintaining the SiC1 detector at the beam entrance.
- reconstructing the PDD distribution with the SiC4 detector; this operation was carried out by interposing a gradually increasing number of EBT3 between SiC1 and SiC4. In this case, the EBT3 films act as absorbers, degrading the beam and moving the SiC4 acquisition point to increasingly greater depths along the dose deposition curve. At each new acquisition point (defined by the number of EBT3 placed between SiC1 and SiC4), the system was subjected to 5 irradiations of 10 seconds.

In *Configuration 2*, the experimental method was kept the same, except for the positions occupied by SiC1 and SiC4 which were reversed. Both detectors were biased with a reverse voltage of 50V. The processing of the output signals of SEM and SiC devices was carried out with the same procedures described in Section 4.4.1.3.

For each set of 5 irradiations, the SiC charge signals were then normalized for the corresponding SEM signals, and their average value and standard deviation were evaluated. Finally, the signal measured at the entrance was corrected using the normalization factor k (equation (4.15)). In particular, in *Configuration 1*, the SiC1 signal was multiplied by k, while in *Configuration 2* the SiC4 signal was divided by k. The PDD distributions reconstructed using the PRAGUE prototype in the two configurations are shown in Figure 4.26 and Figure 4.27. Comparison with the PDD distribution obtained via the EBT3 stack (using Configuration A) is also reported.

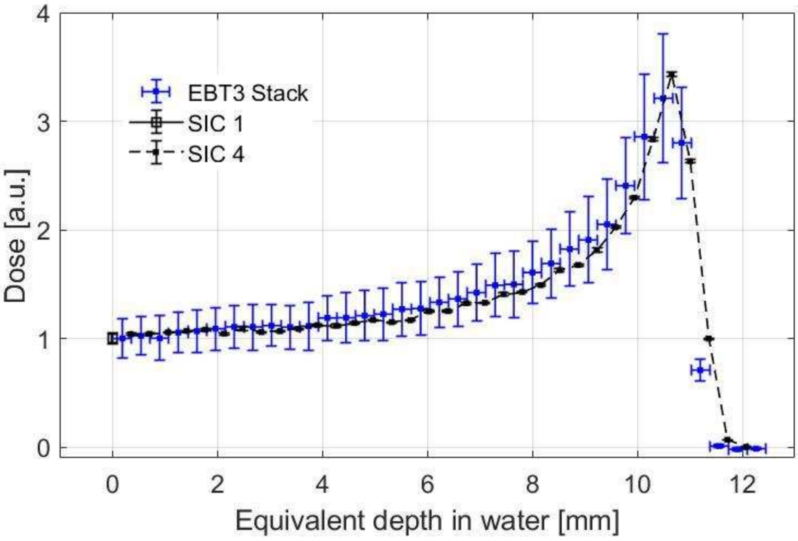

Figure 4.26 PDD distribution (normalized at entrance) reconstructed using the PRAGUE prototype in Configuration 1, with WET_1=0.355±0.17 mm. The average dose released at the entrance, measured by SEM, was evaluated by averaging over all irradiations, obtaining a value of 135±5 cGy. The PDD distribution reconstructed via the EBT3 stack using the experimental setup in Configuration A is also shown (blue data).

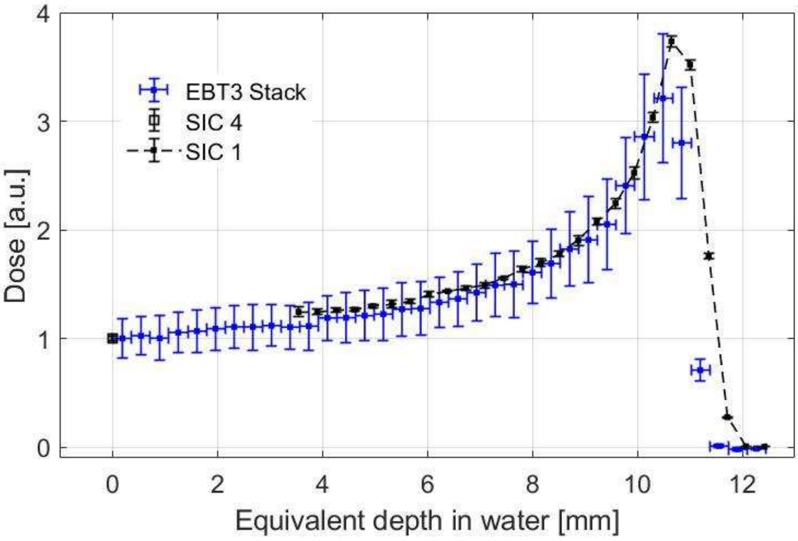

Figure 4.27 PDD distribution (normalized at entrance) reconstructed using the PRAGUE prototype in Configuration 2, with WET_4=3.55±0.17 mm. The average dose released at the entrance, measured by SEM, was evaluated by averaging over all irradiations, obtaining a value of 133±5 cGy. The PDD distribution reconstructed via the EBT3 stack using the experimental setup in Configuration A is also shown (blue data).

The PDD distributions obtained using the PRAGUE prototype in Configuration 1 and 2 were also compared respectively with the PDD distributions obtained using the EBT3 in Configuration B and C. The result is shown in Figure 4.28 and Figure 4.29.

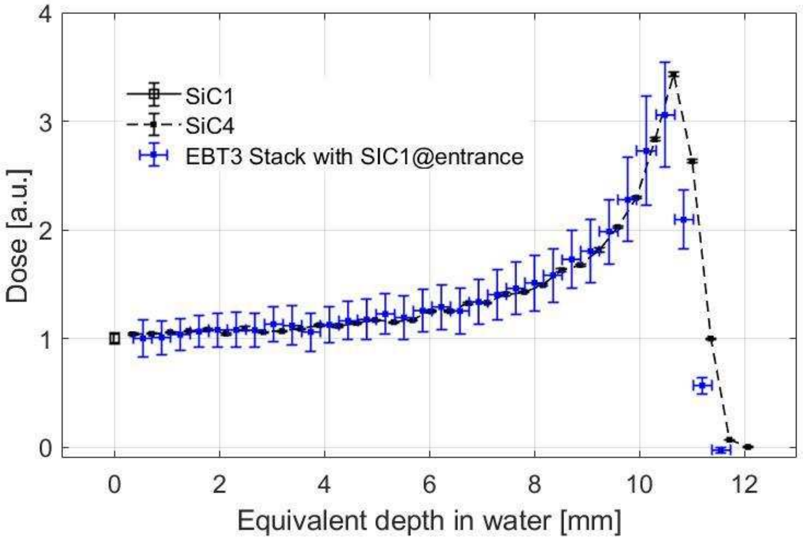

Figure 4.28 PDD distributions (normalized at entrance) reconstructed using the PRAGUE prototype in Configuration 1 (black data) and the EBT3 stack in Configuration B. Both PDD distributions are reconstructed replacing WET_1=0.355±0.17 mm.

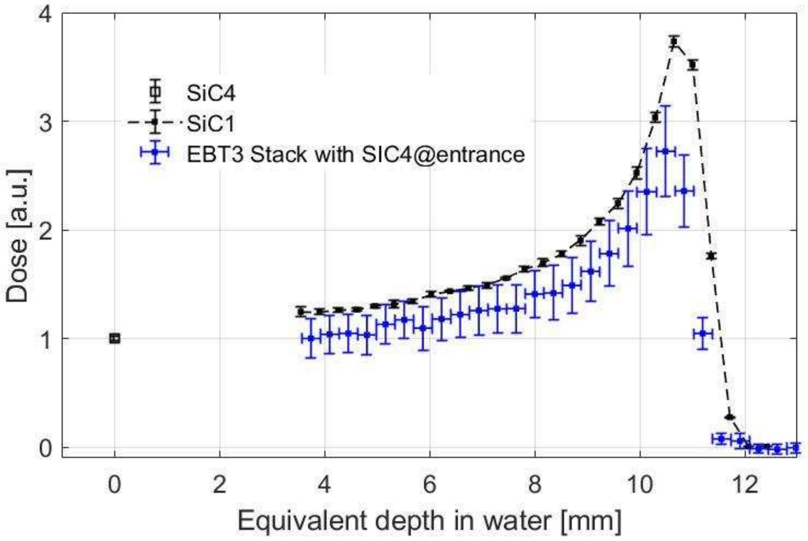

Figure 4.29 PDD distributions (normalized at entrance) reconstructed using the PRAGUE prototype in Configuration 2 (black data) and the EBT3 stack in Configuration C. Both PDD distributions are reconstructed replacing WET_4=3.55±0.17 mm.

To quantify the comparison between the PDD distributions reconstructed with both SiC and EBT3 stack, the following beam quality parameters were evaluated for both detection systems used:

- *Peak-to-plateau ratio*, defined as the ratio between the maximum dose and the dose at the entrance of the PDD distribution.
- *Peak depth*, d_{Peak}, defined as the depth at which the maximum dose value is found.
- *Depth of penetration* (d'_{90}) or *range,* defined as the depth along the beam corresponding to the distal 90% point of the maximum dose value.
- *Peak width*, d_{8080}, defined as the distance between the distal and proximal 80% points of the maximum dose value.
- *Distal-dose fall off* (DDF), defined as the distance in which the dose decreases from 80% to 20% of the maximum dose value.

The results are reported in Table 4.5. In general, SiC shows better pristine Bragg peak reconstruction capabilities than EBT3s, as expected. The improved performance of SiC can be found in the enhanced peak-to-plateau ratio. The estimation of the other parameters leads to results that are comparable to each other. This is attributable to the longitudinal spatial resolution of the adopted method, limited by the thickness of the EBT3.

Device - Configuration	**Peak-to-plateau ratio**	**d_{Peak} [mm]**	**d'_{90} [mm]**	**d_{8080} [mm]**	**DDF [mm]**
SiC - Configuration 1	3.4	10.8	11	0.7	0.6
SiC - Configuration 2	3.7	10.8	11.1	0.9	0.5
EBT3 - Configuration A	3.2	10.6	10.9	1	0.3
EBT3 - Configuration B	3	10.6	10.7	0.8	0.5
EBT3 - Configuration C	3	10.6	10.8	0.9	0.5

Table 4.5 Quality parameters evaluated for pristine Bragg peaks by using linear interpolation when necessary. Uncertainty is 0.2 mm for all the values measured in [mm].

4.4.2 70 MeV at the Proton Therapy Centre, Trento

The second experimental campaign was carried out at the Proton Therapy Centre of Trento (PTC, Italy) [332]. The irradiations were performed with a 70 MeV proton beam accelerated by a cyclotron, with an extraction current of 10 nA and a beam flux of $8 \cdot 10^7$ protons/s at the irradiation point. The adopted experimental setup is reported in Figure 4.30. The beam is transported in vacuum to the experimental room, where it exits the beam pipe by traversing a 70 μm thick titanium layer. Lasers were available for target alignment at 1.25 m from the exit window, defined as "isocenter" in analogy to the treatment rooms. The PRAGUE's prototype, equipped with a 8 mm copper collimator (1 cm thick), was positioned so that the first SiC of the stack was placed at the isocenter. Between the exit window and the isocenter, at a distance of 77.5 cm from the collimator of the prototype, a in transmission Multi-Gap Ionization Chamber (MGIC, 7.5 cm thick) was placed to monitor the beam current. The adopted electronic readout was set with a feedback resistance R_f equal to 10 GΩ (High) for all four SiC devices (see Section 4.2.2).

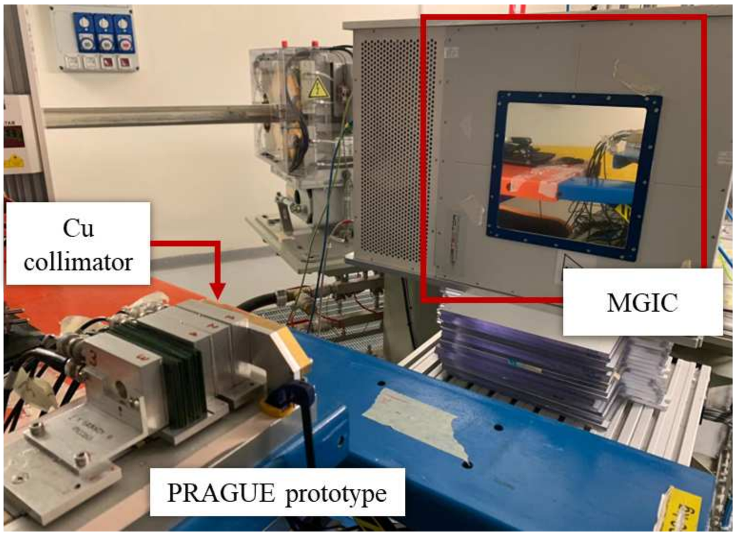

Figure 4.30 Experimental setup used during the experimental campaign conducted on PRAGUE prototype at the Proton Therapy Centre of Trento. A Multi-Gap Ionization Chamber (MGIC), provided by the Centre, placed in transmission along the radiation line, was used to monitor the beam current.

The main aim of the experimental test was to assess the detector's performance in reconstructing the PDD distribution of a proton beam with clinical characteristics. The PDD distribution was reconstructed using the SiC3 device, while SiC1 was positioned at the isocenter, followed by SiC2 and SiC4, arranged sequentially. Similar to the previous setup, EBT3 films served as absorbers. These films were interposed in increasing numbers between SiC4 and SiC3, degrading the beam and shifting the SiC3 acquisition point to progressively deeper depths along the dose deposition curve. A schematic representation of the experimental configuration adopted for acquiring the PDD distribution is illustrated in Figure 4.31.

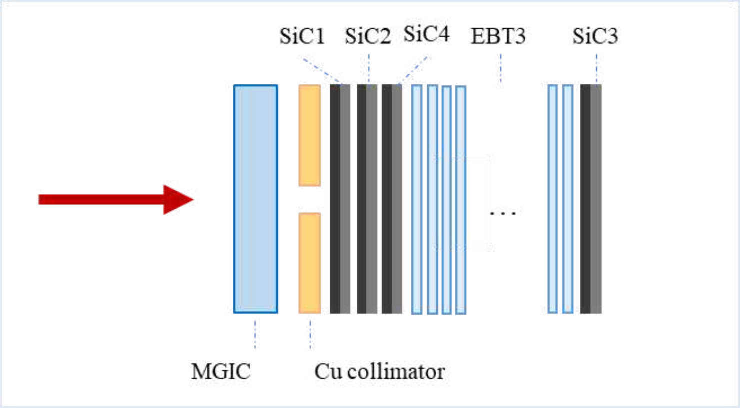

Figure 4.31 Measurement configurations adopted for the acquisition of the PDD distribution of 70 MeV proton beam with the PRAGUE prototype composed of four SiC devices. A set of N EBT3 films was placed between the SiC4 and SiC3 detectors. The number of EBT3 was varied from N=0 to N=98 (in variable steps) to reconstruct the dose distribution in depth.

At each new acquisition point (defined by the number of EBT3 placed between SiC4 and SiC3), the system was subjected to 1 irradiation of 30 seconds. The signal produced by the detectors was converted into charge, and subsequently normalized to the corresponding MGIC output signal. In addition, the signals from the SiC1, SiC2 and SiC4 detectors were multiplied respectively by the correction factors $k_{1,3}$, $k_{2,3}$ and $k_{4,3}$ reported in Table 4.6. The latter were evaluated adopting the same experimental procedure described in Section 4.4.1.3, but with the MGIC replacing the SEM. Figure 4.32 shows the configurations used to carry out the irradiations that led to the determination of the factors $k_{i,3}=M_{3,i}/M_i$, where:

- M_i (i=1, 2, 4), are the mean value of the (normalized) signals produced by SiC1, SiC2 and SiC4 detectors when arranged as in Configuration A (Figure 4.32);
- $M_{3,4}$ is the mean value of the (normalized) signals produced by SiC3 when located in place of SiC4, as in Configuration B (Figure 4.32);
- $M_{3,2}$ is the mean value of the (normalized) signals produced by SiC3 when located in place of SiC2, as in Configuration C (Figure 4.32);
- $M_{3,1}$ is the mean value of the (normalized) signals produced by SiC3 when located in place of SiC1, as in Configuration D (Figure 4.32).

$k_{1,3}$	$k_{2,3}$	$k_{4,3}$
0.7±0.1	0.7±0.1	0.9±0.1

Table 4.6 Correction factors used to normalize SiC1, SiC2 and SiC4 signals as respect to SiC3 signals.

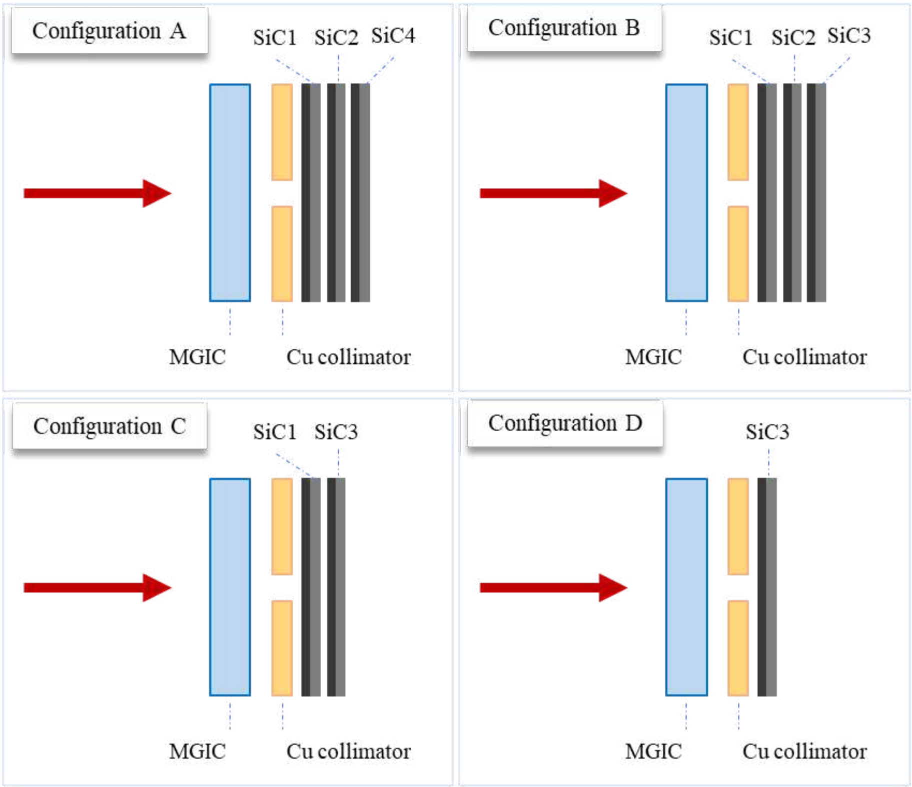

Figure 4.32 Configurations adopted for radiation aimed at evaluating the $k_{i,3}=M_{3,i}/M_i$ (i=1, 2, 4) factors. From Configuration A, the M_1, M_2 and M_4 mean values were evaluated. From Configuration B, C and D, respectively $M_{3,4}$, $M_{3,2}$ and $M_{3,1}$ were evaluated.

The reconstruction of the PDD distribution thus obtained is shown in Figure 4.33. Again, the performance of the prototype was compared to that of the EBT3 films. For this purpose, the PDD distribution of the 70 MeV proton beam was also acquired with a stack of EBT3. The conversion into dose of the OD of each EBT3 of the stack was carried out using a calibration curve previously obtained with a 60 MeV proton beam, delivered at the CATANA proton therapy center, since the LET in water of protons at these two energies is very similar (LET_{60MeV}=1.1 keV/µm, LET_{70MeV}=1.0 keV/µm). To quantify the comparison between the PDD distributions reconstructed with both SiC and EBT3 stack, the beam quality parameters *Peak-to-plateau ratio,* d_{Peak} , d_{8080}, and DDF were evaluated for both detection systems used. The results are summarized in Table 4.7.

Device	**Peak-to-plateau ratio**	**d_{Peak} [mm]**	**d'_{90} [mm]**	**d_{8080} [mm]**	**DDF [mm]**
SiC	3.9	39.8	40.1	1.6	0.9
EBT3	3.2	39.5	40.0	1.8	0.7

Table 4.7 Quality parameters evaluated for pristine Bragg peaks by using linear interpolation when necessary. Uncertainty is 0.2 mm for all the values measured in [mm].

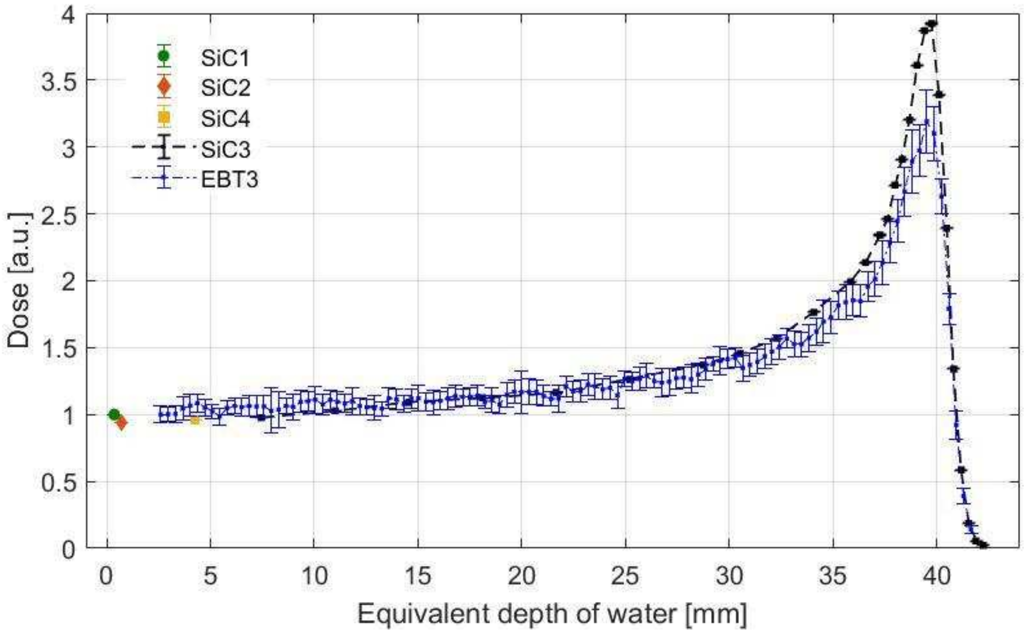

Figure 4.33 PDD distribution (normalized at entrance) reconstructed using the PRAGUE prototype with SiC devices arranged as depicted in Figure 4.37. The depths corresponding to the acquisition points were determined by considering the values WET_1=0.355±0.17 mm, $WET_{2,3,4}$=3.55±0.17 mm. The PDD distribution reconstructed via the EBT3 stack is also shown (blue data).

The results demonstrate the commendable ability of SiC devices in reconstructing the PDD distribution of the 70 MeV proton beam. The measured range (d'_{90}=40.1±0.2 mm) aligns with the range estimated through SRIM simulations, which is 40.2 mm. The comparison with the PDD distribution reconstructed using EBT3 films highlights the better performances of the SiC devices in the reconstruction of the Bragg peak, where the LET of the radiation increases. This is evident from the higher peak-to-plateau ratio obtained.

4.5 Resin coated SiC investigation

4.5.1 Detector description

The feasibility study on resin coating of SiCs was conducted on a device with slightly different characteristics than the ones described in the previous Section. The detector was manufactured in the context of a collaboration between INFN and IMM-CNR. It is a 4H-SiC p^+n planar junction and it was built by using new technological processes developed in collaboration with ST-Microelectronics company (STM) in Catania [319]. The device has an active area of 10 x 10 mm^2, a 0.2 μm thick p-layer with a doping concentration $N_A = 1 \cdot 10^{19}$cm^{-3} and a 10 μm thick n-layer with a doping concentration $N_D = 0.5 - 1 \cdot 10^{14}$ cm^{-3}. The substrate is 350 μm thick, with a doping concentration of $N_D > 10^{18}$ cm^{-3}. It was mounted and bonded on a PCB (1.75 mm thick). After that, the device was embedded in epoxy resin in order to make the detector waterproof (Figure 4.34). In particular, the EPO-TEK® 509FM-1 resin was adopted for the coating process. It is a bi-component, optically opaque epoxy resin designed for potting of semiconductors, PCB and system-level electronics [333]. An aluminium box of 26 · 26 · 4 mm^3 (walls 1 mm thick) for the detector housing was realized (Figure 4.34(1)). A thin layer of resin was deposited on the bottom of the container, on which the detector resting on a layer of adhesive Kapton was placed (Figure 4.34(2)). Finally, an overall resin thickness of approximately 1 mm was used to completely cover the device. In Figure 4.34(3) the SiC detector after the potting process is shown. Subsequently, the SiC was connectorized and the connection cable was coated as well.

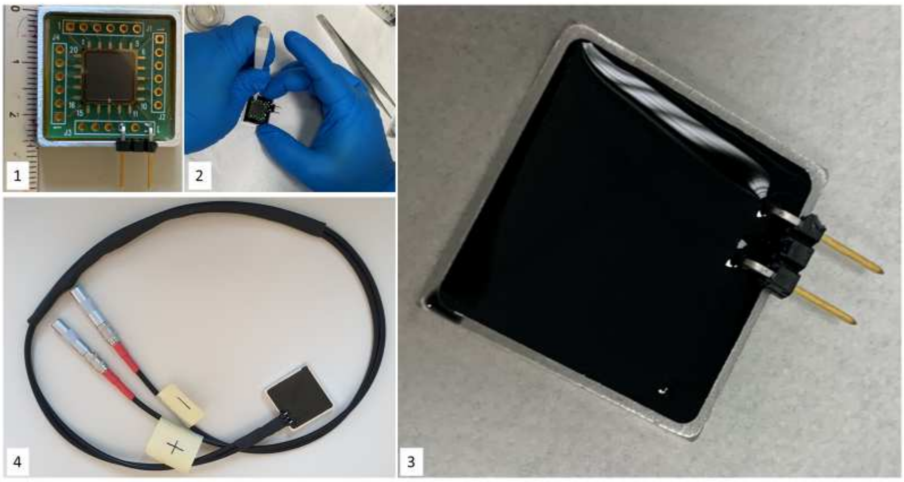

Figure 4.34 Steps of the SiC coating process, from 1 to 4 in chronological order. See text for details. The "-" label indicates the wire connected to the anode of the diode, while the "+" is connected to the cathode.

4.5.2 Electrical characterization

The I-V and C-V profiles of the resin-coated device were measured at room temperature and in air. Experimental tests were conducted at the INFN-LNS using the same experimental setup (readout system and acquisition software) adopted for the electrical characterization of the PRAGUE prototype (Section 4.3).

The I-V profile was studied in the reverse bias voltage range 0 - 300 V (1 V step, 2 nA and 1kV full-scale) and in the forward bias voltage range 0 - 2 V (0.1 V step, 20 nA and 100 V full-scale). In both polarizations, an acquisition time per voltage value equal to 25s, a sampling rate of 2Hz, and and a waiting time of 3s were set. In Figure 4.35, the resulting SiC I-V curves in both polarizations are reported. The reverse trend indicates a deviation from the dark current for voltages exceeding 150 V, but the breakdown voltage is not reached (Figure 4.35(b)). However, at these voltages, the device's response remains less stable, as evidenced by the increase in the associated error. The latter was calculated considering both the error in the mean value and the instrument's accuracy (Figure 4.35(c)).

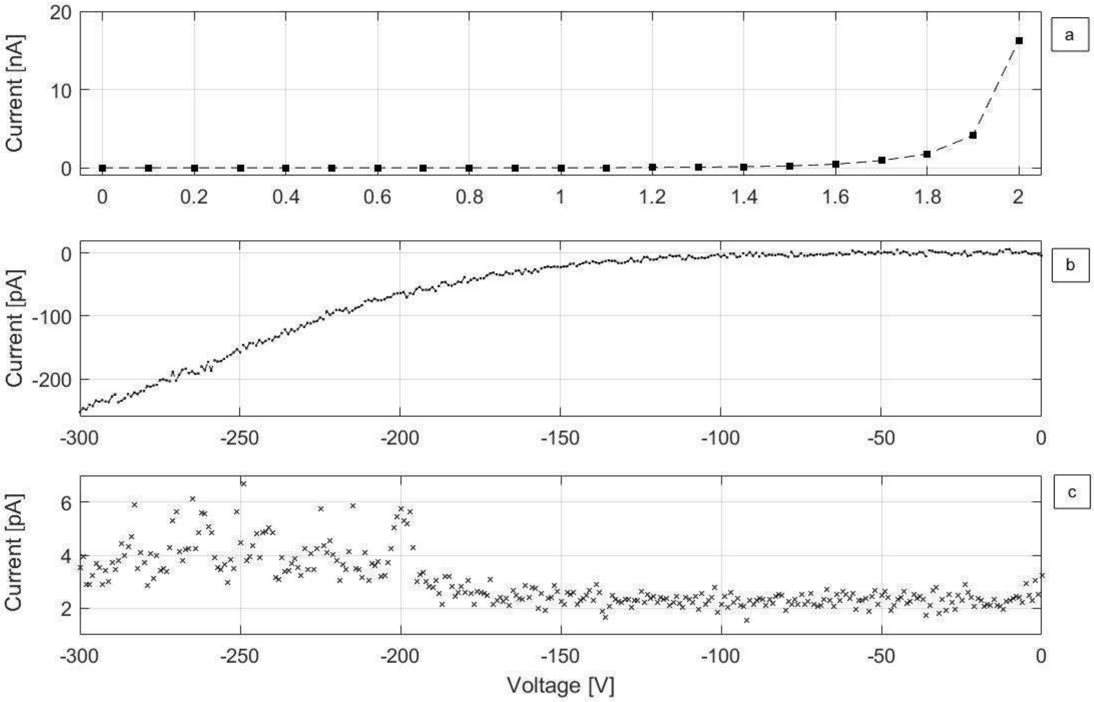

Figure 4.35 I-V profile of the resin coated SiC. a) Direct polarization. Error bars, which are evaluated taking into account the error on the mean and the accuracy of the instrument, are of the order of 5-50 pA and are included in the marker points. b) Inverse polarization. The leakage current at 0-100V voltages does not exceed 10 pA. c) Error associated with the current values reported in the panel (b).

The C-V profile was studied in the reverse bias voltage range of 0–100 V, with a variable step ranging from 0.1 to 5 V (set manually). The adopted capacimeter was set to operate at a full scale of 2 nF with a sample rate of 1 kHz. In the top panel of Figure 4.36 the resulting C-V curve is reported. As previously, starting from the C-V characterization it was evaluated:

1. The saturation capacitance C_s=865 ± 5 pF, determined as the minimum capacitance obtained by increasing the reverse bias voltage. The comparison between C_s and theoretical value $C_s^{th} = \frac{A \cdot \varepsilon_s}{W_N} = 860\, pF$, calculated through equation (4.5) with $A = 10 \cdot 10\, mm^2$ and $W_N = 10\, \mu m$, indicates a good agreement within experimental error.

2. The thickness W of the depletion region in full depletion conditions. W was estimated through equation (4.5) by using the experimental values obtained for C_s: $W = \frac{A \cdot \varepsilon_s}{C_s} = 9.9 \pm 0.1\ \mu m$. In this case as well, there is agreement between the experimental and theoretical values $W_N = 10\ \mu m$ within the uncertainty.

3. The depletion voltage V_D, the built-in potential V_{bi}, and the donor concentration N_D, determined by applying the intersection method on the $1/C^2$ curve as a function of the applied voltage V (see Figure 4.36). The obtained curve exhibits a typical linear trend at low voltages (in the range 0–3 V), while it is almost constant at voltages higher than 40 V. A best-fit procedure was employed to determine the linear functions that best approximate the two trends, denoted as Fit1 and Fit2. Starting from Fit1 and Fit2, it was possible to determine:

   - V_D=1.8±0.3 V, obtained as the voltage value corresponding to the intersection of the two best-fit curves, Fit1 and Fit2 (see Figure 4.36); the theoretical range of values for the depletion voltage is $V_D^{th} = N_D \frac{e W^2}{2 \varepsilon_s} = 4.7 - 9.3\, V$, determined for W=10 μm and N_D = 0.5 - 1 · 10^{14} cm^{-3} through equation (4.8).
   - V_{bi}=1.0±0.1 V, obtained by extrapolating the Fit1 curve to the point where $1/C^2$=0; the theoretical value, estimated through equation (4.2), is equal to $V_{bi}^{th} = \frac{kT}{e} \cdot ln\left(\frac{N_A \cdot N_D}{n_i^2}\right) = 2.9\, V$.
   - $N_D = \frac{2}{e A^2 \varepsilon_s m} = 3.1 \pm 0.1 \times 10^{13} cm^{-3}$, where *m* is the slope of the Fit1 curve, as described by equation (4.10).

   In all three cases, a significant difference of the order of 60-80%, 65%, 40-70%, respectively for V_D, V_{bi}, and N_D, with respect to the attended values was obtained. Finding a lower N_D value than expected aligns with the results obtained for V_D and V_{bi}. All the extrapolated quantities are indeed underestimated compared to the nominal values. As previously disclosed for the SiC devices that comprise the prototype, this significant discrepancy could be attributed to real-world conditions that differ from the assumptions on which the method is founded [322]. As described in Section 4.3.3, this possibility was explored by analyzing the dopant concentration profile along the active thickness of the material. Using the relation (4.5) and replacing C with the experimental values C(V) (depicted in Figure 4.36, top panel), it is possible to indirectly calculate the thickness of the depletion region W(V) as the voltage varies. Determined W(V), the relationship (4.12) was used to study the trend of N_D as a function of V and W(V), by replacing V_{bi} with the values obtained experimentally. In Figure 4.37 the trend thus obtained for W(V) and N_D(W,V) is reported up to 50V.

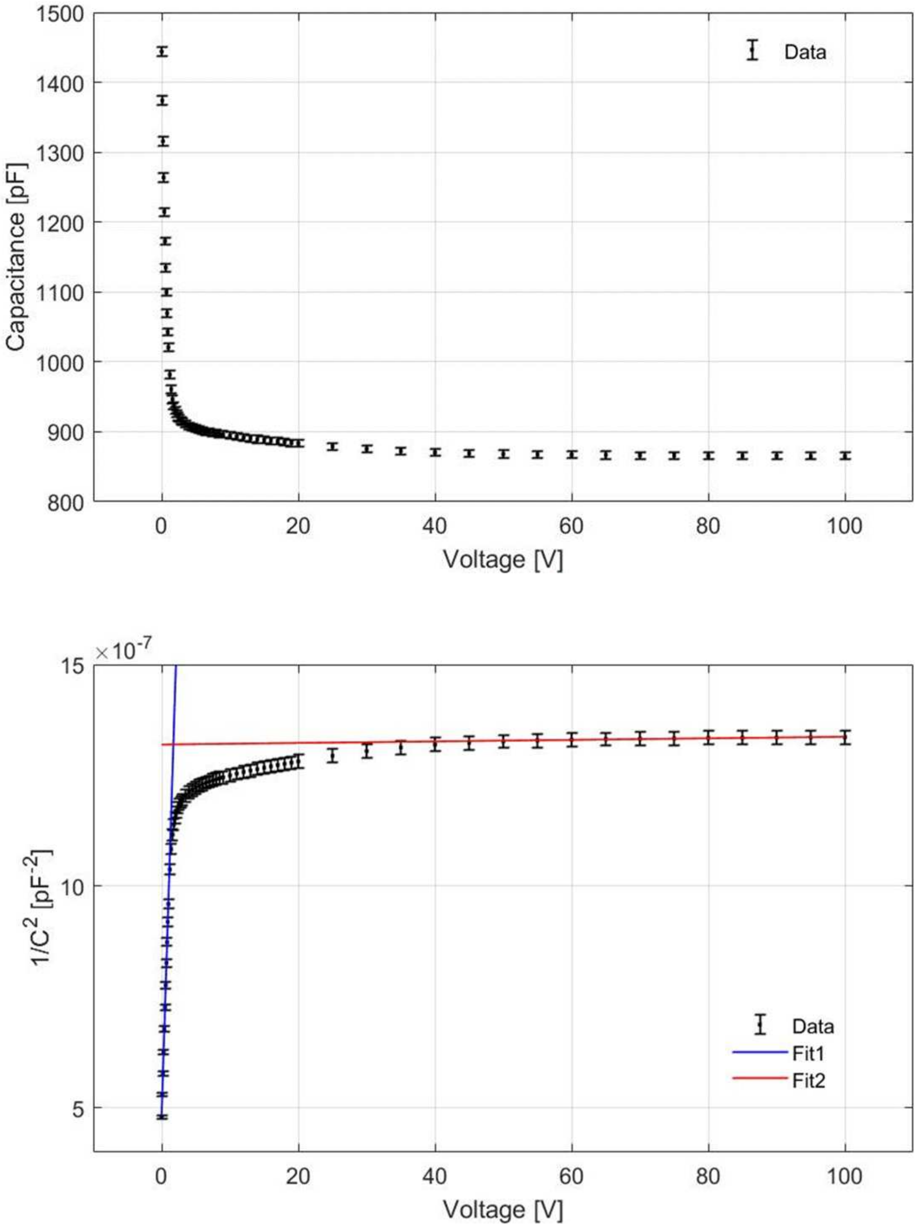

Figure 4.36 C-V profile of resin coated SiC device. Top panel: trend of the measured capacitance C *vs*. applied voltage. Bottom panel: trend of $1/C^2$ *vs*. reverse applied voltage. The linear fits in the low voltage range (Fit1) and in the saturation region (Fit2) are also shown. The error bars in the figure are obtained taking into account the accuracy of the instrument (~5 pF), while the uncertainties related to the extrapolated quantities are calculated by applying the theory of error propagation. The parasitic capacitance of the cables, estimated to be approximately 25 pF, has been subtracted.

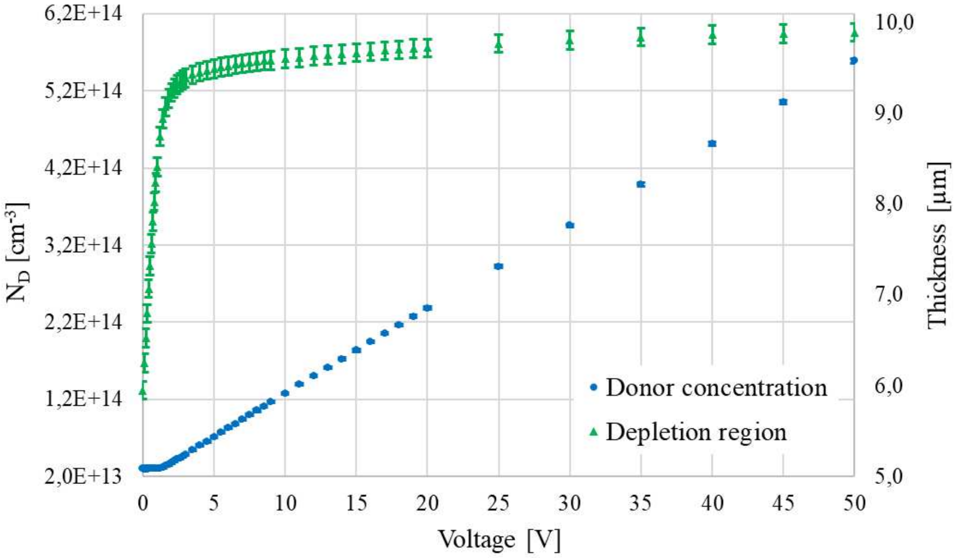

Figure 4.37 Trend of N_D and W of the resin-coated SiC device as the reverse bias voltage applied varies. The error bars are evaluated by applying error propagation. It would appear that the linear trend begins approximately at 5V for N_D (blue line).

It is important to remember that law (4.12) is valid until the full depletion condition is reached, i.e. for applied voltage $V \leq V^{th}_D$ (theoretical depletion voltage). When $V > V^{th}_D$, although V increases, W(V) remains approximately constant and therefore $N_D(W, V)$ grows linearly with V (see blue line in Figure 4.37 at voltage values higher than 5V). This linear growth of $N_D(W, V)$ with V is fictitious and no longer describes the physical trend of N_D within the depletion region. To establish up to which voltage the trend obtained for $N_D(W, V)$ by applying the equation (4.12) can be considered valid for the description of the experimental data, a new methodology based on the identification of an objective threshold was defined. The latter aims to experimentally estimate the V^{th}_D value with better accuracy and precision than the intersection approach. Specifically, the threshold method is based on the exclusion of the N_D values belonging to the linear trend (i.e., for $V > V^{th}_D$). Inherently, this investigation is essential precisely because there is suspicion that N_D is not constant. If this were not the case, considering the depletion voltage V_D found with the intercept method as the limit value of the validity of the law (4.12) would be sufficient. However, V_D appears to be underestimated.

Precisely, to experimentally determine the upper limit of validity of $N_D(W,V)$, its trend as a function of V was initially investigated (Figure 4.38). Through a best-fit procedure applied on the data belonging to the 40-100 V voltage range (where W varies overall by a few hundredths of a µm, and therefore certainly we are in the saturation region, as can also be observed from the C-V curves), the linear function *f(x)* that describes the experimental trend of $N_D(W,V)$ at the invalidity voltages (i.e., for $V > V^{th}_D$ where it assumes a linear trend) was found. Defined the best-fit function *f(x)*, the calculation of residuals (for data belonging to the 40-100 V range) and of Root Mean Square Error (RMSE, σ) was performed. The latter is the standard deviation of the residuals of the points that fall in the

40-100 V range, certainly belonging to the linear trend ($r^2 \simeq 1$ is found in all cases). It was used to define the threshold t mentioned above, as follows:

$$t = \bar{r} \pm 3\sigma \tag{4.18}$$

t contains 99.7% of the residuals calculated for the N_D values belonging to the linear trend, considering a Gaussian distribution centred on the average value of the residuals $\bar{r}$ (tending to 0) and with a standard deviation σ equal to RMSE. At this point, the residuals r_i (with i=1, ..., N, so that r_1 refers to the N_D value corresponding to 0V and r_N refers to the N_D value corresponding to 100V) were calculated, with respect to *f(x)*, for all the *N* experimental data, and were compared to t:

- if $r_i < t \Rightarrow$ the i-th experimental point belongs to the linear trend;
- if $r_i > t \Rightarrow$ the i-th experimental point does not belong to the linear trend.

In particular, proceeding from i=1 to i=N, the last value of r_i that exceeds the threshold t was chosen to identify up to which experimental value (and, therefore, up to which voltage value) the trend of N_D(W,V) can be considered valid. Therefore, the threshold is used to determine the last voltage value corresponding to a residual greater than the threshold, i.e., the voltage beyond which the trend of N_D(W,V) can be considered linear at 99.7%. The resulting voltage value (7.5V) is an estimate of the depletion voltage (see Figure 4.38).

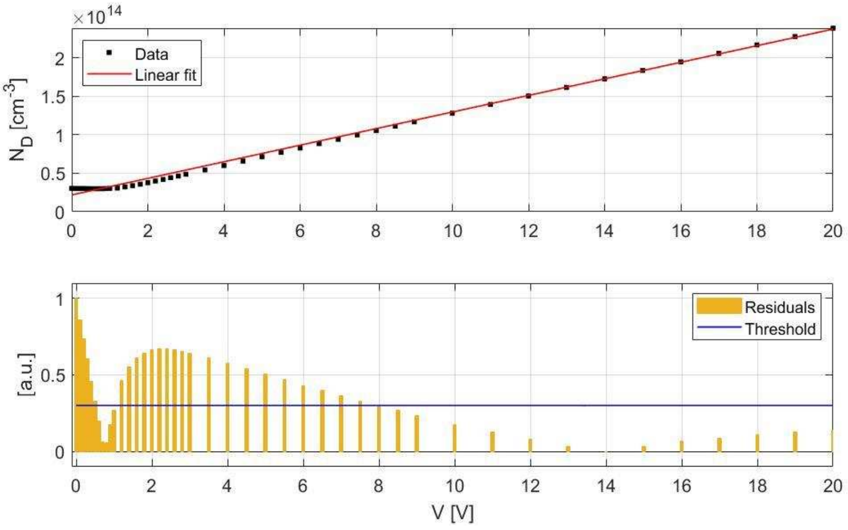

Figure 4.38 Top panel: trend of N_D as a function of V. The linear function *f(x)* obtained through the best fit procedure is also shown. Bottom panel: residual values, calculated between the "Linear fit" function *f(x)* and the data, and threshold line are reported. For convenience the absolute value of the residuals normalized with respect to the maximum value were considered. The threshold line was normalized as well. It can be easily seen that, starting from 0V, the last voltage value corresponding to a residue greater than the threshold is equal to 7.5V.

This strategy, which is based on excluding experimental points whose residuals are part of the residual distribution evaluated on points belonging to the linear trend, introduces a 0.3% error of considering a point belonging to the linear trend as valid for describing the relationship between N_D, W, and V according to (4.12). In other words, there is a 0.3% chance of making an error in deeming acceptable a point that belongs to the residual distribution of points following a linear trend. Figure 4.39 illustrates the trend of $N_D(W,V)$ as a function of W with an uncertainty of 0.3%.

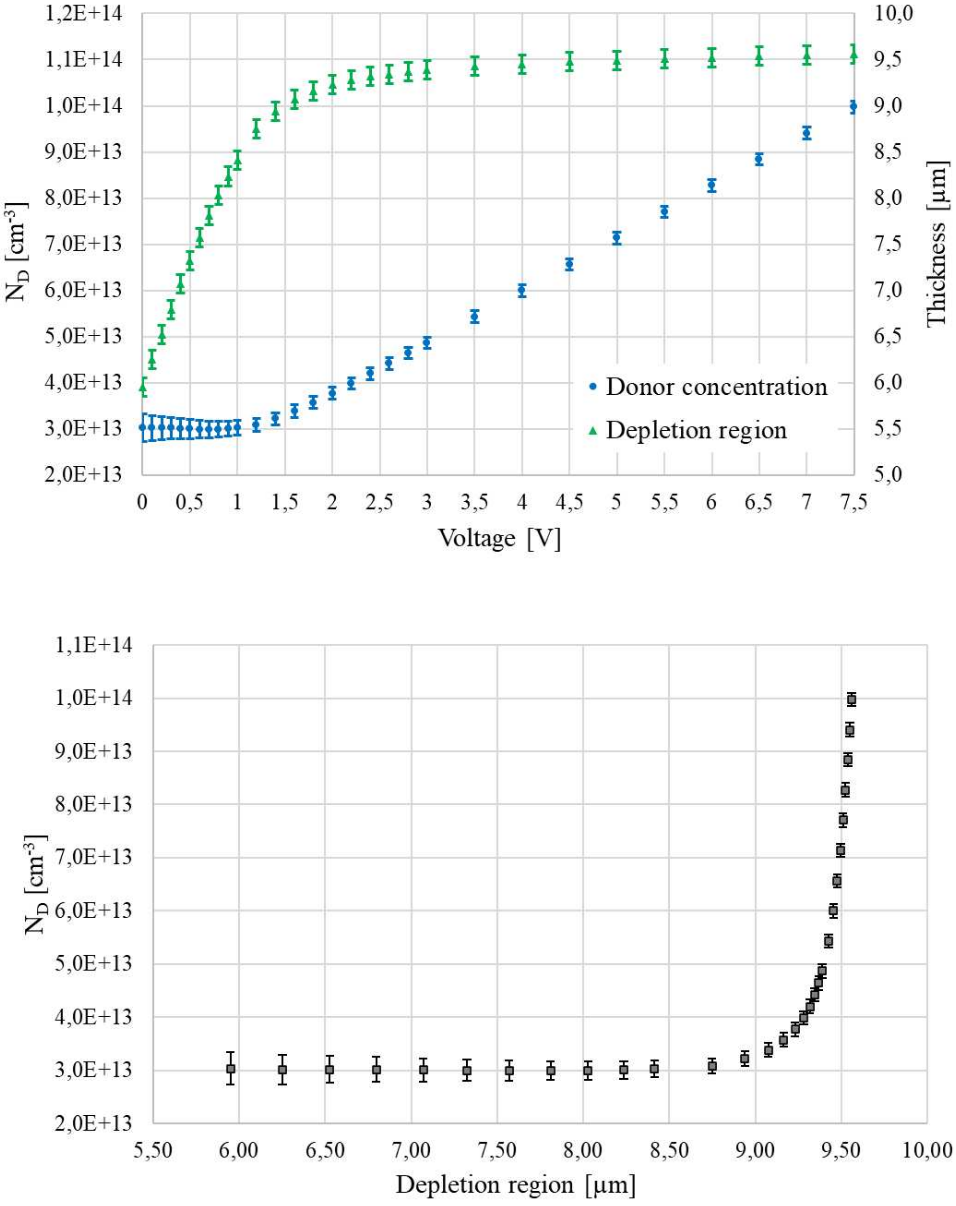

Figure 4.39 Dopant concentration and depletion region profile. Top panel: trend of W(V) and $N_D(W,V)$ as a function of the applied voltage. The curves are shown up to the voltage obtained through the threshold method (7.5V). The latter was evaluated taking into account the residuals calculated over the 40-100 V voltage range. Bottom panel: dopant concentration profile as a function of the thickness of the depletion region

The possibility that the resin covering has damaged or altered the properties of the device is excluded. In fact, although unfortunately it was not possible to carry out a comparative investigation of the characteristics of the detector before and after the resin coating process, if the latter had damaged the detector we would have observed a dark current, saturation capacitance, and altered depletion region accordingly. Therefore, it is suspected that the differences identified are due to errors during the doping process of the device, and in particular, that the actual dopant concentration is lower than expected. The results obtained confirm these suspicions.

4.5.3 Irradiation tests

4.5.3.1 Linearity, stability and reproducibility

The stability, reproducibility and linearity of the detector response were also analyzed. The tests were performed by irradiating the detector with a ^{90}Sr source at INFN-LNS (Catania, Italy). Detector's linearity was further investigated using an X-ray beam. In the latter case, the experimental tests were performed at the Azienda Ospedaliera Universitaria “Gaetano Martino”, in Messina (Italy). Table 4.8 summarizes the experimental test carried out.

	INFN-LNS	**G. Martino**
^{90}Sr source	Stability Reproducibility Linearity	-
X-ray beam	-	Linearity

Table 4.8 Irradiation tests on resin-coated SiC device.

The irradiations with ^{90}Sr source (nominal activity of 33.3MBq) were executed at room temperature, in vacuum (2x10^{-5} mbar), employing a plastic support designed to maintain both the position and the detector-source distance (Figure 4.40). The current/charge produced by the detector was quantified using a KEITHLEY K6517B electrometer. The latter simultaneously served as a voltage source for the detector, which was reverse biased at 50V. The data acquisition was conducted through the I-t/Q-t LabVIEW program (refer to the Appendix) developed in-house (refer to Figure 4.41).

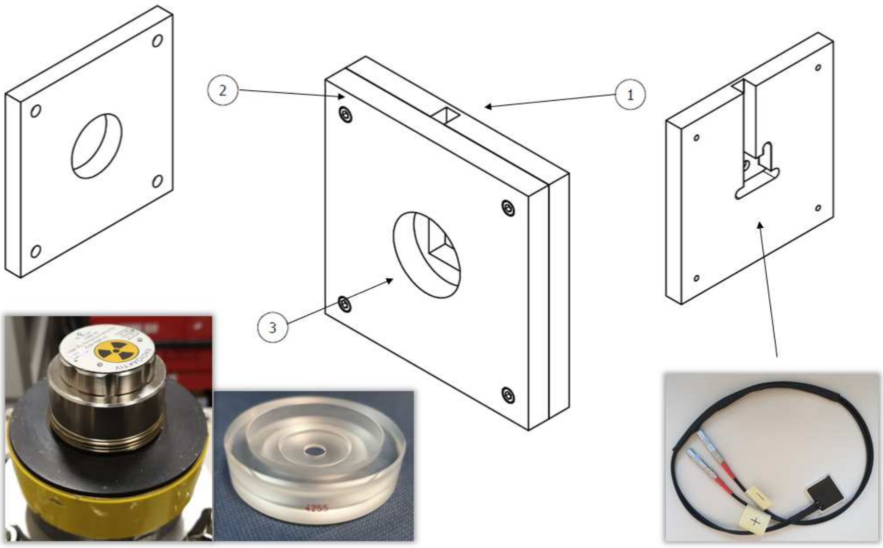

Figure 4.40 PMMA support made specifically to house the resin-coated SiC device and the ^{90}Sr source, maintaining their mutual position unchanged during the different irradiations.

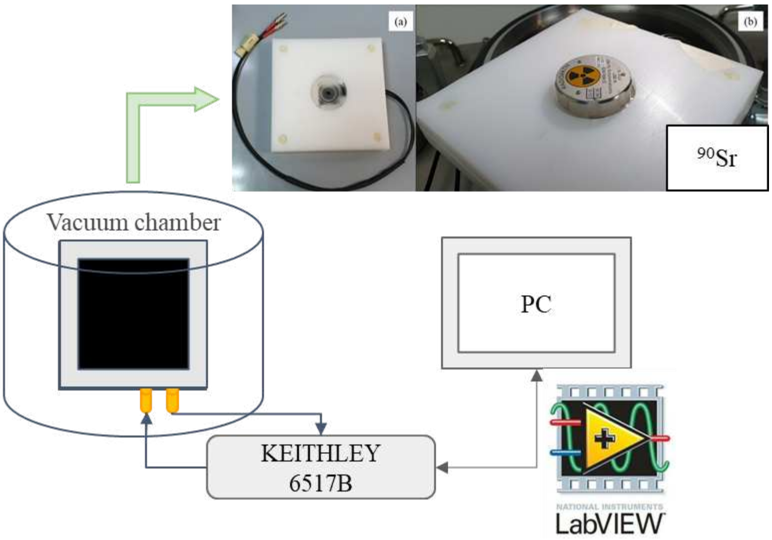

Figure 4.41 Schematization of the experimental setup used during ^{90}Sr source irradiation.

Initially, the device's charge response when exposed to ^{90}Sr source irradiation was examined by varying the irradiation time. A full scale of 20 nC and four different acquisition times (5, 10, 15 and 20 s) were set. Eighty charge measurements for each acquisition time were acquired. The reproducibility of the device's response was estimated by evaluating the standard deviation of the data referring to the same irradiation time. A maximum percentage deviation of 0.3% from the mean value was observed, signifying a high degree of reproducibility in the charge response under these experimental conditions. Figure 4.42(a) shows the average charge values over time. A best-fit procedure was also performed to evaluate the linear trend, resulting in a $r^2 \simeq 1$. To better emphasize any deviation from linearity, the detector sensitivity was calculated. It is expressed as the ratio between the charge and the irradiation time [nC/s] normalized to the expected value obtained through the fit curve. In Figure 4.42(b) the sensitivity as a function of the irradiation time is reported. Deviation from the linearity resulted to be within 0.03%.

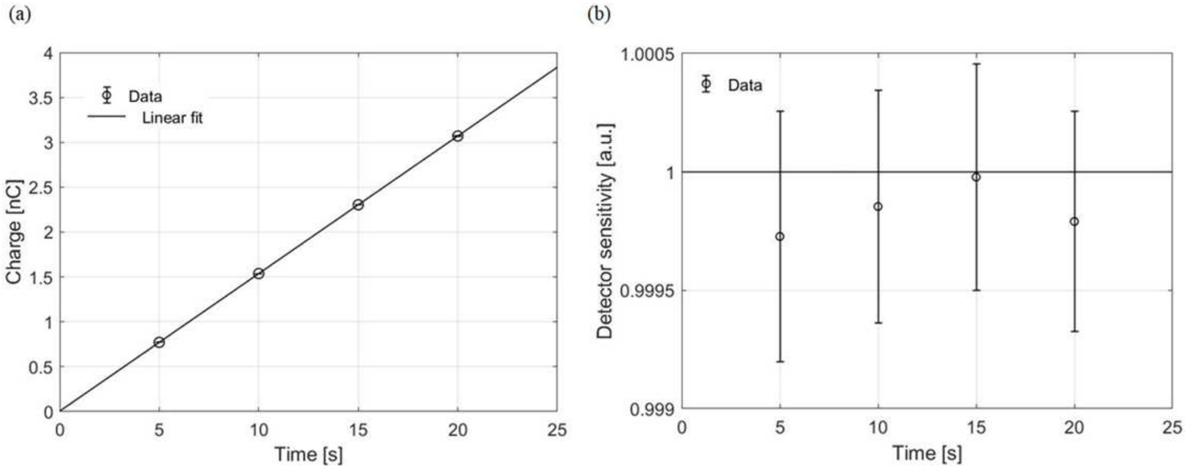

Figure 4.42 (a) Average trend of the detector charge response over time. Error bars are included in the points. They are evaluated taking into account the accuracy of the instrument (~0.01 nC) and the error on mean values. The linear fit is also reported. (b) Deviation of the experimental points from the normalized linear trend.

The detector stability was then evaluated by measuring the current response in the same experimental condition described before. The current signal over time was acquired employing the I-t LabVIEW program. A full scale of 200 pA, an acquisition time of 20 s and a sample rate of 2 Hz were set. Five series of measurements were acquired, for a total acquisition time of 100 s and 200 values of current. To evaluate the oscillations of the current signal, the average value μ (~153.1 pA) and the standard deviation σ (~0.6 pA) were extrapolated, resulting in a relative statistical error of 0.4%. When the instrument's accuracy is also taken into account, the error bar expands to 2 pA.

The linearity of the detector's response was also tested under the irradiation of a LINAC PRIMUS X-Ray tube used for clinical treatments, maintaining the same electronic readout. The charge response of the detector was acquired by means of the Q-t LabVIEW program. The irradiations were performed in air, at room temperature, by varying the MU, while setting the tube acceleration voltage and the dose rate (10 MV with 300 MU/minute were chosen). The SiC device was positioned at a source-to-surface distance (SSD) of ~100 cm, while the field size was 10x10 cm^2. For each irradiation configuration, the charge of the device was acquired 5 times. In Figure 4.43 the trend of the mean values as respect to the MU is reported. A best fit procedure was performed again to evaluate the linearity level of the response, finding a maximum deviation from linearity of ~1.2%.

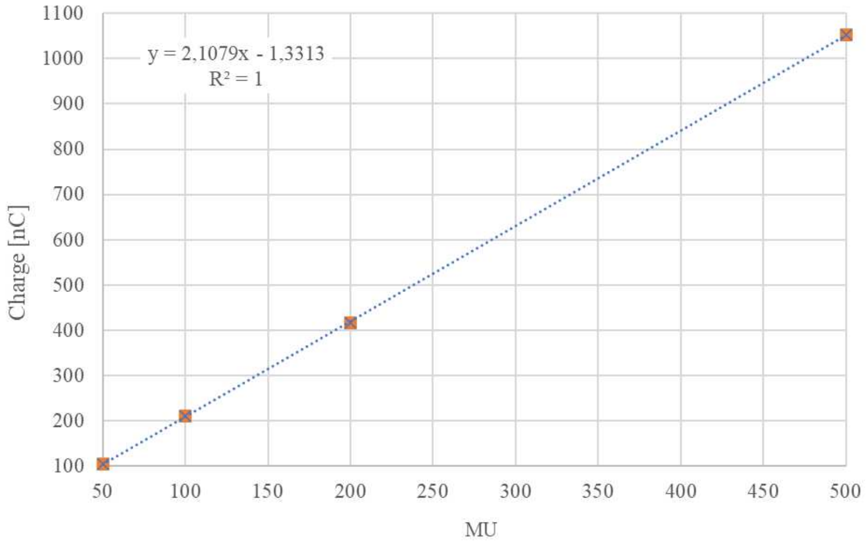

Figure 4.43 Trend of the average net charge values (with background subtracted) by varying the absorbed dose. The error bars (~0.5-9.6 nC) were evaluated taking into account the accuracy of the instrument (~0.5-4 nC) and the oscillations (σ≃0.03-9.5 nC).

The latter was a preliminary characterization, carried out in view of a dosimetric characterization in water, positioning the detector inside a phantom. Unfortunately, it was not possible to carry out that measurement due to a sudden water infiltration into the device (see next Section).

4.5.3.2 Water immersion test

The investigation concerning the resin-coated SiC device also included examining the detector's performance following immersion in water, evaluated in terms of I-V characterization. The I-V acquisition was carried out both before and after its immersion in water, in order to test the possibility of using the device with the same methods foreseen according to the dosimetric protocols, which recommend the use of dosimeters inside water phantoms (Figure 4.44). To be precise, the I-V profile was measured in two different configurations - with and without the ^{90}Sr radioactive source - and the I-V LabVIEW program was used in both cases. The background (i.e., without source) I-V was analyzed again to identify any changes in the intrinsic properties of the detector caused by immersion.

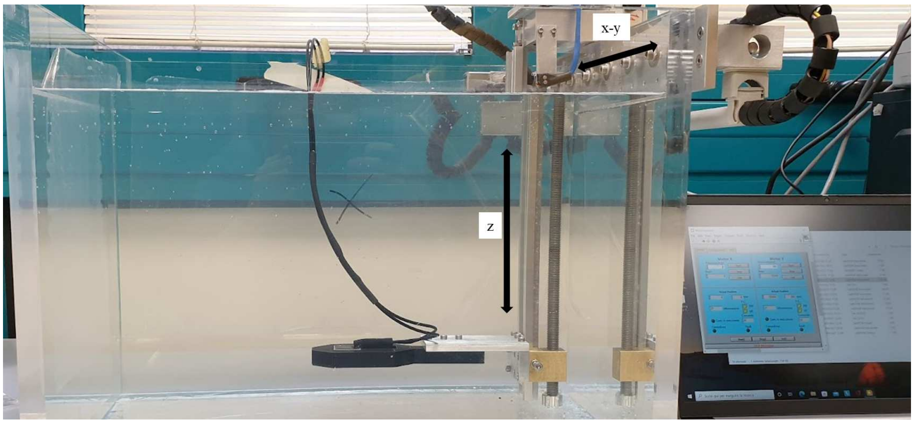

Figure 4.44 Picture of the system set up specifically for the controlled immersion of the resin-coated SiC during its irradiation from above. On the right is the computer-controlled motorized system.

In particular, the I-V profiles were investigated in vacuum (2.5x10^{-5} mbar) by applying a reverse bias voltage in the range between 0 and 100 V (in steps of 5 V). The background pre-immersion acquisition was repeated three times for each voltage value, setting a sampling rate of 2 Hz, a full scale of 20 nA and an acquisition time of 60 s. Keeping the experimental conditions unchanged, three I-V acquisitions were performed also in presence of the ^{90}Sr source, setting a full scale of 200 nA. Figure 4.45 depicts the average trend of the various sets of measurements conducted in both configurations. Error bars are calculated by applying the error propagation theory and are respectively of the order of 2 pA and 0.5 pA for the configuration with and without the radioactive source.

Thereafter, the detector was immersed in water for one hour and both the I-V measurements were repeated under the same condition aforementioned. To establish the reproducibility and stability level of the device response, the I-V acquisition was performed 10 minutes and 10 days after the immersion in water. In Figure 4.46 the comparison between all the measurements is shown. To quantify the effects due to the immersion in water, the differences between pre and post immersion current were evaluated (Table 5.9). The comparison between the leakage currents acquired before and after the diving process exhibited an average difference of the order of 0.5 pA, while the maximum difference is 2.5 pA. Since most of the experimental data after immersion resulted to be within the error bars of the pre-immersion average trend, it was possible to conclude that no significant difference can be appreciated. The current produced by the detector under irradiation 10 minutes after immersion presented an average difference of the order of 20 pA with respect to the values measured before the immersion. The absolute current values read 10 days after immersion in water was on average 3 pA lower than those read 10 minutes after immersion, resulting within the experimental error. These preliminary results seemed to indicate that the immersion had somehow changed the properties of the resin, affecting the charge collection of the detector. Further investigations clarified that the observed effect was actually due to water infiltration at the connector level, after excluding the possibility that it was the manifestation of a priming effect. However, it is possible to assert that the immersion did not damage the detector functionality.

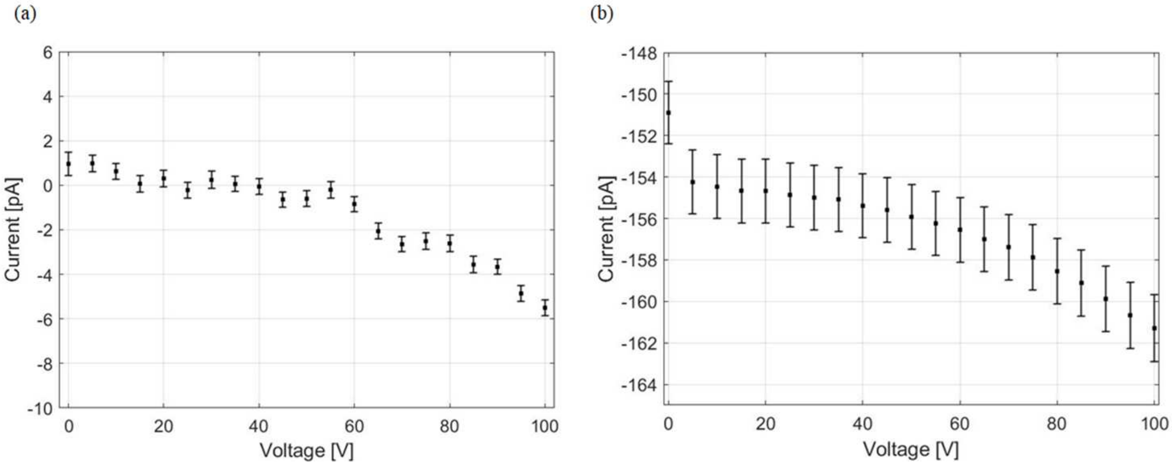

Figure 4.45 Pre-immersion I-V profiles. (a) Leakage current of the detector. (b) I-V detector profile with ^{90}Sr source. The current at 50 V is −156 ± 2 pA. In both cases the breakdown voltage is not reached.

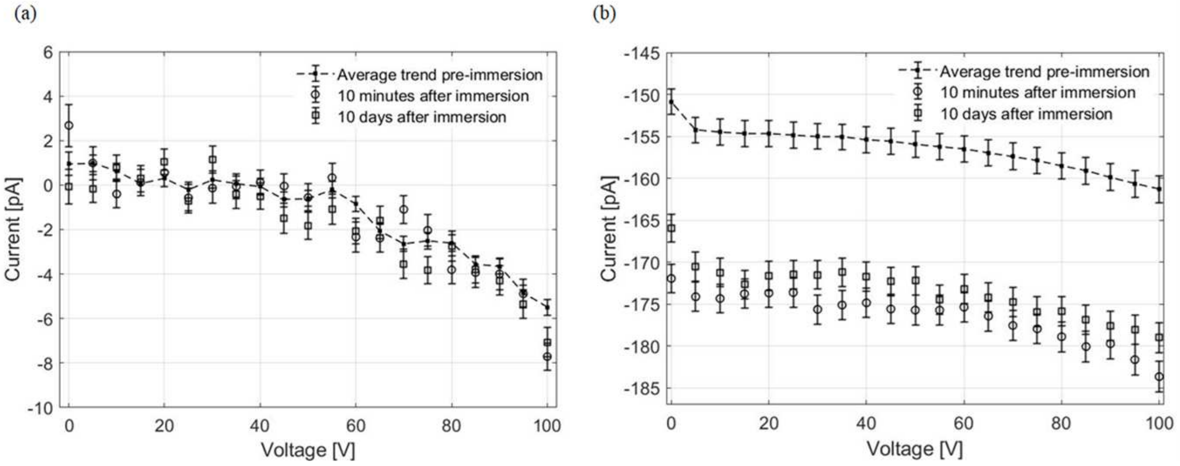

Figure 4.46 Pre and post-immersion I-V profiles. (a) Leakage current of the detector before and after immersion in water. No significant differences can be appreciated for most of the experimental points. (b) I-V profile with ^{90}Sr source before and after immersion in water. The current at 50V reverse bias voltage 10 days after immersion is −172 ± 2 pA, which corresponds to a percentage deviation of the order of 10.5% with respect to the corresponding pre-immersion value. The absolute current values read 10 days after immersion in water are between 0.6% and 3.5% lower than those read 10 minutes after immersion.

	Configurations	**Average differences**
No external source	10 min. and 10 days post-imm. vs. pre-imm.	0.5 pA
With ^{90}Sr source	10 min. post-imm. vs. pre-imm.	50 pA
	10 min. post-imm. vs. 10 days post-imm.	3 pA

Table 4.9 Average difference between current signals acquired before (pre-imm.) and after immersion (post-imm.) in different configurations.

4.5.4 PDD distribution of a 62 MeV proton beam

To investigate the energy dependence of the resin-coated SiC device concerning incident proton beams, an experimental campaign was conducted using a clinical 62 MeV proton beam. The experimental run was performed at the CATANA (Centro di Protonterapia e Applicazioni Nucleari avanzate) proton beam line facility of INFN-LNS [194, 334, 335]. In Figure 4.47 a schematic drawing of the beamline is reported.

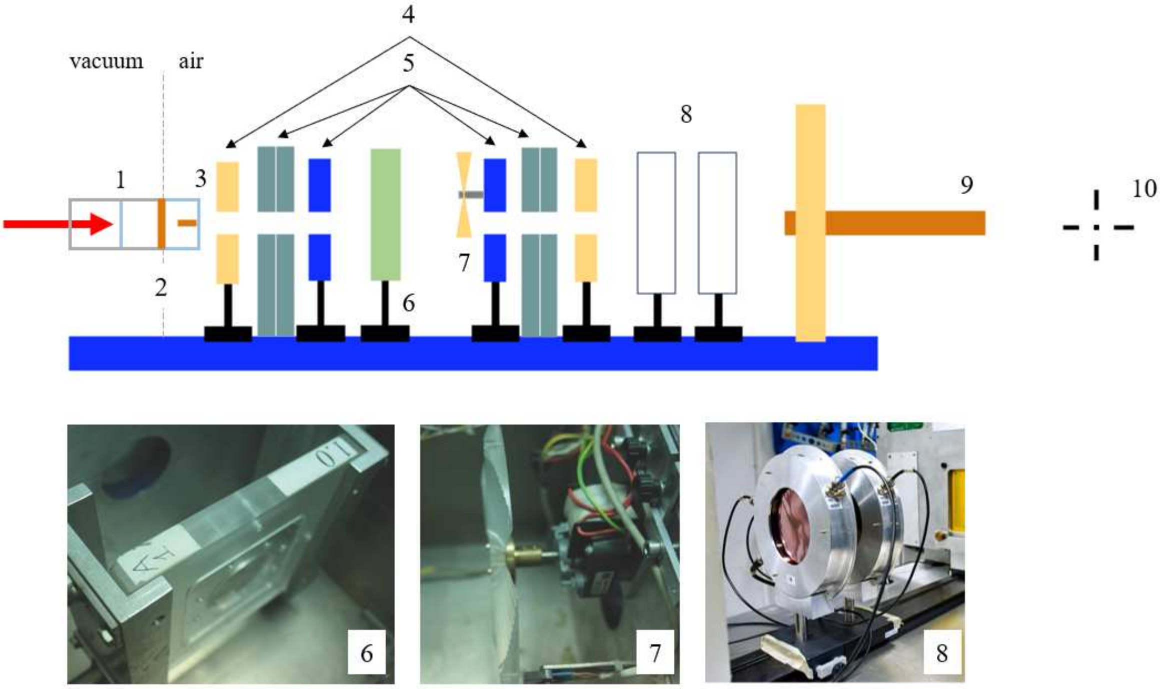

Figure 4.47 Sketch of the delivery system and main beam line elements (not in scale): (1) first scattering foil and SEM detector; (2) kapton window; (3) second scattering foil with a central stopper; (4) plastic collimators; (5) steel collimators; (6) range shifter; (7) modulator wheel; (8) monitor ionization chambers; (9) final collimator; (10) isocenter: a laser system is used to provide its identification.

The proton beam accelerated by the superconductive cyclotron is transported in vacuum to the treatment room where the protons exit into the air through a 50 µm thick Kapton window, positioned at approximately 3 m from the isocenter. The scattering system relies on a double foil configuration with a central brass stopper, positioned in close proximity to the beam exit in air. Moreover, the first 15 µm thick tantalum scattering foil is employed as a SEM, providing a real-time measurement of the proton beam intensity. Right after the scattering system, there is a shielded segment housing a range shifter and a range modulator custom-tailored for each patient. This setup is employed to degrade and modulate the energy of the beam, ensuring the delivery of the dose across the entire tumor volume. Following three intermediate collimators with a diameter of 35 mm, the beam encounters two monitor parallel-plate ionization chambers positioned in transmission. In the final section of the beamline, a 370 mm long brass pipe is used to limit the beam angular spread.

During the experimental measurements, modulator wheel and range shifters were removed, and a circular brass collimator with a diameter of 25 mm (8.3 cm before the isocenter) was used for the dosimetric and beam diagnostic procedures, later replaced by a 10 mm diameter collimator for the acquisition of the PDD distribution. The ionization chamber adopted as the reference device for depth–dose measurements at CATANA is the PTW TM34045 Advanced Markus® Electron Chamber (plane parallel geometry, with an electrode spacing of 1 mm and a sensitive volume $V = 0.02$ cm^3) [336]. The depth dose distribution was acquired in a water phantom, by fixing the dose (i.e., the number of MUs) and the beam current (around 5 nA) and measuring the signal produced by the camera at each depth point.

The same irradiation conditions were maintained for the acquisition of the PDD distribution carried out in air using the SiC dosimeter. The latter was powered and read via the KEITHLEY 6517B electrometer, using the experimental setup shown in Figure 4.48.

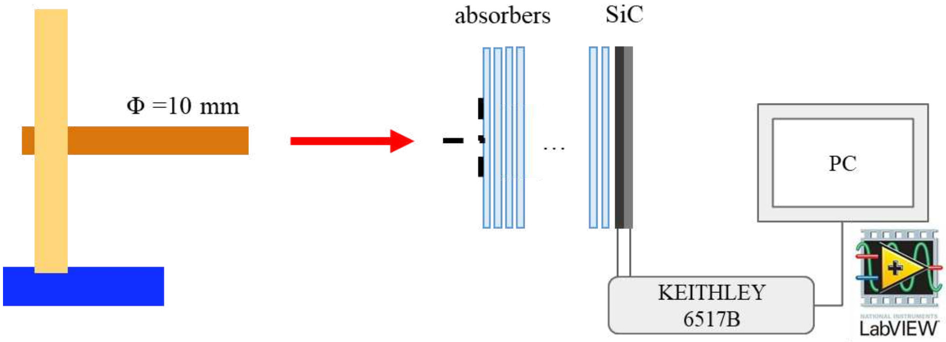

Figure 4.48 Schematization of the experimental setup and DAQ system used to perform the acquisition of the PDD distribution via the SiC device.

The detector was reversely polarized with 50V and the charge was measured through the Q-t LabVIEW program, setting a full scale of 2 µC and a sampling rate of 2Hz. Depth-dose distribution measurements were carried-out by placing an increasing number of water equivalent absorbers (PMMA) between the isocenter and the detector. The acquisition of the

PDD distribution using the SiC was repeated three times. Figure 4.49 shows the average trend of the PDD distributions obtained with the SiC device compared to that obtained using the Markus Chamber.

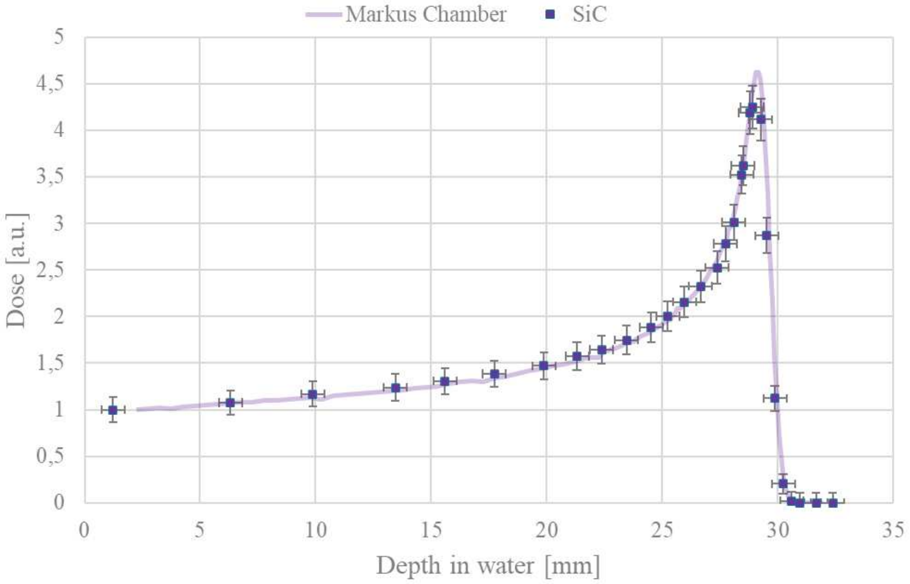

Figure 4.49 Bragg peak curves, normalized at the entrance window of the pristine 62 MeV proton beam. The square represents the signal acquired with the SiC detector, the line refers to the Markus chamber detector signal. The error bars on the position (0.5 mm) were evaluated taking into account the spatial resolution with which the measurement was carried out (linked to the thickness of the absorbers used) and an uncertainty on the thickness of the resin equal to 0.2 mm (20%, equal to ~0.3 mm WET). The error bars on the dose were evaluated taking into account the standard deviation of the three PDD distribution measurements, the uncertainty on the delivered dose equal to 3%, and the accuracy of the instrument.

Generally, SiC exhibits excellent Bragg peak reconstruction capabilities comparable to those of the Markus Chamber (refer to Table 4.10). The diminished peak-to-plateau ratio is attributed to the effective limitation in peak acquisition, arising from the reduced longitudinal spatial resolution of the method employed to advance the detector to greater depths.

Device	Peak-to-plateau ratio	d_{max} [mm]	d'_{90} [mm]	d_{8080} [mm]	DDF [mm]
SiC	4.2	28.9	29.3	1	0.6
Markus chamber	4.6	29.1	29.4	1	0.5

Table 4.10 Quality parameters evaluated for pristine Bragg peaks by using linear interpolation when necessary. Uncertainty is 0.1 mm for the chamber and 0.5 mm for the SiC.

Chapter 5

The final detector

5.1 Introduction

In this Chapter, a comprehensive account of the activities undertaken for the realization of the final PRAGUE detector is provided. This encompassed the characterization, and back-end processing of 80 SiC devices intended for the stack composition outlined in the PRAGUE project (Section 5.2). Simultaneously, a study on the electronic chain was conducted to design and develop a read-out system able to provide a real-time acquisition signal from all detectors in the stack when exposed to irradiation from both conventional and high-intensity beams (Section 5.3).

5.2 SiC devices: geometry and characterization

5.2.1 Detectors description

The SiC devices that will compose the PRAGUE detector were purchased by the Fraunhofer company [337], which was responsible for the front-end processing of the chips, while the wafers were produced by the LPE$^{(R)}$ company [338]. The 80 SiC devices in this study were produced through the CVD process carried out in a low pressure regime at high temperatures (1630 °C). During this phase, a growth of 10 µm 4H-SiC homoepitaxial layers on 100 mm thick wafers was obtained. The wafers were subsequently treated with several photolithographic steps to define the active area of the SiCs and supply the dopants necessary for the realization of a p^+n planar junction. Finally, through the metallization process, the realization of the ohmic contacts was performed. A sketch of the structure of the 80 detectors is shown in Figure 5.1(a). They were obtained by dicing the wafers into 15 x 15 mm^2 dice (Figure 5.1(c)). Each device has a 0.3 µm thick p-layer with a doping concentration $N_A=1 \cdot 10^{19}$cm^{-3} and a 10 µm thick n-layer with a doping concentration $N_D = 0.5 - 1 \cdot 10^{14}$ cm^{-3}. The substrate is 110 µm thick, with a doping concentration of $N_D > 10^{18}$ cm^{-3}. After the electrical characterization (described in Section 5.2.2), each device was mounted on a perforated PCB (with external dimensions of 2.925 x 2.925 x 0.155 cm^3) with silver conductive glue. The electrical connection was realized through a thermocompression bonding process (Al wire, 50 µm diameter) between the SiC pad and the PCB at Terminal 1 (Figure 5.2). Each device is named through an alphanumeric code that allows it to be uniquely identified. This code specifies the batch to which the wafer belongs (W4 or W5) and the number of the single die, visible under the microscope and marked on one of the corners (Figure 5.1(b)).

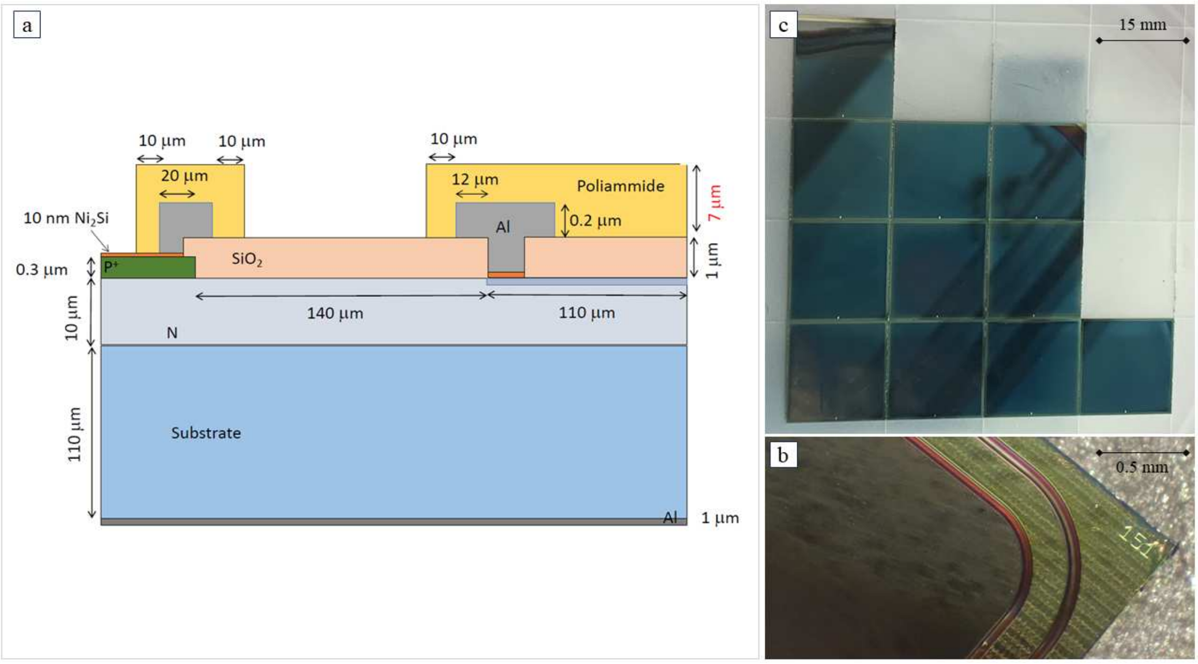

Figure 5.1. a) Structural scheme of SiC devices. b) Microscopic view of a portion of the sensitive area of SiC "W4-151", delimited by guard rings. c) Part of a SiC wafer divided into 15 x 15 mm^2 dice.

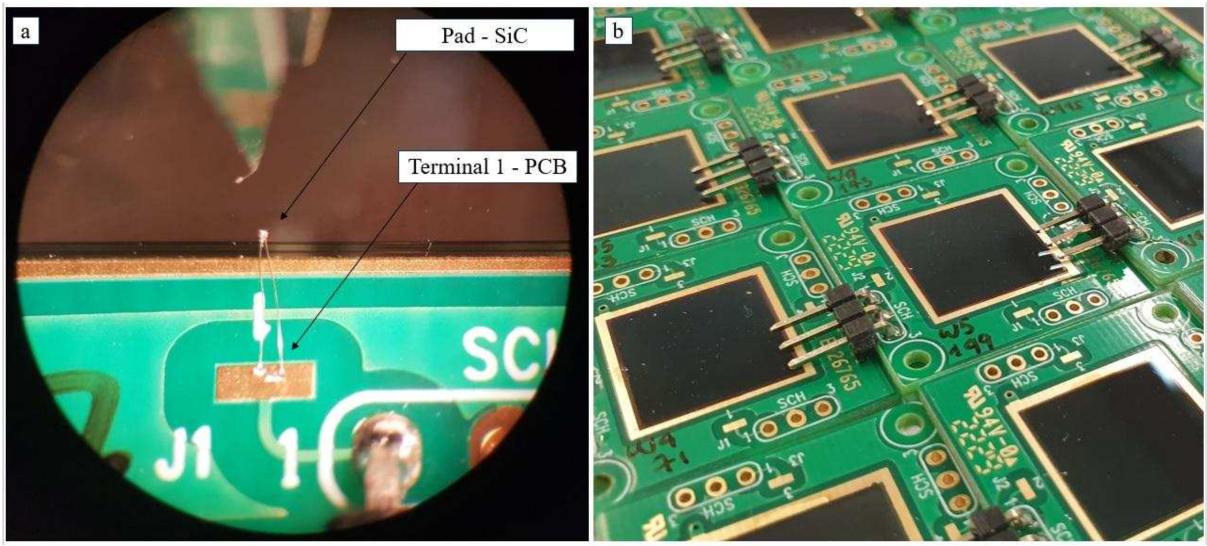

Figure 5.2. a) Microscopic view of SiC during the bonding process. b) SiC devices at the end of the electrical connecturization process. Electrical pins have also been welded to the PCB boards.

5.2.2 Electrical characterization

The electrical characterization of the devices consisted of acquiring the I-V and C-V profiles of the dice before the back-end process, at room temperature and in air. Experimental tests were conducted at the Industrial Engineering Department of the University of Rome "Tor Vergata" (Rome, Italy). During I-V measurements, the current generated by the detector was measured with a K6517B electrometer, which was also used as a detector bias source. To perform the C-V acquisition, the capacitance was measured by means of an LCR meter (Agilent, model 4263B) coupled with an EXT Voltage Bias Fixture (Agilent, model 16065A) [339], while the bias voltage was once again supplied by the K6517B electrometer. The data acquisition was carried out through two automatic programs implemented in the LabVIEW programming environment and developed by the Tor Vergata team. These softwares enable users to configure several acquisition parameters, such as the integration time of the A/D converter of the KEITHLEY (through a parameter called SPEED[58]), voltage step and ramp, acquisition time, and sampling rate. Measurements were performed on bare detectors in order to reduce the contribution of parasitic capacitances and currents. The SiCs were contacted via needle-shaped probe electrodes, as shown in Figure 5.3. The characteristics were obtained by applying a voltage to the p-type SiC layer while earthing the metallic contact. In Figure 5.4, the schematization of the experimental setup used for the two acquisitions is reported.

The I-V profile was studied in the reverse bias voltage range 0 - 200 V (in steps of 2.5 V) and in the forward bias voltage range 0 - 2.5 V (in steps of 0.1 V). The acquisition was repeated for all 80 SiC detectors, setting automatic range mode, a SPEED equal to 5 and an acquisition time of 4 s. In Figure 5.5, the I-V curves of two SiCs in the reverse bias voltage range are presented as examples.

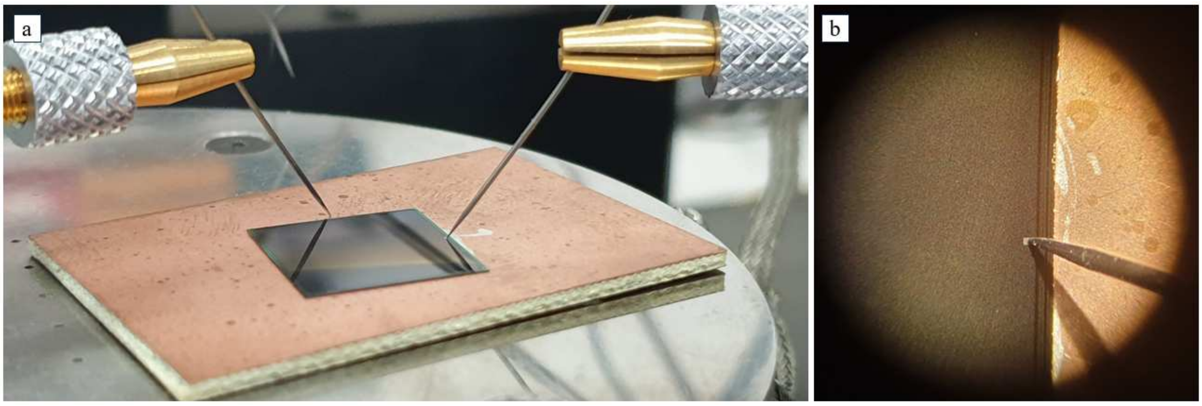

Figure 5.3. a) Probe electrodes placed between the cathode and anode of a bare SiC during I-V characterization. b) Microscopic view of the SiC. The probe electrode positioned on the detector pad can be appreciated.

---

[58] The SPEED parameter sets the integration time of the analog to digital (A/D) converter, the period of time the input signal is measured (also known as aperture) [325].

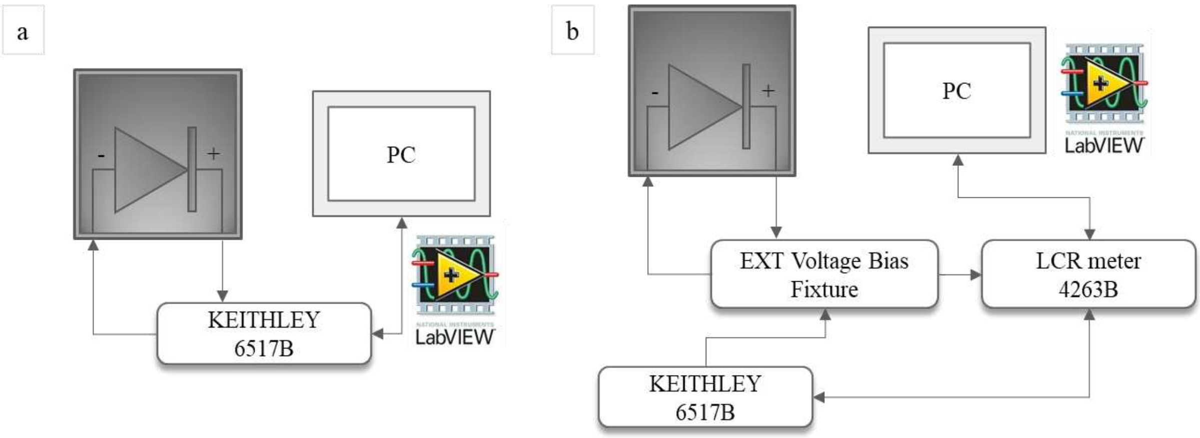

Figure 5.4. a) Schematization of the DAQ system adopted during the reverse I-V characterization. b) Schematization of the DAQ system adopted during the reverse C-V characterization.

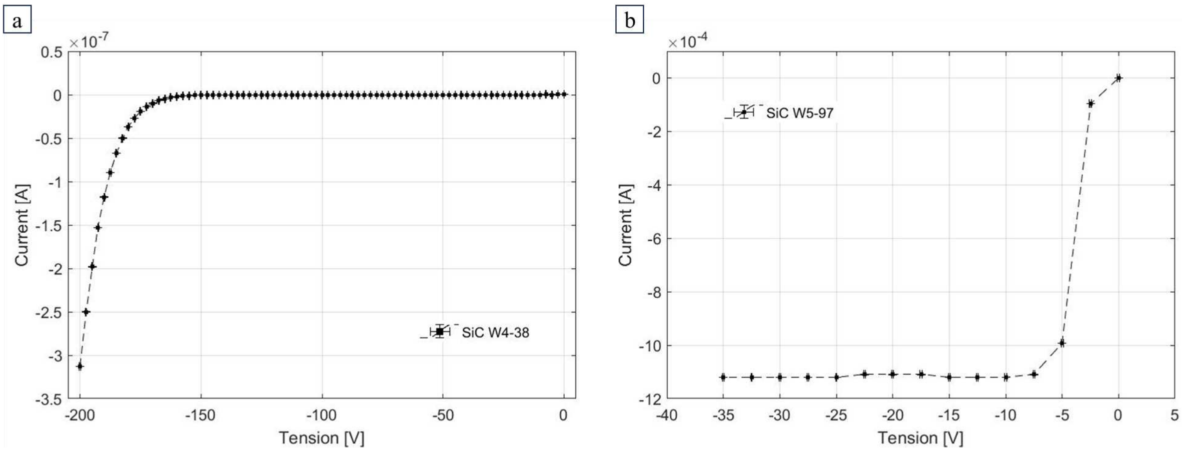

Figure 5.5. a) SiC "W4-38" I-V profile: the trend of the curve conforms to what is expected from a real diode. b) SiC "W5-97" I-V profile: the current stabilizes at -1.1 mA starting from -7.5 V. Error bars are calculated by taking into account the accuracy of the instrument.

Through this characterization, 30 of the initial 80 detectors were rejected. They had I-V profiles different from those characteristic of diodes [322]. Their leakage current reached values on the order of milliamperes with few volts of bias, indicating the presence of structural defects and making them unsuitable for use as particle detectors (Figure 5.5(b)). Due to this, the characterization work proceeded with the remaining 50 SiC devices. The latter exhibits a leakage current <100 pA when reverse biased up to 50 V. Figure 5.6 shows, as an example, the I-V of 10 SiC detectors in the reverse bias voltage range of interest.

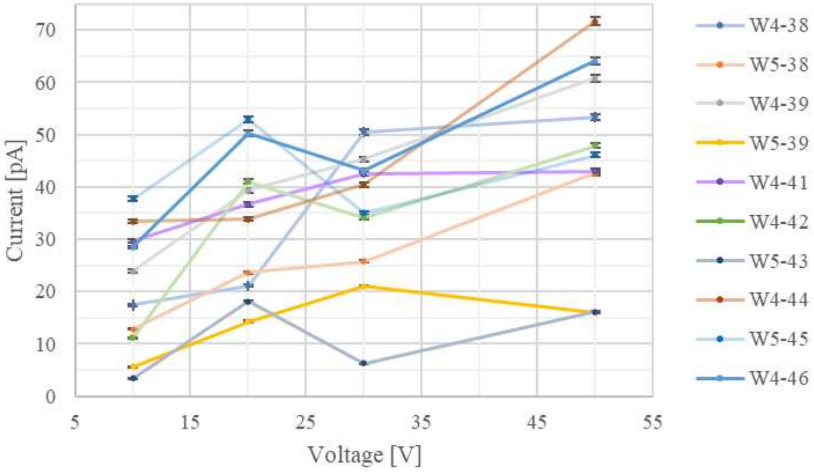

Figure 5.6. I-V of 10 SiC detectors. The current values reported refer to the reverse bias voltage values of interest in the 10-50 V range. Error bars are calculated by taking into account the accuracy of the instrument.

The C-V profile was studied in the reverse bias voltage range of 0–20 V, with a step of 0.25 V. The adopted capacimeter was set to operate at a full scale of 20 nF with a sample rate of 10 kHz and an acquisition time of 2 seconds. Figure 5.7 shows an example of a C-V curve.

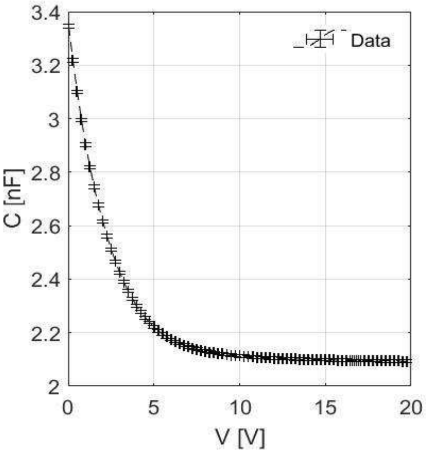

Figure 5.7. C-V profile of SiC W4-39.
Error bars refer to the accuracy of the instruments.

Similar to the experimental cases detailed in the preceding Chapter, this characterization enabled the determination of the following physical quantities for each SiC device.

1. The saturation or junction capacitance (C_s) was experimentally determined as the minimum capacitance value obtained by increasing the reverse bias voltage. Quantifying the saturation capacitance of the junctions is important to properly design the electronic readout chain of the system. Despite being small, junction capacitances can act as parasitic capacitances, causing unexpected signal alterations. This effect can be particularly evident with signals produced by particle beams exhibiting very short temporal dynamics, such as laser-driven ones. The C_s values for the 50 SiC devices range between $C_{s,min}$=2.031 ± 0.004

nF and $C_{s,max}$=2.139 ± 0.005 nF, as reported in Figure 5.8. Here, data are represented by grouping the devices based on the wafer batch (W4 or W5) to more easily highlight any anomalous behaviour attributable to production defects. The experimental values are compared to the theoretical value C_s^{th}, calculated as:

$$C_s^{th} = \frac{A \cdot \varepsilon_s}{W_N} = 1.93\, nF \tag{5.1}$$

where $A = 15 \cdot 15\, mm^2$ is the active area of SiCs, $W_N = 10\ \mu m$ is the nominal value of the thickness of the depletion region, and ε_s is the permittivity of SiC, given by the product between the permittivity of vacuum $\varepsilon_0 = 8.85 \times 10^{-12}\ F/m$ and the relative dielectric constant of SiC, $\varepsilon_r = 9.7$. The results point out a deviation between the experimental values and the theoretical value between 5.2% and 10.8%, while on average no significant difference can be observed between W4 and W5.

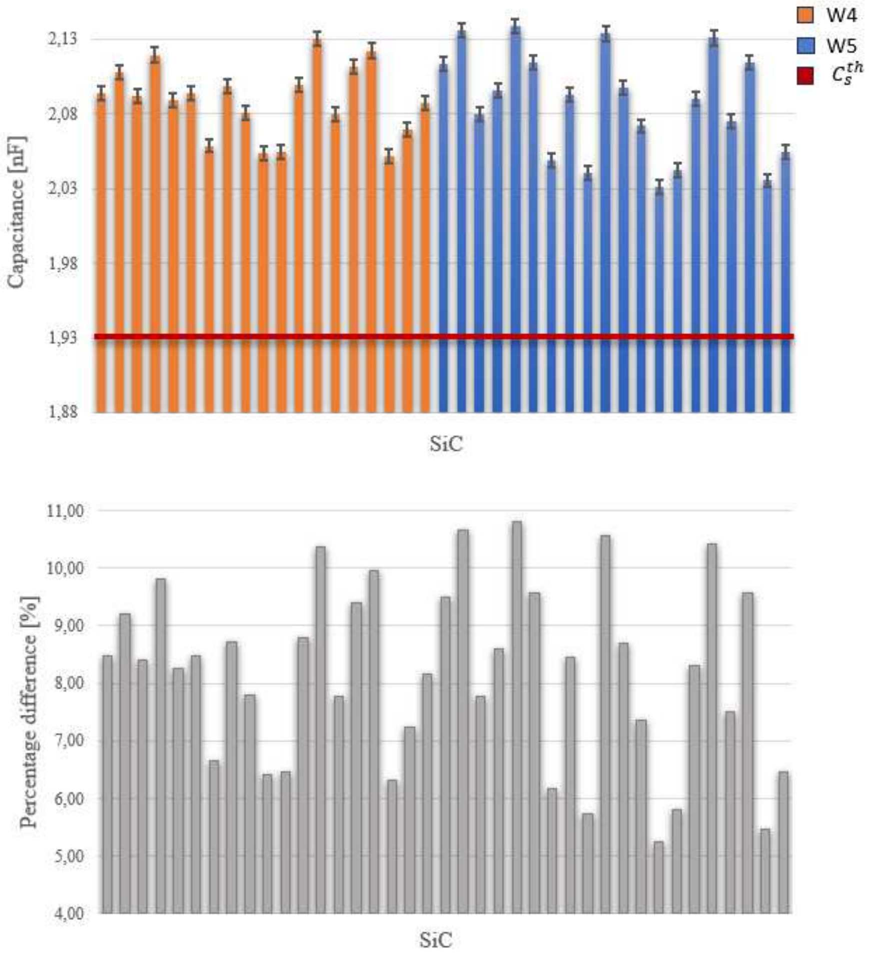

Figure 5.8. Experimental C_s for SiC devices. The order is not important, but it is kept the same between the two graphs. Top panel: SiC saturation capacitance values C_s grouped according to the wafer batch. The expected theoretical value C_s^{th} =1.93 nF is also reported (horizontal red line). The errors were calculated by evaluating the accuracy of the instrument, as suggested by the manufacturer. Bottom panel: percentage difference between the experimental values of C_s and the theoretical value C_s^{th}. It varies in the range 6.3-10.4% for W4 and 5.2-10.8% for W5.

2. The thickness (W) of the depletion region in full depleted conditions was determined. Verifying this quantity's value is crucial for accurately assessing the impact of each device on the reconstruction of the PDD distribution in terms of expected charge produced, beam attenuation, and longitudinal spatial resolution. W was estimated by exploiting the inverse formula of the previous relationship and calculating its value for each detector by using the experimental values obtained for C_s:

$$W = \frac{A \cdot \varepsilon_s}{C_s} \tag{5.2}$$

The results, ranging from W_{min}=9.0±0.1 µm and W_{max}=9.5±0.1 µm, are shown in Figure 5.9. Here, the experimental values are compared to the nominal value W_N. The results point out a deviation between the experimental values and the nominal value between 5% and 10%, while on average no substantial difference can be observed between W4 and W5.

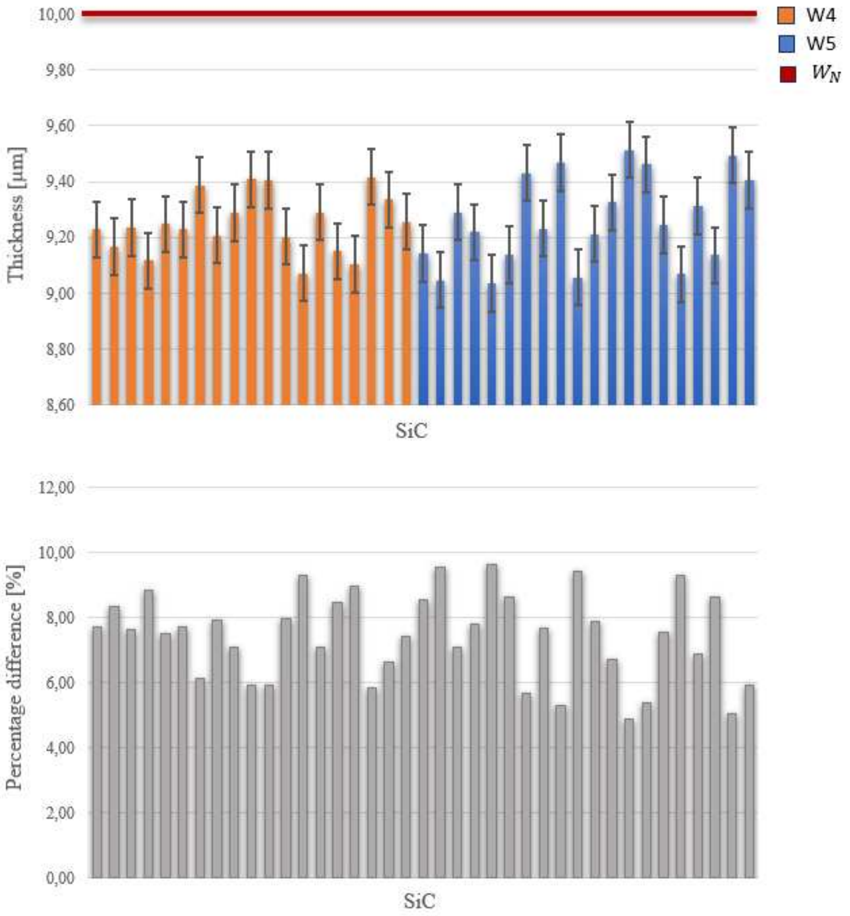

Figure 5.9. Experimental W for SiC devices. The order is not important, but it is kept the same between the two graphs. Top panel: SiC depletion region thickness W values grouped according to the wafer batch. The expected theoretical value W_N =10 µm is also reported (horizontal red line). The errors, calculated by applying the error propagation theory, are of the order of 0.1 µm for all the devices. Bottom panel: percentage difference between the experimental values of W and the theoretical value W_N. It varies in the range 5.8-9.3% for W4 and 4.9-9.6% for W5.

Certainly, a lower depletion region (W) than expected is compatible with the findings related to the experimental saturation capacitance. As demonstrated, the experimental saturation capacitance is greater than the theoretical one by up to 10.8%. Recalculating C_s^{th} using the average value of the thicknesses W found for each device, equal to W_{mean}=9.3 µm, we obtain $C_s^{th'} = 2.09\, nF$, which deviates from the minimum and maximum C_s values measured by less than 3% (Figure 5.10).

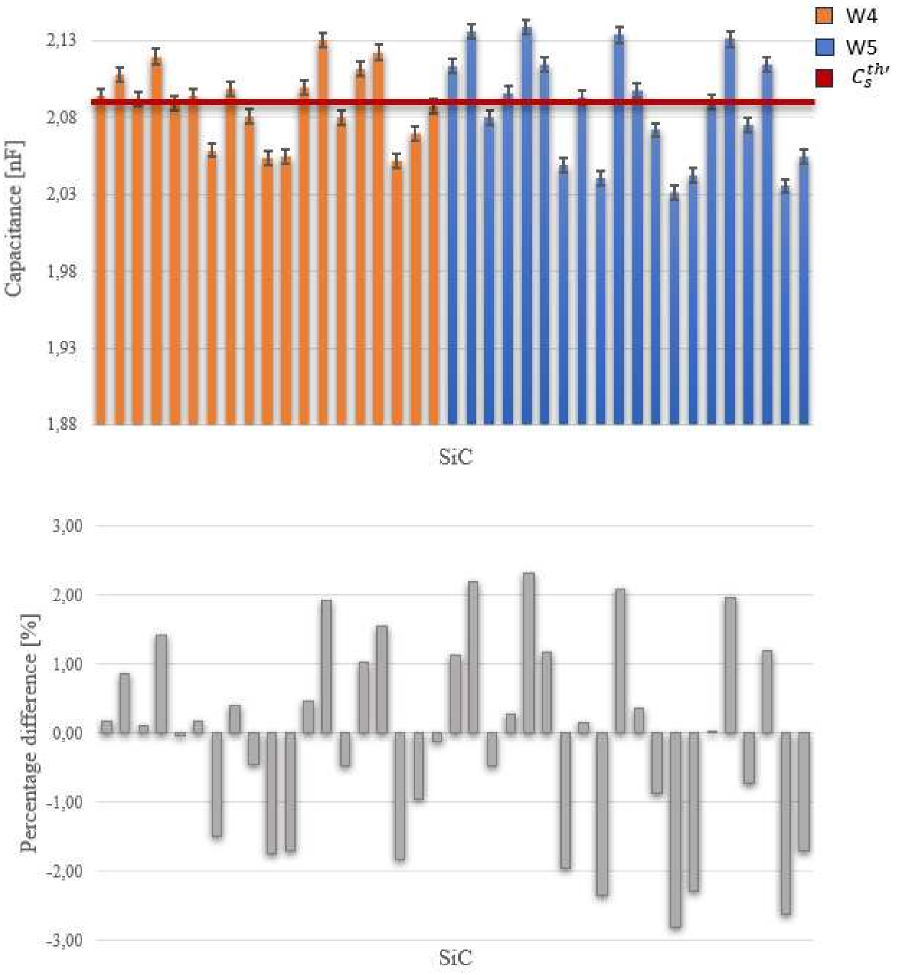

Figure 5.10. Top panel: comparison between the experimental C_s values and the theoretical capacitance value obtained by assuming each SiC as a parallel plate capacitor with active area and thickness A=15x15 mm^2 and W_{mean}=9.3 µm, respectively. Bottom panel: percentage difference between the experimental values of C_s and the theoretical value $C_s^{th'}$. It varies in the range 0.03-1.9% for W4 and 0.01-2.8% for W5.

3. The depletion voltage V_D, the built-in potential V_{bi}, and the donor concentration N_D, determined by applying the intersection method on the $1/C^2$ curve as a function of the applied voltage V. We've seen that for a p^+n junction, as long as the saturation region is not reached (i.e., for $V \leq V_D$), the inverse capacitance squared is a linear function of the applied

reverse-biased voltage, according to the following equation (recalled here for convenience):

$$\frac{1}{C^2} = \frac{2\left(V_{bi}+V\right)}{e\,A^2\,\varepsilon_s\,N_D} \tag{5.3}$$

Ideally, once the full depletion condition is reached, the trend of $1/C^2$ with respect to the voltage settles on a plateau with a constant value equal to C_s. The right panel of Figure 5.11 shows a real example of this behavior. Here, the trend of $1/C^2$ as a function of applied bias has a typical straight trend at low voltages (in the range 0–3 V), while for higher bias, the curve shows a lower slope, until it achieves saturation at approximately 10V.

By applying the best-fit procedure to the two trends of curve $1/C^2$ it is possible to determine:

- V_D, obtained as the voltage value corresponding to the intersection of the two best-fit curves, called Fit1 and Fit2, (see Figure 5.11);
- V_{bi}, by extrapolating the Fit1 curve to the point where $1/C^2=0$;
- N_D, as a function of the slope *m* of the Fit1 curve:

$$N_D = \frac{2}{e\,A^2\,\varepsilon_s\,m} \tag{5.4}$$

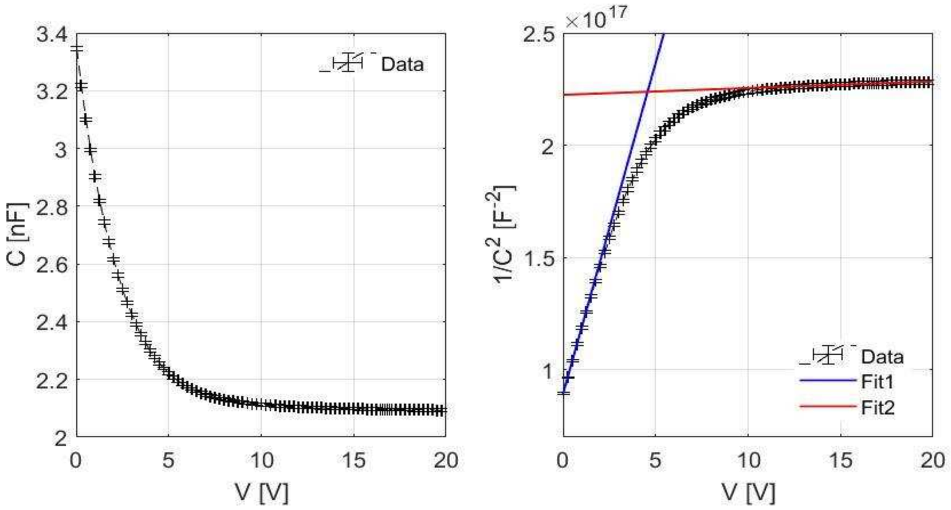

Figure 5.11. C-V profile of SiC W4-39. Left panel: trend of capacitance C *vs.* reverse applied voltage. Right panel: trend of $1/C^2$ *vs.* reverse applied voltage. The linear fits in the low voltage range (Fit1) and in the saturation region (Fit2) are also shown. In this case the depletion voltage obtained was $V_D = 4.7 \pm 0.3$ V, the built-in potential was $V_{bi} = 3.0 \pm 0.1$ V, the donor concentration was $N_D = 1.13\text{x}10^{14} \pm 3.4\text{x}10^{12}$ cm^{-3}, while the saturation capacitance was $C_s = 2.096 \pm 0.005$ nF. The error bars in the figure are obtained taking into account the accuracy of the instruments, while the uncertainties related to the extrapolated quantities are calculated by applying the theory of error propagation.

For the 50 detectors, a depletion voltage V_D ranging from $V_{D,min}$=2 V to $V_{D,max}$=6 V was found by applying this method, as reported in Figure 5.12. Again, by varying the two ranges of the curve on which the fit procedure is performed, a variability up to 0.3 V on the V_D value can be found. This value is comparable to the error bar obtained by propagating the uncertainty on the fit parameters. The experimental values are compared to the theoretical range values of the depletion voltage, defined as:

$$V_D^{th} = N_D \frac{e\,W^2}{2\,\varepsilon_s} = 4.7 - 9.3\,V \tag{5.5}$$

for W=10 μm and N_D = 0.5 - 1 · 10^{14} cm^{-3}. The result obtained for W_{mean}=9.3 μm is instead:

$$V_D^{th'} = 4.0 - 8.0\,V \tag{5.6}$$

and its comparison with experimental data is shown in the bottom panel of Figure 5.12.

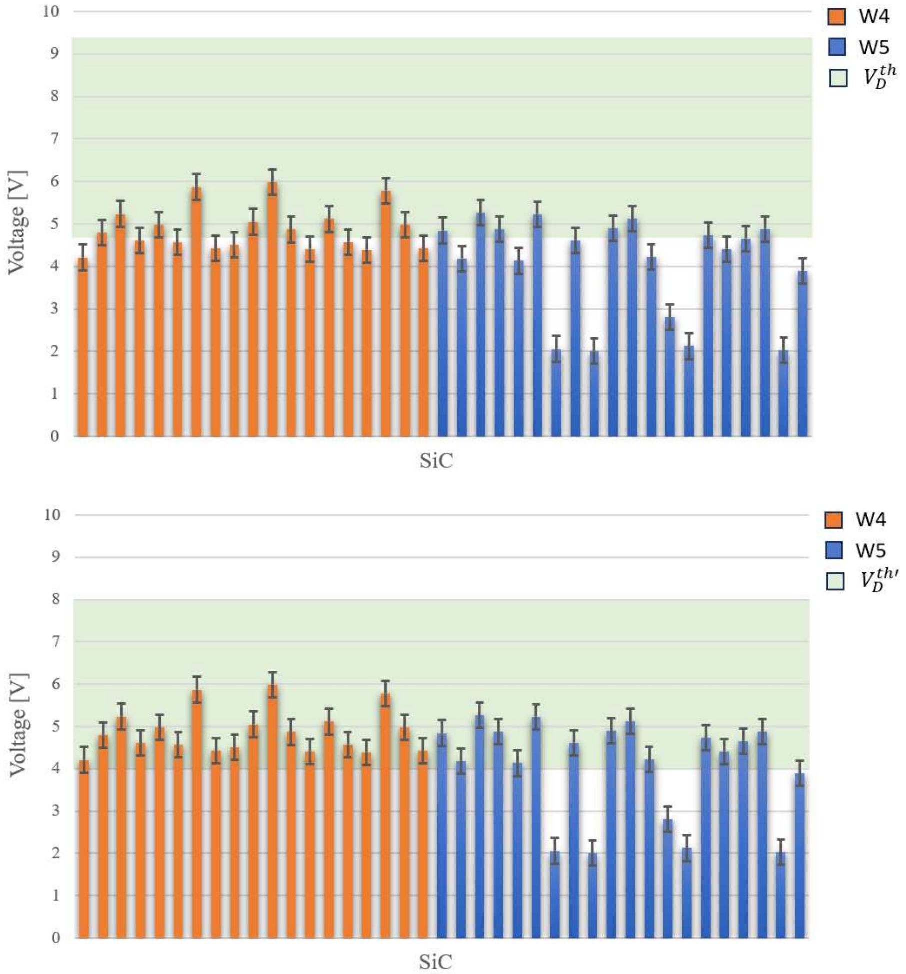

Figure 5.12 SiC depletion voltage values V_D experimentally found through the interception method and grouped according to the wafer batch. The order is not important. The experimental values are compared with the range of theoretically expected values for V_D (light green band), determined considering a dopant

concentration varying in the range N_D = 0.5 - 1 · 10^{14} cm^{-3} and depletion region thickness equal to (top panel) W_N =10 µm and (bottom panel) W_{mean}=9.3 µm.

Unlike C_s and W experimental values, a distinction in the performance of the devices belonging to W4 and W5 is detected for the values of V_D. In fact, in 25% of cases, W5 devices present a V_D significantly different (up to three times higher) from the other SiC detectors belonging to the same batch, while W4 devices present similar characteristics. Excluding these specific cases, it can be observed that all the experimental data fall within the $V_D^{th'}$ range within the experimental errors, even if they remain concentrated on the lower limit of the latter (Figure 5.12, bottom panel). On the contrary, the comparison between experimental data and V_D^{th} fails in ~50% of cases.

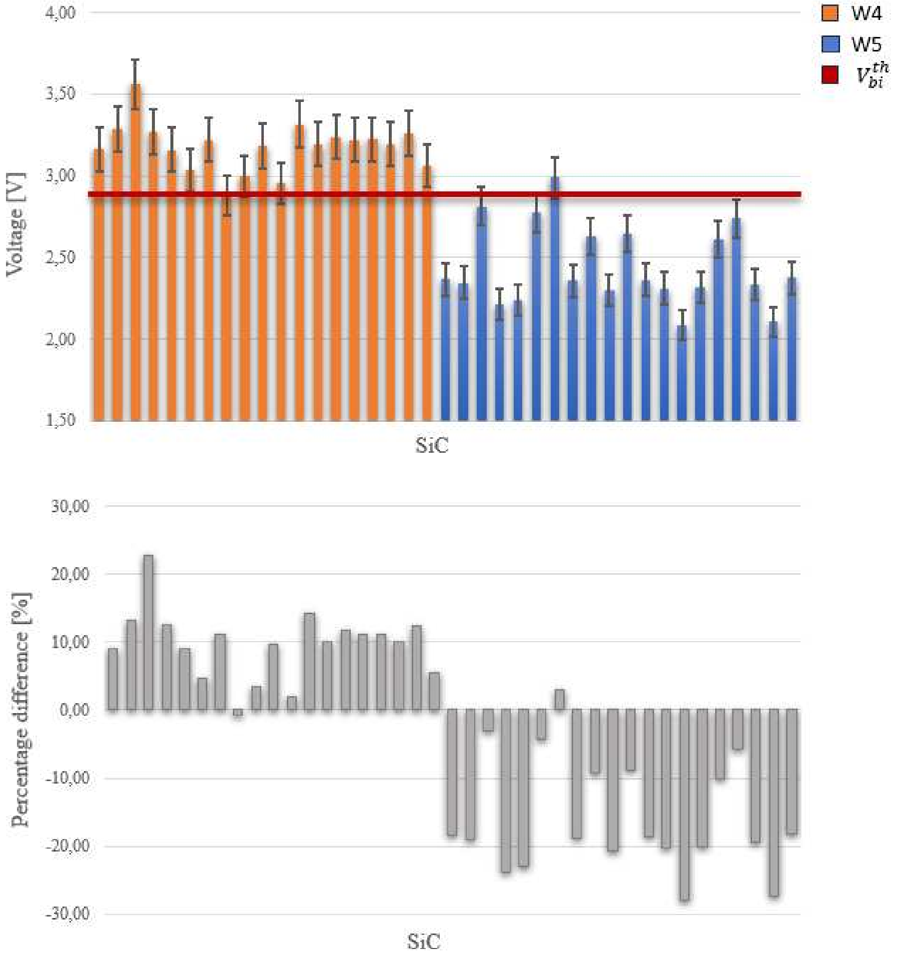

Figure 5.13 SiC built-in voltage values V_{bi} experimentally found through a best-fit procedure applied to the C-V profile and grouped according to the wafer batch. The order is not important, but it is kept the same between the two graphs. Top panel: comparison between experimental V_{bi} and expected theoretical value $V_{bi}^{th} = 2.9\,V$. The error bars in the figure are calculated by applying the theory of error propagation. Bottom panel: percentage difference between the experimental values of V_{bi} and the theoretical value V_{bi}^{th}. It varies in the range 0.8-22.9% for W4 and 3-28% for W5.

The built-in potential values found for the 50 SiC devices range between $V_{bi,min}$=2.1±0.1 V and $V_{bi,max}$=3.6±0.1 V and are reported in Figure 5.13. Here, the comparison with the expected theoretical value V_{bi}^{th} is reported, where the latter is evaluated as:

$$V_{bi}^{th} = \frac{kT}{e} \cdot ln\left(\frac{N_A \cdot N_D}{n_i^2}\right) = 2.9\,V \tag{5.7}$$

The results indicate a deviation between the experimental values and the nominal value ranging from 1% to 14% (with only one case reaching 23%) for SiC devices from wafer batch W4, while a deviation between 3% and 28% is observed for SiC devices from wafer batch W5. Furthermore, for SiC W4 and W5, a built-in potential that is consistently higher and lower than the theoretical one is observed, respectively.

Finally, the donor concentration N_D was experimentally determined. The obtained results compared with the nominal range value $N_D = 0.5 - 1 \cdot 10^{14}$ cm^{-3} are reported in Figure 5.14. In 20% of cases, the values found are outside the theoretical range. In general, a different average trend can be observed for SiC W4 and W5. The W4 devices exhibit a comparable concentration value (within experimental errors), distributed around the maximum value of the theoretical prediction. On the other hand, the W5 devices have a different concentration value (within experimental errors), generally distributed within the theoretical range. This aligns with the previous findings, as this method relies on the slope of the Fit1 curve, on whose parameters the extrapolation of V_{bi} and V_D also depends.

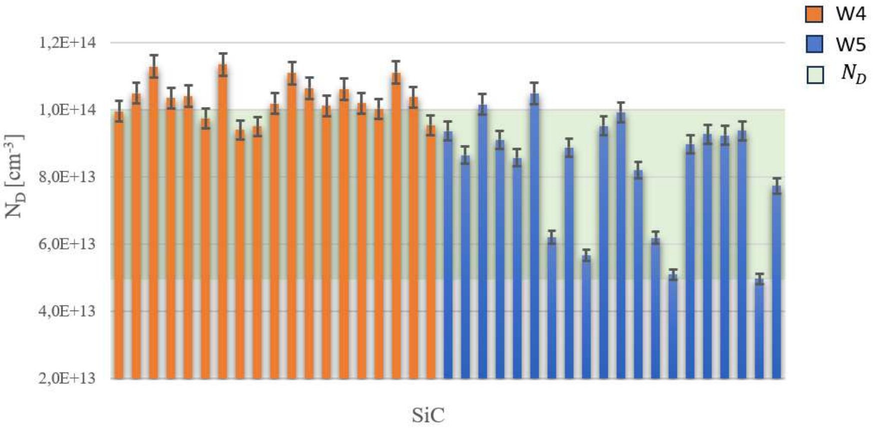

Figure 5.14 Donor concentration values of SiC devices experimentally determined and grouped according to the wafer batch. The order is not important. Comparison with the expected theoretical range $N_D = 0.5 - 1 \cdot 10^{14}$ cm^{-3} is also reported. The error bars in the figure are calculated by applying the theory of error propagation.

The assumptions employed in deriving the previous quantities include uniform doping in both semiconductor regions [322]. The discrepancy between the experimental data and the expected values can be attributed to a non-uniformity of the dopant concentration. For this reason, this possibility was explored by analyzing the dopant concentration profile along the active thickness of the material. As described in Section 4.5.2, using the relation (4.5) and replacing C with the experimental values C(V), it is possible to indirectly calculate the thickness of the depletion region W(V) as the voltage varies. Determined W(V), the relationship (4.12) was used to study the trend of N_D as a function of V and W(V), by replacing V_{bi} with the values obtained experimentally. In Figure 5.15 an example of the trend thus obtained for W(V) and N_D(W,V) is reported.

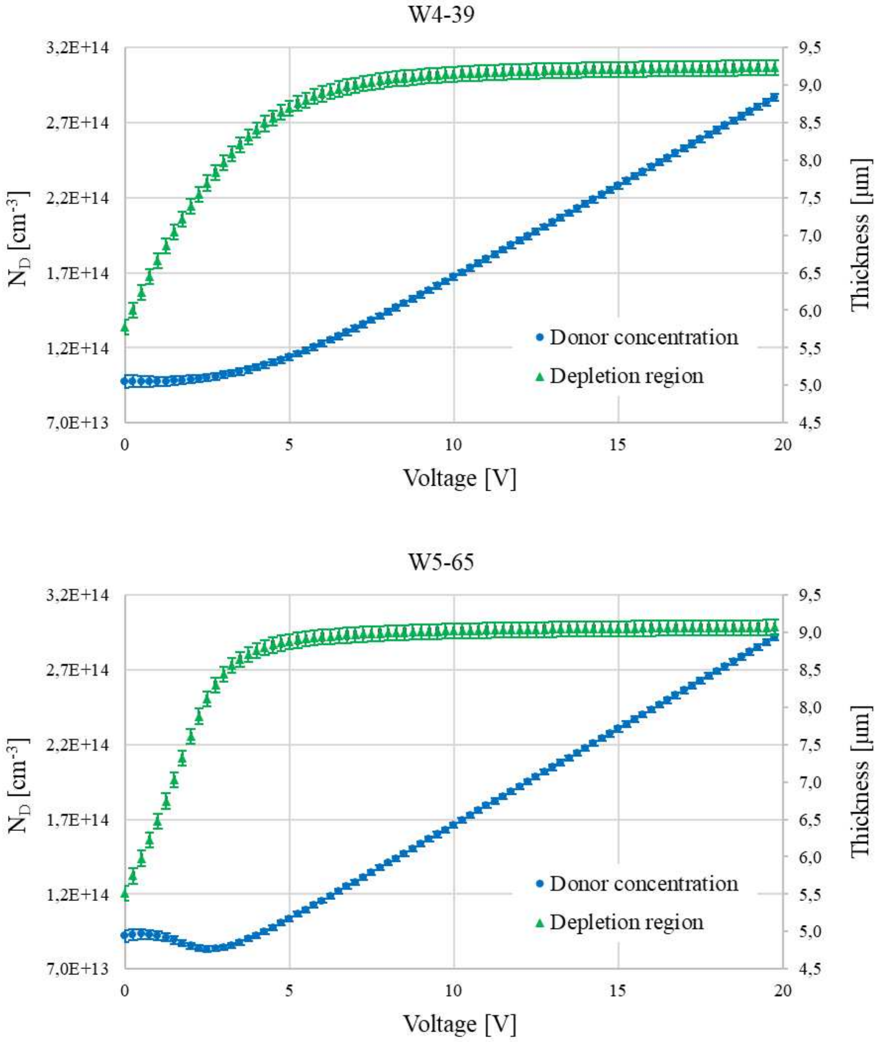

Figure 5.15 Examples of the trend of N_D and W as the reverse bias voltage applied varies for two SiCs. The error bars are evaluated by applying error propagation. In both cases it would appear that the linear trend begins approximately at 5V for N_D (blue lines).

To establish up to which voltage the trend obtained for N_D(W, V) by applying the equation (4.12) can be considered valid for the description of the experimental data, the threshold method was applied. The voltage thus found represents an estimate of the depletion voltage V^{th}_D value with better accuracy and precision than the intersection approach.

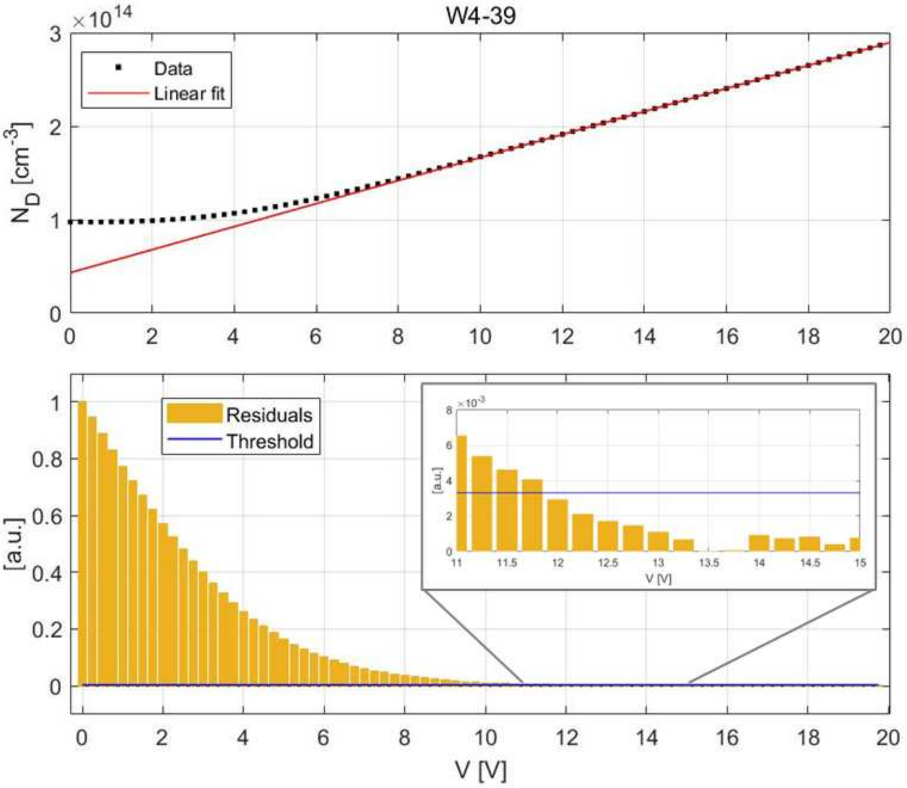

Figure 5.16 Top panel: trend of N_D as a function of V for SiC W4-39. The linear function *f(x)* obtained through the best fit procedure is also shown. Bottom panel: residual values, calculated between the "Linear fit" function *f(x)* and the data, and threshold line are reported. For convenience the absolute value of the residuals normalized with respect to the maximum value were considered. The threshold line was normalized as well. The insertion shows an enlargement of the bottom panel, in which the first residual (and the corresponding voltage) that exceeds the threshold can be observed.

Precisely, the trend of $N_D(W,V)$ as a function of V was initially investigated (Figure 5.16). Through a best-fit procedure applied on the data belonging to the 15-20 V voltage range (where W varies overall by a few hundredths of a μm), the linear function *f(x)* that describes the experimental trend of $N_D(W,V)$ at the invalidity voltages (i.e., for $V>V^{th}_D$) was found ($r^2 \simeq 1$ is found in all cases). Defined the best-fit function *f(x)*, the calculation of residuals (for data belonging to the 15-20 V range) and of Root Mean Square Error (RMSE, σ) was performed. The resulting threshold t, defined as follows:

$$t = \bar{r} \pm 3\sigma \tag{5.8}$$

contains 99.7% of the residuals calculated for the N_D values belonging to the linear trend, considering a Gaussian distribution centered on the average value of the residuals $\bar{r}$ (approaching 0) and with a standard deviation σ equal to RMSE. Subsequently, the residuals r_i (with i=1, ..., N, so that r_1 refers to the N_D value corresponding to 0V and r_N

refers to the N_D value corresponding to 20V) were calculated, with respect to *f(x)*, for all the N experimental data, and were compared to t: the last value of r_i that exceeds the threshold t was chosen to estimate V^{th}_D with an uncertainty of 0.3%. This procedure was executed for each SiC. Figure 5.17 illustrates the trend obtained for some devices.

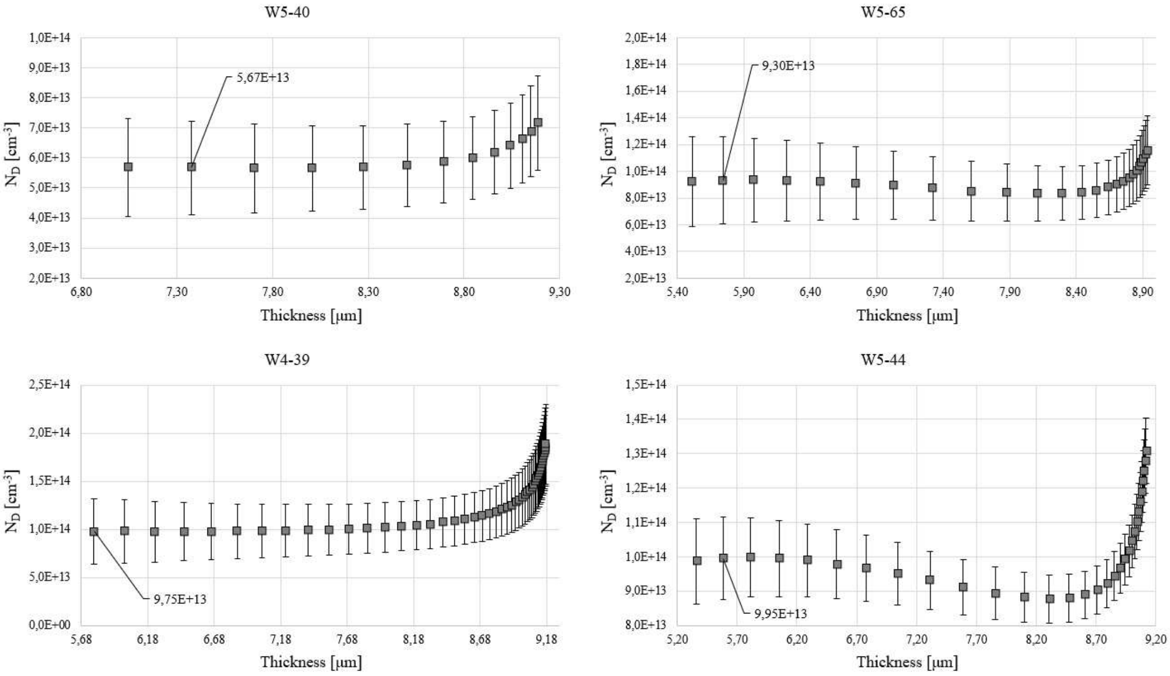

Figure 5.17 The N_D dopant concentration profile is shown for four different SiCs. The concentration value determined using the intercept method is also reported. The voltage corresponding to the maximum values W shown in the figures was established using the threshold method (5.8). It was found $V_{W4\text{-}39}$=11.75 V, $V_{W5\text{-}65}$=6V, $V_{W5\text{-}40}$=3V, $V_{W5\text{-}44}$=7.5V, all larger (up to 3 times) than the corresponding V_D found with the intercept method. The error bars are calculated through the propagation of the errors associated with all the quantities involved.

The results obtained show that this method improves the estimate of the depletion voltage of the devices, which appears systematically up to three times larger than that obtained with the intercept method, consistently with what was expected. The thickness of the depletion region corresponding to these voltage values is comparable with the experimental values obtained via (5.2). Regarding the dopant concentration, in some cases profiles compliant with what was expected are observed (i.e., they are constant and at values belonging to the theoretical range, within the associated error bars), while other times the presence of a non-uniform concentration along W or outside the nominal range was found. The threshold method should be further explored to see how the results obtained change by varying the interval on which the linear fit procedure is carried out and associating an error to the voltage obtained.

5.2.3 Linearity and stability

Linearity and stability tests were carried out by irradiating the SiCs detectors in air with an X-ray beam. Experimental tests were conducted at the Industrial Engineering Department of the University of Rome “Tor Vergata” (Rome, Italy). As an X-ray source, a copper target X-ray tube (Ital Structures Compact 3K5 X-ray Generator) was used, which emits characteristic X-rays mainly at $E_{K\alpha}$=8.0 keV and $E_{K\beta}$=8.9 keV [340, 341]. A scheme of the adopted experimental setup is reported in Figure 5.18.

The distance between the X-ray tube and detectors was approximately 15 cm, ensuring uniform irradiation of the active detector area. A plastic collimator (1 cm diameter) was used to shield the beam. During X-ray irradiation, the measurement of the current produced by the detectors and their polarization was again performed through the KEITHLEY 6517B. All the characterization was performed by applying a reverse bias voltage of 30 V to the p-type SiC layer while earthing the metallic contact. Data acquisition was realized employing a LabVIEW program routine designed to measure the I-t (current *vs*. time) curve. In particular, the response of the detectors was acquired by varying both the current and the energy cutoff of the beam.

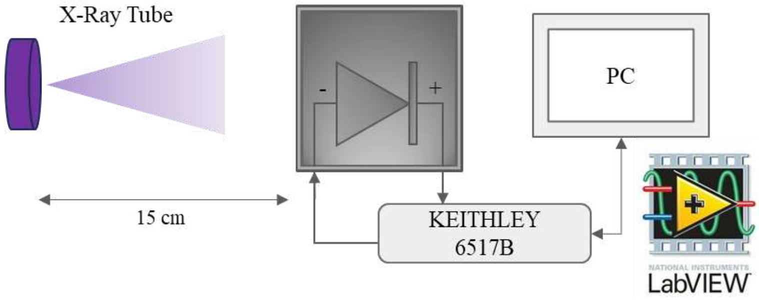

Figure 5.18 Schematization of theDAQ system used during X-Ray irradiation of SiC devices.

The linearity of the response of the devices was studied as the beam current varied. In particular, the X-ray tube acceleration voltage was set to 10 kV, while the X-ray tube current was varied in the range between 2.5 mA and 15 mA (in steps of 2.5 mA). For each SiC detector, the leakage current and the under-beam current (i.e., the current produced when subjected to irradiation) were acquired. The latter, in particular, was measured for an interval of 20 s for each X-ray tube current, setting a full scale of 200 nA and a sampling rate of 3Hz. Figure 5.19 shows the current signal thus obtained for one of the detectors chosen as an example.

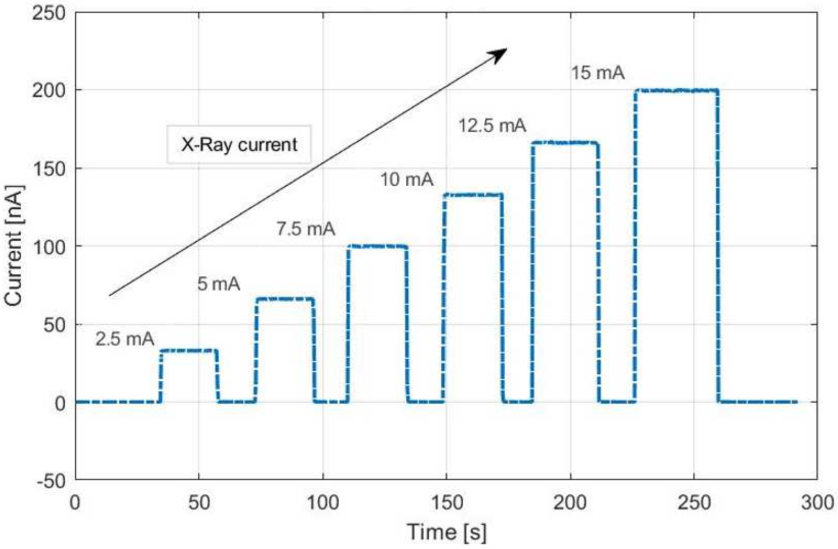

Figure 5.19 Example of the trend of the current produced by the detectors when subjected to the linearity test, varying the current of the incident beam.

For each signal (background or under-beam) the average current value and the standard deviation of the fluctuations were evaluated. The trend of the net signals (i.e., with the background subtracted) was then studied as the X-ray tube current varied (Figure 5.20(a)). A best-fit procedure was performed to evaluate the linear trend, resulting in an r^2 value very close to one for all the detectors. To better emphasize any deviation from the linear trend, the percentage deviation from linearity was evaluated as $\left(I_{measured}/I_{fit} - 1\right) \times 100$ (Figure 5.20(b)). The maximum percentage deviation was found to be up to 0.5% for 56% of detectors, up to 1% for 29% of detectors and up to 1.5% for 15% of detectors, indicating a high level of the response reproducibility in these experimental conditions. Good linearity is a crucial and beneficial feature, as the response function of the detector to different levels of incident radiation is described by a single constant of proportionality.

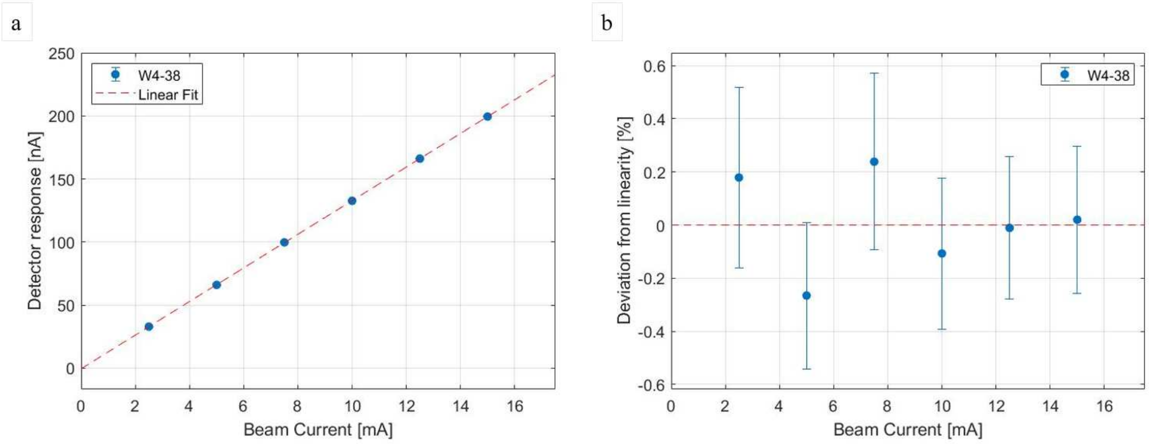

Figure 5.20 Linearity test for a SiC device. The error bars were evaluated taking into account the accuracy of the instrument and the causal oscillations, propagated according to the theory of error propagation. The relative error on the individual average values does not exceed 0.4% a) Detector response plotted against the X-Ray tube current. The best fit curve is also reported. b) Percentage deviation from linearity.

The slope of the best-fit line is a dimensionless quantity proportional to the sensitivity of the detectors, typically expressed in terms of charge collected over the absorbed dose (in nC/Gy). Extrapolating the angular coefficients of the best-fit lines and normalizing them to the minimum value it was possible to evaluate the relative detectors sensitivity (see Figure 5.21). In the adopted experimental conditions, the detectors demonstrate a very similar relative sensitivity, with a response that at most are less than 1.06 times apart.

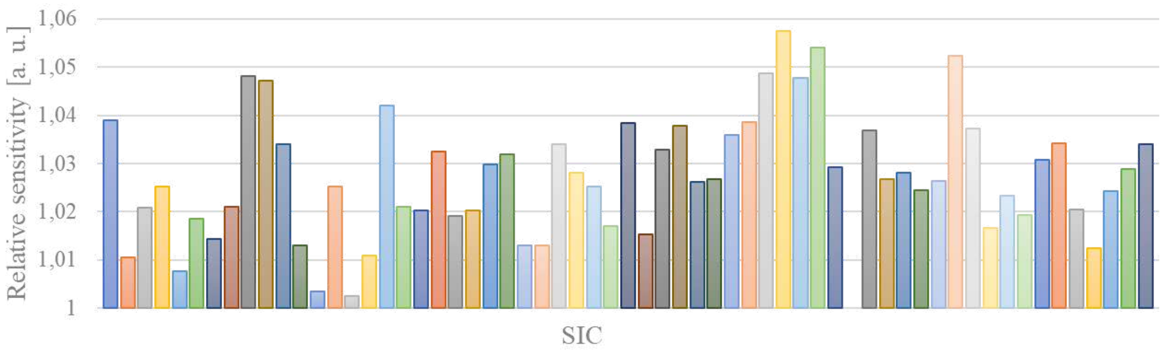

Figure 5.21 Relative sensitivity of SiC devices. The order is not important.

The stability property characterizes the detector's capability to maintain its response function constant over time when exposed to irradiation, with the measurement conditions unchanged. This property was studied by subjecting the detectors to prolonged irradiation sessions, with durations comparable to clinical treatments, and evaluating the oscillations in their current response. In particular, the measurement conditions were kept similar to those described for the linearity test, setting the current and acceleration voltage of the tube at 5 mA and 10 kV respectively. The response of the detectors was acquired for 60 s during their irradiation.

To evaluate the oscillations of the current signals and ascertain that they were oscillations attributable to randomness, a Gaussian fit on the distribution of the current values was carried out, extrapolating the average value μ (~65.5-70.5 nA) and the standard deviation σ (~0.1-0.3 nA), and performing a Chi-Square Goodness-of-Fit Test. The latter was used to determine whether the data comes from a normal probability distribution (with parameters μ and σ), grouping the data into N bins, calculating the observed O_i and expected E_i counts for those bins based on the hypothesized distribution, and computing the *chi-square* test statistic:

$$\chi^2 = \sum_{i=1}^{N} \frac{\left(O_i - E_i\right)^2}{E_i} \tag{5.9}$$

χ^2 is often expressed in terms of *reduced chi-square*, defined as chi-square per degree of freedom df=N-1-ν, χ^2/df, where ν is is the number of estimated parameters used to determine the expected counts. The results obtained with the test always accept the null hypothesis (of belonging to the hypothesized distribution) at a significance level α=1%.

Figure 5.22 shows the results of the *chi-square* test and the current signals produced by a SiC detector under irradiation.

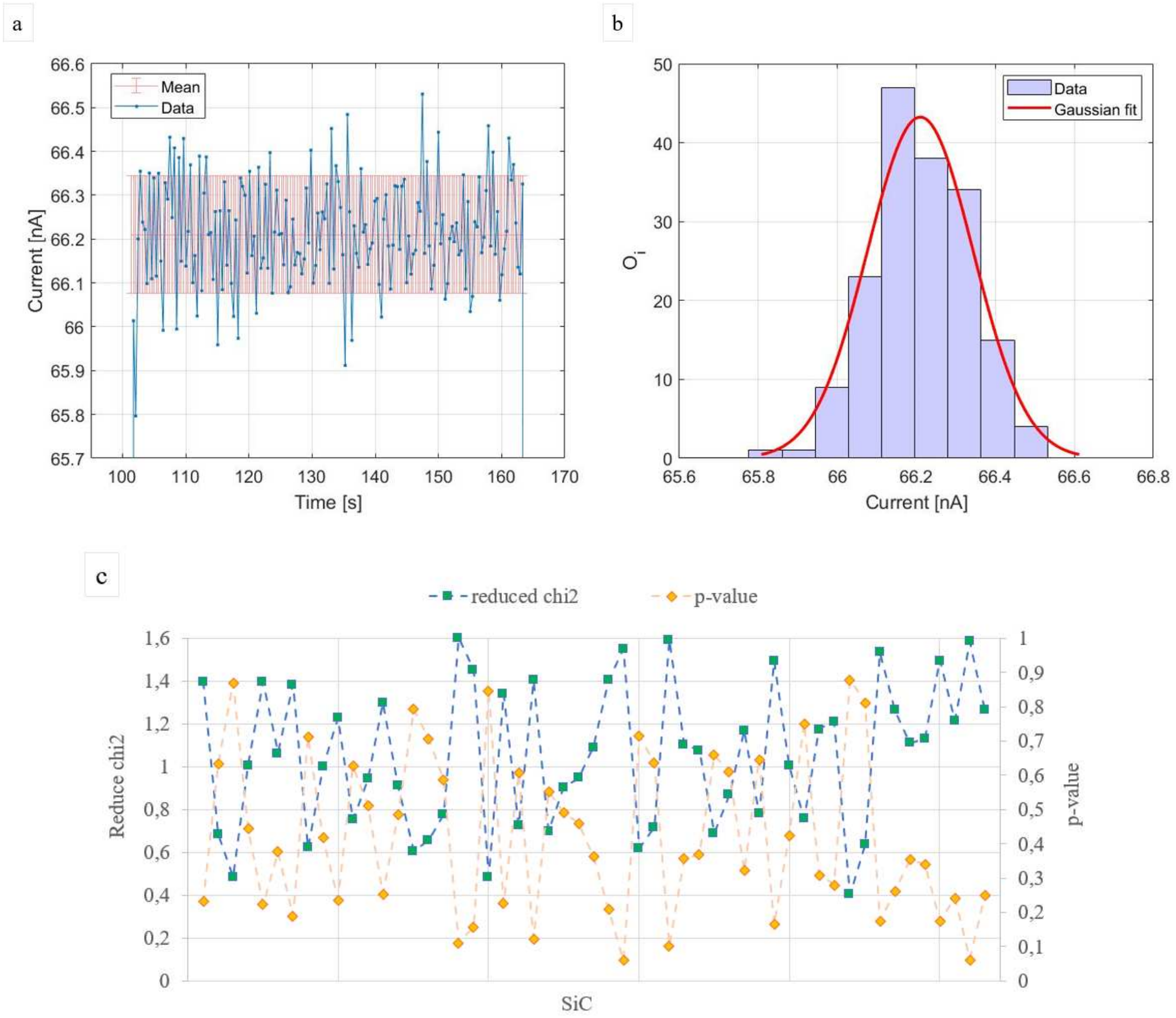

Figure 5.22 Stability test for SiC W4-38. a) Current signal produced by the device when subjected to X-ray irradiation. The pink band represents the range μ±σ=66.2±0.1 nA. b) Histogram of current values; the Gaussian fit is also reported. In this case χ^2/df=0.7, p-value=0.6. c) Reduced chi2 and p-values obtained for each detector.

Here, the μ±σ band, in which 63.8% of the oscillations are located, is highlighted. For all detectors, σ takes values less than 0.5% compared to μ, demonstrating a great level of stability under these experimental conditions. In Figure 5.23 the net mean values of the current read by each detector are compared.

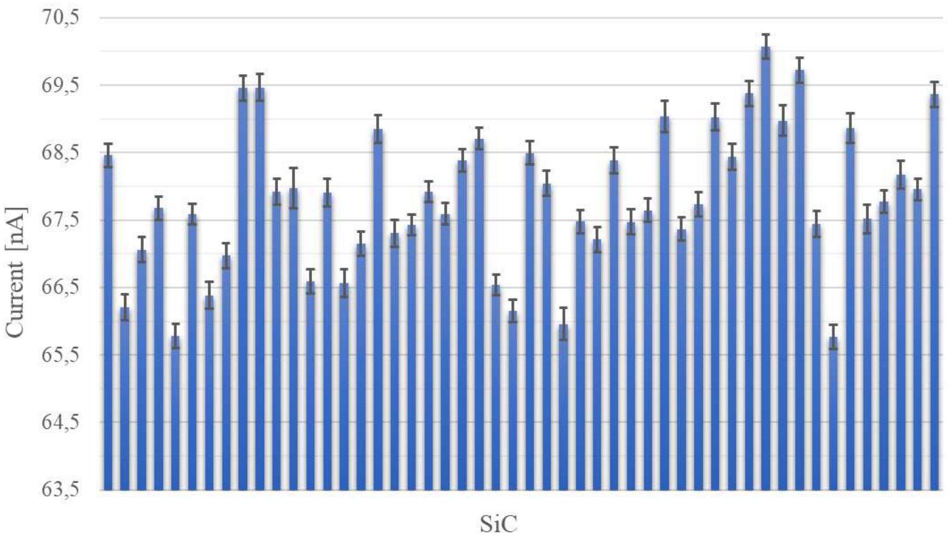

Figure 5.23 Average net current values (with background subtracted) for each detector placed in the same experimental conditions. They range from ~65.5 nA to ~70 nA. The error bars (~0.2-0.4 nA) were evaluated taking into account the accuracy of the instrument (~0.1 nA) and the causal oscillations (σ≃0.1-0.3 nA).

5.2.4 Charge collection efficiency

Junction detectors are normally operated with a reverse bias voltage large enough to work in a full depletion condition. Once the device is fully discharged, a further increase in the applied voltage simply results in a constant increase in the electric field at any point on the wafer. Under these conditions, the detector is said to be over-depleted [43]. At voltages much larger than the depletion voltage, the electric field tends to become more nearly uniform across the entire wafer thickness. The migration of the electrons and holes generated by the incident radiation across the active volume of the detector becomes faster, minimizing the probability of recombination and trapping. As a consequence, an over-depleted device has a better CCE. CCE is defined as the detected Q to generated by radiation Q_0 charge ratio:

$$CCE = \frac{Q}{Q_0}, \quad \text{with} \quad Q_0 = e \cdot \frac{\Delta E}{\varepsilon_{SiC}} \tag{5.10}$$

where e is the elementary charge, ΔE is the particle energy loss in the active layer of the detector and $\varepsilon_{SiC} = 7.78\, eV$ is the e–h pair creation energy in SiC. CCE is usually analyzed through spectroscopic measurements and can allow the verification of the presence of charge-trapping centers and estimation of their concentration. Furthermore, by using different types of radiation, CCE offers the possibility of calculating the carrier mean-free drift length for both the charge carriers [264, 267, 253].

In the context of this work and the final application of the entire device, the investigation of the CCE of SiCs was conducted by measuring their I-V curve during their irradiation with a photon beam, characterized by a fluence comparable to that of clinical beams. The irradiations were performed in the same experimental condition described in Section 5.2.3, but fixing the X-Ray tube parameters. In particular, X-ray tube acceleration voltage was set to 10 kV, while the X-ray tube current was set to 5 mA. The current produced by the detectors when subjected to irradiation was acquired for an interval of 20 s (setting a full scale 200 nA and a sampling rate of 3Hz) at voltage values between 0 and 40 V.

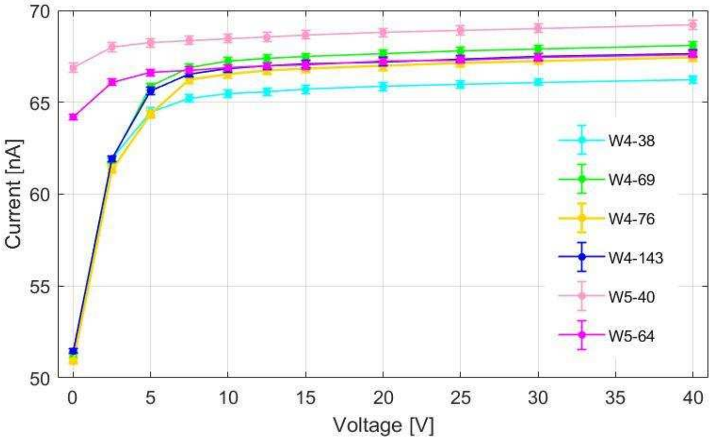

Figure 5.24 Net current produced by different SiC devices when subjected to X-ray irradiation as the reverse bias voltage varies. The error bars (~0.2 nA) were evaluated taking into account the accuracy of the instrument and the causal oscillations, propagated according to the theory of error propagation.

For each detector, the background signal was also acquired, again for approximately 20 s. For each signal (background or under beam) the average current value and the standard deviation of the fluctuations were evaluated. The trend of the net current signals (i.e., with the background subtracted) was then studied as the applied depletion voltage varied (see Figure 5.24). In general, the performance of the detectors - in terms of gradual increase in charge collection - is similar above 10 V (Figure 5.25), where the current produced increases by a few percentages between two consecutive voltage values (around 0.2%), while it differs at voltages close to zero (the percentage variation in current observed between 0 and 2.5 V takes on values ranging from 1% to 17%). Radiation sensitivity is observed also at zero voltage (i.e., in the presence of only V_{bi}), a desirable feature for applications in in-vivo dosimetry, for example. Figure 5.26 shows the trend of the current variation recorded in the devices normalized for the corresponding applied voltage increase, $\Delta I/\Delta V$. In the range between 30 V and 40 V, $\Delta I/\Delta V$ takes on values of the order of 0.01 nA/V, sufficiently small to be considered negligible in terms of a further appreciable increase in CCE. The minimum voltage at which a maximum CCE is reached is therefore considered to be 30 V.

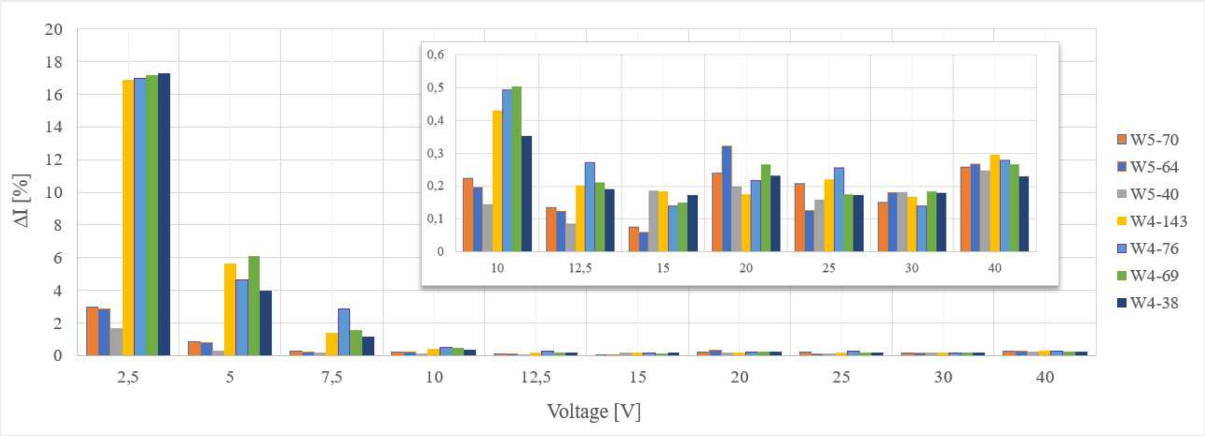

Figure 5.25. Percentage increase suffered by the current produced by different SiC detectors between two consecutive values of polarization voltage. The current variation is calculated with respect to the measurement point with the highest voltage, $I(V_{final})-I(V_{initial})$, and is referred to as V_{final}. The insertion shows a zoom of the values referring to voltages between 10 and 40V.

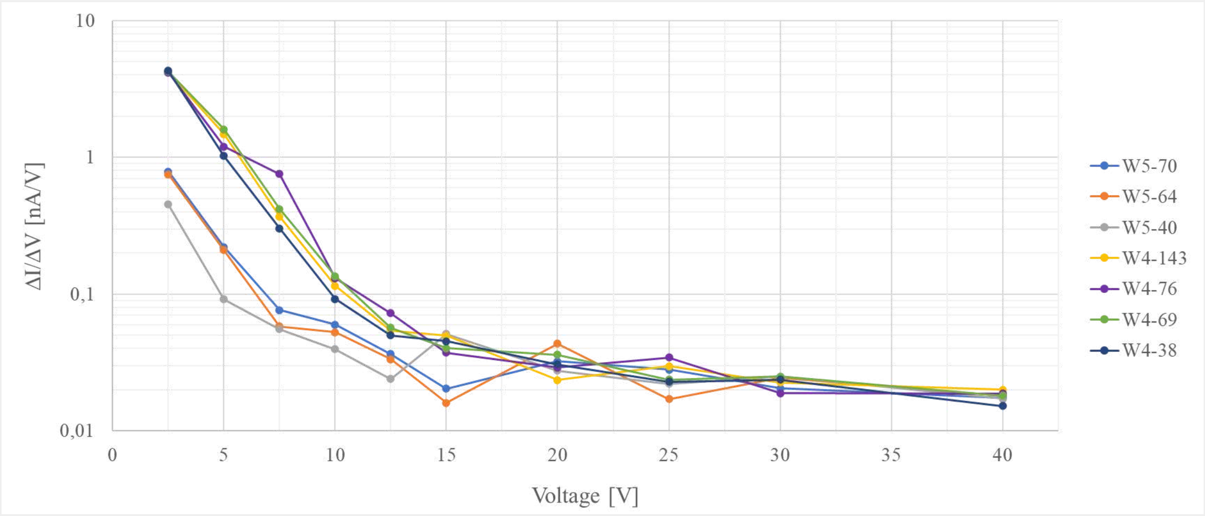

Figure 5.26. Logarithmic scale trend of the current increase relative to the corresponding potential variation, $\Delta I/\Delta V$, where $\Delta I=I(V_{final})-I(V_{initial})$ and $\Delta V=V_{final}-V_{initial}$, for various SiC devices.

5.3 Electronic readout of PRAGUE detector

The electronics read-out for the PRAGUE detector is based on a 64-channel ASIC (Application-Specified Integrated Circuit) chip, designed with a 0.35 µm CMOS (Complementary Metal-Oxide Semiconductor) technology, which features for each channel an independent current-to-frequency/charge-to-count converter followed by a 32-bit synchronous up/down counter. The chip, called TERA08, was developed by the INFN-Torino group and commercialized by the DET.EC.TOR. Srl company [342]. In Figure 5.27 a picture of the chip mounted on its front-end board (called *TERA Board*) is reported. Tailored for beam monitoring in particle radiation therapy, it has been designed to read the data collected by integral and/or segmented ionization chambers and range detectors [199]. However, high beam intensities may lead to an input current above the saturation level allowed for a single channel and a modification of the TERA08 is needed. Each of the 60 SiC detectors of PRAGUE will be read through one of the independent channels of the TERA08: here, a conversion from the input current to a digital pulse frequency (i.e a counting frequency) is performed, where each pulse (count) corresponds to a given charge value (called *quantum charge*) previously set by the user. In this way, it is possible to measure the charge collected by each SiC after irradiation by counting the number of pulses on each channel of the converter. To avoid loss of efficiency in charge measurement with high-intensity beams, a customized interface board between the detectors and the TERA08 is being developed.

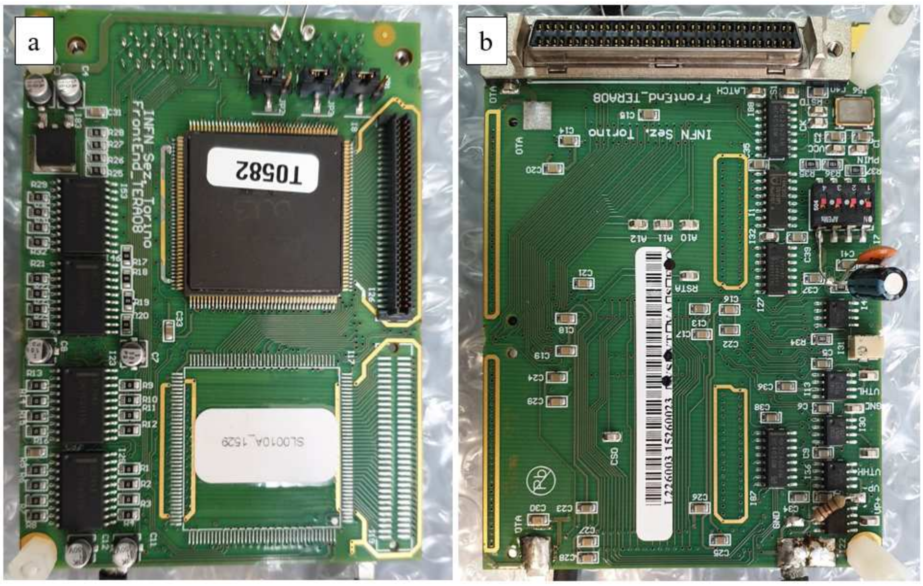

Figure 5.27 TERA08 chip mounted on the TERA Board. The board is supplied by a voltage of 6 V and is designed to host 2 chips. We will use just one. a) Front side. b) Back side.

In particular, the front-end electronics comprehends three PCBs in addition to the PCB where the TERA08 is housed:

1. the first one, called *PRAGUE SiC PCB Board*, is dedicated to housing the SiC devices of the PRAGUE detector; in its first version, it is designed to accommodate 50 devices;

2. the second one, called *PRAGUE TERA Plugin Board*, is designed to allow the connection between the PRAGUE SiC PCB Board and TERA Board, and together with the first one, contains the modification necessary to overcome TERA08 saturation limits;
3. the third one, called *TERA SCSI-VHDCI*, is designed to connect the chassis input/output modules to the TERA08 chip. The board was purchased by the DET.EC.TOR. company.

The Data Acquisition (DAQ) system is augmented by the National Instruments (NI) PXI unit and LabVIEW software. The charge collected from the SiCs is read out through the TERA08 chip, which transmits the digitized signals to the NI PXI crate. The PXI system used for the DAQ is composed of the NI PXIe-1071 chassis [343], equipped with the NI PXIe-8821 controller [344], and the NI PXIe-7821R module [345], where a Field Programmable Gate Array (FPGA, Kintex-7 160T type) is housed (Figure 5.28). The NI PXIe-7821R provides connections for 128 digital input/output (DIO) channels via 4 VHDCI connectors. The VHDCI are used to link the controls and data between the front-end electronics and the NI system. Programming the FPGA through LabVIEW, the system provides high-performance I/O and user-defined hardware processing on the PXI platform. It will be possible to configure the acquisition system to enable features such as customized triggering, control over the synchronization and timing of all signals and operations, as well as to allow differentiated acquisition of signals (by setting the TERA08 parameters, for example), their online processing and visualization. Figure 5.29 illustrates a schematization of the DAQ system of PRAGUE.

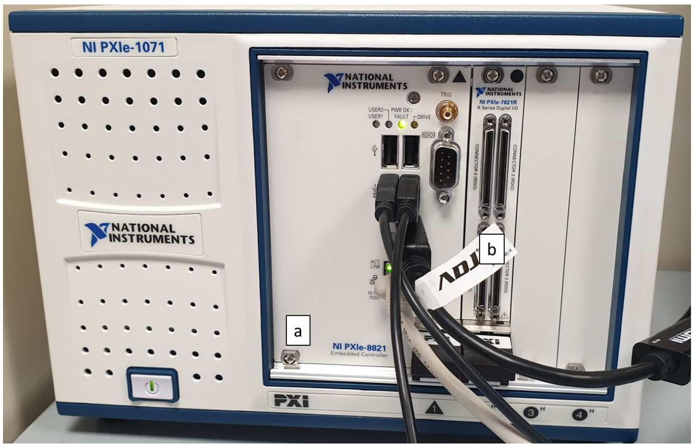

Figure 5.28 NI PXIe-1071 chassis a) The PXIe-8821 has an Intel® Core™ i3 4110E processor (2.6 GHz dual-core processor), all the standard I/O, and a 320 GB (or larger) hard drive. The standard I/O on each module includes one DisplayPort video, one RS-232 serial port, two Hi-Speed USB ports, two SuperSpeed USB ports, one Gigabit Ethernet, a reset button, and a PXI trigger. b) NI PXIe-7821R module; connectors 0 through 3 each contain 32 high-speed DIO channels that can run up to 80 MHz signal frequencies, routed with a 50 Ω characteristic trace impedance. The DIO channels connect to the FPGA through protection circuitry, which has overvoltage and undervoltage protection as well as overcurrent protection.

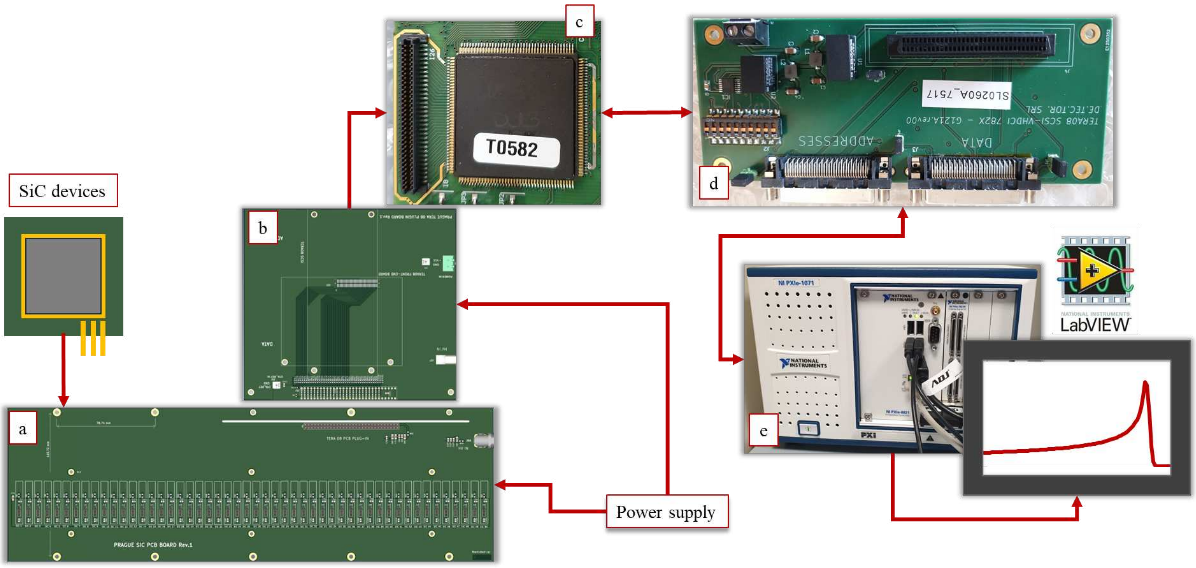

Figure 5.29 Principle diagram of the DAQ system used for the readout of the PRAGUE detector: a) PRAGUE SiC PCB Board; b) PRAGUE TERA Plugin Board; c) TERA Board; d) TERA SCSI-VHDCI; e) NI PXIe-1071 chassis.

5.3.1 TERA08 circuit and chip architecture

The TERA08 chip hosts 64 identical channels integrated in a 4.5mm x 4.5mm die. In Figure 5.30 the schematic of one single channel is shown. The charge-to-count/current-to-frequency conversion of each channel is based on the principle of recycling integration.

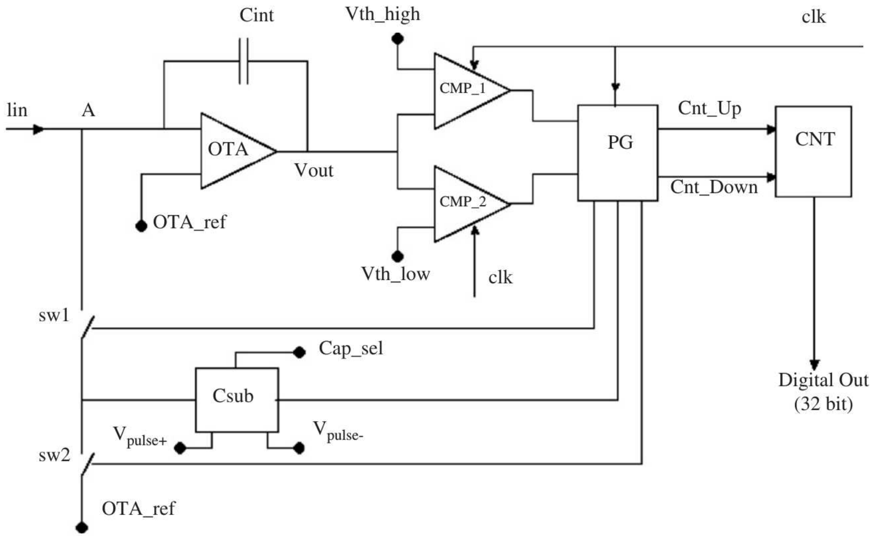

Figure 5.30 Illustrative diagram of the operating principle for the single channel of the TERA08. The OTA_ref, Vth_high and Vth_low, V_{pulse+} and V_{pulse-}, and Csub (common in each channel) can be set externally to the chip.

The input current I_{in} is integrated on the capacitance Cint (integration capacitor, 600 fF) through an operational transconductance amplifier (OTA). Here, the current signal is converted into a voltage signal V_{in} and amplified by a gain factor G, obtaining V_{out}=G(V_{in}-OTA_ref), OTA_ref being the reference voltage with respect to which each channel works (different from ground). It is generated in the TERA Board via an I49 LM385M circuit, which requires a supply voltage of +5 V to function. The integration output V_{out} increases when the input current is negative and decreases when it is positive.

V_{out} is compared with two threshold voltages via two synchronous comparators, called CMP_1 and CMP_2. The threshold voltages of the two comparators, which are fixed externally, are:

- Vth_high; it is the threshold voltage of the comparator CMP_1 and works for negative input currents.
- Vth_low; it is the threshold voltage of the comparator CMP_2 and works for positive input currents.

Whenever V_{out} crosses the associated threshold, the related comparator sets a level at the input of the pulse generator (PG), which sends to the capacitor Csub a positive voltage pulse of 20 ns length. The amplitude of this pulse ΔV is defined as the difference between two reference voltages, called V_{pulse+} and V_{pulse-}. The latter are supplied to the chip by the board and can be set externally in hardware, in the range between 0.5 and 3.3 V. In turn, Csub value can be externally defined by the user: three parallel capacitors of 50, 100, and 200 fF, can be independently added to obtain the total capacitance Csub, for which any value between 50 and 350 fF in steps of 50 fF can be selected. When the pulse generated by the PG meets Csub, two output current signals, δ+ (positive) and δ- (negative), are generated: the positive signal δ+ is generated by the rising edge of the pulse, while δ- is generated from the falling front. δ+ and δ- are characterized by the associated charge quantum Q_0^+ and Q_0^- given by:

$$Q_0^+ = Csub \cdot \Delta V \tag{5.11}$$

$$Q_0^- = -Csub \cdot \Delta V \tag{5.12}$$

These are sent to OTA_ref or to OTA according to the polarity of the input current. If the input current is positive, Q_0^+ is sent to OTA_ref and Q_0^- is sent to OTA, vice versa in the opposite case. This procedure is managed by the PG, which is able to act on the timing of the commands on the switches sw1 and sw2 (Figure 5.31). This results in removing (adding) a fixed amount of charge from Cint, and in a change in the voltage across Cint, given by Q_0/Cint. The residual signal at this point will be lower (higher) than before, and will be subjected to the entire process again. In other words, by appropriately acting on the opening/closing time of the switches, a repeated subtraction (addition) of the quantum charge from (to) the input value is obtained, lowering (increasing) the value of residual V_{out}, until the latter remains above (below) the threshold set on the corresponding comparator. During the process, the PG, in addition to generating ΔV and governing the timing of the switches, sends a pulse to be counted to the up/down counter every time the relative comparator generates an input level. The operations illustrated above are done in parallel for all 64 channels. The total charge Q_{tot} read-out from each detector will be given by the number N of pulses generated during the measurement time multiplied by the value of the known quantum charge Q_0. The relationship between the output pulse frequency and the input current is:

$$\upsilon_{out} = N/\Delta t = I_{in}/Q_0 \tag{5.13}$$

where Δt is the total integration time. All operations are synchronized by an external master clock and are supervised by a digital finite state machine (FSM) implemented in the PG block. At a given clock, any time the PG detects CMP-1 (or CMP-2) active, the next three clock cycles will be used in the charge subtraction and in the pulses to control the switch. Two more clock cycles are also required before re-triggering FSM, which provides OTA enough time to lower the input. In total, 5 master clock pulses are required to generate a count. Therefore, since the clock frequency is v_{clock}=100 MHz, the maximum conversion frequency corresponds to one fifth of v_{clock}, equal to 20 MHz. As a consequence, the maximum input current that the TERA08 can track without going into saturation is:

$$I_{max} = Q_{0,max} \times \upsilon_{max} = \pm\ 22\ \mu A \tag{5.14}$$

This value is lowered to ±0.5 μA using the smallest quantum of charge available. In Table 5.1 the TERA08 specification is summarized. The Cint of all channels can be discharged through a common digital input, resetA (analog reset). This signal is generally used at the beginning of the data acquisition in order to start without charge accumulated in the feedback capacitance. Similarly, all counters can be reset via a common asynchronous digital input, resetD (digital reset).

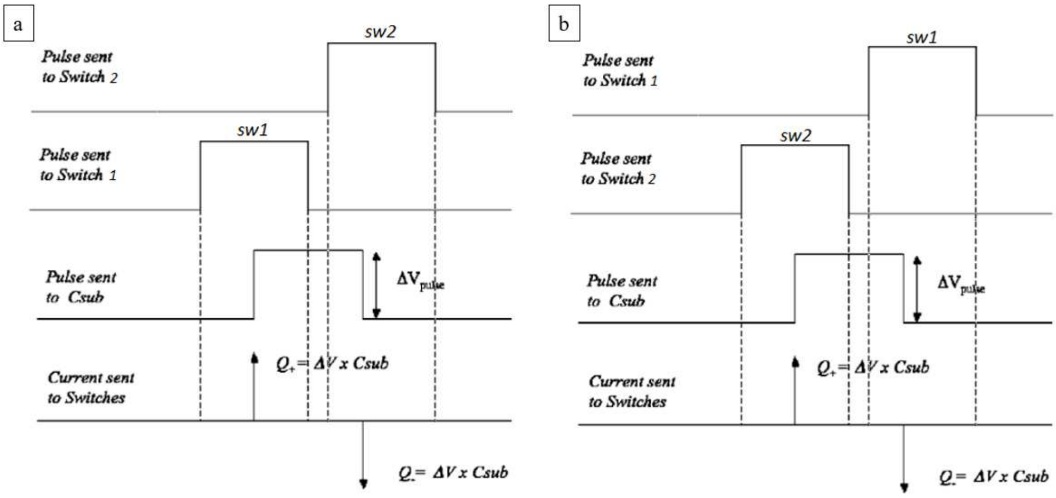

Figure 5.31 Charge subtraction waveforms for a negative (a) and positive (b) current input into OTA. In a) sw1 is closed when Q_0^+ is generated and reopened when the latter has been sent to the OTA. Immediately afterwards, sw2 is closed, sending Q_0^- towards OTA_ref. In situation b) the exact opposite occurs.

Indicator	**Value**
Maximum conversion frequency	20 MHz
Maximum count rate	20 counts/µs
Maximum input current	± 22 µA
OTA_ref	1.65 V ± 0.1 V
C_{int}	600 fF
C_{sub}	50 fC - 350 fC
$\Delta V_{pulse\pm}$	0.5 - 3.3 V
Quantum charge, Q_o	25 fC - 1.155 pC
Linearity range	< 1,5% from 500 pA to 3 µA
External chip voltage	+5 V
Required environmental conditions	15°C - 40°C, 5% - 60% humidity range, atmospheric pressure

Table 5.1 TERA08 specifications.

5.3.2 Front-end boards design

As above mentioned, the PRAGUE detector is engineered to ensure optimal performance in the presence of both high (10^{12}-10^{14} protons/s) and conventional (10^{7}-10^{9} protons/s) intensity beams. Estimating the expected currents produced by SiCs in the hypothesis of irradiating them with proton beams up to 150 MeV with such intensities, it is clear that some adjustments to ensure the proper functioning of TERA08 chip in both irradiation modes are required (refer to Figure 5.32).

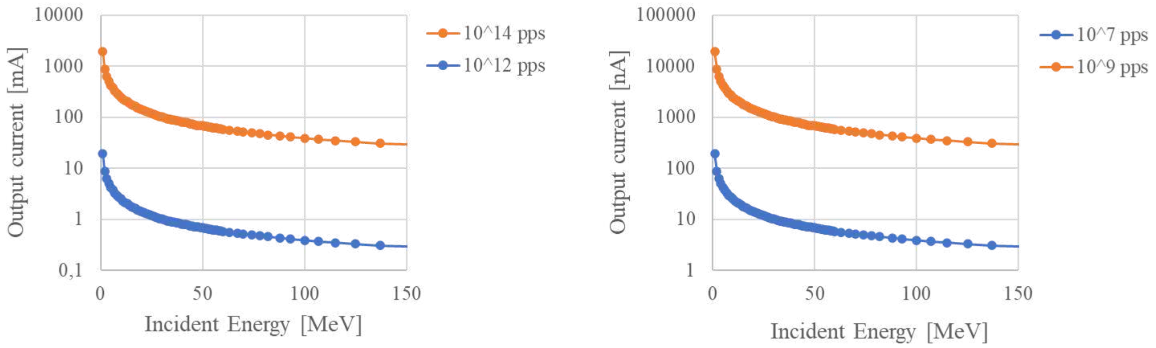

Figure 5.32 Evaluation of the current produced by the detectors as the incident energy and intensity of the proton beam vary. The estimate was made by calculating the energy loss in 10 µm of SiC and assuming that the latter was totally used to produce ionization and that the charge produced within the detectors was all collected.

To meet these requirements, a system comprising two interface PCBs was devised, also facilitating the accommodation of detectors in a stacked configuration. These boards are named the PRAGUE SiC PCB Board and PRAGUE TERA Plugin Board, and their illustrations are presented in Figure 5.33 and 5.34, respectively.

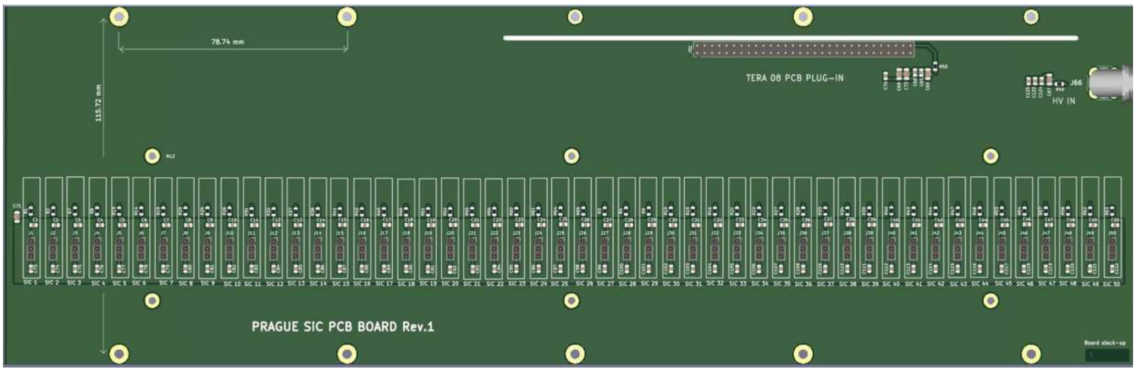

Figure 5.33 Top view of the PRAGUE SiC PCB Board (390x122.9 mm).

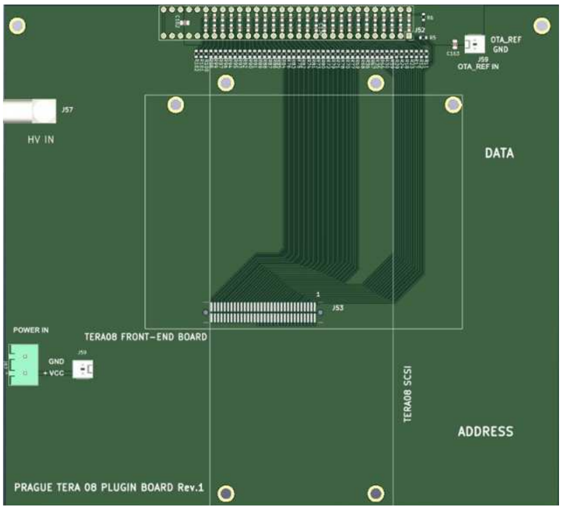

Figure 5.34 Bottom view of the PRAGUE TERA Plugin Board (167x150.8 mm).

Their main function is to insert a modification that involves a variation in the temporal dynamics of the signals produced by the detectors and the addition of a protection filter for the voltage generator. The conceptual diagram of the electrical circuit between the single SiC device and the TERA which is obtained through the combined action of the boards is illustrated in Figure 5.35.

Specifically, the modification consists of inserting an RC_x circuit between each SiC device and the TERA08, making the latter able to “follow” the (slowed down) SiC signal without going into saturation. When the beam impinges a SiC and the $I_{SiC}(t)$ current is generated from the detector, this initially involves charging the capacitor C_x (in a short time). The latter subsequently discharges on the resistor R over a time which depends on the constant $\tau=RC_x$. The RC_x circuit then produces a delay on $I_{SiC}(t)$ of about 5τ, but does not distort the measurement of the total charge produced by the detector following irradiation. Furthermore, a capacitor C is added between the high voltage (HV) generator and each detector to ensure that the bias voltage applied to the diodes, ΔV_{SiC}, is maintained even during irradiation with high intensity, short duration pulsed beams. C acts as a charge "reservoir", providing support to the HV that has an output impedance (an inductive component) that opposes the sudden production of current. For the precaution to work, C must be very large, so that the charge stored inside it, $Q = C \cdot \Delta V_{SiC}$, is much greater than the maximum value of charge we expect to generate, $Q_{max}=\int I_{SiC}(t)\,dt$.

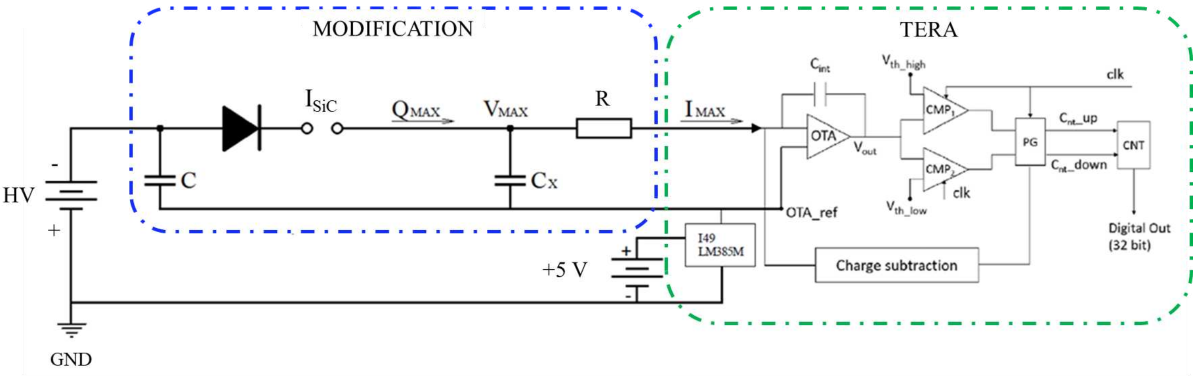

Figure 5.35 Schematic of the electric circuit for each SiC-TERA08 channel. C_x and R are the components of the RC circuit. C is the HV filter capacitance, Q_{max} is the maximum generated charge, V_{max} is the potential difference across C_x. I_{max} is the maximum input current for TERA08. In this configuration diodes will work by default at a potential difference given by $\Delta V_{eff}=\Delta V_{SiC}$-OTA_ref-$V_{max}$, where ΔV_{SiC} is the potential difference applied across the diode through HV, while C and C_x are at potential equal to OTA_ref.

In summary, C must be much larger than both the detector capacitance C_{SiC} and C_x. Considering that C_x is placed in parallel with the series capacitor C_{SiC}-C, and $C \gg C_x$, C_{SiC}, the values of C_x and R must be chosen based on the following relationship:

$$C_x + C_{SiC} = C_{eq} = \frac{Q_{max}}{V_{max}} = \frac{Q_{max}}{I_{max} \cdot R} = \frac{Q_{max}}{v_{max} \cdot Q_0 \cdot R} \tag{5.16}$$

where:

- V_{max} it is the maximum voltage drop we can tolerate on the detector (it must be small enough not to cause a substantial increase in leakage current and to ensure the over depletion condition);
- I_{max} is the maximum current that the TERA08 can receive as input;
- Q_0 is the quantum charge selected on the TERA08;
- v_{max} is the maximum conversion frequency of the TERA08.

Another factor to consider when selecting the values of RC_x components is that the time constant (τ) must align with the temporal characteristics of the utilized beam (e.g., for laser-driven beams, it should be significantly lower than the laser repetition rate).

To choose the values of C_x and R, a set of PSpice simulations of the circuit in Figure 5.35 were performed. PSpice is a simulator that analyzes the behaviour of circuits, using the

Monte Carlo method to determine the performance and combined action of components. Specifically, the effect of the RC_x circuit on the maximum expected current pulse was investigated, simulating a current step with a peak value of 2A and a duration of 100 ns (for a total charge of 200 nC), compatible with what expected with laser-driven beams. Through simulations, it was possible to identify the configuration with C=1μF, C_x=47nF, R=300kΩ (with $5\tau=RC_{eq}\simeq 75$ ms, considering a detector capacitance $C_{SiC}\simeq 2$ nF) as suitable to meet our needs (Figure 5.36). For completeness, the effect of these values was also simulated on a current step with a peak value of 10 mA (for a total charge of 1 nC).

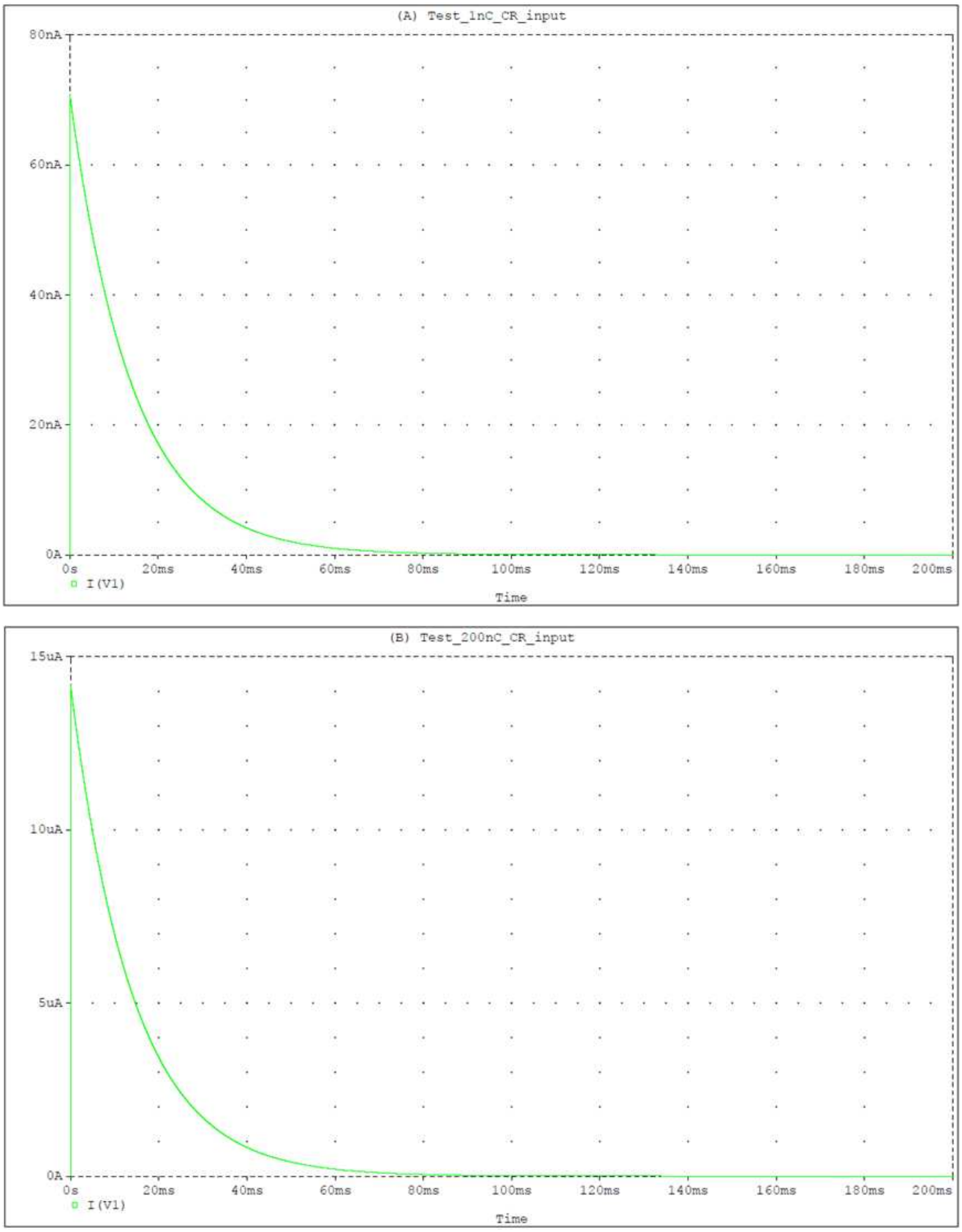

Figure 5.36 PSpice simulation result for a 100 ns current pulse of 10 mA (A) and 2A (B) passing through the RC_x circuit with C_x=47nF, R=300kΩ. The peak current value drops to ~70 nA and ~14 μA respectively. The discharge completes at ~80 ms.

The changes illustrated so far are implemented through the PRAGUE SiC PCB Board. It is designed as a 4-layer PCB, compact and capable of shielding the signal. Its layout is as follow (from top to bottom):

- Layer 1: 95% full guarding layer (at TERA08 reference voltage, OTA_ref = 1.65 ± 0.1V) + housing for RC_x circuits and stripline for SiC detectors;
- Layer 2: 25 signal tracks (0.2 mm in size and spaced by 0.2 mm of insulation) + high voltage (HV) track + OTA_ref track;
- Layer 3: 25 signal tracks (0.2 mm in size and spaced by 0.2 mm of insulation) + high voltage (HV) track + OTA_ref track;
- Layer 4: 95% full guarding layer (at OTA_ref voltage) + housing for C capacitances.

Both RC_x circuits and C capacitor components are placed as close as possible to the detectors. The C capacitances mounted between the OTA_ref and HV tracks will be placed on layer 4, to save space on layer 1 where the striplines for the detectors will be mounted and where the RC_x circuits will be soldered. The detectors will be housed in the striplines, placed 2.54 x 3 = 7.62 mm away from each other, so that the pins are electrically connected as shown in Figure 5.37.

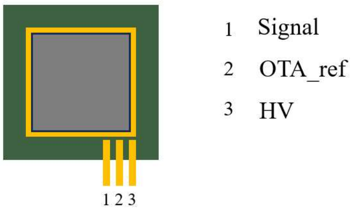

Figure 5.37 Electrical connection of the SiC anode and cathode via the PRAGUE SiC PCB board.

A BNC connector will be installed on PRAGUE SiC PCB Board to provide voltage (via HV) to the detectors. As can be seen from Figure 5.35, the HV ground and that of the voltage generator intended to power the TERA08 are connected. Furthermore, the OTA_ref voltage (generated by the TERA08) must be transported up to the PRAGUE SiC PCB Board. These functions are performed by the PRAGUE TERA Plugin Board, a common 3-layers PCB connected to the PRAGUE SiC PCB Board via a perpendicular edge connector to avoid exposure of the chip to the radiation field. Here, detector signals are carried to the TERA08 through a Mezzanine Connector 120527-1 (Header, 64 Contacts). Using the pinout of the TERA08 chip, the detectors are connected in a manner where the first device in the stack corresponds to the first channel (ch0) of the TERA08, and the last corresponds to the fiftieth channel (ch49). As a precautionary measure, slots are provided for a second system of RC circuits (C=10nF, R=300kΩ) to be mounted just before the Connector 120527-1 (not shown in Figure 5.35 for simplicity). In case of noise issues arising from triboelectric or electromagnetic interference, and if the system fails to provide adequate shielding efficiency, the second RC system mitigates the effects by acting as a filter on noise frequencies while further stretching the signal. Simulations demonstrate that the configuration with two RC systems continues to meet our requirements in terms of signal dynamics (refer to Figure 5.38).

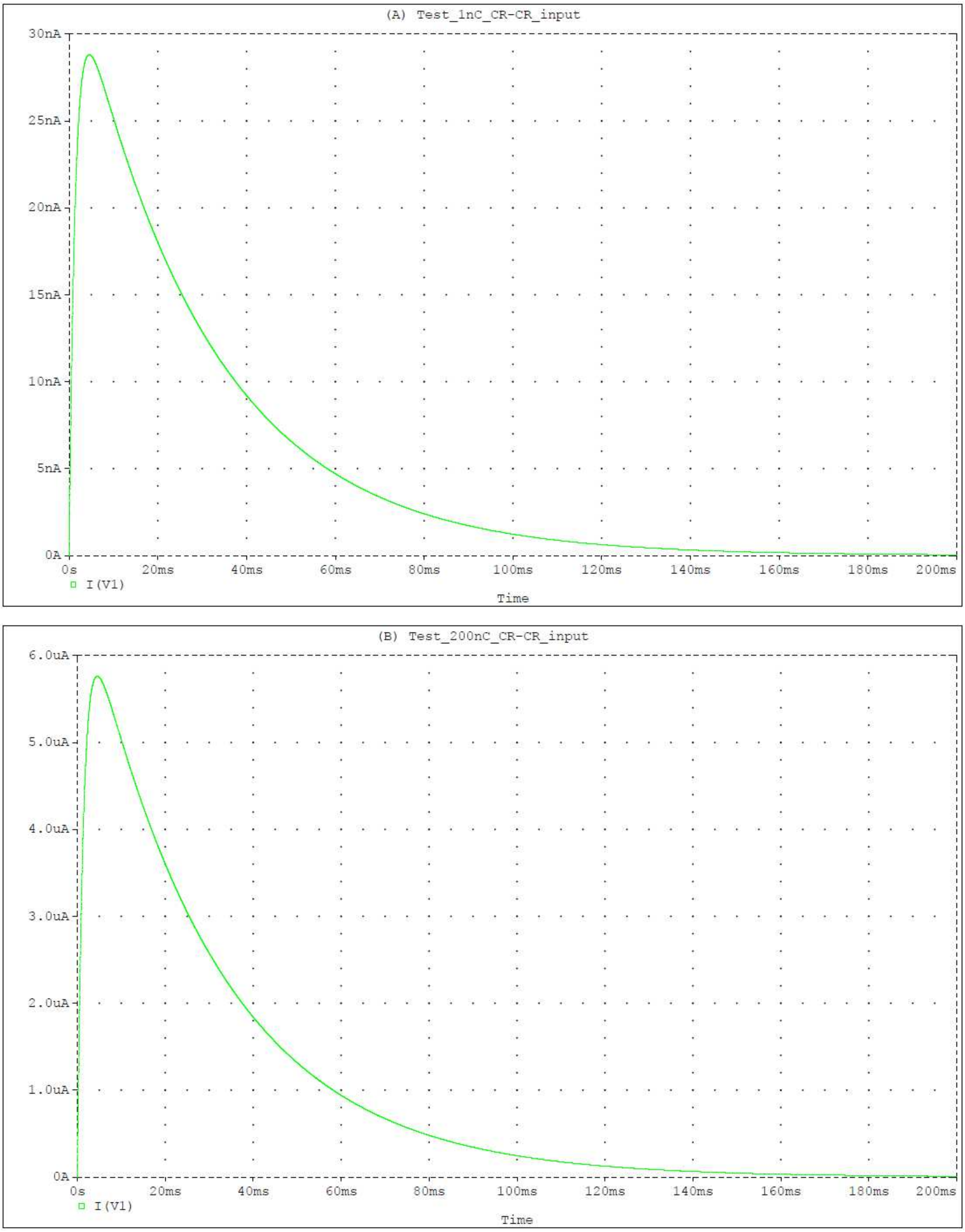

Figure 5.38 Pspice simulation result for a 100 ns current pulse of 10 mA (A) and 2A (B) passing through the 2RC circuit, one with C=47nF, R=300kΩ, and the other with C=10nF, R=300kΩ. The peak current value drops to ~30 nA and ~6 µA respectively. The discharge completes at ~180 ms.

5.3.3 Tests on the electronic chain

The boards are currently under production, and therefore we have not yet been able to carry out tests on the electronic chain. However, the tests that we intend to carry out have been defined. They are listed below and will be performed as soon as possible on the entire DAQ system, by using the customized software developed specifically for the acquisition of the PRAGUE device (see next Section). Of course, the latter must be itself tested as a preliminary step.

☐ Monitoring of the background current of the electronic chain: its absolute value and polarity may vary from channel to channel, and by varying Q_o too; it has to be precisely measured and subtracted from the input to avoid overestimation or underestimation of the actual collected charge; it defines the sensitivity of the readout system. It will be measured by studying the number of counts per second given from each channel for each quantum charge value, when no external current is injected.

☐ Investigation on the linearity of current-to-frequency (or charge-to-count) conversion: the output frequency may not exactly proportional to the input signal, within the range of expected currents, condition that may also vary with different Q_o values. This is something that we must take into account to correctly reconstruct the PDD distribution, since not all the SiC devices along the stack will produce the same current. Linearity will be investigated by injecting crescent current values to all channels and studying the linear correlation to the corresponding output frequency, as the set quantum charge varies.

☐ Evaluation of the charge conversion efficiency: it consists of verifying that the chip, for each channel and each Q_o, is able to read the correct charge sent to it as input. It will be evaluated by sending a steady current to every channel for a defined period of time, and calculating the percentage deviation of the read value in respect to the expected value.

☐ Gain uniformity test: gain uniformity is present if the output response of every channel to an equal input charge is similar (within the margin of error of the counting accuracy that we have, which depends on Q_o). It will be evaluated as a consequence of the previous test, from which we will be able to evaluate a percentage relative deviation of the channels' response to an equal input value.

☐ Investigation of crosstalk phenomena: multiple signals on different tracks can interfere with each other, producing distortion or reducing signal quality. They can be monitored by sending a known signal to just one channel and seeing what happens in adjacent channels, and then doing the same on all channels at the same time.

☐ Evaluation of the stability and reproducibility of the electronic chain: it's important also to test that the previous measurements are not affected by any variation in time and/or during long irradiations. These characteristics can be studied simply by repeating the measurements several times, over a period of time and under prolonged "irradiation".

5.3.4 Acquisition software

A basic LabVIEW acquisition software, able to communicate with the TERA08 via the FPGA module of the NI chassis, was developed in collaboration with the DET.EC.TOR. company. This software represents a good starting point, but still needs to be adapted and customized to the requirements of the PRAGUE application. The screen in Figure 5.39 shows the project of the software. The main implemented routines are "FPGA Target 2", which is used to configure the FPGA, and "TERA08_DAQ", where the sequence of commands previously written in the FPGA are recalled.

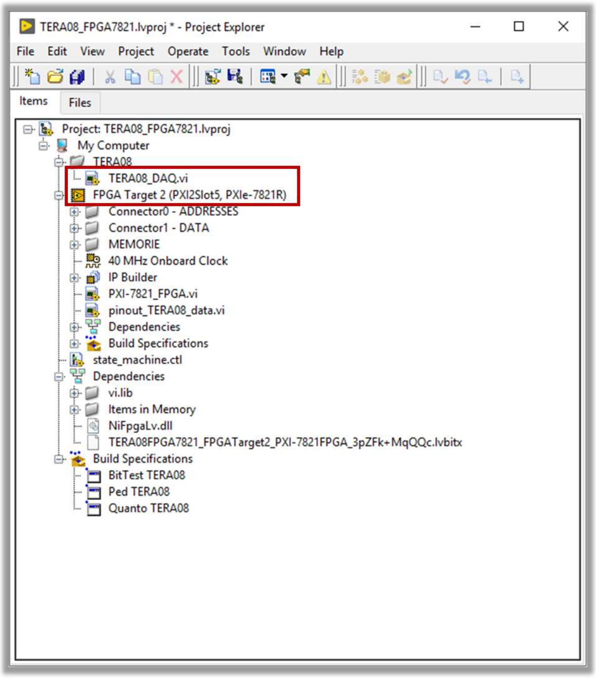

- Project: TERA08_FPGA7821.lvproj
  - My Computer
    - TERA08
      - TERA08_DAQ.vi
    - FPGA Target 2 (PXI2Slot5, PXIe-7821R)
      - Connector0 - ADDRESSES
      - Connector1 - DATA
      - MEMORIE
      - 40 MHz Onboard Clock
      - IP Builder
      - PXI-7821_FPGA.vi
      - pinout_TERA08_data.vi
      - Dependencies
      - Build Specifications
    - state_machine.ctl
    - Dependencies
      - vi.lib
      - Items in Memory
      - NiFpgaLv.dll
      - TERA08FPGA7821_FPGATarget2_PXI-7821FPGA_3pZFk+MqQQc.lvbitx
    - Build Specifications
      - BitTest TERA08
      - Ped TERA08
      - Quanto TERA08

Figure 5.39 Structure of the LabVIEW project developed for communication between TERA08 and FPGA. In the red box, the main routines.

"FPGA Target 2" program contains 3 main loops within it. A loop is dedicated to managing the reset signals and the Csub TERA08 parameter. A second loop is responsible for controlling the LATCH of the chip, thus determining the reading frequency, or how often the data is read from the FPGA. The third loop is dedicated to the simultaneous acquisition of channels and data storage. Here, the differential and integral of each channel is also calculated. At each cycle, the differential is obtained as the value of the integral at n-th acquisition minus the value of the integral at acquisition n-1, while the integral is obtained as the sum of the n-th differential with the previous one. The latter are then recalled by "TERA08_DAQ", whose graphic interface is shown in Figure 5.40. It is the main routine and allows data visualization. Shown in TERA08_DAQ interface are the graphs of the wave function and the differential and integral value of each channel (selectable on the graphic interface via a controller). Additionally, a graph of recorded counts per channel is also shown.

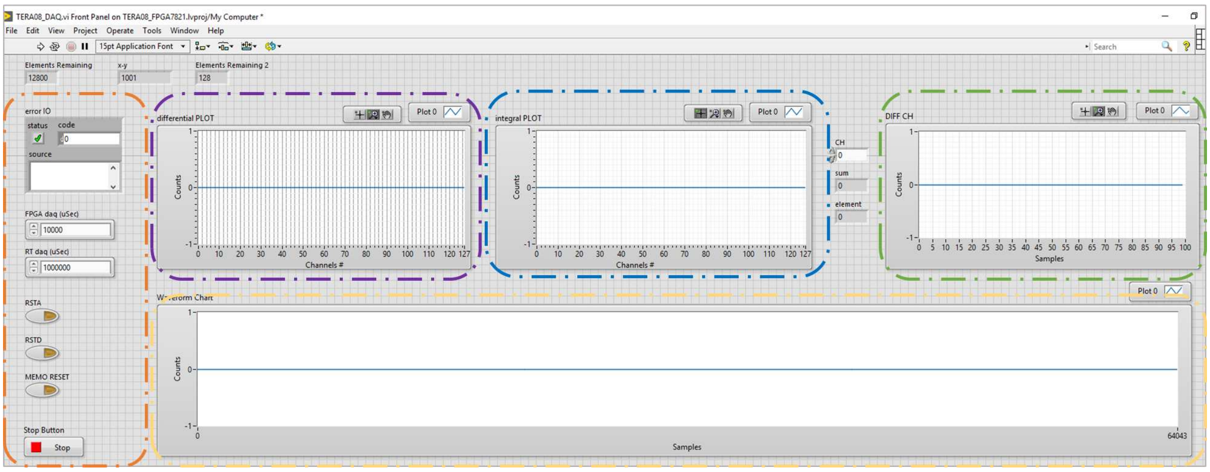

Elements Remaining: 12800
x-y: 1001
Elements Remaining 2: 128
error IO — status: ✓ code: 0 source:
FPGA daq (uSec): 10000
RT daq (uSec): 1000000
CH: 0
sum: 0
element: 0

Figure 5.40 TERA08_DAQ graphic interface. Purple box: differential plot. Blue box: integral plot. Green box: counts/channel plot. Yellow box: waveforms plot. Orange box: interface controllers; “RSTA” and “RSTD” act respectively as resetA and resetD; the “MEMO RESET” controller is used to reset the TERA08 counters only at the FPGA level, while the TERA08 counters are not reset; "FPGA daq (uSec)" controller defines how often to acquire with the FPGA (set to 10 ms by default), while "RT daq (uSec)" defines the time after which the data is published on the interface; the "Error" panel is used to signal the presence of an error.

A data acquisition and processing software more suited to the readout of the PRAGUE detector should be able to initiate data acquisition, visualize detector data in real time in terms of PDD distribution, and store it in text format for further data analysis. These features are currently under development and, specifically, here are the main requirements that are going to be implemented:

- enable the a priori setting of the acquisition time and implement a timer display;
- acquire, record and display the background signals for each channel. Once a certain reverse bias voltage is established on the SiCs, the dark current of each channel-detector pair will be acquired for a certain time; the charge/counts signal is expected to have a linear trend with respect to time: the angular coefficient of the straight line and its associated error will be an estimate of the background value and the indeterminacy of the dark current for that channel-detector pair. These values will be displayed in a dedicated panel.
- acquire and record the SiC detector signals during irradiation, and perform an online background subtraction, which involves taking into account the contribution of the dark current on the total charge/counts output (i.e., for the entire acquisition time). These values will be displayed in a dedicated panel.
- import the calibration coefficients and water equivalent depths for each detector (channel) and display online the net charge values (with background subtracted) converted into dose for each of them as a function of the depth in water; these data will also be stored.

Conclusion

The primary advantages of proton therapy over photon therapy are the superior ballistic capabilities and the finite beam range. However, in clinical practice, range assessment in tissue is fraught with uncertainty due to imaging, patient setup, beam delivery, and dose calculation procedures. Reducing these uncertainties would entail optimizing the methods and technologies employed, facilitating the reduction of the treatment volume. The latter is presently one of hadrontherapy's challenges. The effort to look for innovative methodologies capable of estimating the range of charged particle beams with great accuracy and precision at conventional and FLASH intensity has been intense in recent decades. In this context, due also to technical advances in semiconductor material manufacturing, the adoption of solid-state SiC-based devices for dosimetry is being addressed. The PRAGUE project emerges from this research area. Its primary purpose is to develop, assemble, and test a real-time, multilayer SiC detector capable of reconstructing the PDD distribution of a 30-150 MeV proton beam with conventional and FLASH intensity, as well as a very high longitudinal spatial resolution (approximately 30 m of WET).

This thesis work focused on the development and testing of a prototype version of the PRAGUE detector, as well as the potential of coating the SiC devices with resin. Additionally, it dealt with the characterization of the detectors that would comprise the final device, as well as the assessment and development of the system's electronic readout chain.

The prototype of the final detector was realized to test the feasibility of the system to acquire the PDD distribution of a proton beam. It is composed of four p^+n SiC devices with a sensible area of 1x1 cm^2, an active layer of 10 μm, a passive layer of 120 μm, and a doping concentration $N_D = 0.5 - 1 \cdot 10^{14}$ cm^{-3}. Each detector was located inside an aluminium case mounted on a guide track and able to move along it. Before testing the SiC detectors as dosimeters, their electrical characterization was performed by measuring their I-V and C-V characteristics. The I-V profile was useful to establish the leakage current of the detectors and to monitor their breakdown voltage, while the C-V profile allowed the estimation of the detector's depletion voltage, saturation capacitance, built-in potential, and depletion region thickness. Moreover, it was possible to investigate the dopant concentration profile along the depletion region. The results point out that the devices, when inversely polarized at 0-50V voltages, are characterized by a leakage current that does not exceed 50 pA. The physical quantities inferred from the C-V characterization revealed the presence of a dopant concentration that was not perfectly constant up to the maximum width of the depletion region (unlike the ideal case), and that was generally lower than expected.

The PRAGUE prototype was then tested with conventional proton beams. Specifically, the Percentage Depth Dose distribution of a 30 MeV proton beam delivered at the ÚJV Řež Centre (Czech Republic) and a 70 MeV proton beam delivered at the Proton Therapy Centre of Trento (Italy) was obtained by introducing an increasing number of Radiochromic Films (EBT3 model) between the detectors. The PDD distribution of the same proton beam was also acquired through an EBT3 stack. From the comparison between the results obtained with the two different systems, it was possible to highlight that the PRAGUE prototype was able to obtain a PDD distribution with a better peak-to-plateau ratio value than that obtained with the EBT3 stack. This result complies with what was expected, since unlike SiC devices, it is known that the response of Radiochromic Films suffers from a dependence on the LET of the incident radiation. During this experimental session, the water equivalent thickness of the SiC devices was also estimated by quantifying the shift undergone by the 30 MeV Bragg peak after passing through them, obtaining an experimental value of 350±175 μm. The large relative error associated with this measurement is related to the resolution of the method used. This result was then subsequently validated for energies up to 250 MeV using the thin-target approach known as the Stopping Power Ratio (SPR) approximation.

In this context, the possibility of completing the back-end process with epoxy resin packaging was also explored, to make the final device suitable for the acquisition of PDD distribution of proton beams with energy up to 150 MeV, at the cost of a worse spatial resolution at the beam entrance. The detector in question is a p^+n junction, with a sensible area of 1x1 cm^2, active layer of 10 μm, passive layer of 350 μm, and a doping concentration $N_D = 0.5 - 1 \cdot 10^{14}$ cm^{-3}. It was embedded in a black epoxy resin to make the detector waterproof. The characterization of the resin-coated device once again concerned the measurement of I-V and C-V which led to the estimate of a very small leakage current (10 pA for voltages up to 100V), and a depletion region and saturation capacitance in accordance with the nominal values (within experimental errors). The examination of the resin coating process was also valuable for exploring the potential development of a dosimetric device based on SiC technology, capable of capturing the PDD distribution of clinical beams in water. The water immersion test revealed a procedural error during the resin covering, providing insights that will be beneficial in revisiting the methodology for future use. Overall, it was found that the coating process does not compromise the functionality of the device, which maintained excellent performance in terms of linearity (deviation within 1.2%), stability (0.4%), reproducibility (0.3%), and PDD distribution reconstruction. The latter was acquired at the CATANA facility, at INFN-LNS (Catania, Italy). Here the detector was subjected to irradiation with a 62 MeV clinical (monoenergetic) proton beam. The PDD distribution was acquired by interposing an increasing number of calibrated absorbers between the isocenter and the detector. The response of the resin-coated SiC was then compared to that of an Advanced Markus Chamber, demonstrating a pretty good agreement within experimental errors.

The design, characterization and realization work on the final device involved an investigation into the performance of 80 SiC detectors and the study of the data acquisition system. The 80 devices are p^+n SiC detectors with a sensitive area of 15x15 mm², an active layer of 10 µm, a passive layer of 110 µm, and a doping concentration N_D= 0.5 - 1 · 10^{14} cm^{-3}. At first, the electrical properties of the SiC devices were characterized by measuring their I-V and C-V profiles before their post-processing. I-V and C-V characterizations were carried out at the Industrial Engineering Department of the University of Rome "Tor Vergata" (Rome, Italy). Through the I-V characterization, the leakage current of the detectors was measured, and anomalies in the conductive behaviour were identified, leading to the rejection of 30 out of the 80 available detectors. The remaining 50 detectors exhibit a leakage current <100 pA when reverse biased up to 50 V. From the C-V characterization, it was possible to quantify the values of the saturation capacitance of the devices, the thickness of the depletion region, the depletion voltage, the built-in voltage, and the dopant concentration profile. These values, compared with the expected theoretical values, showed some discrepancies. In particular, a smaller maximum thickness of the depletion region than expected (ranging from W_{min}=9.0±0.1 µm and W_{max}=9.5±0.1 µm) was obtained, together with a larger saturation capacitance value (ranging from $C_{s,min}$=2.031 ± 0.004 nF and $C_{s,max}$=2.139 ± 0.005 nF). The critical issues of the intercept method for estimating the depletion voltage, built-in voltage, and dopant concentration were identified. When dealing with devices exhibiting characteristics deviating from the assumptions underlying this method (such as abrupt junction and uniform dopant concentration in both the p and n regions), an underestimated depletion voltage is obtained. The built-in voltage and dopant concentration are also more sensitive to the chosen fit range in such cases. To address this, an objective method was developed to enhance the estimation of the depletion voltage. This method yielded depletion voltages up to three times greater than those obtained with the intercept method, aligning with expectations. In addition to electrical characterization, detector response was studied by subjecting them to irradiation with an X-ray beam. The linearity of the detectors was evaluated as the beam current varied (resulting in a maximum percentage deviation from linearity of 1.5%), and their stability was assessed (with fluctuations in the current produced within 0.5% of the mean value). Moreover, under the experimental conditions, the detectors demonstrated very similar relative sensitivity, with a response differing by at most 1.06 times. Finally, Charge Collection Efficiency was investigated, revealing 100% collection starting from 30V for all devices.

The work on the data acquisition system encompassed the study and design of the electronic chain, along with the development of the initial version of the acquisition software. The electronics read-out for the PRAGUE detector is based on the 64-channel ASIC chip called TERA08, whose operating principle is based on recycling integration. Each SiC detector of PRAGUE will be read through one of the independent channels of the TERA08, where a current-to-counts conversion is performed. Since each count corresponds to a known *quantum charge* Q_0, the charge collected by each SiC after irradiation can be easily extrapolated by multiplying the overall number of counts by Q_0. Currently, interface boards facilitating communication between the detectors and the TERA08 are in production, although their design has been completed. These boards are tailored to meet the specific operational requirements of the PRAGUE detector, ensuring that the readout system functions correctly in the presence of continuous and conventionally intense beams, as well as in a pulsed regime with ultra-high intensity. The acquisition software was implemented in collaboration with DET.EC.TOR. Srl company, representing a foundational version poised for initial testing once the electronic chain is finalized.

The subsequent steps to finalize the construction of the PRAGUE detector and enable its operation include:

- the design and implementation of a suitable casing for containment and shielding; it should incorporate a compartment for interchangeable custom collimators and an alignment sighting system.
- perform a feasibility study of the entire system through Monte Carlo simulations, involving both conventional and laser-driven beams. The objective is to define parameters such as the inter-plane distance of the detector layers, the position and thickness of absorbers, the placement and dimensions of the holder for biological samples, and the collimator diameter.
- characterization with protons, both on SiC devices individually and on the entire system; in particular, irradiation with conventional low-energy (30 MeV) and high-energy (70-250 MeV) beams is planned; subsequently the system will be tested with selected 30 MeV laser-driven proton beams (at ELI Beamline).
- continue the investigation into the resin coating process.
- the investigation of chemical etching procedures to remove the passive layer of detectors.

Based on the results observed so far and the potential of the final system, once fully characterized and assembled, the possibilities that the PRAGUE detector will be able to offer are unique. To date, there is no detector capable of measuring PDD distributions in real-time which is scarcely subject to radiation damage and capable of offering a similar longitudinal spatial resolution. Thanks to the electronic readout capable of a real-time and shot-to-shot acquisition of the PDD distribution, it will be possible to optimize the irradiation of biological samples with laser-driven ion beams, which are notoriously characterized by a low reproducibility level. This could represent a significant advance for the community interested in probing the radiobiological effects of Flash Radiotherapy. The proposed technology could also change the landscape of quality control programs in conventional ion therapy by providing a device with high spatial resolution, the use of which would be less time-consuming than procedures currently in force.

Appendix

A.1 I-V LabVIEW software

The I-V acquisition program is dedicated to automating the acquisition of the current produced by the device under examination by varying its polarization voltage. Through serial port (RS-232) configuration, it is set to remotely manage the KEITHLEY 6517B multimeter. Figure A.1.1 shows the program's graphic interface.

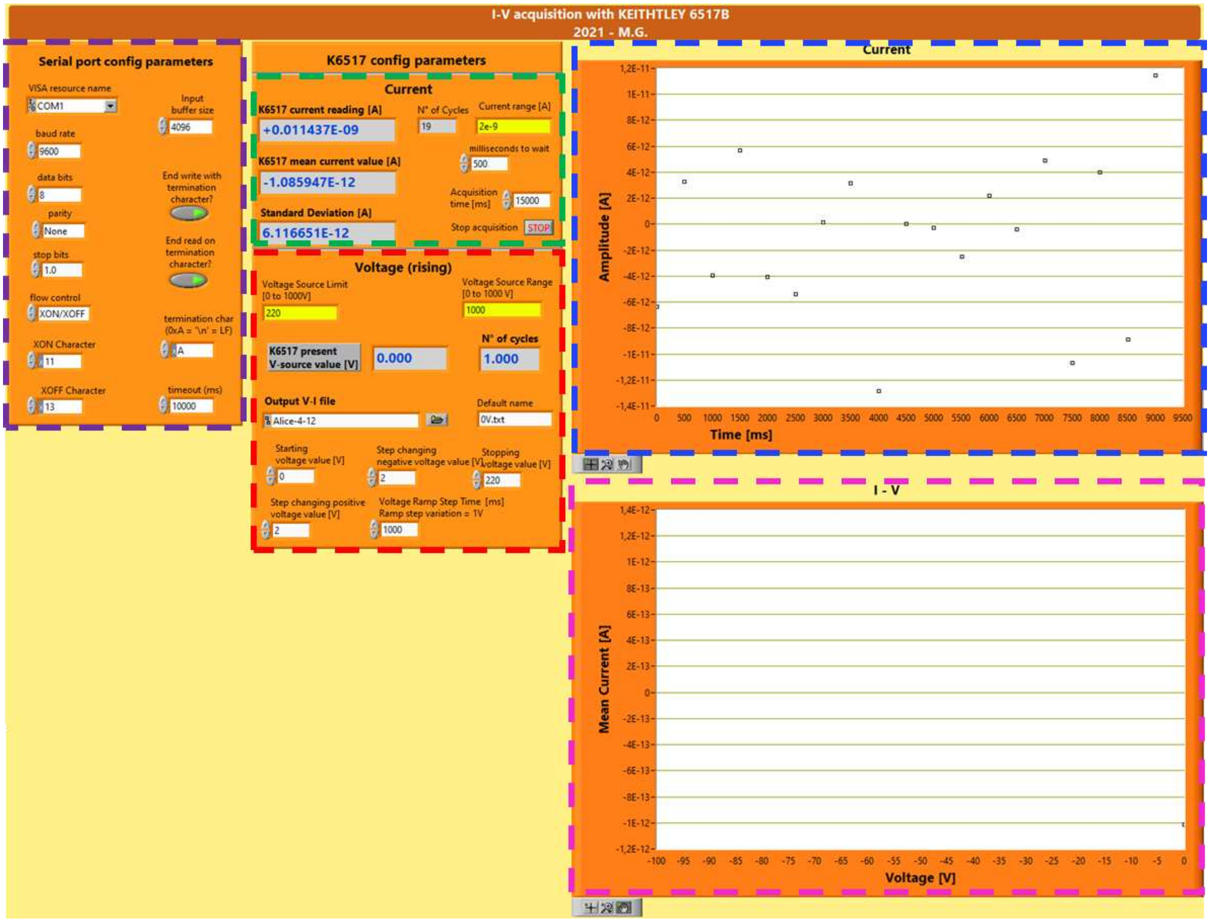

I-V acquisition with KEITHTLEY 6517B
2021 - M.G.

Serial port config parameters

VISA resource name: COM1
Input buffer size: 4096
baud rate: 9600
data bits: 8
End write with termination character?
parity: None
stop bits: 1.0
End read on termination character?
flow control: XON/XOFF
termination char (0xA = '\n' = LF): A
XON Character: 11
XOFF Character: 13
timeout (ms): 10000

K6517 config parameters

Current

K6517 current reading [A]: +0.011437E-09
N° of Cycles: 19
Current range [A]: 2e-9
milliseconds to wait: 500
K6517 mean current value [A]: -1.085947E-12
Acquisition time [ms]: 15000
Standard Deviation [A]: 6.116651E-12
Stop acquisition: STOP

Voltage (rising)

Voltage Source Limit [0 to 1000V]: 220
Voltage Source Range [0 to 1000 V]: 1000
K6517 present V-source value [V]: 0.000
N° of cycles: 1.000
Output V-I file: Alice-4-12
Default name: 0V.txt
Starting voltage value [V]: 0
Step changing negative voltage value [V]: 2
Stopping voltage value [V]: 220
Step changing positive voltage value [V]: 2
Voltage Ramp Step Time [ms] Ramp step variation = 1V: 1000

Figure A.1.1. Graphical interface of the LabVIEW software dedicated to the automatic acquisition of the I-V profile. Purple box: panel containing the KEITHLEY 6517B configuration parameters necessary to correctly set the communication protocol between the latter and the software. Green box: current panel; here it is possible to select the desired full scale, the acquisition time, and the sampling frequency. Furthermore, the acquisition cycle, the instantaneous current value, the average value and the standard deviation of the current measured up to the displayed cycle are indicated. Red box: voltage panel; the voltage ramp and step, the full scale, the initial and final voltage excursion value and their change step can be set. Blue box: graph dedicated to displaying the instantaneous current I(t). Pink box: graph dedicated to displaying I(V).

When the program gets started, the section dedicated to configuring the serial port starts first, resulting in the opening of communication with the instrument, which imports the acquisition parameters set by the user (Figure A.1.2).

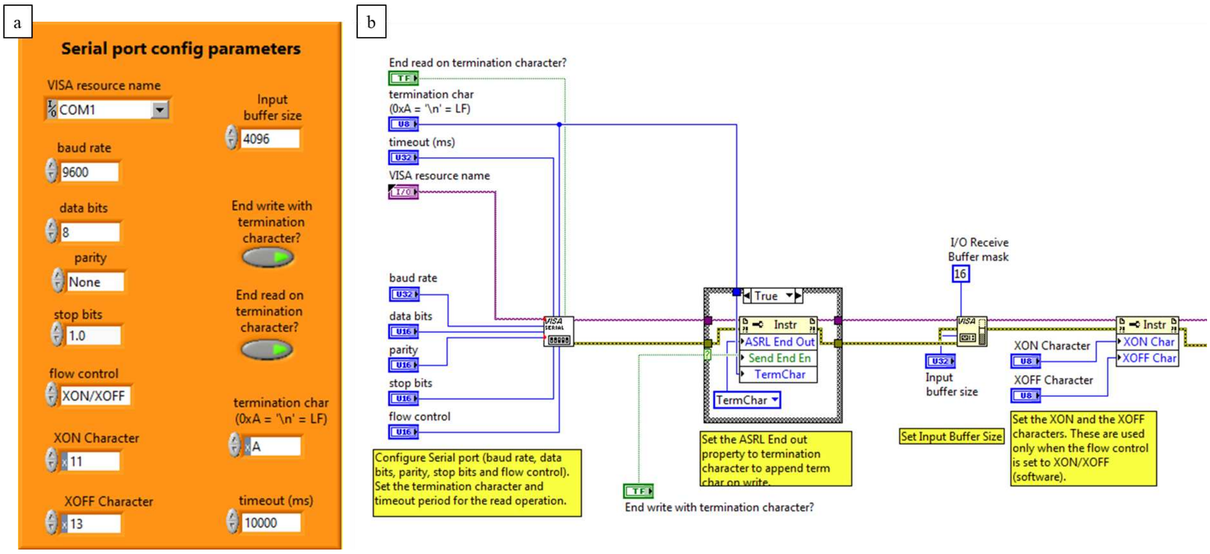

Serial port config parameters

VISA resource name
COM1
baud rate
9600
data bits
8
parity
None
stop bits
1.0
flow control
XON/XOFF
XON Character
11
XOFF Character
13
Input buffer size
4096
End write with termination character?
End read on termination character?
termination char (0xA = '\n' = LF)
A
timeout (ms)
10000

Configure Serial port (baud rate, data bits, parity, stop bits and flow control). Set the termination character and timeout period for the read operation.

Set the ASRL End out property to termination character to append term char on write.

Set Input Buffer Size

Set the XON and the XOFF characters. These are used only when the flow control is set to XON/XOFF (software).

Figure A.1.2. a) Panel containing the KEITHLEY 6517B configuration parameters necessary to correctly set the communication protocol between the latter and the software. b) Extract of the block diagram of the program dedicated to the initialization and configuration of the serial port that allows communication with the KEITHLEY.

Immediately afterwards, a *voltage ramp* begins in steps of 1 V, with a changing speed decided by the user (default value, 1V/s). The latter brings the device to the set negative voltage. This operation is performed without current measurements. Once the *starting voltage value* is reached, the actual acquisition of the I-V begins. It is managed not only by the voltage range (and its variation steps), but also by the acquisition times. Specifically, you can set:

- a *waiting time* between one measurement point and another (a default value of 5s is set, but it can be changed by acting on the block diagram);
- the duration of acquisition time for each current point, called *acquisition time* (in ms);
- the *sampling rate* of the instantaneous current: this is done by defining the clock time of each measurement cycle though *milliseconds to wait*; the default value is 500 ms, which corresponds to a sampling rate of 2 Hz.

For each measurement point (i.e. voltage), the program acquires the current measured by the KEITHLEY with a full scale defined by *current range*, for a time equal to the *acquisition time* and with a sampling frequency defined by *millisecond to wait*, after having waited a certain amount of time (*waiting time,* usually 5s). At the same time, the instantaneous current values are shown in the *Current vs. Time* graph (blu box in Figure A.1.1) and on the dedicated display, while the average current value and the standard deviation are updated at each cycle and are shown on the dedicated displays. At the end of the acquisition for that given voltage value, the *I-V* graph is updated, reporting the final average current value corresponding to the measurement voltage. This repeats until the highest voltage (*stopping voltage value*) value set by the user. After that, a new voltage ramp brings the detector back to zero voltage. Figures A.1.3 and A.1.4 show the panels dedicated to voltage and current respectively. Among the features of the program, there is a block for writing and saving text files (the name and saving destination of which can be defined at the beginning of the acquisition) which at the end of the acquisition produces an output containing voltage, average value and standard deviation on three columns.

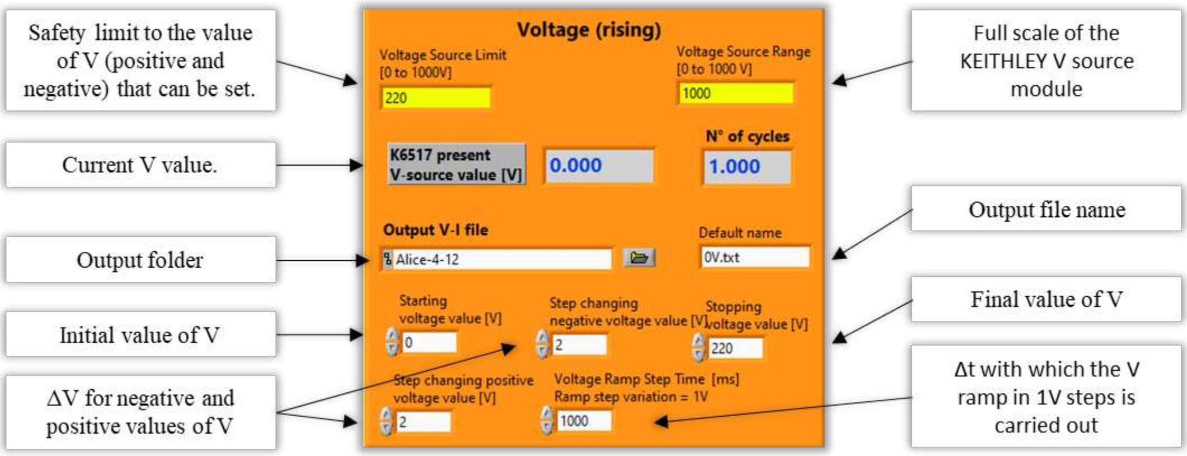

Voltage (rising)

Voltage Source Limit [0 to 1000V]: 220

Voltage Source Range [0 to 1000 V]: 1000

K6517 present V-source value [V]: 0.000

N° of cycles: 1.000

Output V-I file: Alice-4-12

Default name: 0V.txt

Starting voltage value [V]: 0

Step changing negative voltage value [V]: 2

Stopping voltage value [V]: 220

Step changing positive voltage value [V]: 2

Voltage Ramp Step Time [ms] Ramp step variation = 1V: 1000

Figure A.1.3 Detail of the panel dedicated to voltage. The only condition to be respected is that the initial voltage value is lower than the final one.

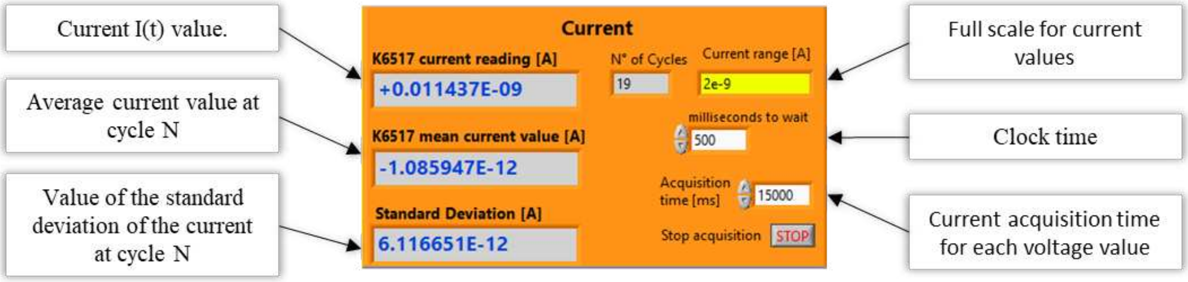

Current

K6517 current reading [A]: +0.011437E-09

N° of Cycles: 19

Current range [A]: 2e-9

milliseconds to wait: 500

K6517 mean current value [A]: -1.085947E-12

Acquisition time [ms]: 15000

Standard Deviation [A]: 6.116651E-12

Stop acquisition: STOP

Figure A.1.4 Detail of the panel dedicated to current. The only condition to be respected is that the initial voltage value is lower than the final one.

A.2 I-t/Q-t LabVIEW software

The I-t/Q-t acquisition program is dedicated to automating the acquisition of the current or charge produced over time by the device under examination, at a certain polarization voltage. Through serial port (RS-232) configuration, it is set to remotely manage the KEITHLEY 6517B multimeter. Figure A.2.1 shows the program's graphic interface.

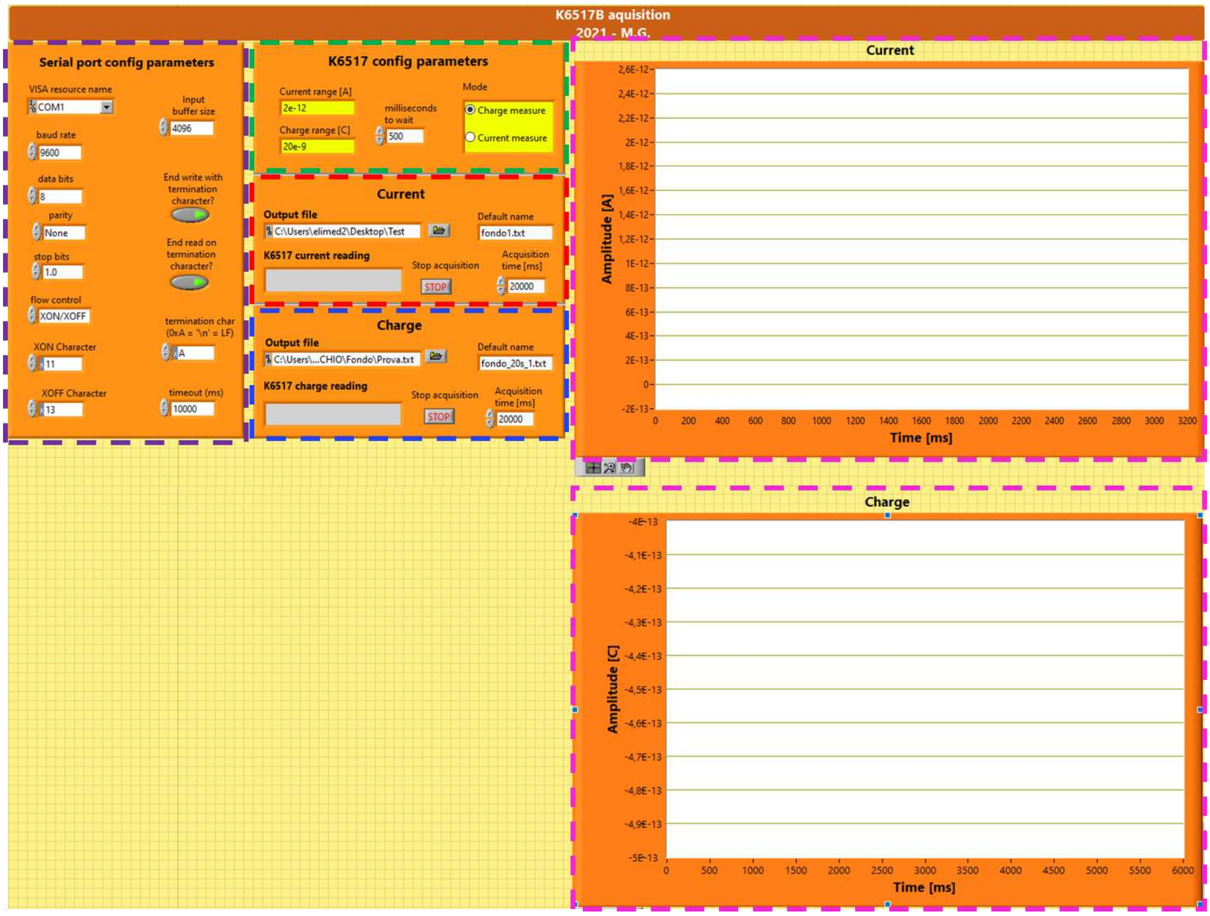

VISA resource name: COM1

baud rate: 9600

data bits: 8

parity: None

stop bits: 1.0

flow control: XON/XOFF

XON Character: 11

XOFF Character: 13

Input buffer size: 4096

End write with termination character?

End read on termination character?

termination char (0xA = '\n' = LF): A

timeout (ms): 10000

Current range [A]: 2e-12

Charge range [C]: 20e-9

milliseconds to wait: 500

Mode: ● Charge measure ○ Current measure

Output file: C:\Users\elimed2\Desktop\Test

Default name: fondo1.txt

Acquisition time [ms]: 20000

Output file: C:\Users\...CHIO\Fondo\Prova.txt

Default name: fondo_20s_1.txt

Acquisition time [ms]: 20000

Figure A.2.1. Graphical interface of the LabVIEW software dedicated to the automatic acquisition of the I-t/Q-t signals. Purple box: panel containing the KEITHLEY 6517B configuration parameters necessary to correctly set the communication protocol between the latter and the software. Green box: here it is possible to select the measurement mode (if you want to measure charge or current), the corresponding full scale and the clock time (i.e., the sampling rate). Red box: current panel; here it is possible to select the current acquisition time, the file name and destination folder. Furthermore, the instantaneous current value is displayed. Blue box: charge panel; here it is possible to select the charge acquisition time, the file name and destination folder. Furthermore, the instantaneous charge value is displayed. Pink box: graphs dedicated to displaying I(t) and Q(t).

The program logic is similar to that described in Section A.1, although considerably simplified, as there is no waiting time and the voltage management module is missing. Furthermore, the average value and standard deviation of the charge/current are not calculated, but its instantaneous value is plotted and saved as time varies.

When the program gets started, the section dedicated to configuring the serial port starts first, resulting in the opening of communication with the instrument, which imports the acquisition parameters set by the user (as shown in Figure A.1.2). At this point, the current or charge begins to be measured by the KEITHLEY and imported by the software, where it is displayed on a graph as a function of time, and on a dedicated display. Furthermore, as the measurement continues, a text file is compiled (at each clock) storing the instant of time and the corresponding current/charge value. Figure A.2.2 shows the panels dedicated to current and charge setting.

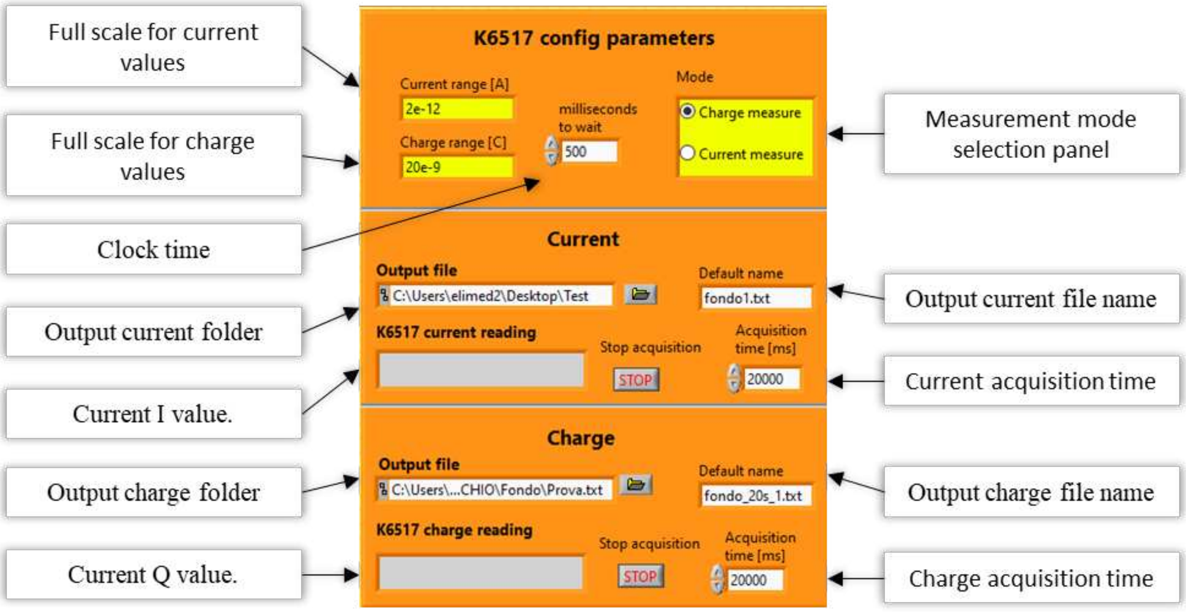

K6517 config parameters

Current range [A]: 2e-12
Charge range [C]: 20e-9
milliseconds to wait: 500
Mode: ● Charge measure ○ Current measure

Current

Output file: C:\Users\elimed2\Desktop\Test
Default name: fondo1.txt
Acquisition time [ms]: 20000

Charge

Output file: C:\Users\...CHIO\Fondo\Prova.txt
Default name: fondo_20s_1.txt
Acquisition time [ms]: 20000

Figure A.2.2 Detail of the panel dedicated to current and charge measurements.

Bibliography

[1] Amaldi, U., et al. "Accelerators for hadrontherapy: From Lawrence cyclotrons to linacs." *Nuclear Instruments and Methods in Physics Research Section A: Accelerators, Spectrometers, Detectors and Associated Equipment* 620.2-3 (2010): 563-577.

[2] Gordon, K., et al. "Fast and Furious: Fast Neutron Therapy in Cancer Treatment." *International Journal of Particle Therapy* 9.2 (2022): 59-69.

[3] Bragg, William Henry. "LXXIII. On the absorption of α rays, and on the classification of the α rays from radium." *The London, Edinburgh, and Dublin Philosophical Magazine and Journal of Science* 8.48 (1904): 719-725.

[4] Wilson, Robert R. "Radiological use of fast protons." *Radiology* 47.5 (1946): 487-491.

[5] Rossi, Sandro. "Hadron Therapy Achievements and Challenges: The CNAO Experience." *Physics* 4.1 (2022): 229-257.

[6] Amaldi, U., et al. "Construction, test and operation of a proton range radiography system." *Nuclear Instruments and Methods in Physics Research Section A: Accelerators, Spectrometers, Detectors and Associated Equipment* 629.1 (2011): 337-344.

[7] Slater, J. M., et al. "Proton beam irradiation: toward routine clinical utilization." *Excerpta Medica International Congress Series* 1073.1. Elsevier, 1994.

[8] Kawachi, K., et al. "Heavy ion medical accelerator facility in Japan", in *Hadrontherapy in Oncology: Proceedings of the First International Symposium on Hadrontherapy*, Como, Italy, 18–21 October 1993;

[9] Particle Therapy Co-Operative Group (PTCOG) web site, URL: https://www.ptcog.site/, last visit: 29/02/2024.

[10] Bulanov, S. V., et al. "Laser ion acceleration for hadron therapy." *Physics-Uspekhi* 57.12 (2014): 1149.

[11] Macchi, A., Borghesi, M., and Passoni, M., "Ion acceleration by superintense laser-plasma interaction." *Reviews of Modern Physics* 85.2 (2013): 751.

[12] Ledingham, Ken W. D., et al. "Towards laser driven hadron cancer radiotherapy: A review of progress." *Applied Sciences* 4.3 (2014): 402-443.

[13] Higginson, A., et al. "Near-100 MeV protons via a laser-driven transparency-enhanced hybrid acceleration scheme." *Nature communications* 9.1 (2018): 724.

[14] Loughran, B., et al. "Automated control and optimization of laser-driven ion acceleration." *High Power Laser Science and Engineering* 11 (2023): e35.

[15] Chaudhary, P., et al. "Cellular irradiations with laser-driven carbon ions at ultra-high dose rates." *Physics in Medicine & Biology* 68.2 (2023): 025015.

[16] Bulanov, S. V., and Khoroshkov, V. S. "Feasibility of using laser ion accelerators in proton therapy." *Plasma Physics Reports* 28 (2002): 453-456.

[17] Bolton, P., Parodi, K., & Schreiber, J. (Eds.). (2018). Applications of Laser-Driven Particle Acceleration (1st ed.). CRC Press.

[18] Brenner, C. M., et al. "Laser-driven x-ray and neutron source development for industrial applications of plasma accelerators." *Plasma Physics and Controlled Fusion* 58.1 (2015): 014039.

[19] Courtois, C., et al. "Characterisation of a MeV Bremsstrahlung x-ray source produced from a high intensity laser for high areal density object radiography." *Physics of Plasmas* 20.8 (2013).

[20] Jaroszynski, D. A., et al. "Radiation sources based on laser–plasma interactions." *Philosophical Transactions of the Royal Society A: Mathematical, Physical and Engineering Sciences* 364.1840 (2006): 689-710.

[21] Galy, J., Hamilton, D. J., and Normand, C. "High-intensity lasers as radiation sources: An overview of laser-induced nuclear reactions and applications." *The European Physical Journal Special Topics* 175.1 (2009): 147-152.

[22] Zylstra, A. B., et al., *Rev. Lett.* 117, 035002 (2016).

[23] Daido, H., Nishiuchi, M., and Pirozhkov, A. S. "Review of laser-driven ion sources and their applications." *Reports on progress in physics* 75.5 (2012): 056401.

[24] Passoni, M., et al. "Advanced laser-driven ion sources and their applications in materials and nuclear science." *Plasma Physics and Controlled Fusion* 62.1 (2019): 014022.

[25] Roth M., et al., *Phys. Rev. Lett.* 86, 436 (2001).

[26] Borghesi, M., et al. "Electric field detection in laser-plasma interaction experiments via the proton imaging technique." *Physics of Plasmas* 9.5 (2002): 2214-2220.

[27] Laschinsky, L., et al. "Radiobiological effectiveness of laser accelerated electrons in comparison to electron beams from a conventional linear accelerator." *Journal of Radiation Research* 53.3 (2012): 395-403.

[28] Bin, J., et al. "A laser-driven nanosecond proton source for radiobiological studies." *Applied Physics Letters* 101.24 (2012): 243701–243705.

[29] McAnespie, C. A., et al. "Laser-driven electron source suitable for single-shot Gy-scale irradiation of biological cells at dose-rates exceeding 10^{10} Gy/s." *arXiv preprint arXiv*:2309.06870 (2023).

[30] Durante, M., Bräuer-Krisch, E., and Hill, M. "Faster and safer? FLASH ultra-high dose rate in radiotherapy." *The British journal of radiology* 91.1082 (2018): 20170628.

[31] Lin, B., et al. "FLASH radiotherapy: history and future", *Front. Oncol.*, 11 (2021) 644400.

[32] Durante, M. "Physical Challenges of FLASH Radiotherapy." *Nuclear Physics News* 32.4 (2022): 28-31.

[33] Barker, H. E., et al. "The tumour microenvironment after radiotherapy: mechanisms of resistance and recurrence." *Nature Reviews Cancer* 15.7 (2015): 409-425.

[34] Kroll, F., et al. "Tumour irradiation in mice with a laser-accelerated proton beam." *Nature Physics* 18.3 (2022): 316-322.

[35] Gaide, O., et al. "Comparison of ultra-high versus conventional dose rate radiotherapy in a patient with cutaneous lymphoma." *Radiotherapy and Oncology* 174 (2022): 87-91.

[36] E. B. Podgorsak, Radiation Oncology Physics: A Handbook For Teachers And Students, International Atomic Energy Agency Vienna, 2005, © IAEA.

[37] Harald Paganetti, Proton Therapy Physics, Taylor & Francis Book, Series in Medical Physics and Biomedical Engineering, Editors: John G Webster, Slavik Tabakov, Kwan-Hoong Ng.

[38] ICRU Report 24 1976 Determination of Absorbed Dose in a Patient Irradiated by Beams of X or Gamma Rays in Radiotherapy Procedures ICRU Report No 24 (Bethesda, MD: International Commission on Radiation Units and Measurements).

[39] Raffaele Fedele Laitano, Fondamenti di Dosimetria delle Radiazioni Ionizzanti, 2015 ENEA, ISBN 978-88-8286-319-7, 4ª edition.

[40] IAEA 2000 Absorbed dose Determination in External Beam Radiotherapy—An International Code of Practice for Dosimetry based on Standards of Absorbed Dose to Water Technical Report Series No 398 (Vienna, Austria: International Atomic Energy Agency).

[41] Lamm, E., Harman, O., and Veigl S. J. "Before watson and crick in 1953 came friedrich miescher in 1869." *Genetics* 215.2 (2020): 291-296.

[42] Watson, J. D., and Crick, F. H. C. "The structure of DNA." *Cold Spring Harbor symposia on quantitative biology*. Vol. 18. Cold Spring Harbor Laboratory Press, 1953.

[43] Glenn F. Knoll, Radiation Detection and Measurement, John Wiley e Sons, Third Edition.

[44] Cussol, Daniel. "Nuclear physics and hadrontherapy." *La Colle sur Loup: Lectures at Ecole Joliot Curie* (2011).

[45] Eric J. Hall, Amato J. Giaccia. Radiobiology for the radiologist, Eighth edition. | Philadelphia : Wolters Kluwer, (2019).

[46] Desai, N., et al. "Immunofluorescence detection of clustered γ-H2AX foci induced by HZE-particle radiation." *Radiation research* 164.4 (2005): 518-522.

[47] Lomax, A. J. "Myths and realities of range uncertainty." *The British journal of radiology* 93.1107 (2020): 20190582.

[48] Joiner, Michael C., and Albert J. van der Kogel, eds. Basic clinical radiobiology. CRC press, 2018.

[49] Nuraini, R., and Widita, R. "Tumor control probability (TCP) and normal tissue complication probability (NTCP) with consideration of cell biological effect." *Journal of Physics: Conference Series*. Vol. 1245. No. 1. IOP Publishing, 2019.

[50] Abi, K. S. T., et al. "Tumor Control Probability (TCP) and Normal Tissue Complication Probability (NTCP) in Mono and Dual-isocentric Techniques of Breast Cancer Radiation Therapy." *Archives of Breast Cancer* (2021): 192-202.

[51] Tseng, H. H., et al. "The role of machine learning in knowledge-based response-adapted radiotherapy." *Frontiers in oncology* 8 (2018): 266.

[52] Mansour, Z., et al. "Study the influence of the number of beams on radiotherapy plans for the hyopfractionated treatment of breast cancer using biological model." *J Adv Physics* 16 (2019): 377-90.

[53] Hall E., Giaccia A., Radiobiology for the Radiologist. Philadelphia: Lippincott Williams & Wilkins (2006).

[54] Zaider, M., and Minerbo, G. N. "Tumour control probability: a formulation applicable to any temporal protocol of dose delivery." *Physics in Medicine & Biology* 45.2 (2000): 279.

[55] Goitein, M. "Tumor control probability for an inhomogeneously irradiated target volume." *Evaluation of treatment planning for particle beam radiotherapy* 5.1 (1987).

[56] El Naqa, I., Pater, P., and Seuntjens, J. "Monte Carlo role in radiobiological modelling of radiotherapy outcomes." *Physics in Medicine & Biology* 57.11 (2012): R75.

[57] Lyman, J. T. "Complication probability as assessed from dose-volume histograms." *Radiation Research* 104.2s (1985): S13-S19.

[58] Jäkel, O. "Radiotherapy with protons and ion beams." *AIP Conference Proceedings* 1231.1. American Institute of Physics, 2010.

[59] Bragg, W. H., and Kleeman, R. "XXXIX. On the α particles of radium, and their loss of range in passing through various atoms and molecules." *The London, Edinburgh, and Dublin Philosophical Magazine and Journal of Science* 10.57 (1905): 318-340.

[60] Schardt, D. "Hadrontherapy." Basic Concepts in Nuclear Physics: Theory, Experiments and Applications: 2015 La Rábida International Scientific Meeting on Nuclear Physics. Springer International Publishing, 2016.

[61] Leo, William R. Techniques for Nuclear and Particle Physics Experiments, Springer Verlag, Second Edition

[62] Bohr, N. "II. On the theory of the decrease of velocity of moving electrified particles on passing through matter." *The London, Edinburgh, and Dublin Philosophical Magazine and Journal of Science* 25.145 (1913): 10-31.

[63] SRIM - The Stopping and Range of Ions in Matter, URL: http://www.srim.org/.

[64] Rutherford, E. "LXXIX. The scattering of α and β particles by matter and the structure of the atom." *The London, Edinburgh, and Dublin Philosophical Magazine and Journal of Science* 21.125 (1911): 669-688.

[65] Schneider, U. "The calibration of CT Hounsfield units for radiotherapy treatment planning-Reply." *Physics in Medicine & Biology* 41.8 (1996): 1526-1527.

[66] Dance, D. R., et al. "Diagnostic radiology physics." *International Atomic Energy Agency* 299 (2014).

[67] Ishikawa, H., et al. "Particle therapy for prostate cancer: The past, present and future." *International journal of urology* 26.10 (2019): 971-979.

[68] ICRU Report 78: Prescribing, Recording, and Reporting Proton-Beam Therapy, Journal of the ICRU, Volume 7, Issue 2 (2007).

[69] Paganetti, H. "Range uncertainties in proton therapy and the role of Monte Carlo simulations." *Physics in Medicine & Biology* 57.11 (2012): R99.

[70] Andreo, P. "On the clinical spatial resolution achievable with protons and heavier charged particle radiotherapy beams." *Physics in Medicine & Biology* 54.11 (2009): N205.

[71] Lomax, A. J. "Myths and realities of range uncertainty." *The British journal of radiology* 93.1107 (2020): 20190582.

[72] Yang, M., et al. "Theoretical variance analysis of single-and dual-energy computed tomography methods for calculating proton stopping power ratios of biological tissues." *Physics in Medicine & Biology* 55.5 (2010): 1343.

[73] Sudhyadhom, A. "On the molecular relationship between Hounsfield Unit (HU), mass density, and electron density in computed tomography (CT)." *PLoS One* 15.12 (2020): e0244861.

[74] Li, H., et al. "Evaluating proton dose and associated range uncertainty using daily cone-beam CT." *Frontiers in Oncology* 12 (2022): 830981.

[75] Nhila, O., et al. "The effect of CT reconstruction filter selection on Hounsfield units in radiotherapy treatment planning." *Journal of Radiotherapy in Practice* 22 (2023): e102.

[76] Vestergaard, C. D., et al. "Tissue-specific range uncertainty estimation in proton therapy." *Physics and Imaging in Radiation Oncology* 26 (2023): 100441.

[77] Urie, M., et al. "Degradation of the Bragg peak due to inhomogeneities." *Physics in Medicine & Biology* 31.1 (1986): 1.

[78] Tommasino, F., and Durante, M. "Proton radiobiology." *Cancers* 7.1 (2015): 353-381.

[79] Marshall, T. I., et al. "Investigating the implications of a variable RBE on proton dose fractionation across a clinical pencil beam scanned spread-out Bragg peak." *International Journal of Radiation Oncology* Biology* Physics* 95.1 (2016): 70-77.

[80] Garbacz, M., et al. "Quantification of biological range uncertainties in patients treated at the Krakow proton therapy centre." *Radiation Oncology* 17.1 (2022): 1-13.

[81] Bai, X., et al. "Robust optimization to reduce the impact of biological effect variation from physical uncertainties in intensity-modulated proton therapy." *Physics in Medicine & Biology* 64.2 (2019): 025004.

[82] Albertini, F., et al. "Sensitivity of intensity modulated proton therapy plans to changes in patient weight." *Radiotherapy and Oncology* 86.2 (2008): 187-194.

[83] Town, C. D. "Effect of high dose rates on survival of mammalian cells." *Nature* 215.5103 (1967): 847-848.

[84] Berry, R. J., et al. "Survival of mammalian cells exposed to x rays at ultra-high dose-rates." *The British journal of radiology* 42.494 (1969): 102-107.

[85] Favaudon, V., et al. "Ultrahigh dose-rate FLASH irradiation increases the differential response between normal and tumor tissue in mice", *Sci. Transl. Med.* 6 (2014).

[86] Montay-Gruel, P., et al. "Irradiation in a flash: Unique sparing of memory in mice after whole brain irradiation with dose rates above 100 Gy/s." *Radiotherapy and Oncology* 124.3 (2017): 365-369.

[87] Vozenin, M. C., et al. "The advantage of FLASH radiotherapy confirmed in mini-pig and cat-cancer patients." *Clinical Cancer Research* 25.1 (2019): 35-42.

[88] Wilson, P., et al. "Revisiting the ultra-high dose rate effect: implications for charged particle radiotherapy using protons and light ions." *The British journal of radiology* 85.1018 (2012): e933-e939.

[89] De Kruijff, R. M. "FLASH radiotherapy: ultra-high dose rates to spare healthy tissue." *International journal of radiation biology* 96.4 (2020): 419-423.

[90] Bourhis, J., et al. "Clinical translation of FLASH radiotherapy: Why and how?." *Radiotherapy and oncology* 139 (2019): 11-17.

[91] Vozenin, M. C., et al. "The advantage of FLASH radiotherapy confirmed in mini-pig and cat-cancer patients." *Clinical Cancer Research* 25.1 (2019): 35-42.

[92] Hughes, J. R., and Parsons, J. L. "FLASH radiotherapy: current knowledge and future insights using proton-beam therapy." *International journal of molecular sciences* 21.18 (2020): 6492.

[93] Polevoy, G. G., et al. "Flash therapy for cancer: A potentially new radiotherapy methodology." *Cureus* 15.10 (2023).

[94] Kang, M., Ding, X., and Rong, Y. "FLASH instead of proton arc therapy is a more promising advancement for the next generation proton radiotherapy." *Journal of applied clinical medical physics* 24.8 (2023).

[95] Vozenin, M. C., Bourhis, J., and Durante, M. "Towards clinical translation of FLASH radiotherapy." *Nature Reviews Clinical Oncology* 19.12 (2022): 791-803.

[96] Mascia, A. E., et al. "Proton FLASH radiotherapy for the treatment of symptomatic bone metastases: The FAST-01 nonrandomized trial." *JAMA oncology* 9.1 (2023): 62-69.

[97] Schüler, E., et al. "Ultra‐high dose rate electron beams and the FLASH effect: From preclinical evidence to a new radiotherapy paradigm." *Medical physics* 49.3 (2022): 2082-2095.

[98] Jolly, S., et al. "Technical challenges for FLASH proton therapy." *Physica Medica* 78 (2020): 71-82.

[99] Montay‐Gruel, P., et al. "FLASH radiotherapy with photon beams." *Medical Physics* 49.3 (2022): 2055-2067.

[100] Gao, F., et al. "First demonstration of the FLASH effect with ultrahigh dose rate high-energy X-rays." *Radiotherapy and Oncology* 166 (2022): 44-50.

[101] Simeonov, Y., et al. "3D range-modulator for scanned particle therapy: development, Monte Carlo simulations and experimental evaluation." *Physics in Medicine & Biology* 62.17 (2017): 7075.

[102] Yokokawa, K., et al. "A new SOBP-formation method by superposing specially shaped Bragg curves formed by a mini-ridge filter for spot scanning in proton beam therapy." *Physica Medica* 67 (2019): 70-76.

[103] Weber, U. A., Scifoni, E., and Durante, M. "FLASH radiotherapy with carbon ion beams." *Medical Physics* 49.3 (2022): 1974-1992.

[104] Tinganelli, W., et al. "FLASH with carbon ions: Tumor control, normal tissue sparing, and distal metastasis in a mouse osteosarcoma model." *Radiotherapy and Oncology* 175 (2022): 185-190.

[105] Wardman, P. "Radiotherapy using high-intensity pulsed radiation beams (FLASH): a radiation-chemical perspective." *Radiation Research* 194.6 (2020): 607-617.

[106] Boscolo, D., et al. "May oxygen depletion explain the FLASH effect? A chemical track structure analysis." *Radiotherapy and Oncology* 162 (2021): 68-75.

[107] Favaudon, V., Labarbe, R., and Limoli, C. L. "Model studies of the role of oxygen in the FLASH effect." *Medical Physics* 49.3 (2022): 2068-2081.

[108] Labarbe, R., et al. "A physicochemical model of reaction kinetics supports peroxyl radical recombination as the main determinant of the FLASH effect." *Radiotherapy and Oncology* 153 (2020): 303-310.

[109] Ramos-Méndez, J., et al. "LET-dependent intertrack yields in proton irradiation at ultra-high dose rates relevant for FLASH therapy." *Radiation research* 194.4 (2020): 351-362.

[110] Jin, J. Y., et al. "Ultra-high dose rate effect on circulating immune cells: A potential mechanism for FLASH effect?." Radiotherapy and Oncology 149 (2020): 55-62.

[111] Oppelt, M., et al. "Comparison study of in vivo dose response to laser-driven versus conventional electron beam." *Radiation and Environmental Biophysics* 54 (2015): 155-166.

[112] McAnespie, C. A., et al. "Laser-driven electron source suitable for single-shot Gy-scale irradiation of biological cells at dose-rates exceeding 10^{10} Gy/s." *arXiv preprint arXiv*:2309.06870 (2023).

[113] Yogo, A., et al. "Application of laser-accelerated protons to the demonstration of DNA double-strand breaks in human cancer cells." *Applied Physics Letters* 94.18 (2009).

[114] Kraft, S. D., et al. "Dose-dependent biological damage of tumour cells by laser-accelerated proton beams." *New Journal of Physics* 12.8 (2010): 085003.

[115] Yogo, A., et al. "Measurement of relative biological effectiveness of protons in human cancer cells using a laser-driven quasimonoenergetic proton beamline." *Applied Physics Letters* 98.5 (2011).

[116] Richter, C., et al. "A dosimetric system for quantitative cell irradiation experiments with laser-accelerated protons." *Physics in Medicine & Biology* 56.6 (2011): 1529.

[117] Doria, D., et al. "Biological effectiveness on live cells of laser driven protons at dose rates exceeding 109 Gy/s." *AIP Advances* 2.1 (2012).

[118] Zeil, K., et al. "Dose-controlled irradiation of cancer cells with laser-accelerated proton pulses." *Applied Physics B* 110 (2013): 437-444.

[119] Raschke, S., et al. "Ultra-short laser-accelerated proton pulses have similar DNA-damaging effectiveness but produce less immediate nitroxidative stress than conventional proton beams." *Scientific reports* 6.1 (2016): 32441.

[120] Manti, L., et al. "The radiobiology of laser-driven particle beams: focus on sub-lethal responses of normal human cells." *Journal of Instrumentation* 12.03 (2017): C03084.

[121] Hanton, F., et al. "DNA DSB repair dynamics following irradiation with laser-driven protons at ultra-high dose rates." *Scientific Reports* 9.1 (2019): 4471.

[122] Bayart, E., et al. "Fast dose fractionation using ultra-short laser accelerated proton pulses can increase cancer cell mortality, which relies on functional PARP1 protein." *Scientific reports* 9.1 (2019): 10132.

[123] Chaudhary, P., et al. "Radiobiology experiments with ultra-high dose rate laser-driven protons: methodology and state-of-the-art." *Frontiers in Physics* 9 (2021): 624963.

[124] Esplen, N., Mendonca, M. S., and Bazalova-Carter, M. "Physics and biology of ultrahigh dose-rate (FLASH) radiotherapy: a topical review." *Physics in Medicine & Biology* 65.23 (2020): 23TR03.

[125] Ashraf, M. R., et al. "Dosimetry for FLASH radiotherapy: a review of tools and the role of radioluminescence and Cherenkov emission." *Frontiers in Physics* 8 (2020): 328.

[126] Kamada, T., et al. "Carbon ion radiotherapy in Japan: an assessment of 20 years of clinical experience." *The Lancet Oncology* 16.2 (2015): e93-e100.

[127] Degiovanni, A., and Amaldi, U. "History of hadron therapy accelerators." *Physica medica* 31.4 (2015): 322-332.

[128] Pidikiti, R., et al. "Commissioning of the world's first compact pencil‐beam scanning proton therapy system." *Journal of applied clinical medical physics* 19.1 (2018): 94-105.

[129] Vilches-Freixas, G., et al. "Beam commissioning of the first compact proton therapy system with spot scanning and dynamic field collimation." *The British journal of radiology* 93.1107 (2020): 20190598.

[130] Shang, C., et al. "Beam characteristics of the first clinical 360° rotational single gantry room scanning pencil beam proton treatment system and comparisons against a multi‐room system." *Journal of Applied Clinical Medical Physics* 21.9 (2020): 266-271.

[131] Krushelnick, K., et al. "Ultrahigh-intensity laser-produced plasmas as a compact heavy ion injection source." *IEEE transactions on plasma science* 28.4 (2000): 1110-1155.

[132] Borghesi, M., et al. "Laser-driven proton acceleration: source optimization and radiographic applications." *Plasma Physics and Controlled Fusion* 50.12 (2008): 124040.

[133] Haberberger, D., et al. "Collisionless shocks in laser-produced plasma generate monoenergetic high-energy proton beams." *Nature Physics* 8.1 (2012): 95-99.

[134] Hegelich, B. M., et al. "160 MeV laser-accelerated protons from CH2 nano-targets for proton cancer therapy." *arXiv preprint arXiv:*1310.8650 (2013).

[135] Ledingham, K. W. D., et al. "Towards laser driven hadron cancer radiotherapy: A review of progress." *Applied Sciences* 4.3 (2014): 402-443.

[136] Antici, P., et al. "Acceleration of collimated 45 MeV protons by collisionless shocks driven in low-density, large-scale gradient plasmas by a 1020 W/cm2, 1 μm laser." *Scientific reports* 7.1 (2017): 16463.

[137] Li, Y. F., et al. "Laser-driven time-limited light-sail acceleration of protons for tumor radiotherapy." *Physical Review Research* 5.1 (2023): L012038.

[138] Esirkepov, T., et al. "Highly efficient relativistic-ion generation in the laser-piston regime." *Physical review letters* 92.17 (2004): 175003.

[139] Paradkar, B. S. "Improved energy spread in the radiation pressure acceleration of protons with a linearly polarized laser." *Physical Review E* 108.2 (2023): 025203.

[140] Badziak, J. "Laser-driven ion acceleration: methods, challenges and prospects." *Journal of Physics: Conference Series*. Vol. 959. IOP Publishing, 2018.

[141] Strickland, D., and Mourou, G. "Compression of amplified chirped optical pulses." *Optics communications* 55.6 (1985): 447-449.

[142] Mourou, Gerard. "Nobel Lecture: Extreme light physics and application." *Reviews of Modern Physics* 91.3 (2019): 030501.

[143] Wilks, S. C., et al. "Energetic proton generation in ultra-intense laser–solid interactions." *Physics of plasmas* 8.2 (2001): 542-549.

[144] Roth, M., and M. Schollmeier. "Ion acceleration-target normal sheath acceleration." *arXiv preprint arXiv:*1705.10569 (2017).

[145] Gizzi, L. A. “Laser-Driven Sources of High Energy Particles and Radiation.” *Springer International Publishing*, 2019.

[146] U. Schramm et al. "First results with the novel petawatt laser acceleration facility in Dresden." *Journal of Physics: Conference Series*. 874.1. IOP Publishing, 2017.

[147] Torrisi, L., Cutroneo, M., and Torrisi., A. "Protons and carbon ions acceleration in the target‐normal‐sheath‐acceleration regime using low‐contrast fs laser and metal‐graphene targets." *Contributions to Plasma Physics* 60.1 (2020): e201900076.

[148] Măgureanu, A.,et al. "Target Characteristics Used in Laser-Plasma Acceleration of Protons Based on the TNSA Mechanism." *Frontiers in Physics* 10 (2022): 133.

[149] Markey, K., et al. "Divergence reduction of laser accelerated proton beams." *High Power Laser Science, Short Pulse Plasma Physics*.

[150] Hadjikyriacou, A., et al. "Novel approach to TNSA enhancement using multi-layered targets–a numerical study." *Plasma Physics and Controlled Fusion* (2023).

[151] Maffini, A., et al. "Towards compact laser-driven accelerators: exploring the potential of advanced double-layer targets." *EPJ Techniques and Instrumentation* 10.1 (2023): 15.

[152] Matys, M., et al. "High-quality laser-accelerated ion beams from structured targets." *Photonics* 10.1. MDPI, 2023.

[153] Puyuelo-Valdes, P., et al. "Implementation of a thin, flat water target capable of high-repetition-rate MeV-range proton acceleration in a high-power laser at the CLPU." *Plasma Physics and Controlled Fusion* 64.5 (2022): 054003.

[154] M. Zimmer, A., et al., “Analysis of laser-proton acceleration experiments for development of empirical scaling laws”, *Physical Review E* 104.4 (2021): 045210.

[155] Fuchs, J., et al. "Laser-driven proton scaling laws and new paths towards energy increase." *Nature physics* 2.1 (2006): 48-54.

[156] Snavely, R. A., et al. "Intense high-energy proton beams from petawatt-laser irradiation of solids." *Physical review letters* 85.14 (2000): 2945.

[157] Gaillard, S. A., et al. "Increased laser-accelerated proton energies via direct laser-light-pressure acceleration of electrons in microcone targets." *Physics of Plasmas* 18.5 (2011).

[158] Wagner, F., et al. "Maximum proton energy above 85 MeV from the relativistic interaction of laser pulses with micrometer thick CH 2 targets." *Physical review letters* 116.20 (2016): 205002.

[159] Neely, D., et al. "Enhanced proton beams from ultrathin targets driven by high contrast laser pulses." *Applied Physics Letters* 89.2 (2006).

[160] Zeil, K., et al. "The scaling of proton energies in ultrashort pulse laser plasma acceleration." *New Journal of Physics* 12.4 (2010): 045015.

[161] Choi, I. W., et al. "Simultaneous generation of ions and high-order harmonics from thin conjugated polymer foil irradiated with ultrahigh contrast laser." *Applied Physics Letters* 99.18 (2011).

[162] Zeil, K., et al. "Direct observation of prompt pre-thermal laser ion sheath acceleration." *Nature communications* 3.1 (2012): 874.

[163] Margarone, D., et al. "Laser-driven proton acceleration enhancement by nanostructured foils." *Physical review letters* 109.23 (2012): 234801.

[164] Ogura, K., et al. "Proton acceleration to 40 MeV using a high intensity, high contrast optical parametric chirped-pulse amplification/Ti: sapphire hybrid laser system." *Optics Letters* 37.14 (2012): 2868-2870.

[165] Kim, I. J., et al. "Transition of proton energy scaling using an ultrathin target irradiated by linearly polarized femtosecond laser pulses." Physical review letters 111.16 (2013): 165003.

[166] Green, J. S., et al. "High efficiency proton beam generation through target thickness control in femtosecond laser-plasma interactions." *Applied Physics Letters* 104.21 (2014).

[167] Zeil, K., et al. "Robust energy enhancement of ultrashort pulse laser accelerated protons from reduced mass targets." *Plasma Physics and Controlled Fusion* 56.8 (2014): 084004.

[168] Margarone, D., et al. "Laser-driven high-energy proton beam with homogeneous spatial profile from a nanosphere target." *Physical Review Special Topics-Accelerators and Beams* 18.7 (2015): 071304.

[169] Passoni, M., et al. "Toward high-energy laser-driven ion beams: Nanostructured double-layer targets." *Physical Review Accelerators and Beams* 19.6 (2016): 061301.

[170] Seimetz, M., et al. "Proton acceleration with a table-top TW laser." *Journal of Instrumentation* 11.11 (2016): C11012.

[171] Higginson, A., et al. "Near-100 MeV protons via a laser-driven transparency-enhanced hybrid acceleration scheme." *Nature communications* 9.1 (2018): 724.

[172] Frazer, T. P., et al. "Enhanced laser intensity and ion acceleration due to self-focusing in relativistically transparent ultrathin targets." *Physical Review Research* 2.4 (2020): 042015.

[173] Falk, F., et al., "Laser-driven low energy electron beams for single-shot ultra-fast probing of meso-scale materials and warm dense matter" *Scientific Reports* 13.1 (2023): 4252.

[174] Ahmed, H., et al., "High energy implementation of coil-target scheme for guided re-acceleration of laser-driven protons" *Scientific Reports* 11.1 (2021): 699.

[175] Bolton, P. R., et al. "Instrumentation for diagnostics and control of laser-accelerated proton (ion) beams." *Physica Medica* 30.3 (2014): 255-270.

[176] ICRU Report 50: Prescribing, Recording, and Reporting Photon Beam Therapy, Journal of the ICRU, Volume os-26 Issue 1 (1993).

[177] ICRU Report 62: Prescribing, Recording and Reporting Photon Beam Therapy (Supplement to ICRU Report 50), Journal of the ICRU, Volume os-32 Issue 1 (1999).

[178] Ku, Y., et al. "Tackling range uncertainty in proton therapy: Development and evaluation of a new multi-slit prompt-gamma camera (MSPGC) system." *Nuclear Engineering and Technology* 55.9 (2023): 3140-3149.

[179] Bertschi, S., et al. "Potential margin reduction in prostate cancer proton therapy with prompt gamma imaging for online treatment verification." *Physics and Imaging in Radiation Oncology* 26 (2023): 100447.

[180] Bertholet, J., et al. "Real-time intrafraction motion monitoring in external beam radiotherapy." *Physics in Medicine & Biology* 64.15 (2019): 15TR01.

[181] Litzenberg, D. W., et al. "On‐line monitoring of radiotherapy beams: Experimental results with proton beams." *Medical Physics* 26.6 (1999): 992-1006.

[182] Tattenberg, S., et al. "Range uncertainty reductions in proton therapy may lead to the feasibility of novel beam arrangements which improve organ‐at‐risk sparing." *Medical Physics* 49.7 (2022): 4693-4704.

[183] Yasui, K., et al. "Dosimetric impact of systematic spot position errors in spot scanning proton therapy of head and neck tumor." *Journal of Cancer Research and Therapeutics* 19.Suppl 1 (2023): S228-S233.

[184] Seo, J., et al. "Study of a plastic scintillating plate-based quality assurance system for pencil beam scanning proton beams." *Journal of Cancer Research and Therapeutics* (2023).

[185] Thasasi, P., et al. "Determination of Integral Depth Dose in Proton Pencil Beam Using Plane-parallel Ionization Chambers." *International Journal of Particle Therapy* 9.2 (2022): 1-9.

[186] Nichiporov, D., et al. "Multichannel detectors for profile measurements in clinical proton fields." *Medical Physics* 34.7 (2007): 2683-2690.

[187] Leverington, B. D., et al. "A prototype scintillating fibre beam profile monitor for Ion Therapy beams." *Journal of Instrumentation* 13.05 (2018): P05030.

[188] Lo Presti, D., et al. "Real-time particle radiography by means of scintillating fibers tracker and residual range detectors." *Applications of Optical Fibers for Sensing. IntechOpen*, 2018.

[189] Karger, C. P., et al. "Dosimetry for ion beam radiotherapy." *Physics in Medicine & Biology* 55.21 (2010): R193.

[190] Stasi, M., et al. "D-IMRT verification with a 2D pixel ionization chamber: dosimetric and clinical results in head and neck cancer." *Physics in Medicine & Biology* 50.19 (2005): 4681.

[191] International Atomic Energy Agency (IAEA) web site, URL: https://www.iaea.org/, last visit: 29/02/2024.

[192] Zhang, R., and Newhauser, W. D. "Calculation of water equivalent thickness of materials of arbitrary density, elemental composition and thickness in proton beam irradiation." *Physics in Medicine & Biology* 54.6 (2009): 1383.

[193] Ashland™, Gafchromic radiotherapy films, URL: http://www.gafchromic.com/gafchromic-film/radiotherapy-films/index.asp, last visit: 29/02/2024.

[194] Cuttone, G., et al. "CATANA protontherapy facility: The state of art of clinical and dosimetric experience." *The European Physical Journal Plus* 126 (2011): 1-7.

[195] Gorjiara, T., et al. "Investigation of radiological properties and water equivalency of PRESAGE® dosimeters." *Medical Physics* 38.4 (2011): 2265-2274.

[196] Büyükyildiz, M. "Charged particle interactions of human organs and tissues in heavy ion therapy; effective atomic number and electron density." *Afyon Kocatepe Üniversitesi Fen Ve Mühendislik Bilimleri Dergisi* 20.2 (2020): 196-206.

[197] Almurayshid, M., et al. "Quality assurance in proton beam therapy using a plastic scintillator and a commercially available digital camera." *Journal of Applied Clinical Medical Physics* 18.5 (2017): 210-219.

[198] Dhanesar, S., et al. "Quality assurance of proton beams using a multilayer ionization chamber system." *Medical Physics* 40.9 (2013): 092102.

[199] Cirio, R., et al. "Two-dimensional and quasi-three-dimensional dosimetry of hadron and photon beams with the magic cube and the pixel ionization chamber." *Physics in Medicine & Biology* 49.16 (2004): 3713.

[200] Farace, P., Righetto, R., and Meijers, A. "Pencil beam proton radiography using a multilayer ionization chamber." *Physics in Medicine & Biology* 61.11 (2016): 4078.

[201] Tommasino, F., et al. "Proton beam characterization in the experimental room of the Trento Proton Therapy facility." *Nuclear Instruments and Methods in Physics Research Section A: Accelerators, Spectrometers, Detectors and Associated Equipment* 869 (2017): 15-20.

[202] Braccini, S., et al. "Segmented ionization chambers for beam monitoring in hadrontherapy." *Modern Physics Letters A* 30.17 (2015): 1540026.

[203] Lee, K. S., et al. "Test of a Multilayer Dose-Verification Gaseous Detector with Raster Scan Mode Proton Beams." *arXiv preprint arXiv*:1506.01517 (2015).

[204] Mirandola, A., et al. "Characterization of a multilayer ionization chamber prototype for fast verification of relative depth ionization curves and spread‐out‐Bragg‐peaks in light ion beam therapy." *Medical Physics* 45.5 (2018): 2266-2277.

[205] Kwon, J. W., et al., "Development of a CCD-scintillator device and a multi-layer Faraday cup for therapeutic proton beam monitoring." *Journal of the Korean Physical Society* 48.9 (2006): 759.

[206] Nesteruk, K. P., et al. "Measurement of the beam energy distribution of a medical cyclotron with a multi-leaf Faraday cup." *Instruments* 3.1 (2019): 4.

[207] Kunert, C., et al. "A Multi-Leaf Faraday Cup especially for proton therapy of ocular tumors." *Proc. 5th International Particle Accelerator Conference* (IPAC'14). 2014.

[208] Archambault, L., et al. "Verification of proton range, position, and intensity in IMPT with a 3D liquid scintillator detector system." *Medical Physics* 39.3 (2012): 1239-1246.

[209] Beddar, S., et al. "Exploration of the potential of liquid scintillators for real‐time 3D dosimetry of intensity modulated proton beams." *Medical Physics* 36.5 (2009): 1736-1743.

[210] Saint-Gobain Crystals. Organic scintillation materials. USA. 2011. http://www.crystals.saint-gobain.com/

[211] Birks JB. The Theory and Practice of Scintillation Counting. Oxford: Pergamon; 1964.

[212] Kirby, D., et al. "LET dependence of GafChromic films and an ion chamber in low-energy proton dosimetry." *Physics in Medicine & Biology* 55.2 (2009): 417.

[213] Russo, S., et al. "Characterization of a commercial scintillation detector for 2-D dosimetry in scanned proton and carbon ion beams." *Physica Medica* 34 (2017): 48-54.

[214] Devic, S. "Radiochromic film dosimetry: past, present, and future." *Physica Medica* 27.3 (2011): 122-134.

[215] Reinhardt, S., et al. "Comparison of Gafchromic EBT2 and EBT3 films for clinical photon and proton beams." *Medical Physics* 39.8 (2012): 5257-5262.

[216] Kaufman, J., et al. "Radiochromic film diagnostics for laser-driven ion beams." *Research Using Extreme Light: Entering New Frontiers with Petawatt-Class Lasers II.* Vol. 9515. SPIE, 2015.

[217] Cirrone, G. A. P., et al. "Use of radiochromic films for the absolute dose evaluation in high dose-rate proton beams." *Journal of Instrumentation* 15.04 (2020): C04029.

[218] Schollmeier, M., et al. "Improved spectral data unfolding for radiochromic film imaging spectroscopy of laser-accelerated proton beams." Review of Scientific Instruments 85.4 (2014).

[219] Karsch, L., et al. "Dose rate dependence for different dosimeters and detectors: TLD, OSL, EBT films, and diamond detectors." *Medical Physics* 39.5 (2012): 2447-2455.

[220] Lehrack, S., et al. "Ionoacoustic detection of swift heavy ions." *Nuclear Instruments and Methods in Physics Research Section A: Accelerators, Spectrometers, Detectors and Associated Equipment* 950 (2020): 162935.

[221] Kellnberger, S., et al. "Ionoacoustic tomography of the proton Bragg peak in combination with ultrasound and optoacoustic imaging." *Scientific reports* 6.1 (2016): 29305.

[222] Jang, K. W., et al., “Measurements of Relative Depth Doses in Induced by High-Energy Proton Beam Using Multi-Dimensional Fiber-Optic Radiation Sensor.” *Proceedings of the KNS spring meeting*,(pp. 1CD-ROM). Korea, Republic of: KNS.

[223] Zhao, L., et al. "Determination of the depth dose distribution of proton beam using PRESAGE TM dosimeter." *Journal of Physics: Conference Series.* 250.1. IOP Publishing, 2010.

[224] Schilling, I., et al. "Measuring the Beam Energy in Proton Therapy Facilities Using ATLAS IBL Pixel Detectors." *Instruments* 6.4 (2022): 80.

[225] Liu, K., et al. "Evaluation of ion chamber response for applications in electron FLASH radiotherapy." *Medical Physics* 51.1 (2024): 494-508.

[226] Yang, Y., et al. "Commissioning a 250 MeV research beamline for proton FLASH radiotherapy preclinical experiments." *Medical Physics* (2023).

[227] Huang, S., et al. "Implementation of novel measurement‐based patient‐specific QA for pencil beam scanning proton FLASH radiotherapy." *Medical Physics* (2023).

[228] Zou, W., et al. "Framework for Quality Assurance of Ultra-High Dose Rate Clinical Trials Investigating FLASH Effects and Current Technology Gaps." *International Journal of Radiation Oncology* Biology* Physics* (2023).

[229] Schmitz, B., et al., "Automated reconstruction of the initial distribution of laser accelerated ion beams from radiochromic film (RCF) stacks." *Review of Scientific Instruments* 93.9 (2022).

[230] Reimold, M., et al. "Dosimetry for radiobiological in vivo experiments at laser plasma-based proton accelerators." *Physics in Medicine & Biology* 68.18 (2023): 185009.

[231] Zhang, Y., et al. "Energy calibration of a CR-39 nuclear-track detector irradiated by charged particles." *Nuclear Science and Techniques* 30.6 (2019): 87.

[232] Istokskaia, V., et al. "Proton Bragg curve and energy reconstruction using an online scintillator stack detector." *Review of Scientific Instruments* 94.7 (2023).

[233] Favaudon, V., et al. "Time-resolved dosimetry of pulsed electron beams in very high dose-rate, FLASH irradiation for radiotherapy preclinical studies." *Nuclear Instruments and Methods in Physics Research Section A: Accelerators, Spectrometers, Detectors and Associated Equipment* 944 (2019): 162537.

[234] Englbrecht, F. S., et al. "An online, radiation hard proton energy-resolving scintillator stack for laser-driven proton bunches." *Radiation Protection Dosimetry* 180.1-4 (2018): 291-295.

[235] Metzkes, J., et al. "A scintillator-based online detector for the angularly resolved measurement of laser-accelerated proton spectra." *Review of Scientific Instruments* 83.12 (2012).

[236] Metzkes, J., et al. "An online, energy-resolving beam profile detector for laser-driven proton beams." Review of Scientific Instruments 87.8 (2016).

[237] Geulig, L. D., et al. "Online charge measurement for petawatt laser-driven ion acceleration." *Review of Scientific Instruments* 93.10 (2022).

[238] Haffa, D., et al. "I-BEAT: Ultrasonic method for online measurement of the energy distribution of a single ion bunch." Scientific reports 9.1 (2019): 6714.

[239] Tsunenobu Kimoto and James A. Cooper, Fundamentals of silicon carbide technology: growth, characterization, devices and applications, © 2014 John Wiley & Sons Singapore Pte. Ltd.

[240] Di Giovanni, F. "Silicon Carbide: Physics, Manufacturing, and Its Role in Large-Scale Vehicle Electrification." *Chips* 2.3 (2023): 209-222.

[241] Wondrak, W., et al. "SiC devices for advanced power and high-temperature applications." *IEEE Transactions on Industrial Electronics* 48.2 (2001): 307-308.

[242] Saddow, Stephen E. Silicon carbide biotechnology: a biocompatible semiconductor for advanced biomedical devices and applications. Elsevier, 2011.

[243] Rius, Gemma, and Philippe Godignon, eds. Epitaxial Graphene on Silicon Carbide: Modeling, Characterization, and Applications. CRC Press, 2018.

[244] Rikner, G. , and Grusell, E. "General specifications for silicon semiconductors for use in radiation dosimetry." *Physics in Medicine & Biology* 32.9 (1987): 1109.

[245] Bruzzi, M. "Novel silicon devices for radiation therapy monitoring." *Nuclear Instruments and Methods in Physics Research Section A: Accelerators, Spectrometers, Detectors and Associated Equipment* 809 (2016): 105-112.

[246] Bertuccio, G., et al. "Silicon carbide detectors for in vivo dosimetry." *IEEE Transactions on Nuclear Science* 61.2 (2014): 961-966.

[247] Bruzzi, M., et al. "Epitaxial silicon devices for dosimetry applications." *Applied physics letters* 90.17 (2007).

[248] Rozenfeld A. B., “Advanced Semiconductor Dosimetry in Radiation Therapy” in Proceedings of Concepts And Trends In Medical Radiation Dosimetry Conference, Wollongong (Australia), 15–18 September 2010, edited by Rosenfeld A., Kron T., D’Errico F. and Moscovitch M., Vol. 1345 (American Institute of Physics) 2011.

[249] Griessbach, I., et al. "Dosimetric characteristics of a new unshielded silicon diode and its application in clinical photon and electron beams." *Medical Physics* 32.12 (2005): 3750-3754.

[250] Ciancaglioni, I., et al. "Dosimetric characterization of a synthetic single crystal diamond detector in clinical radiation therapy small photon beams." *Medical Physics* 39.7Part1 (2012): 4493-4501.

[251] De Angelis, C., et al. "An investigation of the operating characteristics of two PTW diamond detectors in photon and electron beams." *Medical Physics* 29.2 (2002): 248-254.

[252] Schirru, F., et al. "Single crystal diamond detector for radiotherapy." *Journal of Physics D: Applied Physics* 43.26 (2010): 265101.

[253] Manfredotti, C. "CVD diamond detectors for nuclear and dosimetric applications." *Diamond and Related Materials* 14.3-7 (2005): 531-540.

[254] Di Venanzio, C., et al. "Characterization of a synthetic single crystal diamond Schottky diode for radiotherapy electron beam dosimetry." *Medical Physics* 40.2 (2013): 021712.

[255] Marinelli, M., et al. "Dosimetric characterization of a synthetic single crystal diamond detector in a clinical 62 MeV ocular therapy proton beam." *Nuclear Instruments and Methods in Physics Research Section A: Accelerators, Spectrometers, Detectors and Associated Equipment* 767 (2014): 310-317.

[256] Marinelli, M., et al. "Dosimetric characterization of a microDiamond detector in clinical scanned carbon ion beams." *Medical Physics* 42.4 (2015): 2085-2093.

[257] Marinelli, M., et al. "A novel synthetic single crystal diamond device for in vivo dosimetry." *Medical Physics* 42.8 (2015): 4636-4644.

[258] Kampfer, S., et al. "Dosimetric characterization of a single crystal diamond detector in X-ray beams for preclinical research." *Zeitschrift für Medizinische Physik* 28.4 (2018): 303-309.

[259] Marinelli, M., et al. "Design, realization, and characterization of a novel diamond detector prototype for FLASH radiotherapy dosimetry." *Medical Physics* 49.3 (2022): 1902-1910.

[260] Bruzzi, M., et al., “High quality SiC applications in radiation dosimetry”, *Appl. Surf. Sci.*, 184 (2001) 425.

[261] Cannavò et al., in Proceedings of 5th Workshop-Plasmi, Sorgenti, Biofisica ed Applicazioni, Department of Mathematics and Physics, University of Salento (Italy), 15–

14 October 2016, edited by Nassisi V. and Delle Side D., Vol. 2016 (ESE - Salento University Publishing) 2017, pp. 23–27.

[262] Bruzzi, M., et al. "Characterisation of silicon carbide detectors response to electron and photon irradiation." *Diamond and related materials* 10.3-7 (2001): 657-661.

[263] Liu, L. Y., et al. "Properties of 4H silicon carbide detectors in the radiation detection of 86 MeV oxygen particles." *Diamond and Related Materials* 73 (2017): 177-181.

[264] Mandal, K. C., Kleppinger, J. W., and Chaudhuri, S. K. "Advances in high-resolution radiation detection using 4H-SiC epitaxial layer devices." *Micromachines* 11.3 (2020): 254.

[265] Mandal, K. C., Chaudhuri, S. K., and Ruddy, F. H. "Fabrication and characterization of high-resolution 4H-SiC epitaxial radiation detectors for challenging reactor dosimetry environments." *EPJ Web of Conferences*. 278. EDP Sciences, 2023.

[266] Romano, F., et al. "First Characterization of Novel Silicon Carbide Detectors with Ultra-High Dose Rate Electron Beams for FLASH Radiotherapy." *Applied Sciences* 13.5 (2023): 2986.

[267] Nava, F., et al. "Silicon carbide and its use as a radiation detector material." *Measurement Science and Technology* 19.10 (2008): 102001.

[268] De Napoli, M. "SiC detectors: A review on the use of silicon carbide as radiation detection material." *Frontiers in Physics* (2022): 769.

[269] Guarrera, M., et al. "Characterization of a SiC detector for dosimetric application." Il nuovo cimento C 45.4 (2022): 1-9.

[270] Arnault, J. C., Saada, S., and Ralchenko, V. "Chemical vapor deposition single‐crystal diamond: a review." *Phys. Status Solidi–Rapid Research Letters* 16.1 (2022): 2100354.

[271] Lan, L., et al. "Priming effect on a polycrystalline CVD diamond detector under 60Co γ-rays irradiation." *Nuclear Instruments and Methods in Physics Research Section A: Accelerators, Spectrometers, Detectors and Associated Equipment* 672 (2012): 29-32.

[272] Fidanzio, A., et al. "Investigation of natural diamond detector priming effect during electron beam irradiation." *Nuclear Instruments and Methods in Physics Research Section B: Beam Interactions with Materials and Atoms* 245.2 (2006): 421-426.

[273] Bruzzi, M., and Verroi, E. "Epitaxial SiC Dosimeters and Flux Monitoring Detectors for Proton Therapy Beams." *Materials* 16.10 (2023): 3643.

[274] Bertuccio, G., et al. "Silicon carbide for high resolution X-ray detectors operating up to 100 C." *Nuclear Instruments and Methods in Physics Research Section A: Accelerators, Spectrometers, Detectors and Associated Equipment* 522.3 (2004): 413-419.

[275] Bertuccio, G., et al. "Advances in silicon carbide X-ray detectors." *Nuclear Instruments and Methods in Physics Research Section A: Accelerators, Spectrometers, Detectors and Associated Equipment* 652.1 (2011): 193-196.

[276] Sciuto, A., et al. "Visible Blind 4H-SiC P+ -N UV Photodiode Obtained by Al Implantation." *IEEE Photonics Journal* 7.3 (2015): 1-6.

[277] Sumesh, M. A., and Karanth, S. P. "SiC dosimeter for solar ultraviolet exposure monitoring." *ISSS Journal of Micro and Smart Systems* 12.2 (2023): 127-132.

[278] Lioliou, G., et al. "4H-SiC Schottky diodes with Ni2Si contacts for X-ray detection." *Nuclear Instruments and Methods in Physics Research Section A: Accelerators, Spectrometers, Detectors and Associated Equipment* 940 (2019): 328-336.

[279] Bruzzi, M., et al., in Proceedings of the International Symposium on Optical Science and Technology, San Diego (CA, United States), 30 July - 4 August 2000, edited by James R. B. and Schirato R. C., Hard X-Ray, Gamma-Ray, and Neutron Detector Physics II, Vol. 4141 (SPIE) 2000, p. 48.

[280] Altana, C., et al. "Radiation Damage by Heavy Ions in Silicon and Silicon Carbide Detectors." *Sensors* 23.14 (2023): 6522.

[281] Bernat, R., et al. "Response of 4H-SiC detectors to ionizing particles." *Crystals* 11.1 (2020): 10.

[282] Lo Giudice, A., et al. "Average energy dissipated by mega-electron-volt hydrogen and helium ions per electron-hole pair generation in 4H-SiC." *Applied Physics Letters* 87.22 (2005).

[283] Nava, F., et al. "Investigation of Ni/4H-SiC diodes as radiation detectors with low doped n-type 4H-SiC epilayers." *Nuclear Instruments and Methods in Physics Research Section A: Accelerators, Spectrometers, Detectors and Associated Equipment* 510.3 (2003): 273-280.

[284] Bruzzi, M., et al. "Characterisation of epitaxial SiC Schottky barriers as particle detectors." *Diamond and related materials* 12.3-7 (2003): 1205-1208.

[285] Chaudhuri, S. K., et al. "Schottky barrier detectors on 4H-SiC n-type epitaxial layer for alpha particles." *Nuclear Instruments and Methods in Physics Research Section A: Accelerators, Spectrometers, Detectors and Associated Equipment* 701 (2013): 214-220.

[286] Ruddy, F. H., et al. "The charged particle response of silicon carbide semiconductor radiation detectors." *Nuclear Instruments and Methods in Physics Research Section A: Accelerators, Spectrometers, Detectors and Associated Equipment* 505.1-2 (2003): 159-162.

[287] Petringa, G., et al. "First characterization of a new Silicon Carbide detector for dosimetric applications." *Journal of Instrumentation* 15.05 (2020): C05023.

[288] Matsumoto, T., et al. "Development of a SiC semiconductor-based dosimeter for evaluating clinical dose distribution in carbon ion cancer therapy fields." *Nuclear Instruments and Methods in Physics Research Section B: Beam Interactions with Materials and Atoms* 542 (2023): 151-157.

[289] Yamaguchi, K., et al. "Linear energy transfer (LET) spectroscopy and relative biological effect estimation by SiC-based dosimeter at clinical carbon-beam cancer therapy field." *Journal of Physics: Conference Series*. 2326.1. IOP Publishing, 2022.

[290] Kada, W., et al. "Development of wide-bandgap semiconductor-based dosimeter for LET distribution measurement in carbon therapy filed." *Journal of Physics: Conference Series*. 1662.1. IOP Publishing, 2020.

[291] Margarone, D., et al. "Full characterization of laser-accelerated ion beams using Faraday cup, silicon carbide, and single-crystal diamond detectors." *Journal of Applied Physics* 109.10 (2011).

[292] Torrisi (2015) - Torrisi L. et al., in Proceedings of the 4th Workshop-Plasmi, Sorgenti, Biofisica ed Applicazioni, Lecce (Italy), 17-18 October 2014, edited by Nassisi V., Delle Side D. and Giuffreda E., Vol. 2014 (ESE - Salento University Publishing) 2015, pp. 69–73.

[293] Milluzzo, G., et al. "Laser-accelerated ion beam diagnostics with TOF detectors for the ELIMED beam line." *Journal of Instrumentation* 12.02 (2017): C02025.

[294] Bertuccio, G., et al. "Silicon carbide detector for laser-generated plasma radiation." *Applied Surface Science* 272 (2013): 128-131.

[295] Berzelius, J.J. (1824) Ann. Phys. Chem. Lpz., 1, 169.

[296] Acheson, E.G. (1892) English Patent 17911 Production of artificial crystalline carbonaceous materials, carborundum.

[297] Lely, J.A. (1955) Darstellung von einkristallen von siliziumcarbid und beherrschung von art und menge dereingebauten verunreinigungen. Ber. Dtsch. Keram. Ges., 32, 229.

[298] Tairov, Y. M., and Tsvetkov, V. F. "Investigation of growth processes of ingots of silicon carbide single crystals." *Journal of crystal growth* 43.2 (1978): 209-212.

[299] WOLFSPEED Company web site, URL: https://www.wolfspeed.com/, last visit: 29/02/2024.

[300] Silicon carbide, Wikipedia page, URL: https://en.wikipedia.org/wiki/Silicon_carbide, last visit: 29/02/2024.

[301] Electronics Weekly web site, URL: https://www.electronicsweekly.com/news/business/manufacturing/sts-first-200mm-house-sic-wafers-2021-07/, last visit: 29/02/2024.

[302] Matsunami, H., et al. "Epitaxial growth of α-SiC layers by chemical vapor deposition technique." *Vapour Growth and Epitaxy*. Elsevier, 1975. 72-75.

[303] Mynbaeva, M., et al. "Chemical vapor deposition of 4H–SiC epitaxial layers on porous SiC substrates." *Applied Physics Letters* 78.1 (2001): 117-119.

[304] Kimoto, T., et al. "Reduction of doping and trap concentrations in 4H–SiC epitaxial layers grown by chemical vapor deposition." *Applied Physics Letters* 79.17 (2001): 2761-2763.

[305] Yuebin, H. Y., and Jianxin, S. "Advances in Chemical Vapor Deposition Equipment Used for SiC Epitaxy." *Journal of Synthetic Crystals* 51.7 (2022).

[306] Tudisco, S., et al. "SiCILIA—silicon carbide detectors for intense luminosity investigations and applications." *Sensors* 18.7 (2018): 2289.

[307] Di Paolo Emilio, M., "Improving the SiC Wafer Process", URL: https://www.powerelectronicsnews.com/improving-the-sic-wafer-process/, last visit: 29/02/2024.

[308] Kyoto Semiconductor Company web site, URL: https://www.kyosemi.co.jp/en/knowledgecenter/semiconductor_process/, last visit: 29/02/2024.

[309] US|3025589|Hoerni, J. A.: Method of Manufacturing Semiconductor Devices filed May 1, 1959.

[310] US|3064167|Hoerni, J. A.: Semiconductor device filed May 15, 1960.

[311] Waits, R. K. "Evolution of integrated-circuit vacuum processes: 1959–1975." *Journal of Vacuum Science & Technology A: Vacuum, Surfaces, and Films* 18.4 (2000): 1736-1745.

[312] Lojek, Bo (2007). History of Semiconductor Engineering. Springer Science & Business Media. p. 120. ISBN 9783540342588.

[313] Hunter, G. W., Kremic, T., and Neudeck, P. G. "High temperature electronics for Venus surface applications: A summary of recent technical advances." (2020).

[314] Neudeck, P. G., et al. "Recent Progress in Extreme Environment Durable SiC JFET-R Integrated Circuit Technology." *International Conference and Exhibition on High Temperature Electronics* (HiTEC). 2023.

[315] Rysy, S., Sadowski, H., and Helbig, R. "Electrochemical etching of silicon carbide." *Journal of Solid State Electrochemistry* 3 (1999): 437-445.

[316] Consiglio Nazionale delle Ricerche web site, URL: https://www.cnr.it/it/istituto/057/istituto-per-la-microelettronica-e-microsistemi-imm, last visit: 29/02/2024.

[317] Nida, S., et al. "Silicon carbide X-ray beam position monitors for synchrotron applications." *Journal of synchrotron radiation* 26.1 (2019): 28-35.

[318] Dahal, R. P., et al. "Fabrication of thick free-standing lightly-doped n-type 4H-SiC wafers." *Materials Science Forum.* 897. Trans Tech Publications Ltd, 2017.

[319] STMicroelectronics Company web site, URL: https://www.st.com/content/st_com/en.html, last visit: 29/02/2024.

[320] DT547x Power Supply, URL: https://www.caen.it/subfamilies/up-to-5-kv-dt547x/, last visit: 29/02/2024.

[321] NI-9223, URL: https://www.ni.com/it-it/shop/model/ni-9223.html, last visit: 29/02/2024.

[322] Donald A. Neamen, Semiconductor Physics & Devices: Basic Principles, Fourth Edition, 2012

[323] Gerhard Lutz, Semiconductor Radiation Detectors, Springer-Verlag Berlin Heidelberg 1999, 2007

[324] S. M. Sze, Kwok K. Ng, Physics of Semiconductor Devices, 2007, John Wiley & Sons, Inc.

[325] KEITHELY 6517B, URL: https://www.tek.com/en/datasheet/6517b-electrometer-high-resistance-meter, last visit: 29/02/2024.

[326] HP 4284A Precision LCR Meter, URL: https://xdevs.com/doc/HP_Agilent_Keysight/HP%204284A%20Operation.pdf, last visit: 29/02/2024.

[327] Ústav jaderné fyziky AV ČR, v. v. i. web site, URL: https://www.ujf.cas.cz/en/, last visit: 29/02/2024.

[328] Trento Institute for Fundamental Physics and Applications (TIFPA) web site, URL: https://www.tifpa.infn.it/, last visit: 29/02/2024.

[329] Schillaci, F., et al. "The ELIMAIA Laser–Plasma Ion Accelerator: Technological Commissioning and Perspectives." *Quantum Beam Science* 6.4 (2022): 30.

[330] Xu, X. H., et al. "Detection and analysis of laser driven proton beams by calibrated Gafchromic HD-V2 and MD-V3 radiochromic films." *Review of Scientific Instruments* 90.3 (2019).

[331] ImageJ, URL: https://imagej.net/ij/, last visit: 29/02/2024.

[332] Tommasino, F., et al. "Proton beam characterization in the experimental room of the Trento Proton Therapy facility." *Nuclear Instruments and Methods in Physics Research Section A: Accelerators, Spectrometers, Detectors and Associated Equipment* 869 (2017): 15-20.

[333] EPO-TEK 509FM-1, URL: https://www.epotek.com/docs/en/Datasheet/509FM-1.pdf, last visit: 29/02/2024.

[334] Givehchi, N., et al. "Online monitor detector for the protontherapy beam at the INFN Laboratori Nazionali del Sud-Catania." *Nuclear Instruments and Methods in Physics Research Section A: Accelerators, Spectrometers, Detectors and Associated Equipment* 572.3 (2007): 1094-1101.

[335] Cirrone, G. A. P., et al. “Clinical and Research Activities at the CATANA Facility of INFNLNS: From the Conventional Hadrontherapy to the Laser-driven Approach.” *Front. Oncol* 7, 223 (2017).

[336] Advanced Markus® Electron Chamber, URL: https://www.ptwdosimetry.com/en/products/advanced-markus-electron-chamber, last visit: 29/02/2024.

[337] FRAUNHOFER Company web site, URL: https://www.fraunhofer.de/en.html , last visit: 29/02/2024.

[338] LPE Company web site, URL: https://www.lpe-epi.com/, last visit: 29/02/2024.

[339] 4263B LCR Meter, URL: https://www.keysight.com/us/en/product/4263B/lcr-meter-100-hz-to-100-khz.html , last visit: 29/02/2024.

[340] Thompson, A.C., et al., “X-Ray Data Booklet”, *Lawrence Berkeley National Laboratory*, 2009.

[341] Nguyen, T., et al. "Note: A simple-structured anode exchangeable X-ray tube." *Review of Scientific Instruments* 84.5 (2013).

[342] Detector Company web site, URL: https://detector-group.com/, last visit: 29/02/2024.

[343] PXIe-1071, URL: https://www.ni.com/it-it/shop/model/pxie-1071.html, last visit: 29/02/2024.

[344] PXIe-8821, URL: https://www.ni.com/docs/en-US/bundle/pxie-8821-specs/page/specs.html, last visit: 29/02/2024.

[345] PXIe-7821, URL: https://www.ni.com/docs/en-US/bundle/pxie-7821-specs/page/specs.html, last visit: 29/02/2024.